THÈSE

Pour obtenir le grade de

DOCTEUR DE L'UNIVERSITÉ GRENOBLE ALPES

Spécialité : BIS - Biotechnologie, instrumentation, signal et imagerie pour la biologie, la médecine et l'environnement

Arrêté ministériel : 25 mai 2016

Présentée par

Larry O'CONNELL

Thèse dirigée par **Pierre MARCOUX**,Ingénieur chercheur, Université Grenoble Alpes
et codirigée par **Yoann ROUPIOZ**, CNRS

préparée au sein du **Laboratoire Systèmes Moléculaires et Nano Matériaux pour l'Énergie et la Santé**
dans **l'École Doctorale ISCE - Ingénierie pour la Santé la Cognition et l'Environnement**

Test optique de susceptibilité aux bactériophages par SPR (résonance plasmonique de surface)

Optical Bacteriophage Susceptibility Test by Surface Plasmon Resonance

Thèse soutenue publiquement le **31 mai 2022**,
devant le jury composé de :

Monsieur PIERRE MARCOUX
Ingénieur docteur, CEA CENTRE DE GRENOBLE, Directeur de thèse
Monsieur CHRISTOPHE GANTZER
Professeur des Universités, UNIVERSITE DE LORRAINE, Rapporteur
Madame MAGALI PHANER-GOUTORBE
Professeur, ECOLE CENTRALE LYON, Rapporteure
Monsieur YOANN ROUPIOZ
Directeur de recherche, CNRS DELEGATION ALPES, Co-directeur de thèse
Monsieur DONALD MARTIN
Professeur des Universités, UNIVERSITE GRENOBLE ALPES, Examinateur
Monsieur GREGORY RESCH
Professeur assistant, Université de Lausanne, Examinateur
Monsieur BRUNO LE PIOUFLE
Professeur des Universités, ENS CACHAN, Président

Acknowledgements

No PhD is the work of one person alone. I would like to express my gratitude to everyone who helped make this work possible. I would like to start with my *Directeur de Thèse*, Pierre Marcoux, for throwing me a lifeline during a difficult interval by bringing me on board his project, for introducing me to a new world of bacteriophages, and for acting as my advocate in our collaborations. His enthusiasm for his work and his sense of curiosity serve as an example to us all. I would also like to thank my co-*Directeur de Thèse*, Yoann Roupioz, for welcoming me to the team at CREAB, for having confidence in me to suggest we pursue a *thèse sur article*, and for being available at all times for guidance and endless corrections. I would also like to express my sincere gratitude to labex ARCANE, who financed my PhD.

I'd like to thank the rest of the team at CREAB as well: Camille Raillon, for her encouragement and sympathetic ear, advice on microfluidics, and leaving me a bottle of much-needed PDMS. Jose Galvez, for his support and for keeping us stocked with everything we needed, and patience with incessant requests for product references and order updates. Raphael Mathey, for assistance with innumerable aspects of lab work. Pierre-Henri Elchinger and Elise Jacquier, for help with atomic force microscopy, and Christine Saint-Pierre for help with DLS characterization of my phages. Loïc Leroy, for initiating me into the world of surface plasmon resonance, frequent advice regarding SPR phenomena, and his invaluable help with the setup of the electronic side of electrokinetic SPR experiments. Marie Gaillard, for encouragement and for invaluable advice about hiking routes around Grenoble. Charlène Plénière not only for her assistance with peptide arraying, but also for being a pleasure to share an office with.

At Y.SPOT, I had the pleasure of fruitful collaboration with the two reigning managers of the fablab during my time. I'd like to sincerely thank Brice Poirier for being someone I could bounce ideas off, and for his efforts on laser patterning which enabled a large part of my PhD. I can only hope to find more colleagues like Brice in the future. Hubert Teyssedre I would like to thank for his endless patience, who surpassed all reasonable expectations to help develop the laser patterning process.

I'd also like to thank the colleagues that I was able to collaborate with over the years. Emmanuel Picard, for his trust in providing me with microscopy equipment and encouragement in pursuing my papers. Simon Glicenstein, for assistance with his optical bench and adaptability despite my frantic schedule. Pierre-Henri Jouneau for assistance with electron microscopy, without whom I would have left CEA without ever actually seeing my phages.

At DTBS, I'd like to thank Sophie Morales for her heart-felt encouragement and investment in my development at CEA. Marie Escudé for training on the ultrasound probe. Ondrej Mandula, for facilitating a whole new dimension of one of my papers with the construction of a phase-imaging microscope. Bilal Demir, for help with

dialysis and generally making the lab a more cheerful place. Prisca Perlemoine, for helping me take my very first steps in bacteriophage culture.

Not only at CEA but also further afield. At Institut de Biologie Structurale there was Christine Chatellard who was always available for assistance with nanoparticle tracking analysis, and Daphna Fenel who assisted with transmission electron microscopy.

I thank Marianne Weidenhaupt at Grenoble-INP for participation in my CSI but also for giving me the opportunity to work together on the Nano@School outreach program.

I'd also like to thank Tiphaine Belloir, for welcoming me to CEA and showing me the ropes during my weeks on the site. Jonathan Weerakkody, for making me feel welcome at CREAB from the day I arrived to share his office, and for years of friendship and advice afterwards. Oleksii, a fine colleague and friend, who helped not only with my experiments but also the human side of PhD life.

Closer to home, I can never thank enough my parents Rosemary and Philip for their constant support, not only during this PhD but also in the years before. I'd like to thank my brother Rúairí for encouragement and for going above and beyond to provide equipment, without which much of the work of my PhD would not have been possible.

Lastly and most of all, I thank my fiancée Genevieve, who continues to be a model to aspire to as an academic, a partner, and a friend. I knew that whatever happened, you were always in my corner.

Preamble

The ability to overcome common bacterial infections and enjoy the benefits of routine medical procedures has come to characterize modern civilization at such a profound level that it is difficult to conceive of what we would recognize as a functioning society without these luxuries. Equally, it makes it easy to become complacent about the prospect of ever losing our capacity to exercise such fine control over our immediate microbial environment. The availability of antimicrobials informs decision-making in areas as diverse as social welfare, recreational and professional sports, military strategy, reproductive health, space exploration, agriculture and many others. It is difficult to find a technology that is comparably crucial to the proper functioning of society as microbial control.

However, the widespread overuse of antibiotics has led to the proliferation of antimicrobial resistant (AMR) bacteria. This phenomenon is having an increasing and profound impact on health outcomes worldwide, with recent data reporting an overwhelming burden of 1.27 million deaths attributable to bacterial antimicrobial resistance in 2019,[1] poised to grow to 10 million per year by 2050.[2] Given the societal upheaval associated with the 3.5 million deaths attributable to covid-19 in 2021,[3] it is clear why the World Health Organization (WHO) has declared that AMR is no longer a looming threat, but a contemporary crisis.[4]

The exploitation of antibiotics was, in some sense, entirely rational. Shedding humanity's vulnerability to bacterial pathogens allowed unprecedented improvements in quality of life. The intensive farming of livestock permitted by prophylactic administration of antibiotics provided a cheap source of animal protein[5] to a global population that swelled from 1.7 to 6.1 billion people over the course of the 20th century. [6,7] Now, just as with our reliance on fossil fuels, we are coming to appreciate the temporary nature of the reprieve afforded by classic antimicrobials, and new solutions are urgently being sought.

It is within this context that bacteriophage (phage) therapy is receiving increased attention as an alternative therapeutic pathway to classical antibiotics. In order to facilitate a paradigmatic transition to phage therapy, new tools are needed to support a nascent phage therapy infrastructure.[8]

Keywords: bacteriophage susceptibility testing, surface plasmon resonance imaging, purification, immobilization, microfluidics, bioactive surfaces, nanoparticle tracking analysis, phage microarray, laser ablation, rapid prototyping, dielectrophoresis, electro-osmosis

Table of Contents

List of Figures

Chapter 1

Introduction

1.1 The History of Antibiotics

The discovery of penicillin in 1928 by Alexander Fleming led to a paradigm shift in the treatment of bacterial infections. Prior to its discovery, death was a common outcome resulting from routine medical procedures and what would now be considered mild bacterial infections.[9]

As with many 20th century technological developments, the use of antibiotics became widespread after being leveraged for the purposes of military conquest, in this case by the United States. Although penicillin was discovered in peacetime, World War II provided the impetus to scale up mass production, which established antimicrobial molecules as the "magic bullet" for treatment of any bacterial infection in wider society (**Figure 1.1**).[10]

Penicillin was the first of a major category of antibiotics known as the beta-lactam class, named for the presence of a beta-lactam ring in the structure of these molecules. The mechanism of action of beta-lactam antibiotics (BLA) relies on their ability to inhibit synthesis of peptidoglycan, a principal component of the

Figure 1.1 United States propaganda promoting the use of penicillin in the armed forces.
Reproduced from Life Magazine, August 14, 1944.

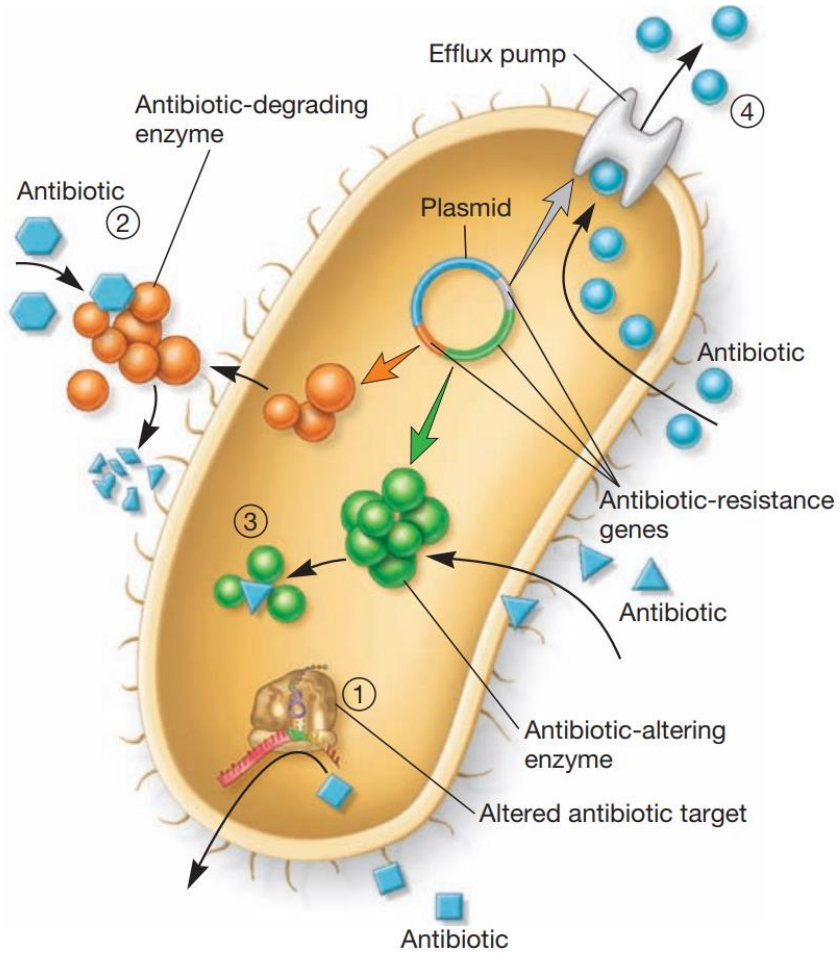

Figure 1.2 Antibiotic resistance mechanisms.
Bacteria can resist the action of antibiotics by (1) preventing access to (or altering) the target of the antibiotic (*e.g.*, modification of penicillin-binding proteins), (2) degrading the antibiotic (*e.g.*, using beta-lactamases), (3) altering the antibiotic, and/or (4) rapid extrusion of the antibiotic using efflux pumps. Reproduced from Prescott *et al.*[19]

bacterial cell wall.[11] In the absence of resistance mechanisms, BLAs cause bacteria to shed their cell walls during division and form osmotically vulnerable spheroplasts that lyse easily, killing the cell.[12]

1.1.1 Antimicrobial Resistance Mechanisms

While there exist several classes of antibiotics with various mechanisms of action, BLAs are the most widely used.[13] A brief discussion of bacterial resistance to BLAs is instructive to understand the general principles behind resistance to other classes of antibiotic.

The widespread overuse of BLAs led to a proliferation AMR mechanisms against them[9] including production of beta-lactamases (enzymes that degrade most BLAs by hydrolyzing the beta-lactam ring[14]), drug efflux pumps[15] (cell membrane structures that actively and selectively pump antibiotics out of the bacterial cell), and alterations to bacterial proteins (*e.g.*, penicillin-binding proteins[16]) (**Figure 1.2**). In response, clinicians began to administer BLAs with beta-lactamase *inhibitors*, enzymes which inactivate beta-lactamase by various mechanisms, thus restoring the efficacy of co-administered BLAs against resistant bacteria.[17] True to form, bacteria continued the arms race by evolving to produce beta-lactamases resistant to inhibition.[18]

This pattern lays bare an inherent problem with antibiotics: that they are static molecules with transmissible loss of efficacy over time.[20] As such, they are “stationary targets” for bacterial adaptation, incapable of modifying their mechanism or spectrum of action to maintain their potency against bacteria.

1.1.2 Antibiotic Stewardship

Exposure of bacteria to an antibiotic, be it in the body or in the environment, applies an evolutionary pressure on the exposed bacterial strains which inevitably increases the abundance and distribution of ubiquitous and ancient genes coding for resistance mechanisms.[21,22]

This evolutionary selection increases the probability that resistance genes will be recruited from environmental genetic reservoirs into clinically relevant pathogenic bacteria through various mechanisms of horizontal gene transfer,[23] most importantly plasmid exchange.[24]

The 20th century saw a steady drumbeat of discoveries of novel antimicrobials, followed by their widespread overuse, and then the seemingly *ex nihilo* appearance and propagation of resistance mechanisms in human and animal pathogenic bacteria, and finally an increase in treatment failures with these agents (**Figure 1.3**). There is thus a need to limit the administration of novel antimicrobials so that we may prolong their efficacy as long as possible.[20]

For this reason, a patient presenting with an antibiotic-resistant infection should be treated first with more frequently used, clinically safer antibiotics before progressing to drugs which are de-prioritized on account of their value against resistant bacteria but also due to carrying increasingly severe side effects. These latter drugs may be effective against an AMR pathogen but the associated side effects may lead to worse health outcomes, post-treatment sequelae, or shorten the available duration of antibiotic treatment due to drug-induced organ failure. One of the final antibiotics in such a sequence — colistin — is known as an "antibiotic of last resort" due to its high nephrotoxicity despite being effective against multi-resistant bacteria.[25]

This strategy of holding antibiotics in reserve is one aspect of a healthcare policy known as *antibiotic stewardship*.[20] However, although important, such policies can only delay the inevitable proliferation of resistance to all known and future antibiotics.[26] Indeed, the plasmid-borne *mcr-1* gene conferring resistance even to colistin was first reported in 2015[27] and similar genes have since been observed in many distantly related bacterial species.[28]

At the heart of this crisis are the so-called ESKAPE pathogens — *Enterococcus faecium*, *Staphylococcus aureus*, *Klebsiella pneumoniae*, *Acinetobacter baumannii*, *Pseudomonas aeruginosa*, and *Enterobacter spp.* are a small coterie of pathogenic bacterial strains which are resistant to many antibiotics and cause the vast majority of nosocomial (*i.e.*, hospital acquired) infections.[9] Special focus is given to the ESKAPE pathogens since they are considered to represent the full suite of AMR mechanisms that are available to pathogenic bacteria. Not only do these strains possess a diverse range of resistance mechanisms, they also frequently retain them as mobile genetic elements such as plasmids, which aid the dissemination of these mechanisms in the environmental resistome.

1.1.3 The Discovery Void

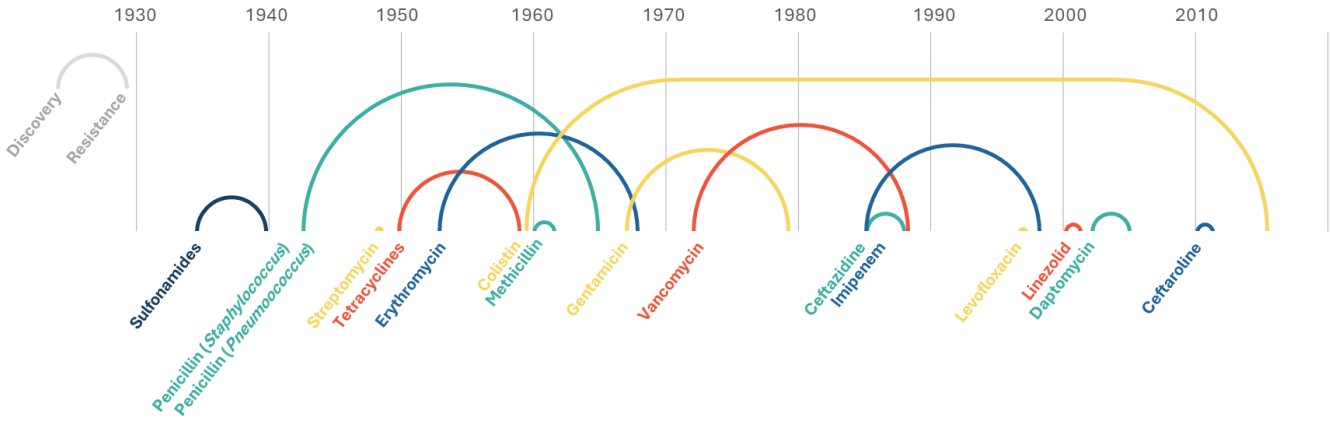

Figure 1.3 Timeline of deployment of various antibiotics throughout the 20th and 21st century vs. the date of observed resistance to each compound. Adapted from the 2019 CDC Report on Drug Resistance.[29]

The phenomenon of AMR must also be understood within the economic context of profit-driven antibiotic discovery and a reluctance on the part of the pharmaceutical industry to develop novel antimicrobials. A 2017 paper estimated a cost of 1.6 billion US dollars to bring a new antibiotic to market,[30] at which point the product is likely to be reserved as the new antibiotic of last resort and only used — and thus generating revenue for its manufacturer — once other treatment options have been ruled out. This creates an environment which makes the development of new antimicrobials unprofitable — and thus unviable — for pharmaceutical companies.[30] A weak development pipeline for new therapies has led to a "discovery void" wherein very few novel classes of antibiotics have been discovered in over three decades since the discovery of daptomycin.[31,32] A 2020 review by the WHO found that out of 43 antibiotics currently under development, only two represent a novel class and none are intended for treatment against extensively or multidrug-resistant gram-negative bacteria.[33] Most "new" antibiotics are actually just tailored derivatives produced through peripheral modifications to scaffolds which were discovered in the 1930s-1960s.[32]

Now, just as with our reliance on fossil fuels, we are now coming to appreciate the temporary nature of the reprieve afforded by classic antimicrobials, and new solutions are urgently being sought.

1.2 Bacteriophages

One such alternative to traditional antibiotics is presented by bacteriophages (phages).[33] Phages are obligate intracellular parasitic viruses which replicate exclusively by infecting a cell of a host bacterium, hijacking its molecular machinery before directing it towards the synthesis and assembly of new progeny phage particles (**Figure 1.4**).[34] These progeny phages then leave the host cell and can initiate a new infection in a subsequent cell, completing the life cycle. Given a supply of suitable host bacteria, phage numbers increase exponentially, killing all host cells. In this way, phages have an intrinsic ability to act as antimicrobials.

Phages are the most numerous replicating biological entity on Earth, with an estimated 10^{31} phage particles contained within the biosphere, compared to an estimated 10^{30} bacterial cells.[35,36] Phages have been found in terrestrial soil,[37] Tibetan hotsprings,[38] deep-sea sediments,[39] inside industrial bioreactors,[38] and even as the main component of DNA sequenced from soil from under the Arecibo space telescope.[40] Indeed, the estimated daily turnover of 15% of all bacterial cells due to phage lysis is a testament to their crucial role in microbial ecology.[41]

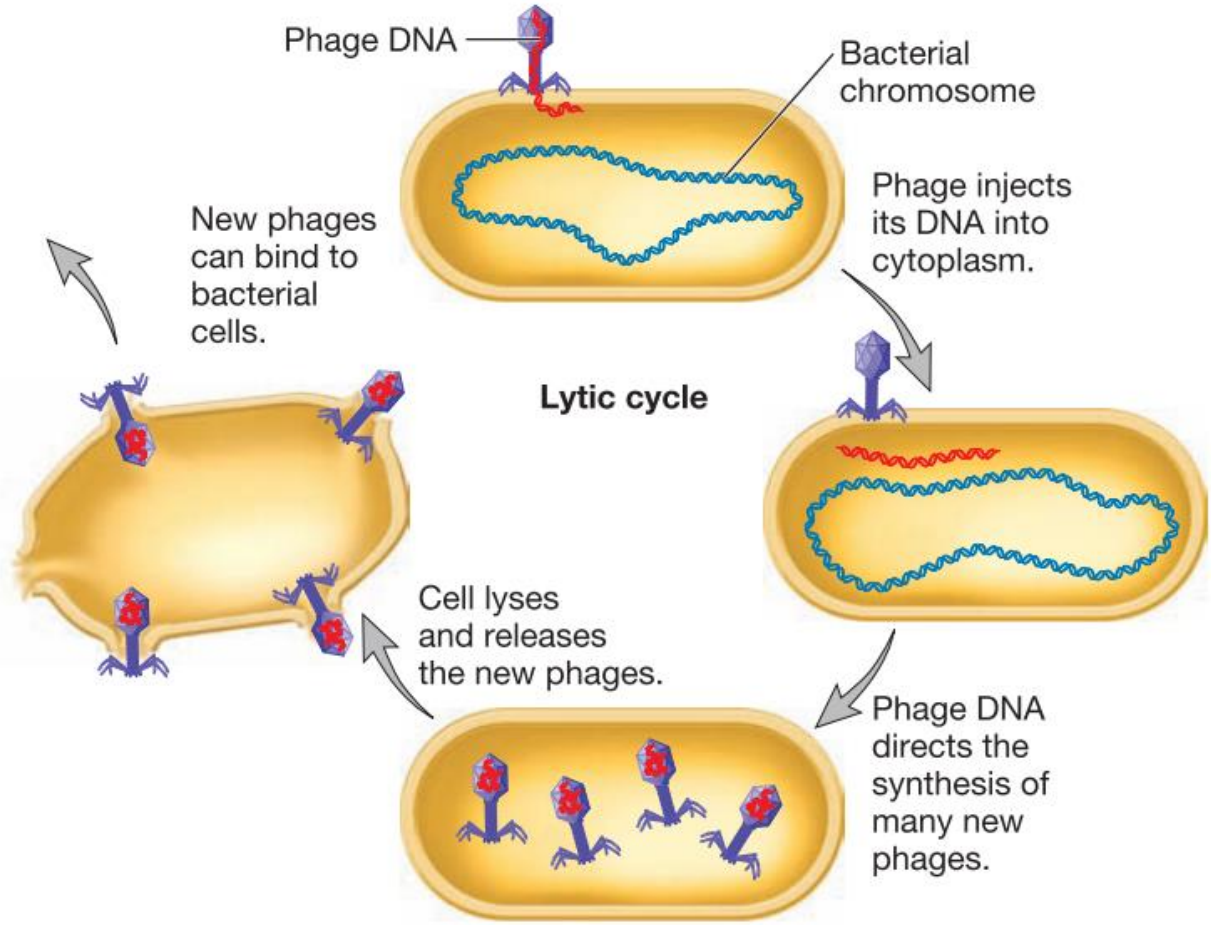

Figure 1.4 The lytic replication cycle of bacteriophage T4. Adapted from Prescott *et al.*[42]

1.2.1 The History of Phage Research

The independent discovery of phages is attributed to microbiologists Frederick Twort in London in 1915 and Felix d'Herelle in Paris in 1917.[43] Mirroring the popularization of antibiotics by the US military, phages first saw widespread adoption in the Soviet Union for the treatment of routine bacterial infections, beginning in the 1938 Soviet military campaign in Finland and later in World War II.[44] Bacteriophage therapy was an area of intense research behind the Iron Curtain, but the period following the second World War was characterized by geopolitical paranoia and a lack of scientific cooperation between so-called first and second world-aligned states. The Soviet obsession with secrecy extended to the reporting of phage research within its institutions. A glaring example of this was a large-scale, randomized, double-blinded, placebo-controlled phage therapy trial involving 30 000 children in the 1960s which was reported in only a single article featuring only 75 lines of text and one table of data.[45,46] In most cases such studies suffered from critical flaws including insufficiently purified and low-concentration phage preparations, narrow host range, incompatibility of phage with excipients etc. In comparison to the broad spectrum of action of antibiotics, phage therapy increasingly came to be dismissed in the west as obsolete and needlessly onerous,[47] which led to a progressive dismissal of the technology and a policy of unfettered use of antibiotics, which continues to this day.[48] In the 1970s, up to 70 patients underwent phage therapy every year to treat bone and joint infections in Croix Rousse Hospital, Lyon, France[49]; but such therapy was discontinued by the end of the decade.

The fall of the Soviet Union saw a largescale abandonment of phage therapy in the former Soviet bloc, with the torch being passed almost entirely to the Hirszfeld Institute in Wroclaw, Poland; and Georgian researchers at the Eliava Institute of Tblisi, in particular.[50]

It should be noted that while research into the therapeutic use of bacteriophages was deprioritized during the end of the 20th century, fundamental research on phages themselves continued. Indeed, phage research facilitated many landmark discoveries in biology, not least of which was a contribution to the understanding of the structure of nucleic acids and the molecular basis of heredity,[51,52] and more recently the discovery of the CRISPR-Cas bacterial adaptive immune system used for gene editing.[53]

With the growing appreciation of the urgency of identifying alternatives to antibiotics, interest in phage therapy is resurgent and poised to benefit from the intervening years of fundamental research on phage biology. However, before widespread adoption of phage therapy is feasible, largescale, double-blind, scientifically controlled clinical trials are absolutely essential. Studies of this type are unfortunately sparse. This is partly because of the trend that phage therapies are often sought after on an individual basis and used as an "exotic" last resort intervention for acute or chronic antibiotic-resistant infections.[54]

1.2.2 Current Therapeutic Use of Phages

The history of phage therapy can be delineated into two categories. On the one hand are early and foundational trials that lacked scientific rigor yet nevertheless produced encouraging results. The earliest of such studies were famously carried out by d'Hérelle to treat dysentery in Paris in 1919,[55] and later bubonic plague in Egypt and cholera in India beginning in the 1920s.[56] Phage therapy trials against dysentery were also carried out in Poland during the interwar period[10] as well as in Brazil.[57] The results of extensive phage therapy testing in the Soviet Union and Poland are reviewed by Alisky *et al.*[58] and Sulakvelidze *et al.*[59], with the authors noting that basic details of studies were absent or of questionable reliability.

On the other hand are contemporary studies, usually small in scale, which contain good reporting of experimental methods and observe exciting results but are still hampered by a lack of scientific controls. Without such controls, these studies amount to a large quantity of anecdotal evidence, the plural of which, as the saying goes, is not data. A selection of these studies is outlined here briefly.

Pre-adapted bacteriophages from Eliava Institute have been shown to be highly effective in clearing an infection of pan-drug resistant *K. pneumoniae* that had not responded to antibiotic treatment for a period of 702 days following an injury incurred during the 2016 terrorist attacks at Brussels Airport.[60] The pre-adapted phages were selected from a phage bank at the Eliava Institute and personalized to the patient's specific strain of *K. pneumoniae*.

A 2017 paper reported the treatment of a 68-year-old diabetic with a multidrug-resistant *A. baumannii* infection.[61] Iterative administration of cocktails of different permutations of nine bacteriophages resulted in clearance of the *A. baumannii* infection and a return to good health.

In 2019 it was reported that a 15-year-old cystic fibrosis patient suffering from recurrent *Mycobacterium abscessus* infection was successfully treated with a three-phage cocktail.[62] Emphasized in that work was the importance of screening of a large number of candidate phages against the *M. abscessus* isolated from the patient. A summary of phage treatment of pulmonary infection can be found in the work of Abedon.[63]

One widely anticipated trial was the PhagoBurn project that sought to produce high-quality data from a phase I/II clinical trail on the use of phages against bacterial colonization of burn wounds, jointly supervised by French, Swiss, and Belgian drug safety agencies.[64]

However, the PhagoBurn project was repeatedly reduced in size and scope from its initial conception, eventually leaving aside treatment of *Escherichia coli* to focus only on *P. aeruginosa*, and recruiting only 27

patients compared to the planned number of 110.[65] Finally, the PhagoBurn project saw poor outcomes after patients inadvertently received a 1 000-fold to 10 000-fold lower dose of phages than intended due to phage decay during storage.[64,66] Although patients receiving phages experienced fewer adverse events compared to the control, the former group took significantly longer to exhibit reduction in bacterial bioburden. This is a disappointing result that speaks more to the need for optimized phage storage and preparation practices than to the weakness of phage therapy itself. As discussed below, phage therapy can be extraordinarily effective when properly carried out, especially in synergistic therapy combined with antibiotics (See Bacteriophage Therapy Case Study).

Of note is that out of the four studies described above, three concerned pathogens of the ESKAPE group, which reflects their outsized contribution to nosocomial and AMR infections.

Interestingly, there is evidence that some current medical procedures inadvertently involve a form of phage therapy. Although unappealing, fecal transplants from healthy donors are currently by far the most effective treatment against persistent infections of *Clostridium difficile*,[67] which otherwise cause severe illness and multi-month stays in hospital.[68] It was assumed that the mechanism of action of such transplants was the introduction of commensal intestinal bacteria from a healthy donor, which outcompete *C. difficile* and restore the balance of normal intestinal microbiota. However, it has been shown that fecal transplants are effective even when the material has been filter-sterilized through a membrane of 0.2 µm pore size which allows phages but not bacteria to pass.[69] Such results have led to speculation that the success of fecal transplants lies in the transfer not only of the bacterial population of the donor, but of the phage population too.[70]

Compared to antibiotics, phages have many desirable features and advantages over antibiotics. They have been found to be remarkably safe pharmaceuticals.[71] Purified phages do not illicit any life-threatening immune response in the body, even when administered intravenously.[72,73] The narrow spectrum of action of phages circumvents problems with dysbiosis associated with killing of normal commensal bacteria by broad spectrum antibiotics.[71]

In contrast to the grimly reliable appearance of antibiotic resistance, no permanent mechanism of pan-phage resistance has developed. Unlike the stationary target of an antimicrobial molecule, phages are capable of circumventing anti-phage resistance mechanisms on the basis of their genetic plasticity and rapid replication.[74] This is partly why phage therapy is seen as a promising emerging strategy for treatment of ESKAPE pathogens.[75]

Bacteriophage Therapy Case Study

In December 2001, three Georgian forestry workers were hiking in the forested region east of the town of Lia. Despite the cold weather of mid-winter, they came upon a clearing of melted snow surrounding two small metal canisters producing significant amounts of heat.[76] Without understanding the nature of the canisters, the three men camped in the melted clearing to take advantage of the mysterious warmth, sleeping for several hours with their backs to the objects at a distance of ~10 cm.[76] Unknown to the men, the objects were highly radioactive strontium-90 cores of a thermoelectric generator, a long-term nuclear power source abandoned from an incomplete ex-Soviet radio relay system.[77]

All three men were exposed to significant doses of radiation and were transferred to hospital — first in nearby Zugdidi and then T'bilisi — suffering from acute radiation syndrome. Exposure to ionizing radiation resulted in large skin lesions on the backs of two of the men. As is frequently the case in large surface area tissue damage[78], a persistent *Staphylococcus aureus* infection developed in the lesions.[76]

Over the course of 23 days, despite administration of a sequence of different antibiotics (ceftriaxone, gentamicin, levomycetin, and vancomycin) no elimination of *S. aureus* infection was observed in the infected lesions. The strain of *S. aureus* infecting the mens' lesions had acquired a suite of multiple resistance mechanisms, making it highly resistant to all antibiotics used, and wound healing could not progress as a result of the bacterial infections.[79] When it became clear that antibiotics were unlikely to prove effective, the doctors explored the use of bacteriophages.

One month after admission to hospital, the patients were treated with PhagoBioDerm, a commercial phage preparation consisting of a polymer dressing impregnated with ciprofloxacin and a mixture of bacteriophages with lytic activity against *S. aureus*, *Pseudomonas aeruginosa*, *Escherichia coli*, *Streptococcus*, and *Proteus.*[80] The results were striking. Within 2 days, purulent drainage from the lesion ceased and *S. aureus* was eliminated from the wound sites within 7 days for both patients, allowing closing of the open wounds and healing.[79]

Following phage treatment, the two patients suffering from lesions survived, with their recovery being attributed to the lytic activity of the bacteriophage treatment.[79]

1.2.3 Bacteriophage Structure and Life Cycle

Phages are grouped into three main categories on the basis of their life cycle. *Lytic phages* terminate their replicative cycle with the biochemical lysis of their host cell, rupturing the cell membrane and releasing up to several hundred progeny virions in one burst (**Figure 1.6**).[51] In contrast, *lysogenizing* phages incorporate their genetic material into the genome of the bacterial host (either into the chromosome or as a plasmid[81]) lying dormant before shifting to a lytic cycle. Finally, some phages may instead continually produce a smaller number of phages which are shed from the host on a continuous basis in what is known as a *chronic* infection.

Phage structure exhibits large variation which falls within a few stereotyped morphologies. Broadly speaking, phage morphology can be grouped into long contractile-tailed myoviruses, long non-contractile-tailed siphoviruses, short-tailed podoviruses, non-tailed tectiviruses and cystoviruses, and filamentous inoviruses (Figure 1.5).[82] Siphoviridae are more frequently seen in *Streptococci*, *Actinomycetes*, *Coryneforms*, and *Lactococci*; while myoviruses and podoviruses are more frequent in *Pseudomonads*, *Bacilli*, and *Clostridia*.[34]

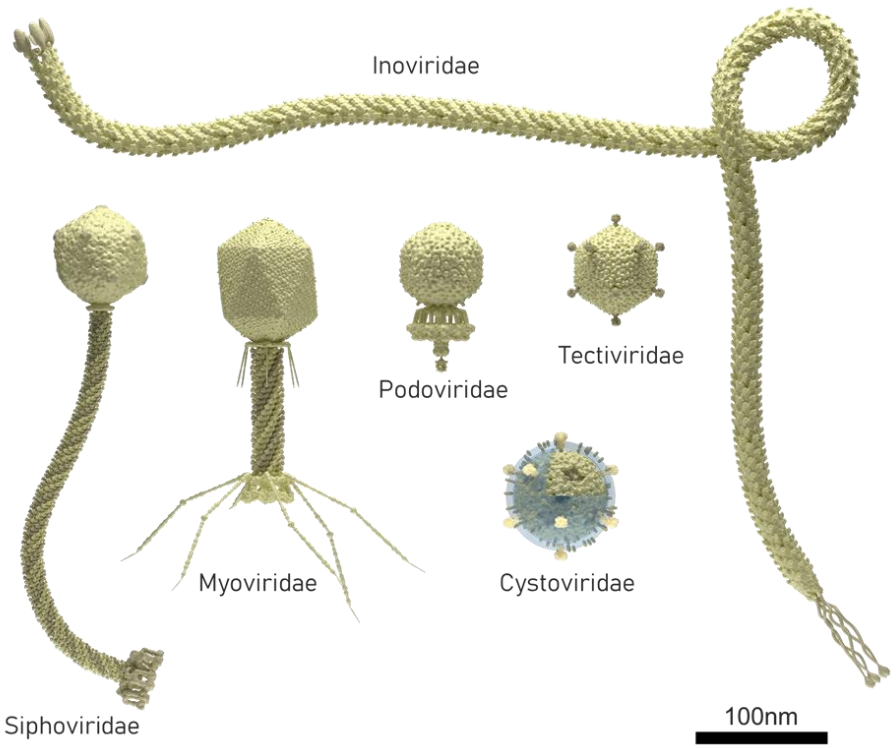

Figure 1.5 Illustrations of the most common bacteriophage morphologies.
The *Inoviridae* family comprises filamentous phages such as fd and M13. The *Myoviridae* family features long contractile-tailed phages and includes Remus and the well-known T4 coliphage. The *Siphoviridae* family features long non-contractile-tailed phages such as D29. Meanwhile, the *Podoviridae* family are short-tailed and includes P68, 44AHJD and gh-1. Relative scales are approximate.

1.2.4 Phage Specificity

The host range of a phage depends on several factors but most strongly on its ability to specifically recognize and bind to cells of host bacterial strains *via* host-range-determining regions on the receptor-binding domains of the phage capsid.[83] Because of this specific binding, phages have a narrow host range that is species or even strain-specific. This constrained spectrum of action is advantageous since an administered phage targeting a given pathogen need not disturb the normal commensal flora of the patient,[84] in contrast to antibiotics which typically have a much larger spectrum of action.[32] However, this narrow host range also presents challenges that must be mitigated, namely that screening must be performed to ascertain the susceptibility of a given bacterial pathogen to a range of candidate phages in order to develop a cocktail personalized to each patient, composed only of phages to which the pathogen is susceptible.[71]

Bacteriophages are frequently administered in a cocktail of several different species in order to reduce or eliminate the selection for phage resistant bacteria[71] and to expand the host range.[71] Phage cocktails may also interact synergistically, achieving greater efficacy than any of the component phages in isolation. For example, one study demonstrated a synergistic effect of a cocktail of five phages against *A. baumannii* in a mouse model.[85] In isolation, four of the five phages did not kill the bacterial host, while the fifth merely slowed bacterial growth *in vitro*. However, when combined, the lytic action of one of the phage strains shifted the bacterial population towards emergent uncapsulated bacteria, which were then susceptible to the remaining four phages.

Also of note is the synergistic effect of phage when administered with antibiotics. Some antibiotic drugs are known to both inhibit cell division — increasing cell mass at sub-lethal doses — while also causing accelerated phage lysis. Phages have been shown to have evolved to take advantage of the former to boost burst size and the latter to spread more rapidly.[86]

The expanded host range of cocktails may present an economic and regulatory advantage. Demonstrating the safety — and obtaining regulatory approval — of a “lumped together” group of phages allows a manufacturer

to circumvent red tape by developing a single commercial phage preparation that can then be deployed in a variety of contexts.[71]

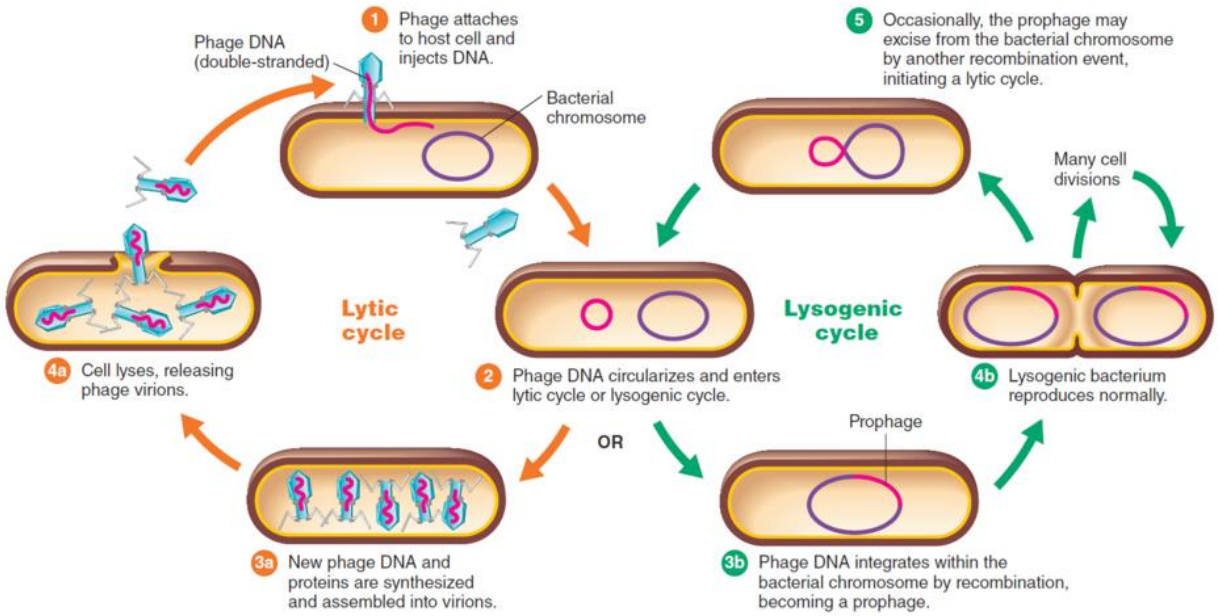

Figure 1.6 Illustration of the lysogenic replication cycle, with relation to the lytic cycle. Adapted from Tortora *et al.*[87]

Of the different morphologies and lifecycles exhibited by phages, only some are appropriate for phage therapy. Temperate phages must be avoided since lysogeny can confer virulence factors to the host bacteria *via* genetic transduction, increasing their pathogenicity.[88] Lytic phages are thus preferred since they are immediately lethal to their host bacterium and are less likely to enable horizontal gene transfer or induce superinfection immunity.[89] For these reasons, phages must be characterized and vetted on the above criteria (*inter alia*) before being incorporated into a library as suitable therapeutic agents.[88]

Thus, in order to facilitate a wholesale or partial transition from traditional antimicrobials to phage therapy, new tools are needed for the rapid and multiplexed screening of large libraries of candidate bacteriophages in order to provide a personalized phage to each patient. This process is known as phage susceptibility testing (PST).

1.3 State of the art

Antibiotic Susceptibility Testing (AST) is an *in vitro* process necessary to ascertain the susceptibility of a clinical, pathogenic strain of bacteria to the suite of antibiotics available, which depends on the resistance mechanisms the strain may have acquired.[90]

To minimize off-target effects of an antibiotic, it is necessary to establish the lowest concentration of the drug that shows no growth of the pathogen, known as the *minimum inhibitory concentration* (MIC).[90] Where in the range of concentration the MIC falls for a given pathogen/drug pair will determine which label that pathogen is given among the labels “Susceptible”, “Susceptible – Dose Dependent”, “Intermediate”, and “Resistant”. These labels are delineated by what are known as *clinical breakpoints* — boundaries predetermined for each drug that depend on that drug’s toxicity and side-effects at different concentrations.[91]

Since the prevalence and distribution of antibiotic resistance mechanisms will vary from one region to another — and even one facility to the next — antibiotic susceptibility surveillance data may be aggregated into

regional or facility-level antibiograms in order to give more locally-tailored guidance on therapeutic strategies.[92] Such antibiograms must also be regularly updated due to increasing prevalence of AMR.

A brief discussion of the parallels between AST and phage susceptibility testing (PST) is instructive because, to date, both tasks have benefitted from analogous attempts at automation and scalability. While automation of AST has been demonstrated since the 1990s, PST automation is a more recent undertaking.

1.3.1 Antibiotic Susceptibility Testing

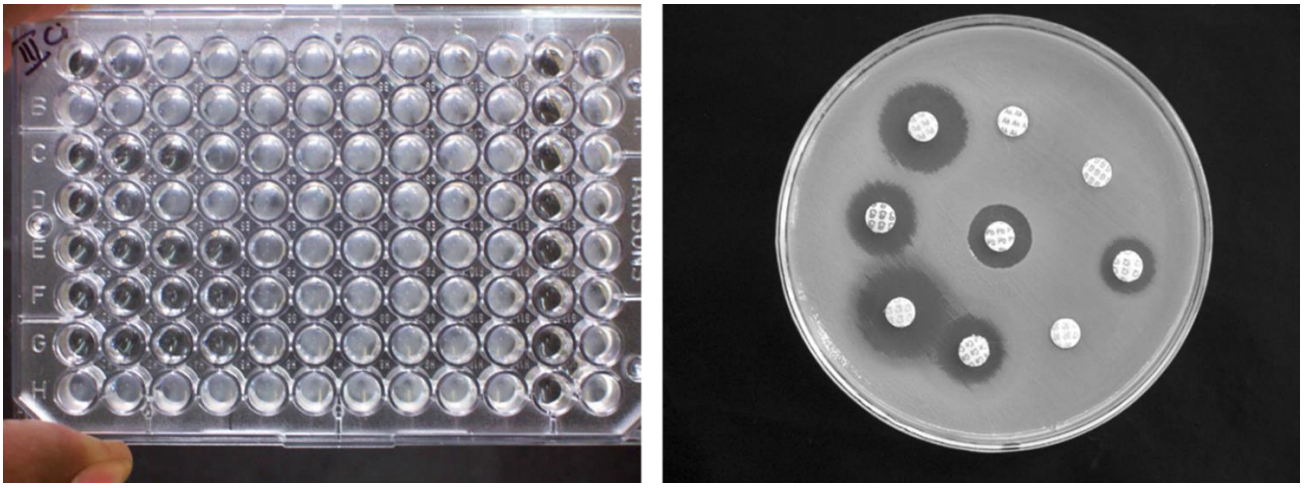

Figure 1.7 Left: An example of a completed broth microdilution antibiotic susceptibility test (AST).The minimum inhibitory concentration of an antimicrobial is that of the well with the least concentration that shows no growth. Right: A typical Kirby-Bauer disk diffusion AST. Zones of inhibition of various sizes form in a bacterial lawn surrounding disks of different antimicrobial agents. Images adapted from Wikimedia commons, distributed under a CC-BY 3.0 license (left) and public domain (right).

The gold standard *in vitro* method for establishing antimicrobial susceptibility is the broth micro-dilution test.[91] Serial two-fold (or other factor) dilutions of an antimicrobial agent are made in adjacent wells of a multi-well plate. A stock bacterial culture is then added to broth in each well and the plate incubated 16–24 hours, allowing a quantitative assessment of antibiotic susceptibility on the basis of the observed growth in the presence of each concentration of a given drug (**Figure 1.7**, left).[91]

Another, more qualitative AST method is the *Kirby-Bauer* or *disk diffusion test*, developed in the 1960s.[93] In this method, a small absorbent disk is impregnated with an antimicrobial agent of interest (**Figure 1.7**, right). The disk is then placed on a recently inoculated bacterial lawn on a standard agar plate. The antimicrobial will diffuse out of the disk into the surrounding agar, thus inhibiting the proliferation of bacteria in a visible region known as the *zone of inhibition*. The size of this zone relies on several factors, one of which is the level of susceptibility of the bacterial strain to inhibition by that antimicrobial. In this way, the size and morphology of the zone of inhibition gives qualitative information on the susceptibility of the bacterial lawn to the deposited antimicrobial agent.

The broth dilution method has been subject to automation in commercial devices. The Vitek 2™ (bioMérieux) is one example of a combined automated bacterial identification and AST apparatus. The mechanism of the Vitek 2™ involves aspirating a liquid culture of analyte bacteria into a cartridge containing an array of fluidic compartments, each containing a different lyophilized antimicrobial agent (**Figure 1.8**). The cartridge is then incubated and the optical density periodically measured in each compartment. The time-varying change in the optical density reveals the growth curve of the bacterial strain and hence its susceptibility to growth inhibition by each antimicrobial. This technique allows bacterial identification since each strain will have a characteristic set of growth curves in response to the array of antimicrobials, which form a fingerprint that can be associated to a strain using machine learning and reference to a previously established database.

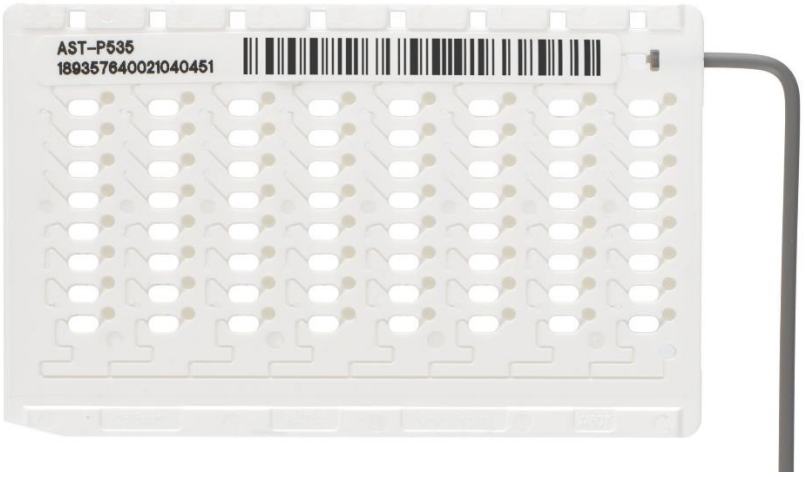

Figure 1.8 The Vitek 2™ cartridge
This consumable contains an array of separated fluidic compartments, each filled with a different lyophilized antibiotic. A bacterial liquid culture is automatically aspirated through the tube at right and aliquoted into each compartment. Bacterial growth is monitored optically for indications of growth inhibition which reveals the susceptibility of the strain to the antibiotics and also identification.

The Vitek 2™ is considered the gold-standard of AST tests by Clinical & Laboratory Standards Institute (CLSI) and has been approved for *in vitro* diagnostic use in Europe and by the United States Food and Drug Administration.[94] Other automated ASTs exist, with comparable performance, cost and convenience.[95]

Some automated time-saving methods such as the Vitek 2™ can reduce the time-to-results to, at best, 4-8 hours but more typically in the range of 9-13 hours.[95] In practice this effectively limits the AST to an overnight workflow.[96]

1.3.2 Phage Susceptibility Testing

Similarly to AST, PST is commonly carried out in broth and solid phases. In the broth method, serial dilutions of phage (or a phage cocktail) are placed in adjacent wells of a multi-well plate and co-cultured with a challenge strain of bacteria.[97] Either the broth becomes transparent, indicating lytic phage replication; or becomes turbid, indicating bacterial growth. In contrast, the agar overlay method involves the inoculation of bacterial host and a phage into molten, low-agar-content tryptic soy agar (TSA, ~6 g/L), which is then poured over another TSA layer of higher agar concentration (~15 g/L) in a standard petri dish and incubated.[98] After several hours, lysis plaques may become visible as regions of transparency embedded in the growing bacterial lawn (**Figure 1.9**).

These two types of PST in fact give complementary measurements. While the broth method yields an equivalent quantity to the MIC of an antibiotic: the minimum concentration of phage needed to prevent bacterial growth; the agar method yields a measurement of the efficiency of plating (EOP), a measure of the number of lysis plaques that can be produced by a phage suspension relative to the concentration of phage particles.[99]

Currently, the most frequently exploited methods for PST automation rely on the broth method of phage-bacteria co-culture since, of the methods available, liquid culture lysis is the technique that appears to be the most easily extensible to scalable automation. Lysis culture assays can be carried out in industry-standard microdilution transfer plates[100] which can feature as few as six and as many as several hundred individual wells (**Figure 1.10**). This method also permits combinatorial assays to establish phage synergy/antagonism with other phages or other antimicrobial agents, through a form of pair-wise checkerboard assay.[101]

In 2011, Cooper *et al.* adapted the Bioscreen C analyzer – a plate reader – to monitor optical density of bacteria-phage co-culture, in order to select for rapidly-infecting phages against *P. aeruginosa*.[102] This device allows the incubation of two 100-well plates simultaneously.

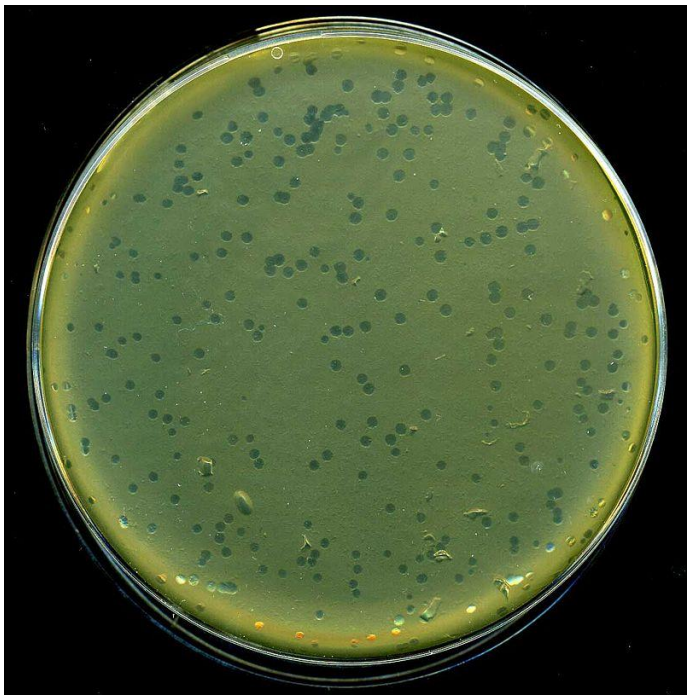

Figure 1.9 A typical agar overlay assay.
Lysis plaques are visible as pock-marked regions in a smooth bacterial lawn, caused by the reproduction of phages and lysis of bacterial cells *en masse* within each plaque. Each lysis plaque is regarded as originating from a distinct successful replication event of a single phage.

A drawback of this approach is that bacterial debris can continue to contribute to the optical density measurements, confounding interpretation of phage activity. To circumvent this, in 2007 McLaughlin enhanced optical density measurements of phage activity by the addition of tetrazolium to phage bacteria co-cultures.[103] Reduction of tetrazolium to formazan occurs only in actively metabolizing cells and produces a change in absorbance at 590 nm, allowing the identification of phages with lytic activity against *Salmonella enterica*.

In 2012 Henry *et al.*[104] and in 2016 Estrella *et al.*[105] combined tetrazolium enhancement of optical density methods with an adapted Omnilog system – another plate reader – to create an automated, high-throughput liquid lysis assay. The OmniLog system accepts fifty 96-well plates to allow up to 4 800 simultaneous individual phage-bacteria permutations.

All of these works rely on an optical density or colorimetric change with time-to-results of several hours. They are currently being used for isolation and identification of new phages[97], upstream from purification and characterization and potential inclusion in a phage library. To the author's knowledge, there is no indication in the literature of these methods being used directly for the parallel comparison of phage-host affinity for the purposes of providing personalized phage cocktails.

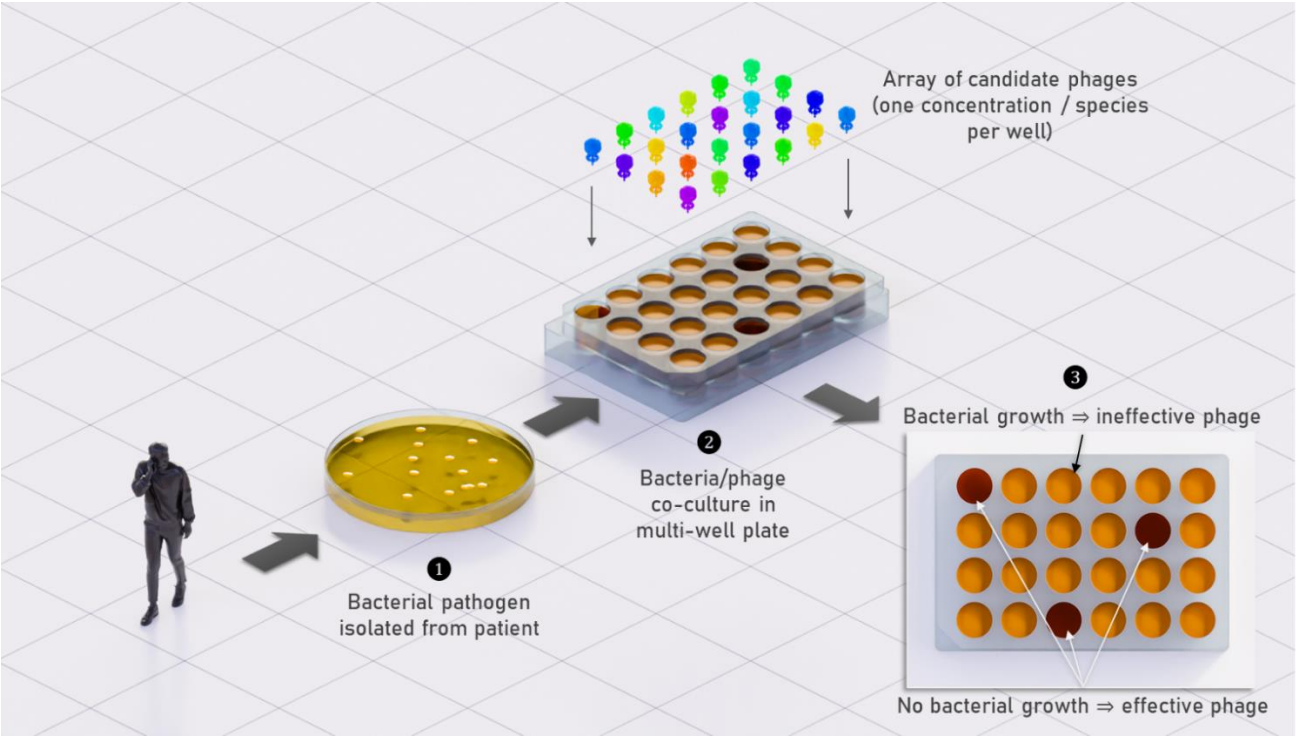

Figure 1.10 Multiplexed phage susceptibility testing (PST). Here PST is shown as currently carried out by broth microdilution in multi-well plates. (1) A bacterial pathogen is isolated from a patient. (2) The bacterial strain is co-cultured with an array of candidate bacteriophages. (3) Lytic replication of effective phages results in difference in optical density (or other transduction mechanism), revealing the effective phage. Shown here is a 24-well plate for ease of illustration. Plates with 96 or several hundred wells are common.

Outside of published literature, private biotechnology companies may be exploiting liquid culture lysis-based PST. As of October 2019, the website of Pherecydes Pharma claimed as an objective a time-to-result of 6 hours with scalability to ~100 tests daily. Publicity images on their website indicated that their system was based on optical density measurements at 600 nm and results after 6-8 hours, although this information is no longer present on their website as of March 2022. Adaptive Phage Therapeutics is an American company offering, as of 2022, "precisely matched therapy within 24 hours after a patient's bacterial colony sample".[106] The OmniLog system also appears to form the basis of Adaptive Phage Therapeutics' *Host Range Quick Test*.[61]

While these methods have been demonstrated both in academic and industrial applications, the time-to-results of several hours limit the feasibility of phage therapy for fast-evolving phage infections. It is worth quoting the 2018 report in the Lancet on the outcome of PhagoBurn clinical trials:[64]

> *"If phagogram duration can be shortened (currently 2 days via a manual system, and would need to be shortened to about 0·5 days), a selected phage strategy would also be applicable to infections that evolve quickly."*

1.4 The SPR Phagogram

Real time monitoring of the interaction of each of a large array of candidate phages with a challenge bacterial strain would reveal those which are suitable for inclusion in a phage cocktail against that strain.

For an effective clinical PST system, each patient would necessitate the testing of at least five different phage, in different combinations (to exclude antagonistic effects), at several different concentrations. The number of individual permutations quickly becomes very large.

The aim of this PhD is thus to demonstrate a proof-of-concept parallel, multiplexed phage susceptibility screening assay based on surface plasmon resonance imaging (SPRi). To this end, a biosensing layer featuring an array of different candidate bacteriophages is covalently immobilized on the gold surface of an SPRi prism, producing a measurable signal correlated with interactions between immobilized phages and bacterial cells introduced to the sensor surface (**Figure 1.11**).

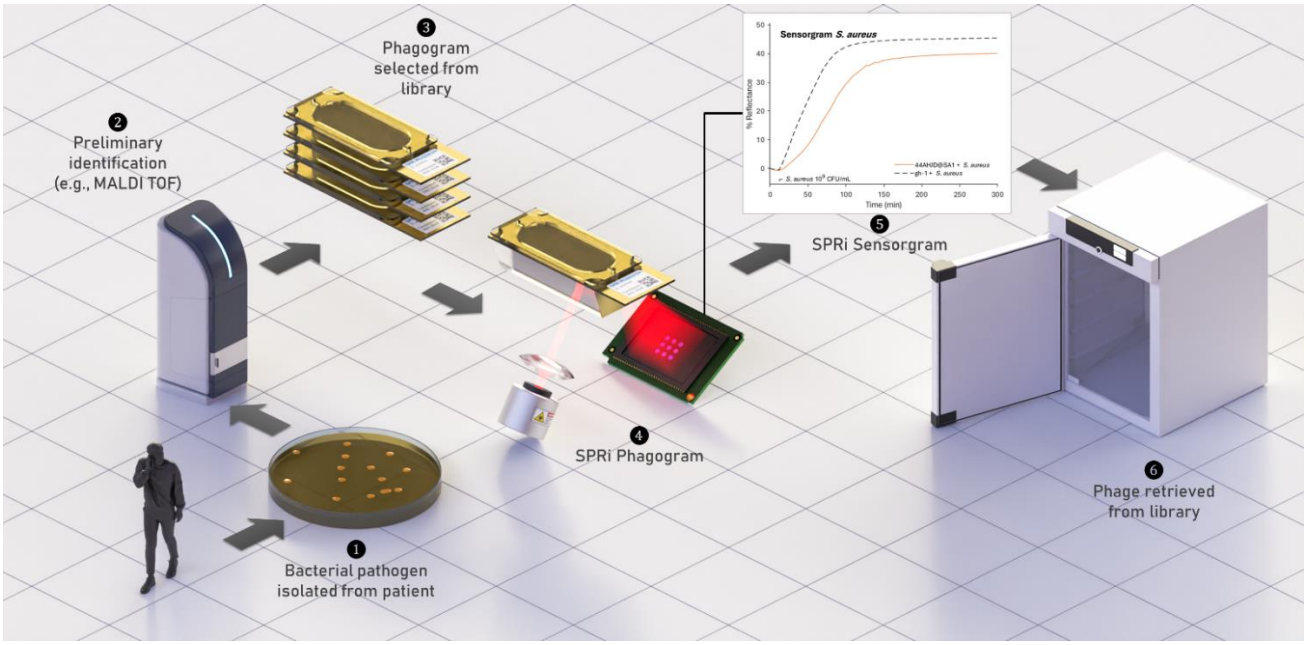

Figure 1.11 The envisaged SPRi phagogram as part of a phage therapy workflow.(1) A patient presents with a bacterial infection. (2) A preliminary identification of the bacterial species is made to narrow down the range of possible candidate phages. (3) A phagogram cartridge is selected. (4) An SPRi experiment is carried out, exposing the bacterial isolate to an array of several hundred candidate phages. (5) The SPRi sensorgram reveals the phages that are capable of binding this bacterial strain. (6) These phages are selected from a pre-prepared library to produce a personalized phage cocktail for the patient.

The envisaged phage therapy with SPR phagogram workflow would involve something like the following: First, a bacterial isolate(s) would be obtained from a patient presenting with an AMR bacterial infection (**Figure 1.11**). This isolate would then be cultured and exposed to a large number of candidate phages to ascertain which phage were capable of lysing and killing the challenge strain. A preliminary identification of the isolate may be performed (*e.g.*, by MALDI TOF* or some other means) to narrow down the range of candidate phages to a number that is practical for testing, but this is not strictly necessary if a presumptive identification can be made.[71] A SPR phagogram consumable, previously prepared with an array of candidate bacteriophages, would be interfaced with an SPR device and exposed to a carrier liquid containing the challenge bacteria. Phages that are capable of lysing the challenge strain (*i.e.*, on-target phage) produce a measurably different change in reflectivity compared to phages that are incapable of lysing the challenge strain (*i.e.*, off-target phage).

In this sense, the envisaged assay would take the form of a single-use SPRi consumable, in analogy to the Vitek 2™ or other rapid antibiotic susceptibility testing systems. In other words, we substitute a cartridge with compartments embedded with lyophilized antibiotic for a gold surface embedded with immobilized bacteriophages.

The envisaged SPRi-based PST would improve on currently used optical density and colorimetric methods, yielding a signal more rapidly and potentially in a more compact package. To the author's knowledge, this work represents the first time SPRi has been exploited for PST. A 2019 review of phage isolation and

* Matrix-assisted laser desorption ionization time-of-flight mass spectrometry

characterization techniques made no mention of SPR-based methods of PST[97] and the authors are aware of no such precedent in the literature.

1.4.1 SPR Theory

Surface plasmon resonance sensing relies on the coupling of light to surface plasmons — collective oscillations of delocalized conduction electrons in the interface between a thin metal layer and a dielectric analyte.[107] In what is known as the Kretschmann configuration, this interface is illuminated from the metal side and the reflected light collected on a sensor (**Figure 1.12**). For certain combinations of wavelength and angle of incidence there is a coupling of transverse magnetic-polarized incident light to surface plasmon modes, creating surface plasmon polaritons (SPPs) at the metal-dielectric boundary. At a certain incident angle, instead of reflection from the interface, this coupling results in loss of photons to SPPs which radiatively propagate along the interface, and a commensurate loss of reflectivity of the incident beam. The angle at which this loss of reflectivity occurs is highly sensitive to changes in the refractive index (RI) within the penetration depth of the evanescent wave — a depth which varies based on wavelength and refractive index but is approximately 430 nm in this work.[107] Binding of material on the metal-dielectric interface leads to mass uptake which in turn modulates the refractive index, altering the plasmon resonance conditions and yielding a shift in the plasmon curve (**Figure 1.13**). This plasmon curve shift can be monitored, thus transducing physical binding phenomena into an optical signal. For a more detailed treatment of the mechanism of SPR, refer to Homola[108] and Schasfoort.[107]

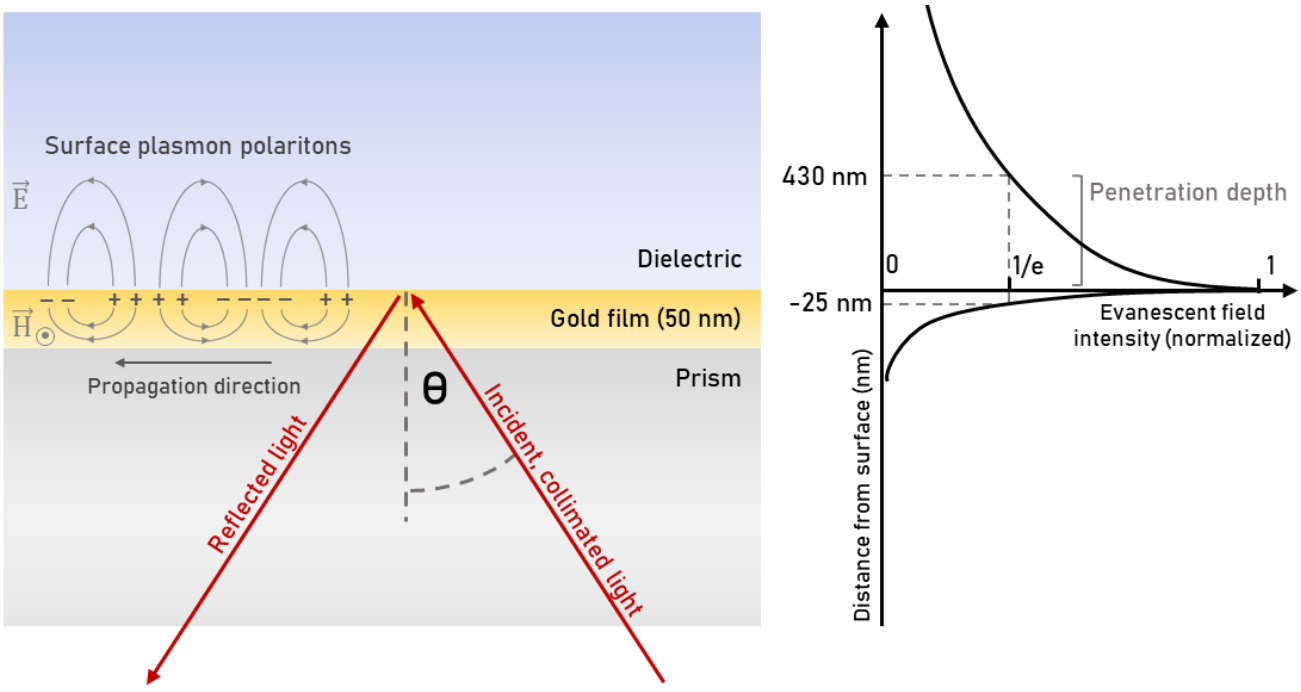

Figure 1.12 The principle of surface plasmon resonance. 0Incident light illuminates the metal-dielectric interface from the metal side in what is known as the Kretschmann configuration. For certain combinations of wavelength and incidence angle (Θ), light couples to surface plasmon modes to create surface plasmon polaritons, which radiatively propagate at the metal-dielectric interface. The penetration depth is a function of several variables, including electrical permittivity of the dielectric and the wavelength of light used. In this work collimated illumination at 880 nm was used, giving an evanescent wave that decays by 1/e at 430 nm from the interface in pure water and 25 nm in the gold layer. Not to scale.

A key strength of SPR is its high sensitivity to changes in the refractive index within the penetration depth of the sensor surface and exclusion of contributions beyond this region, allowing even small mass uptake of 0.01-

10 pg/mm^2 of proteinous material to yield a measurable signal.[107] Crucially, SPR transduces RI changes directly into an optical signal, and is thus a label-free method.

Surface plasmon resonance imaging (SPRi) builds on the strength of SPR by imaging the entire surface of a sensor that has been functionalized with many different ligands, simultaneously monitoring the interaction of each functionalized region in a single, parallel, multiplexed assay.[109,110] SPRi has been demonstrated for the specific detection — and potentially even identification and typing — of challenge bacteria using arrays of immobilized antimicrobial proteins.[111] In contrast to state-of-the-art PST methods involving optical measurements of bacteria/phage co-culture in multiwell plates, SPRi arrays can feature many hundreds to thousands of probes arrayed on a single sensor surface. The Plexera system, for example, allows arraying of up to 5 000 ligands on a single 1.4×1.4 cm surface.[112]

Since the release of the first commercial SPR device in 1990, SPR has become a widely popular method[113] since it allows label-free, real-time monitoring of surface phenomena, does not normally require complicated nanofabrication processes (as is the case for SERS[114]), and the adaptation for SPR imaging allows significant multiplexing.[107] The demonstrated capability of SPRi to permit simultaneous, parallel monitoring of probe-analyte interactions makes it a promising choice for rapid bacteriophage susceptibility testing.

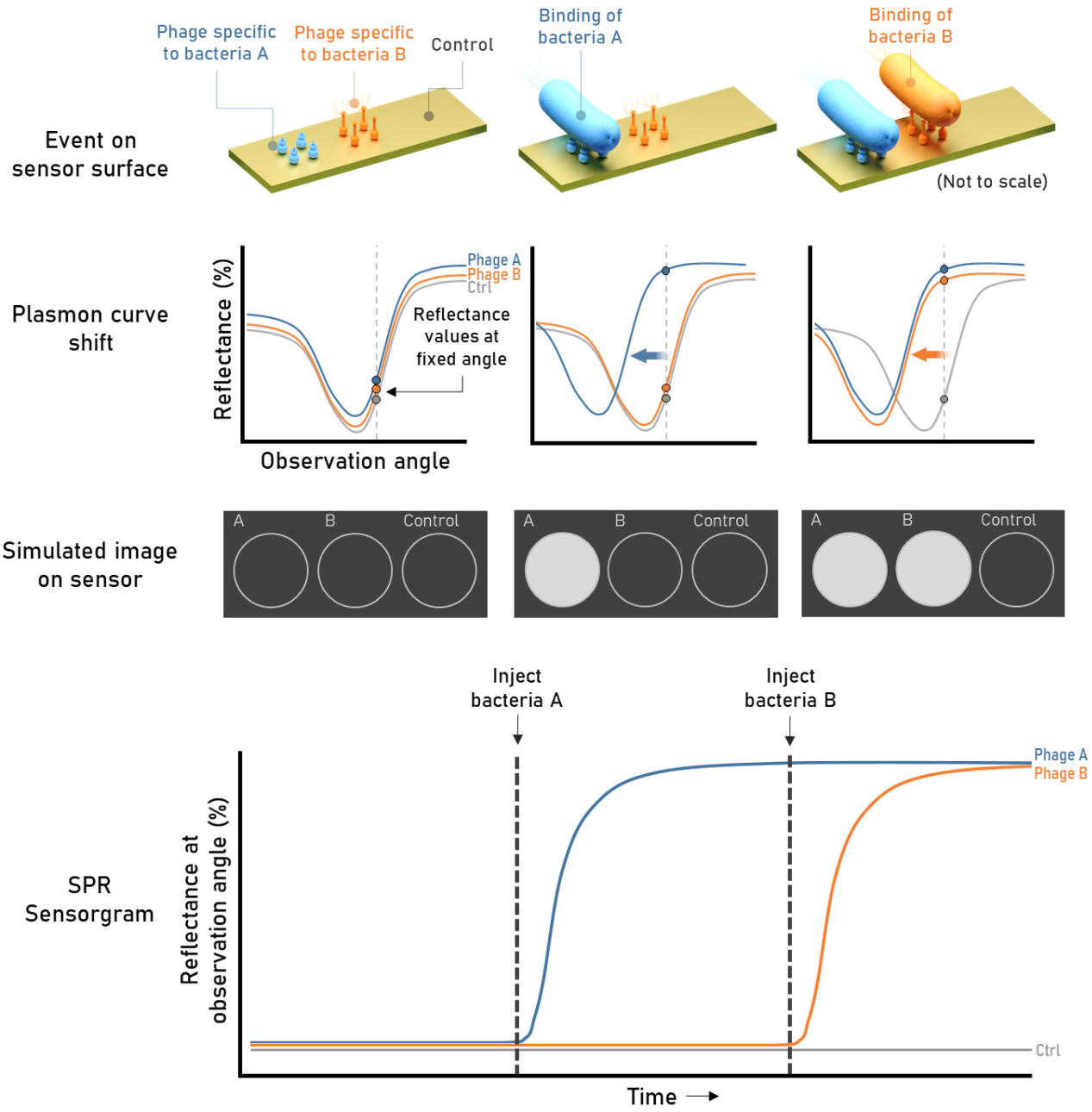

Figure 1.13 Illustration of the general principal of an idealized surface plasmon resonance sensing experiment with immobilized phages as probes. Left column: At the beginning of the experiment, the phages are immobilized at different regions on the surface, the plasmon curves of all three regions (A, B, and Control) are closely aligned, the image formed on the sensor does not change from its initial value, and the sensorgram curves of reflectance are stable. Middle column: When bacteria A are introduced to the surface, they are bound by phage A, but not by phage B or the control region (a bare gold surface). This causes an increase in the refractive index within the penetration depth of the evanescent wave from the sensor surface, and thus the plasmon curve shifts only for region A. Since the surface is monitored at a fixed working angle, the reflectivity increases, and the sensorgram indicates mass uptake in region A. Right column: When bacteria B are introduced to the surface, they are bound by phage B, resulting in a change in reflectance in region B and the sensorgram indicates mass uptake in region B.

1.5 Phage-phage Interference Necessitates Parallel Phage Susceptibility Testing

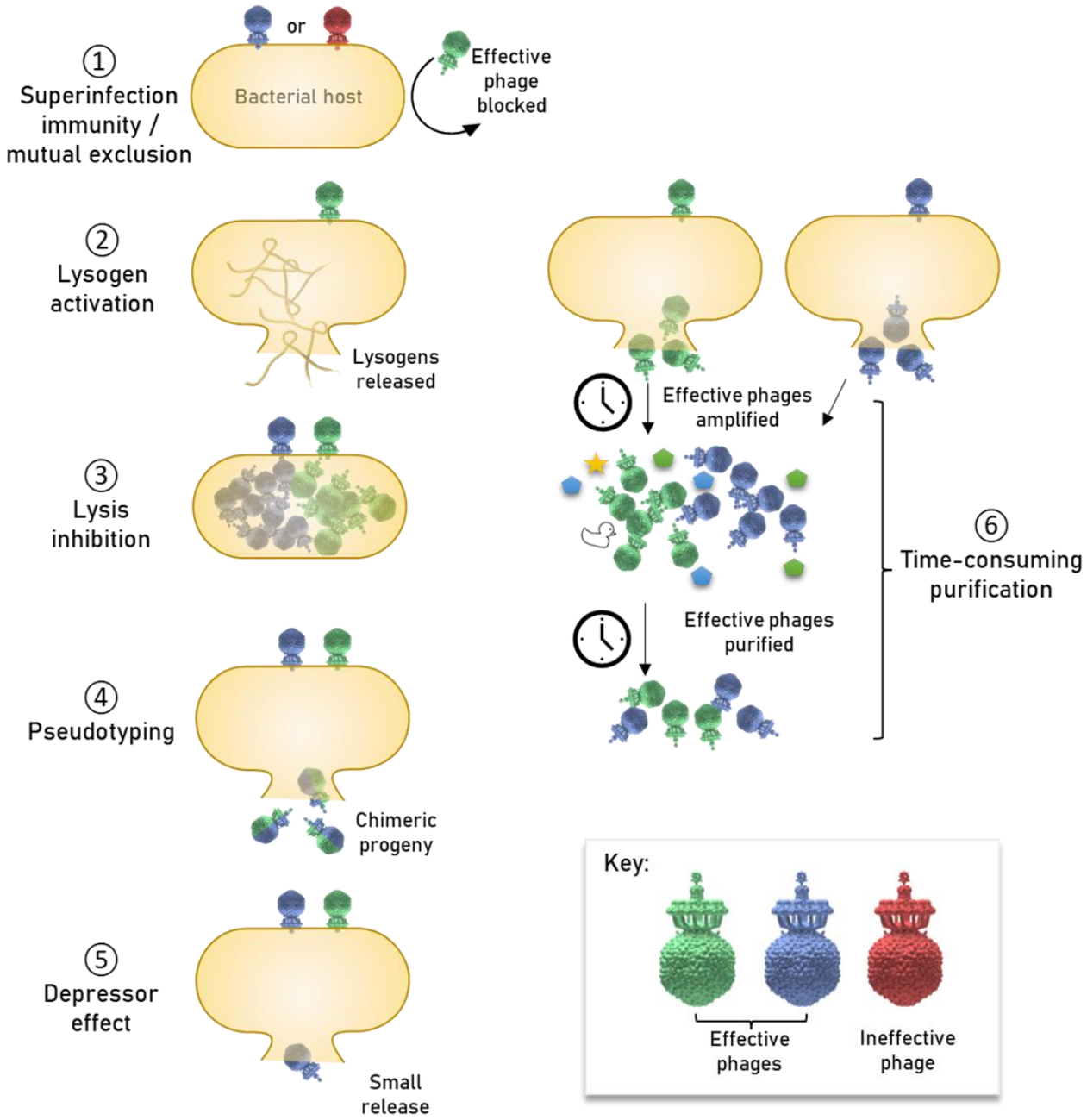

Figure 1.14 Illustrations of a non-exhaustive selection of potential problems arising from batch phage susceptibility testing.

The astute reader may identify a shortcut in the proposed SPR phagogram workflow, and indeed that of any personalized phage therapy. If the phages are themselves able to replicate exponentially when in the presence of a suitable bacterial host, it may seem advantageous to simply co-culture the target pathogen with a mixture of dozens or even of hundreds of candidate phages simultaneously. We can make a distinction between this strategy, hereafter referred to as “batch PST”; and the “parallel PST” of the SPR or broth microdilution PST method. In batch PST, one would expect only the phages most adapted to replication in the target pathogen to increase their numbers exponentially in the culture. These phages could then be purified and administered to the patient, bypassing the need for phage susceptibility testing, and essentially comprising a single-step

combined PST/amplification/pre-adaptation procedure. This is a compelling argument that may seem to undermine the necessity of parallel PST, and so it merits a brief discussion.

Firstly, batch PST will select for a phage subpopulation that has a growth advantage within the culture conditions. Due to the exponential growth of phage numbers during amplification, even a small difference in burst size or latent period would allow one phage to quickly dominate the population. This phage would deplete the bacterial culture of available hosts, thus obfuscating other effective phage strains.

Apart from this effect is the well-known issue of phage-phage interference, which is actually a collection of related phenomena (**Figure 1.14**).[115] Infection of a bacterium with two phages can result in one of a variety of outcomes that depend on the phages involved and factors such as their similarity and the timing of their adsorption on the cell.

Superinfection immunity or *superinfection exclusion* is an effect whereby infection by one phage prevents coinfection by closely related phages. This could allow for a candidate phage with high binding affinity for the challenge strain to proliferate despite a lower burst size, longer latent period, or other characteristic which otherwise makes it a poor therapeutic choice, while blocking the amplification of more suitable phages that have a lower binding affinity. Although this effect is more commonly associated with temperate phages, the same behavior is also seen in lytic phages.[116,117] Even in the absence of superinfection immunity, many coliphages exhibit *lysis inhibition* wherein infection of a host cell by a second phage will delay or even prevent lytic rupture,[118,119] having unpredictable effects on the number of phage released — referred to as the *burst size*.

In addition, coinfection by two phages can result in production of progeny of only one of the phages, known as the *mutual exclusion effect,*[120] which may prevent otherwise effective phage from being surfaced by batch PST. Even if a phage is unable to replicate in a host, it may reduce the burst size of an effective, coinfecting phage in what is known as the *depressor effect*.[120]

Alternatively, *phage pseudotyping* is a phenomenon where coinfection of a host cell results in progeny phage that are a phenotypic mix of the parental viruses with either the capsid proteins of one parent and the genome of the other, or a mixture of both genomes and proteins.[121] Such phages would be unsuitable for phage therapy since their composition is an unknown and could lead to undesirable outcomes *in vivo*.

As shown in the work of Ghebremedhin *et al.* and others, bacteriophages can cause a selection pressure that drives the bacterial population to a new phenotype.[85] Performing batch PST could have the effect of shifting the bacterial population into a form that privileges replication of phages that are no longer relevant to the bacteria *in vivo*.

As discussed before, temperate phages are unsuitable as a therapeutic agent. Although the candidate phage library can be screened to remove temperate phages, the strain isolated from the patient may harbor dormant prophages which will activate in response to the stress of culture conditions[122,123] or exposure to the candidate phages. This would result in the release of unknown lysogenizing phages into the lysate alongside the replicating candidates. Purification of the resultant phage lysate would then risk unintentional amplification of this lysogen, inclusion in the therapeutic cocktail, and administration to the patient with unpredictable effects. Lysogenizing phages are known to confer virulence factors and superinfection immunity. Indeed, most environmental and commensal bacteria are found to harbor dormant prophages.[115]

All of the above effects superimpose in complex ways for mixtures of small numbers of phages. The interplay of these phenomena in a batch of hundreds of phages would be even more unpredictable and is likely to negatively affect reproducibility. The above effects will be less prevalent while the ratio of phage to bacterial

cell (*i.e.*, the multiplicity of infection) is less than 1, since coinfection will be rare.[71] However, as phage numbers increase exponentially, these effects may dominate.

Finally, as we shall see in Chapter 2 , even in the event of successful phage amplification of only a suitable group of phages, the amplification and purification of phages is a time-consuming process that can require protocols tailored to each phage. It is preferrable to have pre-prepared banks of vetted and purified phages on-hand rather than try to prepare new phage suspensions using amplification on a clinical isolate.

The rapid appearance of bacterial resistance to a given phage means that several different cocktails may be successively administered to a patient.[124] Batch PST produces only a single lysate containing unknown phages, without a means (at present) of separating the different subpopulations for the preparation of cocktails of different permutations of the effective phages.

The above considerations are speculative on the part of the author, however, and while they may not entirely preclude batch PST, they at least place parallel PST as a preferable method. Although batch PST is appealing, the above phenomena effectively necessitate parallel PST.

1.6 Outline of the Manuscript

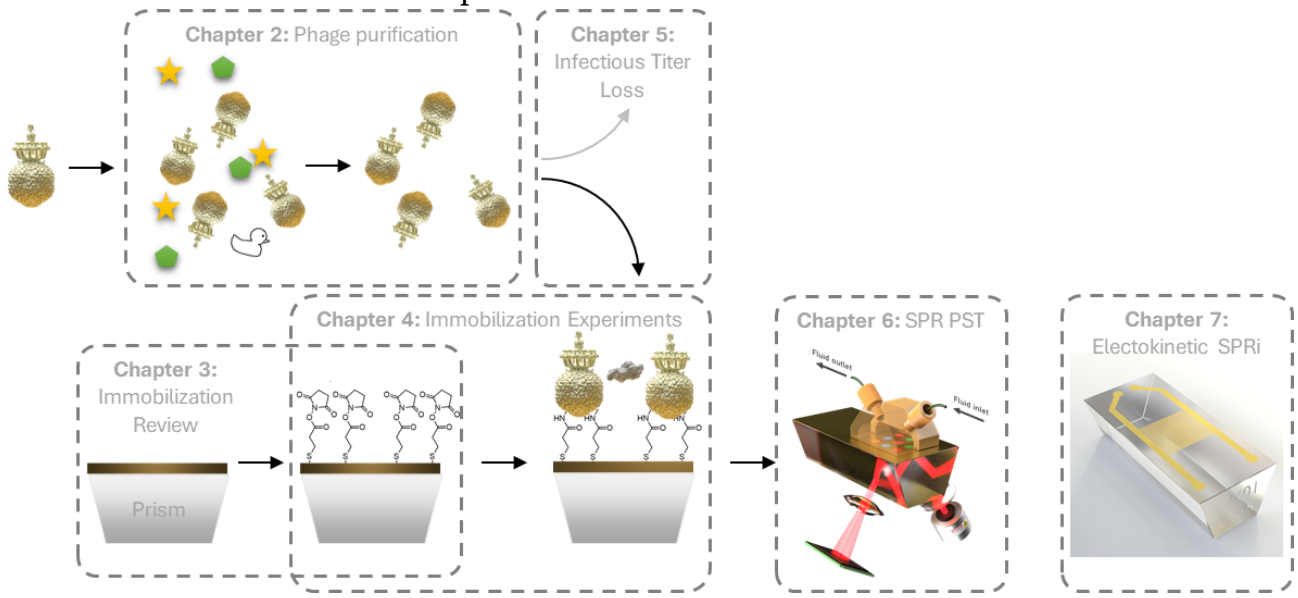

Figure 1.15 Graphical summary of the structure of the manuscript. Chapter 2 concerns purification of crude phage lysate. Chapter 3 reviews the phage immobilization literature. Chapter 4 details immobilization of phage by various means. Chapter 5 concerns loss of infectious titer during storage of purified phage suspensions. Chapter 6 presents the results of surface plasmon resonance (SPR) experiments. Chapter 7 concerns rapid fabrication and use of electrokinetically active SPR prisms.

Phage propagation generates a significant amount of bacterial cellular debris alongside the phage particles. The phages must be separated from this debris before they can be used for sensor functionalization. Chapter 2 details the available options for bacteriophage purification, the rationale behind the choice of methods tested during this PhD, and finally the outcome of purification experiments.

Once suitably pure phage suspensions are obtained, they must be immobilized on the biosensor surface. Since there are a variety of strategies that may be pursued, a review was carried out to survey the methods demonstrated in the literature and to identify those most promising for the development of the SPR phagogram. Chapter 3 takes the form of a **published literature review** on the topic of phage immobilization strategies.

Informed by the findings of this literature review, immobilization experiments were carried out on the four phages used in this work. Chapter 4 takes the form of a **submitted article** detailing the execution of these experiments and the resultant phage sensing layers that were obtained.

In parallel with immobilization and purification experiments, it was observed that the phage strains used in this work, once purified, suffer significant degradation during storage. Experiments seeking to elucidate the root cause of this phenomenon led to new insights into phage stability as a function of storage container material, and **a published article** on the subject, which forms Chapter 5.[125]

With phages immobilized on the surface, it was possible to carry out SPR experiments. Chapter 6 takes the form of a **published article** on a successful demonstration of the SPR PST proof-of-concept, and complementary measurements using phase-imaging microscopy that offer insights into the basis of the observed SPR responses during PST experiments.

As a means of improving the performance of the SPR phagogram, the possibility was explored of incorporating two electrokinetic effects — dielectrophoresis and electro-osmosis — into the SPR assay. As a result of this, a novel rapid fabrication method was developed for the patterning of interdigitated electrodes by laser ablation. Chapter 7 takes the form of a **submitted article** of a demonstration of this fabrication process and its

application to electrokinetic manipulation and biosensing of bacteria using an immobilized array of antimicrobial peptides.

Chapter 2

Phage Purification

2.1 Context: Contaminants of bacteriophage lysates

The process of phage replication necessarily liberates large quantities of biomaterial from the host bacterium into the surrounding medium in a process referred to as the "viral shunt".[126] Biomaterial including bacterial DNA,[126] lipopolysaccharide (endotoxin),[127] flagella[128] and other components[129] can all be found in the crude phage lysate even before considering additional contaminants that may originate in the bacterial culture medium and labware. Tryptic soy broth (TSB), for instance, contains large quantities of free peptides and amino acids by design.

In the context of phage therapy, intravenous injection places special requirements on the purity of phage preparations, since such a route bypasses the gut and skin barrier. Significant and damaging inflammatory responses can be mobilized by the body in response to the presence of even low levels of bacterial debris, particularly endotoxin. As a result, a low level of protein contaminant in phage suspensions is a *sine qua non* for phage therapy.

In the context of phage immobilization, contaminants must be removed from the phage lysate and separated from the phages before the latter can be used for functionalization of substrates, since many immobilization techniques will equally – if not preferentially – bind these contaminants to the surface along with the phages of interest.[130] Bacteriophages are unusually large compared to molecular ligands that are normally employed as probe molecules in the biological sciences (*e.g.*, antibodies, oligonucleotides, aptamers etc.). As a result, values for the diffusion coefficient of bacteriophages are typically of the order of 5×10^{-8} cm^2/second[131] — many orders of magnitude smaller than for smaller probes. The result is that more rapidly diffusing impurities than the phages will be preferentially bound to the substrate surface unless removed from phage suspensions.

Effective upstream purification of phage suspensions is thus a preoccupation of both phage therapy researchers and medicine regulatory agencies.[132] It has been shown that the purification protocol immediately preceding immobilization can have a large effect on the success, homogeneity, and overall quality of the immobilized phage layer[130] with removal of lysate interferents improving surface coverage and phage binding ability.[128]

Typically, immobilization of phages requires first the isolation of a high-purity, high-titer phage suspension. Typical phage concentrations used for immobilizations range between 10^{10} and 10^{12} plaque-forming units per milliliter (PFU/mL), although some success has been seen with lower infective titers.[133]

Many articles incorporating phage immobilization describe rudimentary purification protocols based only on filtration[134] or centrifugation,[135,136] seem to mistakenly make use of trisaminomethane (tris) buffer[137–140] which immediately blocks any activated esters on the surface[141,142]; or trust the purity of a phage suspension provided by a collaborator.[140,143,144] Insufficient purity of phage suspensions results in competitive immobilization of contaminants left over from the crude phage lysate, which reduces the quality of the final phage layer.

What follows is a brief summary of a selection of the most common methods used — either in isolation or in combination — for purification of bacteriophages.

2.2 Comparison of existing phage purification methods

2.2.1 Dead-end filtration

Dead-end filtration through 0.45µm and 0.2µm pore-size membranes is typically employed, along with differential centrifugation, as an initial first purification step to rid phage suspensions of the largest bacterial debris and leftover culture medium constituents. Phages pass through, while larger components remain on the filter membrane forming a cake. With increasing volume filtered through a membrane, biomaterial builds up on the membrane, the flowrate reduces, and the effective pore size can reduce to a size that no longer permits phage to pass in a process known as *gel polarization* (**Figure 2.1**A and B).[145] This phenomenon can reduce the infectious titer by an order of magnitude.

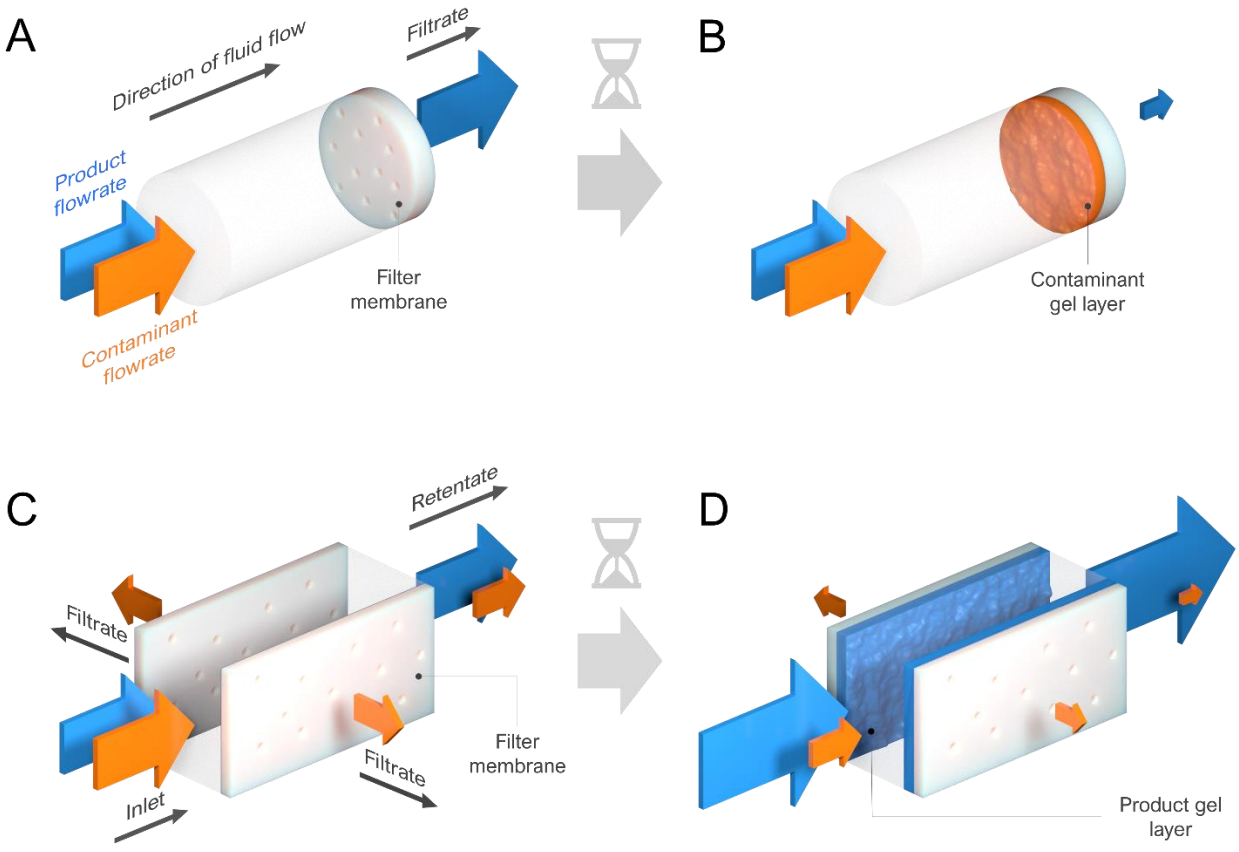

Figure 2.1 Tangential Flow Filtration. In a typical direct flow filtration (DFF) setup, the membrane is in series with the fluid circuit, perpendicular to the direction of fluid flow (A). Species smaller than the membrane pores may pass through and are retained downstream of the membrane. Species larger than the membrane are trapped and remain on the filter membrane.
With increasing filtration, the DFF membrane becomes clogged (B). The species of interest must traverse this contaminant layer, changing the effective pore size of the membrane and impeding filtration performance.
In a tangential flow filtration (TFF) setup, the membrane is parallel to the direction of fluid flow (C). Back pressure in the circuit forces a portion of the fluid through the filter membrane. Only species larger than the membrane pores will be retained. In contrast to DFF, as the sample is filtered in by TFF, the circulating volume decreases while the dry mass of species larger than the pore size will stay

relatively stable, increasing their concentration. Since the volume reduces at approximately the same rate as the contaminant dry mass, the contaminant concentration should stay relatively stable.
With increasing filtration, species larger than the TFF pore size will be retained and form a gel layer on the membrane (D), which must be dislodged at the end of the purification by increasing fluid velocity across the membrane surface.

2.2.1 Tangential flow filtration

Tangential flow filtration (TFF) — also known as cross-flow filtration — is a concentration and purification technique that presents several potential advantages over DFF and other phage purification techniques.

In contrast to DFF, TFF places the filtration membrane in parallel with the direction of fluid flow. The liquid passes parallel to the membrane in a cross-flow regime, with a shear force between the membrane surface and the liquid. Pressure in the circuit causes suspended species to pass through the membrane, perpendicular to the direction of fluid flow, while species that are unable to pass through the membrane are retained and continue to circulate rather than clogging the membrane (**Figure 2.1**C and D).

Diafiltration allows one to reduce the concentration of the original liquid phase (or some dissolved species which is sufficiently small to traverse the filter membrane into the filtrate) in your sample, while maintaining the concentration of some species in the retentate. Replacement liquid is added to replace the liquid that passes into the filtrate circuit. When a volume of replacement fluid, equal to the original sample volume, has been added to the sample while the same volume has been extracted as filtrate, we say that one *diafiltration volume* has been passed.

To date, TFF has been little exploited for phage lysate purification (although there is ample precedent for purification of viruses[146]). Most reviewed papers discussing TFF for phage purification do so within the context of isolation of phages in low concentration from environmental samples.[147–151] While TFF was demonstrated by Rembhotkar *et al.* for the purification of λ phage from a crude lysate, no measurements of purity or infectious titer were presented, making comparison difficult.[152]

2.2.2 Microfiltration, ultrafiltration, and nanofiltration

Micro-filtration (MF), ultra-filtration (UF), and nano-filtration (NF) are fundamentally similar processes, relying on size exclusion by a semi-permeable membrane. However, the three methods differ in the nominal pore size which specifies the diameter or molecular weight cut-off (MWCO) of the membrane used. Microfiltration commonly refers to filtration through pore size 0.1-10 µm, ultrafiltration through 0.01-0.1 µm, and nano filtration through 1-10 nm.[145] Of course, the fabrication process and material properties required to produce these membranes may differ between MF, UF, and NF — but treatment of this topic falls beyond the scope of this chapter.

Membrane filters will in reality have a distribution of filter sizes around the nominal value, which reduces the precision of separation of solutes. As a result of this, it is recommended to use a MWCO that is half the size of the smallest solute to be removed.[145] It is also generally recognized that there must be a minimum 10-fold difference in the sizes of two species that are to be separated.[145]

In this work, ultrafiltration through 100 kDa MWCO membranes was regularly employed to remove material smaller than approximately 3 nm in diameter, or 500 kDa membranes to remove material smaller than approximately 6 nm.[153]

2.2.3 Differential Centrifugation

In differential centrifugation, the components of a sample with a density greater than the solvent are fractionated depending on their sedimentation coefficient *s* which is given by[154] (**Figure 2.2**):

$$s = \frac{v}{\omega^2 R}$$

Where *v* is the particle's sedimentation speed (in m/s), ω is the angular velocity of the centrifuge rotor, and *R* is the distance of the particle from the centrifuge rotor axis. The terminal velocity for a spherical particle, away from the rotor axis of rotation, is given by:

$$v = \frac{m\omega^2 R}{6\pi\mu r}$$

where *m* is the particle mass, *r* is the particle radius, and μ is the dynamic viscosity of the centrifuge medium.

From this formulation, it is evident that a particle's sedimentation behavior is a function of its size and density, together with the viscosity of the centrifugation medium.[154] Suspended species with a high sedimentation coefficient will form a pellet early during differential centrifugation. With continued centrifugation over time the particles with successively lower sedimentation coefficient will sequentially pellet at the bottom of the centrifuge tube. With enough time, all fractions would form a pellet at the bottom of the tube and so duration and force of differential centrifugation must be tailored to separate species of interest from contaminants. This can be achieved either by pelleting the target and discarding the supernatant, or conversely by pelleting contaminants and retaining the target in the supernatant.

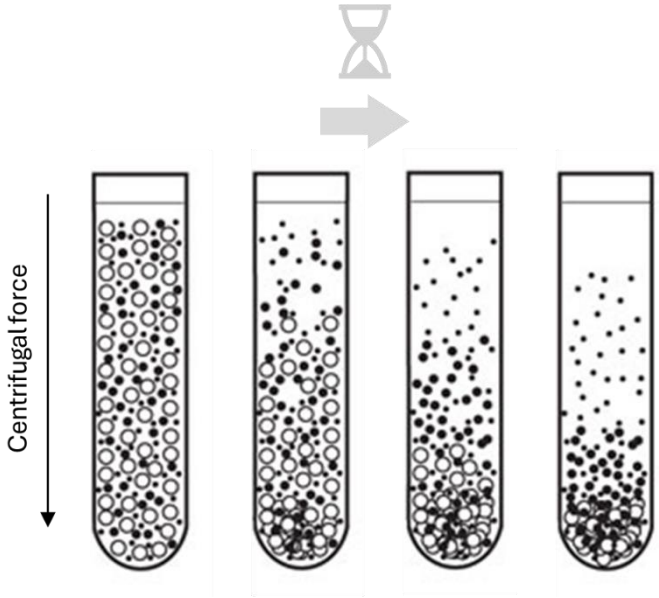

Figure 2.2 Differential Centrifugation. Different components pellet at the bottom of the tube at different times. Adapted from *Methods of Cell Separation*, Sharpe (1988).[154]

2.2.1 Polyethylene Glycol Precipitation

Precipitation with polyethylene glycol (PEG) is another established technique for concentration and purification of viruses.[155–158] PEG is a polymerized form of ethylene glycol, available in different molecular weights (MWs) ranging from 200 to 4 000 000 dalton.[155] PEG with MW in the 1 500 – 8 000 range[159], but most often 6 000[160–163] is typically used for purifying viruses.

PEG has many interesting biological properties but most relevant to the topic of phage purification is its role as a fractional precipitating agent which separates proteins by virtue of their solubility. Briefly, PEG acts as an inert solvent sponge, reducing solvent availability. With increasing concentration of PEG the effective protein concentration is increased until solubility is exceeded and precipitation occurs. Thus, larger proteins will

precipitate at lower concentrations of PEG and can be separated by differential centrifugation.[164,165] PEG precipitation is regarded by some as "*a crude and non-specific technique*".[165]

In this work, the purification of phages, PEG precipitation is used first to precipitate phages and larger proteins by bringing the phage lysate to 8% w/v of PEG 6000 and 500 mM NaCl (the latter acting to "salt out" the larger proteins in much the same way as described above for PEG) and then centrifuging with at moderately high centrifugal force of 16 500 *g*. Smaller proteins remain in the supernatant and are discarded while the pellet containing phage and larger proteins are resuspended in buffer with a lower ionic strength of 154 mM NaCl. Next, the larger proteins are selectively pelleted by centrifugation at 5 000 *g*. This allows the phage to be retained in the supernatant while contaminants are discarded in the pellet.

2.2.2 Density Gradient Ultracentrifugation

Density gradient ultracentrifugation (DGU), also known as *isopycnic centrifugation*, is distinct from differential centrifugation. DGU fractionates the components of a sample based on their buoyant density and necessitates centrifugation at very high acceleration (>80 000 *g* for 4-6 hours is typical [159]), in smaller volumes (~6 mL) and the careful selection and preparation of centrifugation media (**Figure 2.3**).[166]

Rather than using a centrifugation medium of homogenous density, instead the density increases along the central axis of the tube. When a sample is centrifuged along with this centrifugation medium, the different sample species will migrate to the region of medium that has the same density, also known as that component's *isopycnic point* within the tube. With increasing centrifugation time, each component will not form a pellet but will instead form an increasingly well-defined band within the tube.[154]

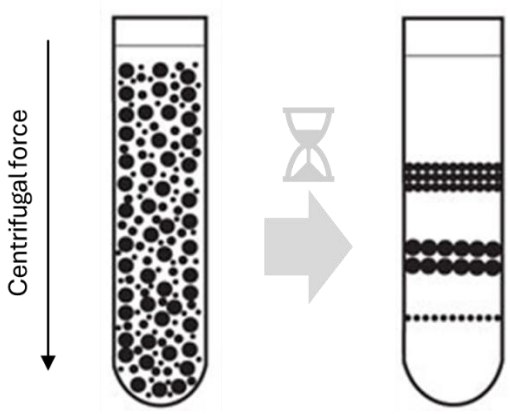

Figure 2.3 Isopycnic centrifugation. Components come to rest where the medium matches their density. Adapted from *Methods of Cell Separation*, Sharpe (1988).[154]

The density gradient can have different forms of density profile: smooth or step-wise, linear or exponential, concave or convex depending on the application; but is always monotonically increasing in density from the top towards the bottom of the tube.[154] A shallow gradient exhibits a small difference in density along the tube axis, which allows high-resolution separation between different fractions with similar buoyant densities, provided that their density lies within the interval of the gradient. In contrast, a steep gradient has low resolution but may be advantageous, for example for quick purification of a fraction that has a known and very distinct density from other components.

DGU is sufficiently performant to permit the separation of terminated viruses from empty ghost particles.[167] Potential drawbacks of DGU include the high cost of ultracentrifuge equipment, the potential for phage aggregation due to high ionic strength of centrifugation media,[168] the difficulty in harvesting the final product,

and finally the necessity of dialysis or ultrafiltration to remove residual centrifugation medium. DGU purification has also been found to lose un-tailed phages [169] and can yield solutions contaminated by large quantities of host bacterium flagella fragments.[128,170] Despite these disadvantages, the use of DGU has become an established technique for the isolation and purification of virus particles. [167,171–175]

DGU can be performed with a variety of centrifugation media, a selection of which were investigated for use in experimental work of this PhD. DGU media must be evaluated based on several criteria including[154]:

1. Non-toxicity to the target to be purified
2. High enough density at reasonable solution concentration. DGU requires that the gradient achieve a density at least higher than the target to be purified.
3. Easy removal following centrifugation

The use of a sucrose gradient would require an unfeasibly high concentration to match the 1.45 g/mL density of gh-1, which disqualifies it as an option due to viscosity and possibility of osmotic pressure effects on the phages.

Percoll is a centrifugation medium composed of silica particles 15-30 nm in diameter. Its main advantage is that it produces an iso-osmotic gradient. However, this is not considered an advantage in the purification of bacteriophages and so the introduction of nanoparticles of similar length scale as phages would seem to create unnecessary complication.

Another possibility considered was Optiprep, a relatively expensive aqueous solution of iodixanolin. However, Optiprep's low density of 1.32 g/mL precludes its use for purification of phages; gh-1 has a higher buoyant density of 1.45 g/mL.[176,177]

Aqueous solutions of Cesium Chloride are by far the most popular choice for DGU purification of phages. Upon addition to a solvent, CsCl dissociates into Cs^+ and Cl^- ions. Upon ultracentrifugation, the massive Cs^+ ions are concentrated towards the bottom of the tube by the centrifugal force, but they are also simultaneously subject to thermal jostling associated with Brownian motion. An equilibrium is reached between these two producing a gradient of increasing concentration of both Cs^+ and Cl^- ions towards the bottom of the tube, commensurately increasing the local medium density in that region.

In this way, ultracentrifugation of a CsCl solution naturally produces a *self-forming* gradient. However, the formation of a smooth CsCl gradient may take several hours of centrifugation, so it is common practice to manually create a pre-formed step-wise gradient that develops out into a smooth gradient in less time. The latter approach was the one adopted for DGU during this thesis.

2.2.3 Chromatography

A minority of publications describe various forms of chromatography for the purification of phages.[178] In 2004, Boratynski *et al.* used size-exclusion chromatography to produce phage suspensions with endotoxin levels low enough for intravenous administration.[127] In 2012, size exclusion chromatography was used by Naidoo *et al.* to avoid CsCl DGU and PEG precipitation, giving a total process time of only 3 hours.[128]

In 2013, Ceglarek *et al.* demonstrated a hybrid method exploiting genetic engineering and chromatographic separation of phages. Recombinant *E. coli* cells were modified to produce *highly immunogenic outer capsid* (Hoc) protein and *small outer capsid* (Soc) proteins fused to one of two standard affinity tags: glutathione S-transferase (GST) or polyhistidine-tag (His-Tag).[178] The tag-modified surface proteins are then incorporated into the phage capsid, allowing their purification by affinity chromatography. While elegant, this method relies on genetic modification of each host bacterium. This method was not judged to be practical for the purposes of this thesis since obtaining genetically modified hosts for each strain would be unreasonably onerous

compared to the other purification techniques in the literature and would place constraints on transport and manipulation of the hosts do the legal regulation pertaining to genetically modified organisms.

In 2015, Adriaenssens *et al.* demonstrated anion-exchange chromatography as an alternative to CsCl DGU for the purification of 11 morphologically distinct phages, each belonging either to *Myoviridae* or *Podoviridae*, infecting clinically relevant strains including *A. baumanii*, *P. aeruginosa, P. putida*, and *S. aureus.* The authors conclude that although this method presents easier scalability for industrial-scale throughput compared to CsCl DGU, it requires more extensive optimization of purification parameters for each phage including the choice of column chemistry, loading, buffer, and elution conditions.[179]

For these reasons, the optimization process needed for chromatography was deemed unnecessarily time-consuming for the purposes of this PhD and was not pursued.

2.3 Choice of methods to pursue

For this PhD, PEG precipitation, DGU, and TFF were selected for development of phage purification protocols. For reasons outlined above, and also after consulting with other researchers in the field regarding their preferred strategies, these methods were seen to benefit from precedent in the literature and rely on equipment and chemical products that are readily available. In addition, since the objective of this PhD is to demonstrate a multiplexed assay with a variety of phages, it was decided that this selection of strategies was most likely to yield performant protocols without the need for tailoring for several different phage strains after mastering the purification of phage gh-1.

2.4 Characterization of phage suspensions

2.4.1 Agar overlay

A typical unit operation in bacteriophage research is enumeration of a phage suspension using the soft agar overlay technique.[99] The agar overlay method involves the preparation of a mixture of soft agar (tryptic soy agar (TSA) with approximately half the typical agar-agar content), and while still molten adding the bacterial host together with a phage solution. The mixture is then poured over a standard TSA petri dish and incubated. After several hours, lysis plaques will become visible as regions of transparency embedded in the growing bacterial lawn. The number of lysis plaques, together with the volume and dilution factor of the added phage suspension, are used to calculate the number of phage present in the parent suspension and is reported in plaque-forming units per millilitre (PFU/mL).

If the concentration of bacteria is too high in either a liquid or agar culture, even after all cells have been lysed towards the end of the amplification process, you may have a significant loss of viruses which have bound to cellular debris (*i.e.*, free-floating membrane fragments may be encountered by phages and trigger their attachment and injection mechanism).

2.4.2 Absorbance

A small minority of papers attempt to circumvent the relatively laborious agar overlay method and instead make use of a UV-visible spectroscopic technique.[180–184] Measuring the absorbance of a phage suspension at 269 nm and 320 nm allows the calculation of the quantity of ssDNA present in the solution.[185] If the size (in number of base pairs) of the phage genome is known, and assuming the absence of any genetic material liberated from the host or prematurely ejecting phages, the phage titer can be calculated using a simple relation.

However, the assumption that all genetic material in the phage suspension is localized within infective phage is far from reasonable. Care should be taken in the interpretation of UV-vis enumeration technique it is less accurate than the agar overlay method, since contaminants in the phage suspension can contribute to absorbance.[103]

Furthermore, this formula is applicable only to phage storing their genetic material in the form of single-stranded DNA. Since gh-1[186] and all other phage used in this work are instead double-stranded DNA phages, this spectrophotometric phage titering method was not appropriate. Indeed, preliminary comparison between plaque-counting experiments and UV-vis spectroscopic enumeration did not yield a satisfactory correlation, and so this method was not explored further.

2.4.3 Dynamic Light Scattering

Dynamic Light Scattering (DLS) is a technique for determining the size distribution of particles in a suspension.[187]

When monochromatic laser light passes through the sample, it forms a speckle pattern on the far side composed of brighter and darker regions. These regions are not due to simple occultation of the laser beam by particles. Rather, this pattern is due to constructive and destructive interference of monochromatic light that has been *scattered* by the particles. Due to Brownian motion of the scattering centers, there is a time-dependent fluctuation of the scattering intensity. A key aspect of the Brownian motion normally undergone by particles in a suspension, is that larger particles will move more slowly, as governed by the *Stokes-Einstein* equation[188]:

$$D = \frac{k_b T}{6\pi\eta r_h}$$

Where D is the diffusion coefficient, k_b is Boltzmann's constant, T is temperature of the carrier liquid, η is the carrier liquid viscosity, and r_h is the hydrodynamic radius.

An autocorrelation function is fitted to the intensity trace at a particular point in the speckle pattern. The time in which the autocorrelation of the intensity trace drops to zero is dependent on the size of the scattering centers. Larger scattering centers will move more slowly and hence the intensity trace at a given point will show a longer autocorrelation timescale. From this measurement one can also extract the variance in sizes of the scattering centers (*i.e.*, the suspensions degree of *polydispersity*).

DLS measurements were not found to give interpretable results for phage suspensions, most likely due to the high polydispersity of suspensions following various purification methods (data not shown). For this reason, DLS data were not relied on for characterization of phage suspensions during this PhD.

2.4.4 Nanoparticle Tracking Analysis

Nanoparticle tracking analysis (NTA) relies on trajectory tracking of individual particles within an analyte suspension. A roughly planar laser beam illuminates a thin slice of a volume of the sample, at a location calibrated to coincide with the focal plane of a microscope objective lens connected to a camera (**Figure 2.4**).

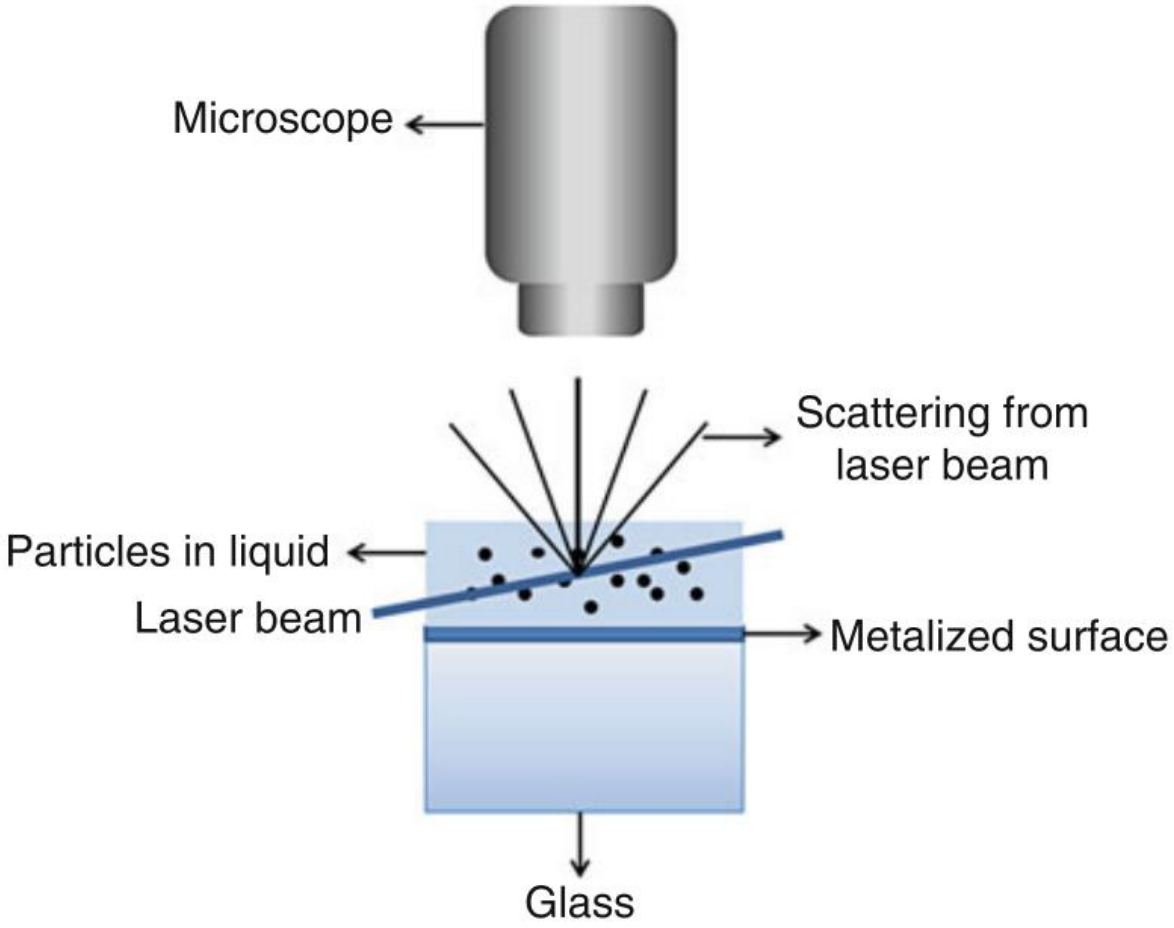

Figure 2.4 Schematic illustration of the principal of nanoparticle tracking analysis. Adapted from Lu and Murphy.[188]

This allows the exclusion of particles outside of a narrow, almost planar sampling volume which is bounded laterally by the frustum of the visual field of a microscope and in the z-direction by a roughly planar laser beam.[189]

Within this region, computer vision allows label-free tracking of the movement of individual illuminated particles. Using the Stokes-Einstein equation (See 2.4.3 Dynamic Light Scattering), the Brownian movement of each particle is used to calculate the diffusion coefficient of each individual particle. Since the temperature and viscosity of the carrier liquid are known quantities, this allows the calculation of the hydrodynamic diameter of the particle.[188]

The number of particles counted within each size bin is then extrapolated, based on the dilution factor, to find the total concentration of particles in the parent sample. Particles can only be tracked — and therefore included in the size distribution — while they are visible to the camera within this volume. However, the laser beam intensity is gaussian in the z-direction, and larger particles will scatter light more effectively than smaller ones on the periphery of the beam, and thus may over-contribute to the size distribution in the case of polydisperse suspensions. Furthermore, the limit of detection (LOD) of NTA depends on the refractive index of the particle material. Metal nanoparticles may be observed down to a diameter of 15 nm but for proteinous material such as viruses, the limit is closer to 30-40 nm.[189,190] For this reason, analysis of species with small refractive index (such as protein) necessitates setting the camera to use the maximum available signal gain.[189]

NTA yields individual particle information across statistically significant sample sizes[191] and has been demonstrated for the study of bacteriophage[192,193] and viral suspensions[190,194]. In contrast, dynamic light scattering (DLS) yields ensemble averages of diffusion coefficients (and extrapolated distributions of hydrodynamic radius). While DLS is an established technique for analysis of nanoparticle dispersions, it can struggle to give interpretable results for suspensions with significant polydispersity. NTA thus presents advantages over DLS in the study of bacteriophage suspensions, particularly in cases where aggregation is suspected, and yields more granular data.

When interpreting NTA measurements, it is necessary to keep in mind the distinction between infectious titer and the concentration of viral particles in a phage suspension. The infectious titer is a measure of the presumed viral load of a parent suspension, as calculated from the observed count of lysis plaques produced in plaque-counting methods, together with the dilution factor of the plated sample. Neither the drop cast or double layer agar method is capable of detecting empty phages or distinguishing between a single phage and aggregates of multiple phage particles. In contrast, nanoparticle tracking analysis reveals the hydrodynamic radius and optical scattering properties of individual particles, with little discrimination between viable phages, empty phages, phage aggregates, or contaminants.

Plaque-counting techniques and NTA can thus form complementary measurements which reveal deeper insights into the phage population of a sample, for example the concentration of inactivated phage and the aggregation state of the suspension (Chapter 5).

2.5 The *P. putida* gh-1 model

Bacteriophage gh-1 (ATCC 12633-B1) is a lytic bacteriophage that completes a lytic replication cycle in its host, the type strain of *Pseudomonas putida* (ATCC 12633).[195] Sedimentation analysis indicates that gh-1 carries its genetic payload in the form of dsDNA[177], inside an icosahedral capsid 50 nm in diameter.[195] One-step growth experiments indicate that latent period of gh-1 is approximately 21 min, with a burst size of 103.[195]

P. putida is a Gram-negative, halotolerant, psychotrophic species, which grows optimally at neutral pH and temperature between 25 and 30 °C.[196] *P. putida* is capable of growth in extreme conditions and contaminated environments. The characteristic flagellar mobility of the species contributes to its dispersal in aqueous soils and aquatic environments.[197] The species *P. putida* is found in most soils and aquatic habitats where there is available oxygen.

Phage gh-1 serves as a representative surrogate for a range of bacteriophage since, like 95% of backteriophages[198], it is tailed and represents a common *podovirus* morphology. Furthermore, the lytic cycle of gh-1 stands in contrast to temperate and chronic infection pathways, wherein the bacterial host is not lysed and phage are instead continually shed as they pass through the intact cellular membrane. Since the purpose of this set of experiments is to compare purification performance, it was advantageous to study a phage-host system that involves the release of cellular debris, as is the case in the lytic cycle of gh-1.

The use of gh-1/*P. putida* also reduces risk of phage contamination of biomaterial of colleagues sharing the same working area. Use of a classic phage such as T4 may risk contaminating and interfering with experiments involving more frequently used species such as *E. coli*, for example. In addition, *P. putida* is a biosafety level 1 organism, which simplifies handling and experimentation.

2.6 Materials & Methods

2.6.1 Amplification and preliminary preparation of bacteriophage gh-1

Phage gh-1[195] and bacterial host *P. putida* (ATCC 12633) were obtained from the *Félix d'Hérelle Reference Center for Bacterial Viruses* of the Université Laval, Quebec, Canada.Bacterial cultures of *P. putida* were

routinely prepared in Soybean Casein Digest Broth TSB (Sigma-Aldrich, Saint Quentin Fallavier, France) at 30 °C.

A parent bacteriophage suspension was prepared using the soft overlay agar method.[99] 100 µl of an overnight liquid preculture of *P. putida* was inoculated into fresh TSB and allowed to proliferate until reaching 10^8 CFU /mL as confirmed by optical density at 550 nm. Then, 200 µl bacterial host and 100 µl bacteriophage suspension (5×10^3 PFU/ml) were inoculated[†] into 15 mL falcon tubes filled with 5 mL molten agar (TSB prepared with 7.5 g/L agar (Sigma-Aldrich, Saint Quentin Fallavier, France)) at 51.5 °C, vortexed, and poured over 20 mL solidified tryptic soy agar (TSA, 15 g/L agar) in a standard 90 mm petri plate (VWR, France). Plates were then incubated overnight until lysis plaques became confluent in the top agar layer, which was then collected and soaked for 4 h at room temperature in sterile 154 mM NaCl solution (OTEC, VWR) in a 50 mL polypropylene tube to allow bacteriophage to diffuse out of the agar matrix. Each tube was then twice centrifuged for 20 min 5 500 *g* at 4 °C and the supernatant retained each time.

Finally, the suspension was filtered using a 0.45 µm syringe filter, followed by a 0.2 µm syringe filter. This produced the minimally processed phage lysate parent sample that was then be subject to further purification by each of the methods tested.

2.6.2 Purification protocols

2.6.2.1 Tangential flow filtration

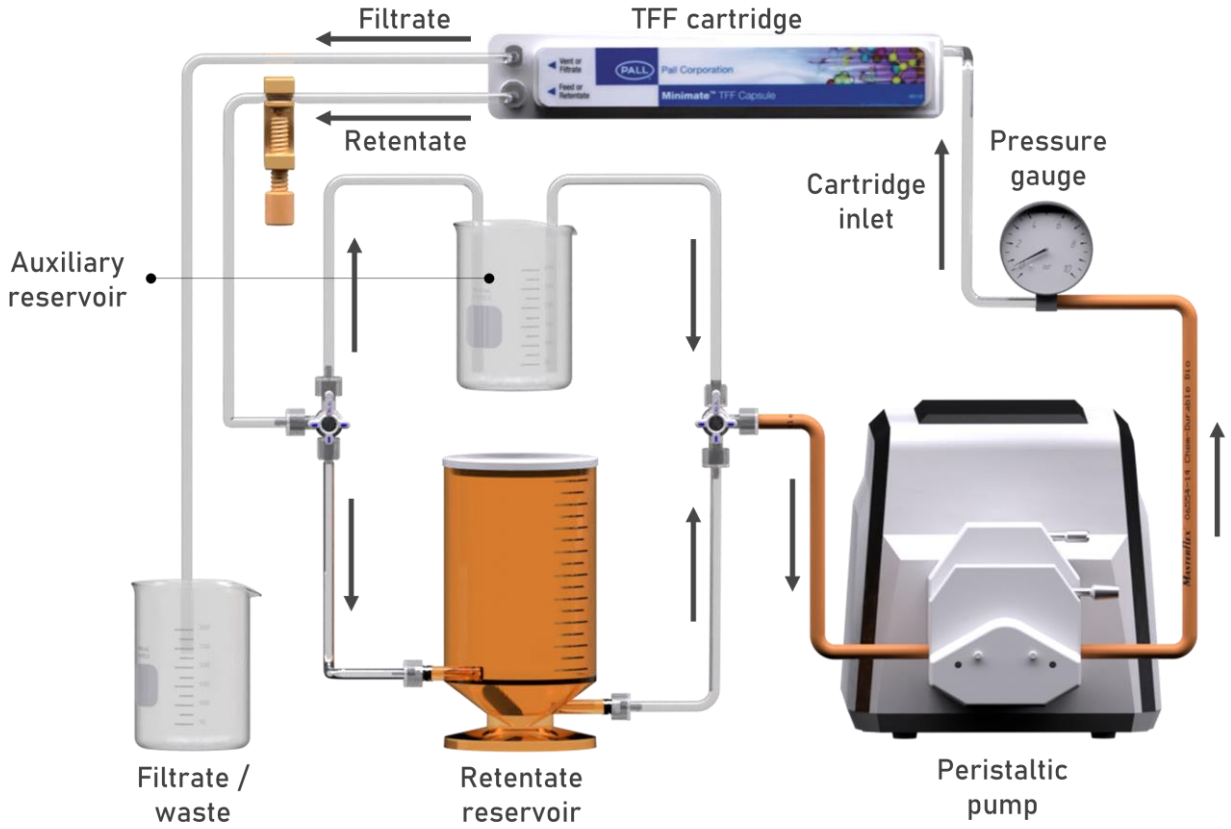

Figure 2.5 Schematic illustration of the tangential flow filtration (TFF) circuit as used in this PhD. The circuit is slightly modified from the standard TFF circuit recommended by the manufacturer's documentation: two 3-way luer valves are added on either side of the

[†] Previous experiments indicated that aiming for ~500 lysis plaques maximises the infectious titer of the final solution of gh-1.

retentate reservoir, permitting the flow to be easily diverted to bypass the retentate reservoir and instead flow through an auxiliary reservoir, which is useful for rinsing and cleaning steps.

A Minimate Tangential Flow Filtration system was purchased (Pall Corp., Glen Cove, NY, USA) and fitted with a 500 kDa MWCO cartridge (**Figure 2.5**).

After appropriate rinsing of the circuit and cartridge (see manufacturer's documentation), 50 mL of gh-1 lysate was diluted to 500 mL in the Minimate reservoir using isotonic physiological saline (154 mM NaCl). The peristaltic pump was set to circulate at 40 mL/min, while the retentate clamp was adjusted to constrict the flow, regulating the backpressure to between 20-25 PSI. Over the course of 45 minutes to 1.5 hours, the retentate volume was allowed to concentrate from 500 mL down to approximately 10 mL. The retentate was diluted a second time to 500 mL and the filtration step was repeated.

Once a volume of approximately 10mL remained in the circuit and retentate, the filtrate outlet was closed, creating a closed loop in the TFF circuit. The flow rate was then increased to 50-80 mL/min and the suspension allowed to circulate for 10 minutes. This step recovers a gel layer of retentate from the cartridge membrane. The remaining 10 mL was drained into a 50 mL falcon tube and the circuit appropriately rinsed. The retentate suspension was then centrifuged at 5 000 *g* for 20 min in order to pellet any large debris originating from the Minimate circuit and cartridge.

Ultrafiltration was then performed on the resulting suspension, as below.

2.6.2.2 Ultrafiltration

The upper chamber of 100 kDa MWCO Vivaspin 20 ultrafiltration tubes were first rinsed with 0.2 µm-filtered 154 mM NaCl solution. The parent phage suspension was then placed in the upper chamber and centrifuged for 20 min at 5 000 *g* at 4°C. The dead stop volume of 5 µL of concentrated phage was resuspended in 154 mM NaCl.

2.6.2.3 Density gradient ultracentrifugation

CsCl solutions were prepared of the following concentrations: 1.7 g/mL (12.84 g CsCl in 10 mL DIW), 1.54 g/mL (9.37 g CsCl in 10 mL DIW), 1.34 g/mL (5.15 g CsCl in 10 mL DIW). In 5 mL, Open-Top Thinwall Ultra-Clear ultracentrifuge tubes (Beckman Coulter, Villepinte, France), 1.5 mL of each CsCl solution was carefully overlayered using a micropipette, and finally the parent phage suspension was gently placed on top to fully fill the tube. The gradients were then centrifuged for 2 hours at 36 500 RPM (100 000 *g*) at 4 °C in a SW 55Ti swinging bucket rotor (Beckmann Coulter) mounted on an Optima l-90K Ultracentrifuge (Beckman Coulter).

Following ultracentrifugation, the phage lysate formed two distinct bands in the CsCl gradient. Four fractions were separately collected from the gradient and previous plaque-counting experiments showed that the second visible band from the top contained 10^{11} PFU/mL phage while the next most numerous fraction contained 10^{8} PFU/mL, indicating that phage are concentrated in the former. The second band was thus retained

Following DGU, CsCl and small molecular weight contaminants were removed from this fraction (6 mL volume) by dialysis in ZelluTrans 25 mm 12-14 kDa MWCO dialysis membrane (Roth Sochiel, Lauterbourg, France) against 800 mL 154 mM NaCl in a 1L beaker at 100 RPM for 24 hrs.

2.6.2.4 PEG precipitation

The parent phage suspension was brought to 500mM NaCl and 8% w/v of PEG 6000 and agitated for 20 min to completely dissolve the PEG. This molecular weight of PEG was chosen since it has been shown to be the least detrimental to phage titer for a variety of morphologies including *podoviridae*.[199] Suspensions were then left overnight at 4°C. The following day, the suspension was centrifuged for 20 min at 16 500 *g* at 4°C. The

supernatant was discarded and the pellet resuspended in the same volume of 154 mM NaCl solution and then centrifuged for 20 min at 5 000 *g* at 4°C. Finally, the supernatant containing the phages was extracted and retained.

2.6.1 Bacteriophage titer enumeration

Serial 10-fold dilutions were made of each phage suspension (100 µL diluted in 900 µL mL 154 mM NaCl solution). All phage titer counting was carried out using the same agar overlay method described above for amplification, with the difference that for titer counting, serial dilutions of each phage suspension are separately plated, aiming to produce approximately 50 plaques in the soft agar layer in order to minimize overlap bias (See Annex: Calculation of Experimental Uncertainty in Plaque-counting Experiments). No harvesting or purification of the soft agar layer is performed for titer counting. Lysis plaques are counted after overnight incubation at 30 °C. The phage titer of the parent solution is then calculated using the equation:

$$\text{Sample phage titer}\left(\frac{\text{PFU}}{\text{mL}}\right) = \text{No. plaques} \times \text{plated volume}^{-1} \times \text{dilution factor}$$

2.6.2 NTA

Nanoparticle tracking analysis (NTA) was carried out using a Nanosight NS300 (Malvern Pananalytical Ltd., Malvern, United Kingdom) fitted with a 488 nm laser module and a sCMOS detector. Samples were diluted with 154 mM NaCl to produce suspensions of 10^8-10^9 particles/mL, and the dilution factor noted. Each sample was injected by syringe pump into the analysis chamber and measured five times with each measurement lasting 60 s, according to the manufacturer's protocol. All suspensions were analysed with a consistent camera level of 16 and detection threshold of 10. Preliminary data processing was performed using NTA Analytical software (v3.4.4). Semi-log size spectra and scattering intensity scatter plots were produced using custom code implemented in MatLab R2021a (v9.10).

2.6.3 Negative staining TEM

Transmission electron microscopy (TEM) was carried out at the Institut de Biologie Structurale (IBS), Grenoble; according to the negative stain-mica-carbon flotation technique (MFT): phage suspension were adsorbed to the clean side of a carbon film on mica, stained with uranyl acetate (AcUr) $UO_2(CH_3COO)_2{\cdot}2H_2O$ at 2% in distilled water (pH 4.2-4.5), and transferred to a 400-mesh copper grid. The images were taken under low dose conditions (<10 $e^-/Å^2$) with defocus values between 1.2 and 2.5 µm on a Tecnai 12 LaB6 electron microscope at 120 kV accelerating voltage, using a Camera Gatan Orius 1000 CCD. At least eight images were taken of each sample.

2.7 Results and Discussion

Purification of phage suspensions was performed in three rounds, following the same experimental procedure, each with a different but similar parent sample of phage gh-1 (**Figure 2.6**). The results of rounds 1-3 informed the purification procedures used to produce phage suspensions for other experiments during the first months of this PhD. Also included for comparison are the results of characterization of a suspension of phage gh-1 purified using a method optimized much later near the end of the PhD. This later method comprises a hybrid of the most performant methods described and tested in this chapter (**Figure 2.6**). While this suspension was not prepared as part of the initial three rounds of purification experiments, it represents the evolution of the purification method that was developed as part of later experiments, which yields superior results to purification with any one method in isolation.

A significant variable in this series of experiments is introduced during preliminary processing of the parent sample after the first set of low-acceleration centrifugation runs and before DFF (**Figure 2.6**). At this step, following each centrifugation, the supernatant is decanted into a fresh container. The choice of the amount

of liquid to retain at this step is a compromise between maximizing the retained volume of liquid (and thus total number of phage) and withdrawing liquid only far from the pelleted material (and thus minimizing contaminants). The pellet may make up as much as a third of the volume after the first centrifugation and so it is tempting to withdraw liquid from near the pellet, but this must be avoided. At this step it is preferable to retain a smaller volume of supernatant than to risk resuspending contaminants of the pellet. Differences between results of purification in rounds 1, 2, and 3 (columns in **Figure 2.6**) may be due to this variability, while differences between the rows of **Figure 2.6** can be attributed to purification method.

Figure 2.6 Flow diagram illustrating the various purification steps which followed from initial amplification of the parent sample. The bottom row shows the provenance of each sample characterized during this set of experiments.

2.7.1 Negative staining TEM

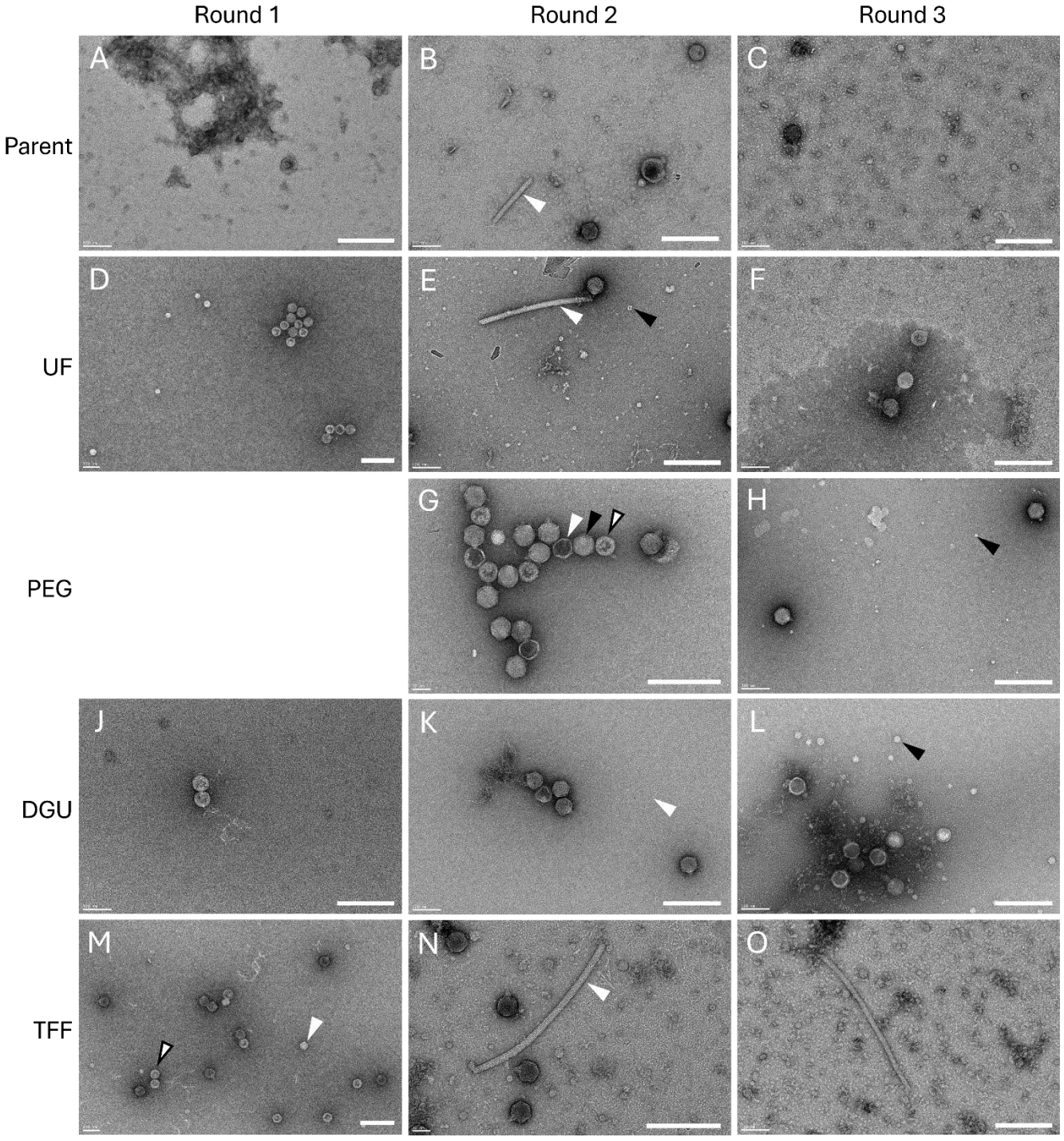

Figure 2.7 Transmission electron micrographs of phage suspensions. The parent phage suspension in its minimally processed form (first row), and purified by ultrafiltration (second row), PEG precipitation (third row), density gradient ultracentrifugation (fourth row, and tangential flow filtration (bottom row). All suspensions have been negative-stained with uranyl acetate for contrast. TEM analysis of a PEG-purified sample was not possible during the first round. All scale bars indicate 200 nm.

In order to obtain qualitative information on phage suspension purity following purification, TEM analysis was performed on each suspension with at least eight images taken of each. A representative selection of images is shown in **Figure 2.7**.

In each round, the parent sample was found to be heavily contaminated with material of a range of length scales. This is to be expected due to the minimal processing performed on the parent sample.

In all suspensions, but particularly in PEG-purified suspensions, we can distinguish three different subpopulations of phage particles. The first is the icosahedral head typical of an infective phage gh-1 (**Figure 2.7**G, black arrow). Also present are phage procapsids (**Figure 2.7**G, white arrow with black border).[200] The third particle type are what appear to be phage which, although exhibiting the icosahedral head of a mature virion, appear to be empty with penetration of the negative stain into the head (**Figure 2.7**G, white arrow). This last group are most likely phage which have ejected their genetic material, known as *ghosts*. Also visible were very thin (a few nanometres), filamentous material in DGU, which was most likely nucleic acid (**Figure 2.7**K, white arrow).

The parent sample contained filamentous structures approximately 20 nm in diameter and of various lengths on the order of hundreds of nanometres, which were presumed to be flagella fragments (**Figure 2.7**B, white arrow).[128] These flagella were observed to persist from the parent sample to UF and TFF suspensions (**Figure 2.7**E and N, white arrows). Another possibility is that these extended structures are filamentous phages, but this was deemed improbable due to the lack of terminal tail fibers and the variable length of the structures (one would expect a uniform length for each filamentous phage strain). Furthermore, their frequent appearance in TEM imagery would imply inovirus replication in the culture despite the absence of prophage DNA in the *P. putida* genome. Flagella have been known to persist in DGU purification.[128,170]

Also observed was the frequent appearance of many sub-30 nm objects which appear to feature two sub-units, which suggests that they are bacterial ribosomes (**Figure 2.7**E, H and L, black arrows). As a prokaryote, *P. putida* (the host of phage gh-1) features 70S ribosomes, composed of a larger 50S subunit and a smaller 30S subunit, together forming a ~25 nm-diameter macromolecule.[201] Bacteria also downregulate ribosomal activity by dimerizing 70S ribosomes into an inactive 100S ribosomal complex.[202,203] Bacterial cells are known to house thousands of ribosomes per cell, compared to the burst size of “only” 103 gh-1 particles generated for each lysis event.[195] We may then expect to see as much as an order of magnitude more ribosomes than phage present in the crude lysate, which must be separated from the phage during purification.

The presence of apparently dimerized particles TEM imagery suggests that ribosomes are purified alongside phage for several purification methods including DGU. While the small size of ribosomes should allow them to pass the 0.2 µm filter pores during DFF and survive PEG precipitation alongside phage, they should be excluded by DGU. The 50S and 30S ribosomal subunits have a buoyant density of 1.67 and 1.63 g/mL, respectively, while that of gh-1 is lower at 1.45 g/mL.[176,177] We would thus expect ribosomes to be present in the band that formed below the 1.54g/mL region of the CsCl gradient, while the phage remain above, effectively separating them.

While round 1 and 2 showed little to no contaminants of this type in DGU suspensions, the appearance of putative ribosomes in round 3 may reflect the difficulty in manual collection of bands following DGU, during which small amounts of contaminants may be extracted alongside the phage of interest due to poor pipetting technique.

Ultimately, the relevance of possible ribosome contamination to the work of this thesis will be decided if they appear on the substrate following immobilization, which was observed to not be the case (Chapter 4). We can thus reasonably conclude that any ribosome contamination is minor.

Note that it is difficult to draw conclusions on the aggregation state of phage suspensions from TEM imagery (for example **Figure 2.7**D and G) since the staining and drying process can easily create drastically different conditions than the phage would be exposed to in normal phage buffer. It is likely the case that any aggregates may have formed in the moments before TEM and so do not reflect the aggregation state of the phage suspension.

2.7.2 NTA

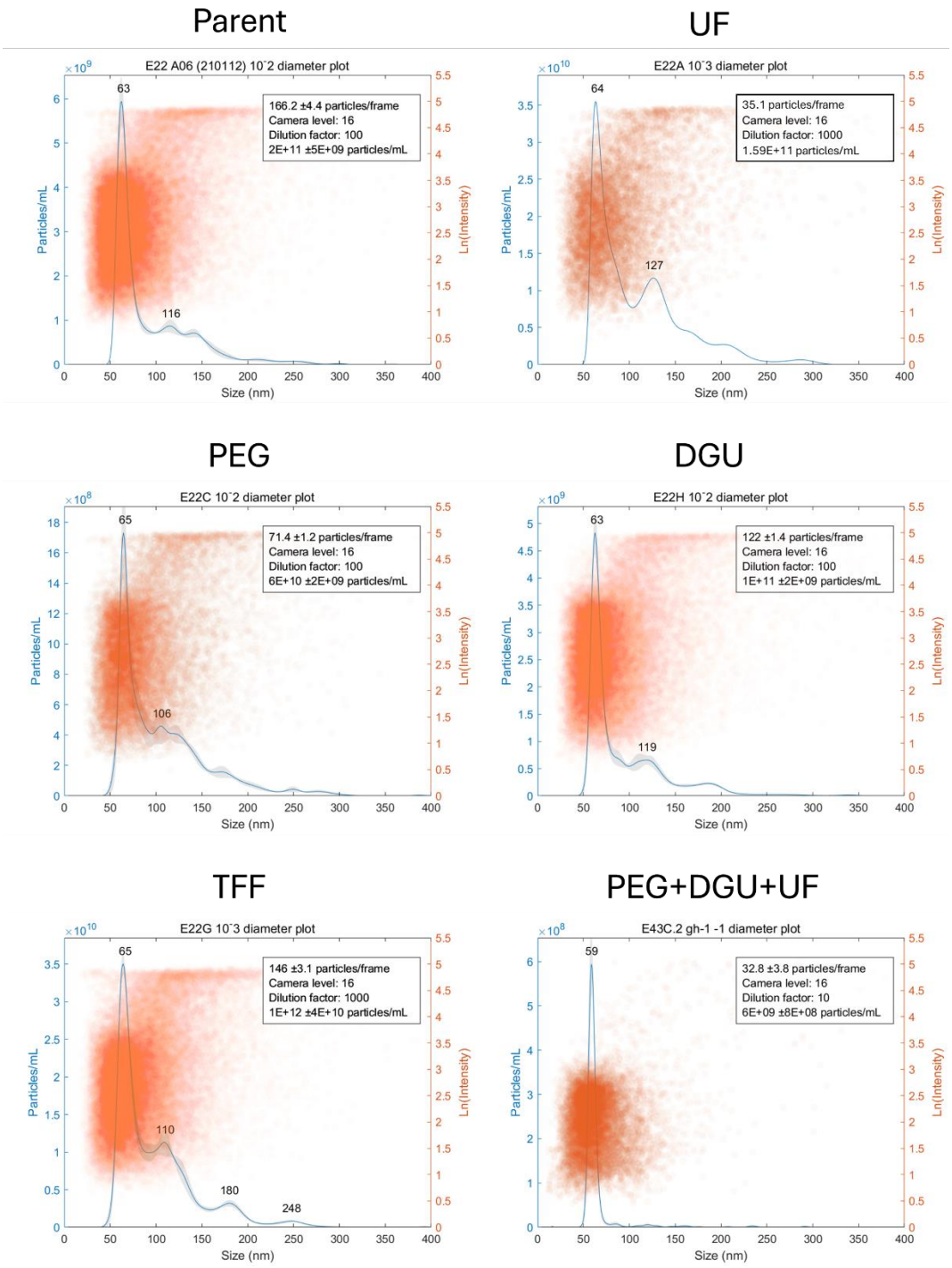

Figure 2.8 Nanoparticle Tracking Analyis Results. Results of nanoparticle tracking analysis of the minimally purified parent sample and suspensions purified by various methods, each shown as a dual-axis figure with a semi-log plot of particle concentration (left-hand blue axis) with standard deviation of six replicates shown in grey. Each figure also shows the scattering intensity vs. size for each individual particle (right-hand axis, orange).

NTA results for the third round of purification are presented in **Figure 2.8**. While three rounds of purification were performed, the process was subject to improvement and optimization in between each iteration which makes NTA analysis of the final round more useful for assessing the size distribution profiles that result from each purification method. For brevity, only the NTA results from round 3 of purification are presented. The NTA data for each sample are shown in **Figure 2.8** as a dual axis figure with a semi-log plot of particle

concentration (left-hand blue axis), and the standard deviation of six replicates shown in grey. Each figure also shows the scattering intensity vs. size for each individual particle (right-hand axis, orange). The scattering intensity is an underutilized datum that is produced by NTA for each particle individually, potentially allowing one to distinguish particles with different material properties.[188] The NTA camera has a finite dynamic range, and since some particles scatter a sufficient quantity of light to saturate the sensor, a ceiling is observed in the size-intensity plot.

Several insights can be extracted from the NTA results of purification. Immediately obvious is the sharp drop in observed particles below 50 nm in diameter. This is due to a key weakness of NTA that must be taken into account when interpreting NTA data. As discussed above, the low refractive index of proteinous material (*e.g.*, phage capsids) limits the ability of NTA to observe material smaller than approximately 30-40 nm. [189,190] This is all the more relevant since, as discussed above, contaminants smaller than 50 nm are the most important for the purposes of immobilization since they will diffuse to and be immobilized on the substrate faster than the phages. For this reason, TEM is an important complimentary measurement of phage suspension purity, which assesses — at least in a qualitative way — the amount of material smaller than the phage.

Another feature that is apparent is the polydispersity of the parent sample. A pure, unaggregated, monodisperse suspension of phage gh-1 should yield a single sharp peak near 60 nm. The parent sample shows significant amounts of material both down to the LOD below 50 nm but also as high as 200 nm. This agrees with TEM observations of the same sample, which shows significant amounts of material other than phage (**Figure 2.7**C).

Ideally, we would observe a sharp peak near 60 nm in all purified suspensions, indicating a monodisperse suspension of unaggregated phage. However, the size spectra of UF, PEG and TFF indicate poor removal of contaminants and a relative *reduction* of the population of single phage particles relative to phage aggregates and other material. This result indicates that these methods may not be effectively purifying phages and/or may be inducing aggregation.

Peaks at the position of integer multiples of the particle diameter can be observed in several samples, which is most likely due to the presence of aggregates of one, two, three particles and so on. This can be seen for all suspensions but is particularly obvious in TFF with a peak at 65 nm (the approximate hydrodynamic diameter of gh-1), followed by peaks at 110, 180, and 248 nm. In the absence of contaminating material, such a result may be used to assess the aggregation state of a phage suspension.

Also apparent is the cut-off in the size spectrum of material above 200 nm, which comports with the passage of these suspensions (except PEG+DGU+UF) through a 0.2 µm filter membrane. Interestingly, there is much less material above 200 nm for the PEG+DGU+UF purified sample, which supports the conclusion that the initial DFF step is unnecessary if followed soon after by other purification methods (other than to assure sterility by excluding bacteria).

The most important conclusion that can be drawn from the NTA data is the high purity, high monodispersity, and low aggregation of the PEG+DGU+UF sample. A sharp peak is observed at 59 nm and there is very little other material. The smaller vertical extent of the scattering intensity point cloud (orange) reveals that this suspension is composed of particles with a narrow distribution of scattering intensity, and thus is composed of more similar material (*i.e.*, phages) than the other suspensions.[204] Unfortunately, TEM analysis of PEG+DGU+UF samples would be needed to confirm the absence of material smaller than the NTA LOD, but this was not possible due to time constraints. However, extensive SEM analysis was performed on surfaces functionalized with this suspension, which are treated in detail in Chapter 4.

Furthermore, it is reasonable to conclude that the combination of purification methods will remove small contaminants more effectively than any method in isolation and would not introduce additional contaminating

material. Together with the absence of contaminants observed by SEM (Chapter 4), we can thus reasonably conclude without TEM observation that the phage samples are very effectively purified by the synergy of PEG precipitation, DGU on a CsCl gradient, and finally ultrafiltration.

2.7.1 Plaque assay

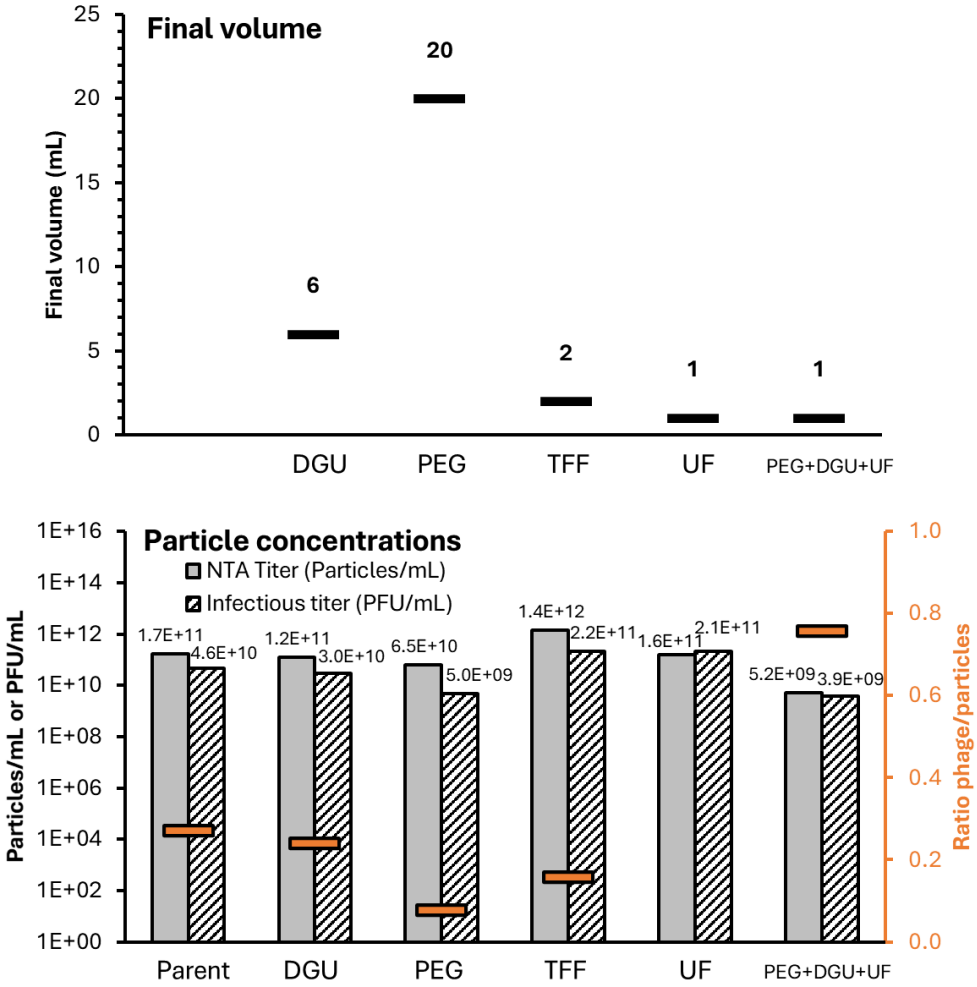

Figure 2.9 Characteristics of purified phage suspensions.Top: Comparison of final volume produced by each purification method. Bottom: Histogram comparing infectious titer as measured by plaque counting (solid gray bars), with particle concentration as measured by nanoparticle tracking analysis (hatched bars). The ratio of infectious titer to total particle concentration is indicated (orange, right-hand axis).

Plaque-counting experiments were performed to assess the concentration of infective phages in each suspension. Key figures of merit for comparison of purification methods include the final volume and the infectious titer. For the purposes of this PhD, only small volumes are required since phage-functionalization of only small regions of the sensor surface was envisaged. For this reason, the purity and infectious titer were more important than volume, so long as of the order of 1 mL was produced.

There is a subtle distinction between infectious titer and the concentration of viral particles in a phage suspension. The infectious titer is a measure of the presumed viral load of a parent suspension, as calculated from the observed count of lysis plaques produced in a plaque counting method, together with the dilution factor of the plated sample. Neither the drop cast or double layer agar method is capable of detecting empty

phages or distinguishing between a single phage and aggregates of multiple phage particles. In contrast, nanoparticle tracking analysis reveals the hydrodynamic radius and optical scattering properties of all particles, with little discrimination between viable phages, empty phages, phage aggregates, or contaminants. For this reason, complementing NTA with plaque-counting measurements can yield richer information into phage suspension composition, as explored in Chapter 5.

As is typical, the particle concentration (or *NTA titer*) was observed to be higher in these experiments than the infectious titer. This is logical since only a subset of particles will be phages, and only a subset of these will be infectious. Although UF seems to have a higher infectious titer than NTA titer, this is due to a smaller number of replicates during NTA measurement. In any case the NTA and infectious titer are within measurement errors for the UF sample.

While TFF produced the suspension with the highest infectious titer (2.2×10^{11} PFU/mL), the active phages form only a small proportion of the total particle population. In contrast, PEG+DGU+UF yields the highest ratio of infective phage to total particle number. This correlates with the smaller vertical extent of the scattering intensity point cloud for this PEG+DGU+UF suspensions in **Figure 2.8**, indicating a homogenous population of phages produced with this protocol.

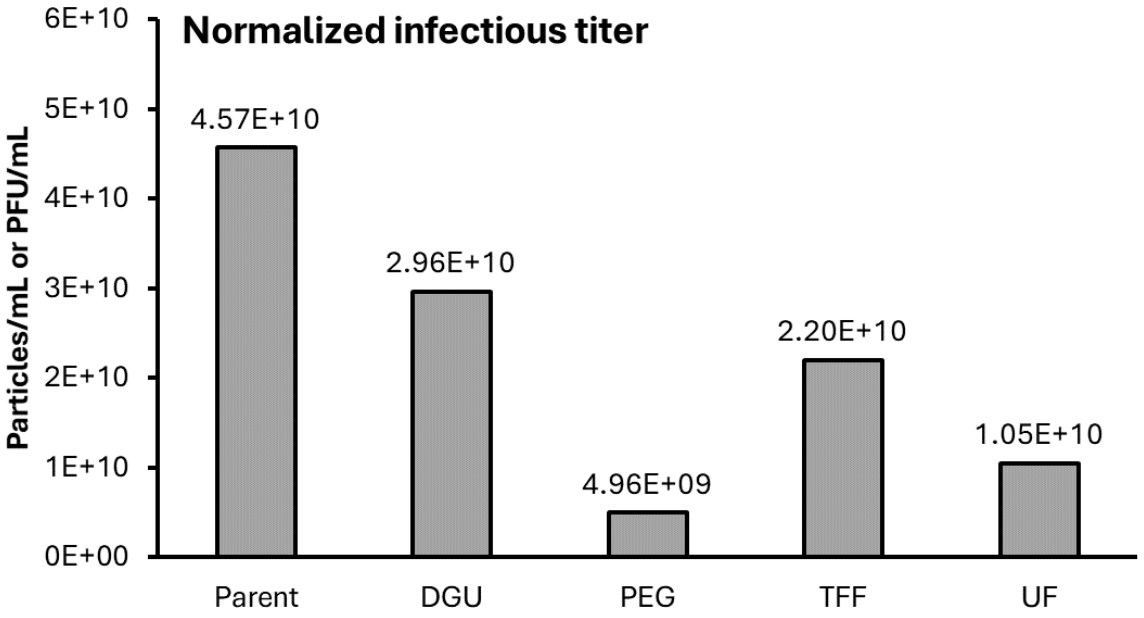

Figure 2.10 Histogram plot of the normalized infectious titer, obtained by dividing the infectious titer resulting from each protocol (measured by plaque assay) by the concentration factor for the respective method.

However, a comparison between the particle concentrations resulting from different purification methods must also take into account the change in volume as a result of the protocol. We define the *concentration factor* as the ratio of the final volume of phage suspension to the volume at the beginning of each protocol. A volume of 20 mL was purified in each case (except in DGU which involved only 6 mL), but the final volume varied. **Figure 2.10** shows the *normalized* infectious titer which is the infectious titer divided by the concentration factor for each method. Considering the data this way, one can see that DGU results in the loss of the least amount of phage titer.

Note that although **Figure 2.9** shows PEG+DGU+UF with the lowest titer at 3.9×10^{9} PFU/mL, this is because this sample was the only available for NTA measurements. Infectious titer values of 10^{11}-10^{12} PFU/mL were frequently achieved with PEG+DGU+UF purification.

2.8 Conclusions

NTA yields individual particle information across statistically significant sample sizes[191] and has been demonstrated for the study of bacteriophage[192,193] and viral suspensions[190,194]. While DLS is an established technique for analysis of nanoparticle dispersions, it can struggle to give interpretable results for suspensions with significant polydispersity as in the case of phage suspensions. NTA thus presents advantages over DLS in the study of bacteriophage suspensions, particularly in cases where aggregation is suspected, and yields more granular data.

While TFF had been considered a promising choice for phage purification early in the work of this PhD, initial good results in round 1 were not replicated in subsequent rounds. The first TEM observations of TFF-purified suspensions (**Figure 2.7**M) indicated a superior level of purification than the other methods tested. However, this was not replicated in rounds 2 or 3 (**Figure 2.7**N and **Figure 2.7**O). After observing the appearance of extensive contamination in suspensions produced in rounds 2 and 3 of TFF purification, the tubing and cartridge were changed with the assumption that accumulated material from previous purification rounds was being released back into the circuit. However, no improvement was seen in TFF-purified samples despite these efforts.

As a result, PEG purification was used for subsequent immobilization experiments, and later the combination of PEG precipitation, DGU, and UF was found to produce incredibly high-quality immobilized phage layers, as described in more detail in Chapter 4.

We can make an assessment of the suitability of TFF for purification of phage lysates independent of a mechanistic understanding of the failure of TFF observed in these experiments. A brief description of the problems encountered with TFF purification is outlined below.

The hope was that TFF would present a more convenient alternative to purification by DGU or PEG. However, this expectation was not met since significant time was required to rinse and prime the TFF circuit, followed by continual monitoring of the diafiltration process (since the circuit must not be allowed to run dry) which limited the feasibility of carrying out other work in parallel with the purification process, which can take several hours.

On one occasion, several days' work was lost after friction with the peristaltic pump rotor created a puncture in the tubing, quickly leaking the phage suspension out of the circuit. This is obviously an event that is expected by the manufacturer, since the TFF Minimate kit houses the entire circuit above a basin with raised edges to catch such leaks. Aside from the frustration of lost time, the leaking of crude phage lysate has obvious biosecurity and lab cleanliness implications, especially since much of the system cannot be autoclaved — including the sample reservoir. This design choice — to make large sections of the circuit incompatible with autoclaving — makes the TFF kit of limited use for purification of multiple of biological species, but especially phages. An entirely new circuit (including pressure gauge, valves, sample reservoir, cartridge, connectors, and tubing) must be used for each phage, otherwise immediate and unacceptable cross-contamination will result.

In addition, recirculating passage of phage through the circuit exposes phage (in increasingly higher concentration) to surfaces composed of polyethylene (membrane plate) polypropylene (seals and valves) and polypropylene-based thermoplastic elastomer (peristaltic pump tubing), among other materials. Recent publications have highlighted the detrimental effect of exposure of phage suspensions to polymer and other common labware surfaces,[205] and indeed an experimental study of these effects forms the basis of Chapter 5

of this work.[125] Exposure of phage to such a large surface area inside the TFF circuit, together with agitation, may prove to have detrimental effects to varying degrees depending on the phage used.

Despite the grievances with TFF expressed in this chapter, this method might still be used by phage therapy researchers seeking to produce low-endotoxin phage preparations for human therapeutic use, provided that TFF purification relies on single-use TFF cartridge and single-use tubing, including reservoirs and valves . While this method of purification is a relatively expensive way to produce a phage preparation (a Pall Minimate TFF cartridge costs on the order of €500 in 2021), the cost is negligible within the context of healthcare.

In comparison, although DGU presupposes access to an ultracentrifuge which represents a significant up-front capital investment and maintenance costs, ultracentrifugation presents numerous advantages compared to TFF. DGU proceeds largely unmonitored for one or more hours, there is less of an issue with exposure to large surface areas of labware, and leaks are not a frequent problem. Overall DGU was found to be much less onerous than TFF, despite the need to follow up with UF or dialysis to remove CsCl. Furthermore, given the superior purification performance observed by TEM of DGU and PEG relative to TFF, the latter was no longer judged a compelling alternative and was abandoned for the development of a PEG+DGU+UF protocol, which is treated in Chapter 4 .

Chapter 3

Strategies for Surface Immobilization of Whole Bacteriophages: A Review

Published article in ACS Biomaterials Science & Engineering (2021)
DOI: 10.1021/acsbiomaterials.1c00013

Larry O'Connell[1,2], Pierre R. Marcoux[1], Yoann Roupioz[2]

[1] Univ. Grenoble Alpes, CEA, LETI, F38054 Grenoble, France

[2] Univ. Grenoble Alpes, CNRS, CEA, IRIG, SyMMES, 38000 Grenoble, France

Keywords: Biomaterials, Biosensing, Functional surfaces, Surface functionalization, Bacteriophage

Abstract

Bacteriophage immobilization is a key unit operation in emerging biotechnologies, enabling new possibilities for biodetection of pathogenic microbes at low concentration, production of materials with novel antimicrobial properties, and fundamental research on bacteriophages themselves.

Wild type bacteriophages exhibit extreme binding specificity for a single species – and often for a particular subspecies – of bacteria. Since their specificity originates in epitope recognition by capsid proteins, which can be altered by chemical or genetic modification, their binding specificity may also be redirected towards arbitrary substrates and/or a variety of analytes in addition to bacteria. The immobilization of bacteriophages on planar and particulate substrates is thus an area of active and increasing scientific interest.

This review assembles the knowledge gained so far in the immobilization of whole phage particles, summarizing the main chemistries, and presenting the current state-of-the-art both for an audience well-versed in bioconjugation methods as well as for those who are new to the field.

3.1 Introduction

Bacteriophages, obligate intracellular parasitic viruses that replicate only in the cells of their host bacterium, are the most numerous replicating biological entity on Earth, with an estimated 10^{31} phage particles contained within the biosphere, compared to an estimated 10^{30} bacterial cells [35,36]. Indeed, the estimated daily turnover of 15% of all bacterial cells due to phage lysis is a testament to their crucial role in microbiological ecology [41].

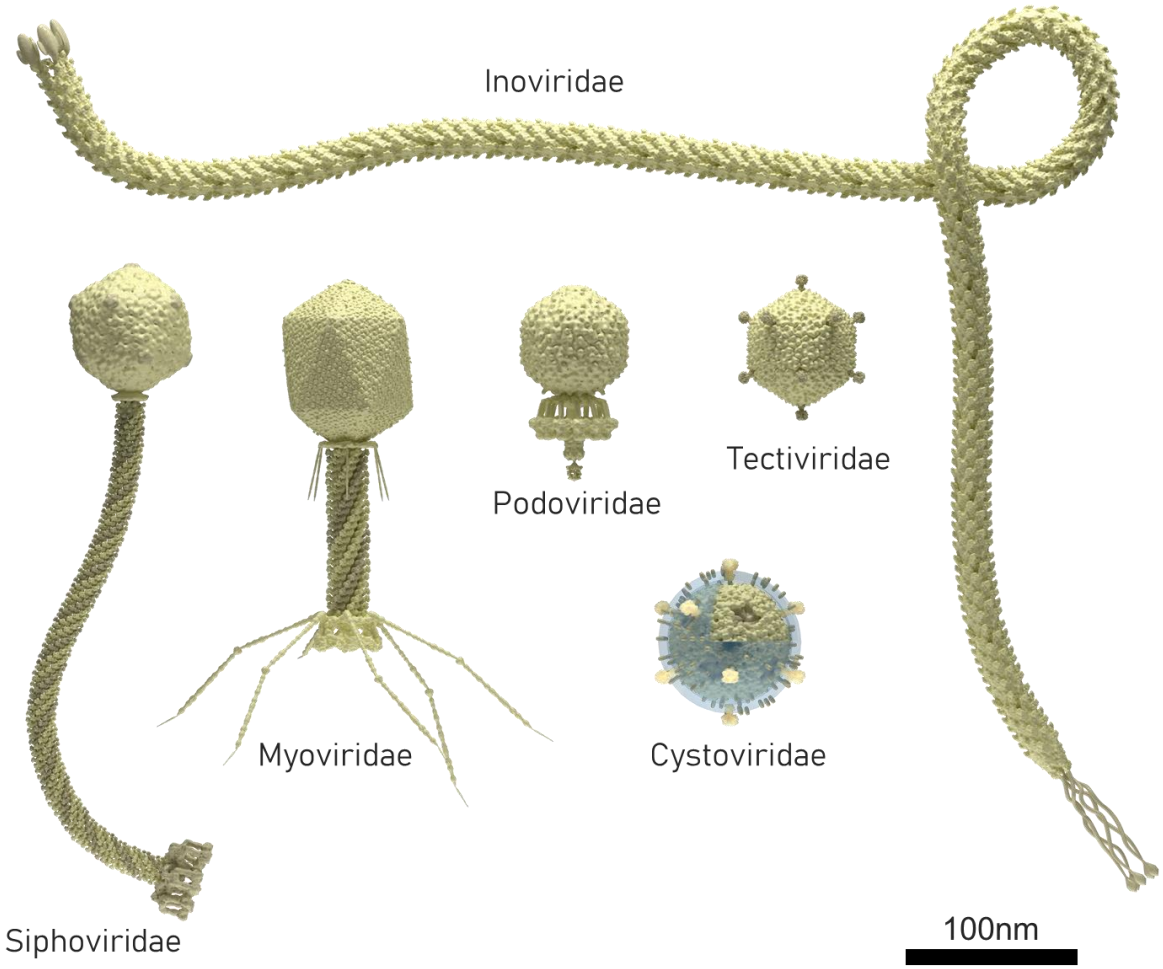

Figure 3.1 Illustrations of the bacteriophage morphologies that appear most often in the phage-functionalization literature.The *Inoviridae* family comprises filamentous phages such as fd and M13. The *Myoviridae* family features long contractile-tailed phages and includes the well-known T4 coliphage. The *Siphoviridae* family features long non-contractile-tailed phages such as D29. Meanwhile, the *Podoviridae* family are short-tailed and include P22. Relative scales are approximate.

Phage structure exhibits large variation which falls within a few stereotyped forms (**Figure 3.1**). A small number of phage morphologies are over-represented in the phage immobilization literature and include: long contractile-tailed phages (*Myoviridae, e.g.*, T4), long non-contractile-tailed phages (*Siphoviridae*), short-tailed phages (*Podoviridae, e.g.*, T7 or P68), filamentous phages (*Inoviridae, e.g.*, M13 and fd) [206]. Less frequently seen in the phage immobilization literature are tailless phage families *Tectiviridae* (comprising non-tailed icosahedral phages, such as PRD1) and *Cystoviridae* (featuring an outer lipid membrane and no tail, such as phage phi6). Phages are also described in terms of their replication cycle. *Lytic phages* terminate their replicative cycle with the biochemical lysis of their host, rupturing the cell membrane and releasing up to several hundred progeny virions in one burst. In contrast, upon infection of a suitable host, temperate phages incorporate their genetic material into that of the bacterial cell and may lay dormant before shifting to a lytic

cycle, or may instead continually produce a smaller number of phages which are shed from the host on a continuous basis [207].

3.1.1 History

Bacteriophages were independently discovered by microbiologists Frederick Twort in London in 1915 and by Felix d'Herelle in Paris in 1917 [43].It should be noted that extensive research on phage phenomena was also carried out in Poland during the interwar period[10], as well as in Brazil. Indeed, the oft-cited pioneering 1919 work by d'Hérelle in the use of phage to treat dysentery in French soldiers was followed relatively soon afterwards by similar trials in 1923 in both Poland[10] and Brazil[57].

Such research eventually led to the widespread use of phages in the Soviet Union for the treatment of routine bacterial infections, with phage therapy being extensively mobilized to meet the needs of the Soviet military beginning in 1939 with the Winter War with Finland, and later in World War II [44].

Meanwhile in the West, the discovery by Alexander Fleming in 1928 of penicillin, a broad-spectrum antibiotic, led to a paradigm shift in medicine that relied heavily on the widespread administration of what was seen at the time as a "magic bullet".

The geopolitical paranoia of the Cold War and a lack of scientific rigor in reporting of early soviet phage therapy studies resulted in a progressive dismissal of phage therapy in Western medicine [47]. In the 1970s, up to 70 patients per year underwent phage therapy to treat bone and joint infections (BJI) in Croix Rousse Hospital, Lyon [49]. However, non soviet-aligned states instead pursued a policy of unfettered use of antibiotics [48], the profligate administration of which has now led to widespread antimicrobial resistance (AMR), threatening to return medicine to the "dark ages" before widespread availability of microbial control [208]. With the World Health Organization (WHO) announcement in 2014 that AMR was no longer a looming threat but a contemporary crisis [4], the problem of antibiotic resistance is proving increasingly salient [2].

In a global context where common pathogenic bacterial strains are rapidly gaining new resistance mechanisms, the pharmaceutical sector is largely withdrawing from the antibiotic discovery field, which has led to a failure to discover any new classes of antimicrobial agents in over three decades [31,209].

A growing appreciation for the importance of antibiotic stewardship and the urgency of identifying novel therapies has led to renewed interest in phage therapy as a plausible replacement for antibiotics [89]. In the field of biodetection, too, researchers have leveraged the high specificity of bacteriophages for their hosts to create biosensors with single strain specificity for a variety of common human pathogens and with extremely low detection limits. New use cases are also being explored, including the use of phages for antimicrobial, bioactive packaging [210,211] or as nanostructural scaffolds for various supramolecular structures [184].

Within this context, biomedical, agricultural, and environmental monitoring applications of bacteriophages would be aided by well-characterized, repeatable, versatile, and (ideally) morphology-agnostic immobilization methods.

3.1.2 State of the art

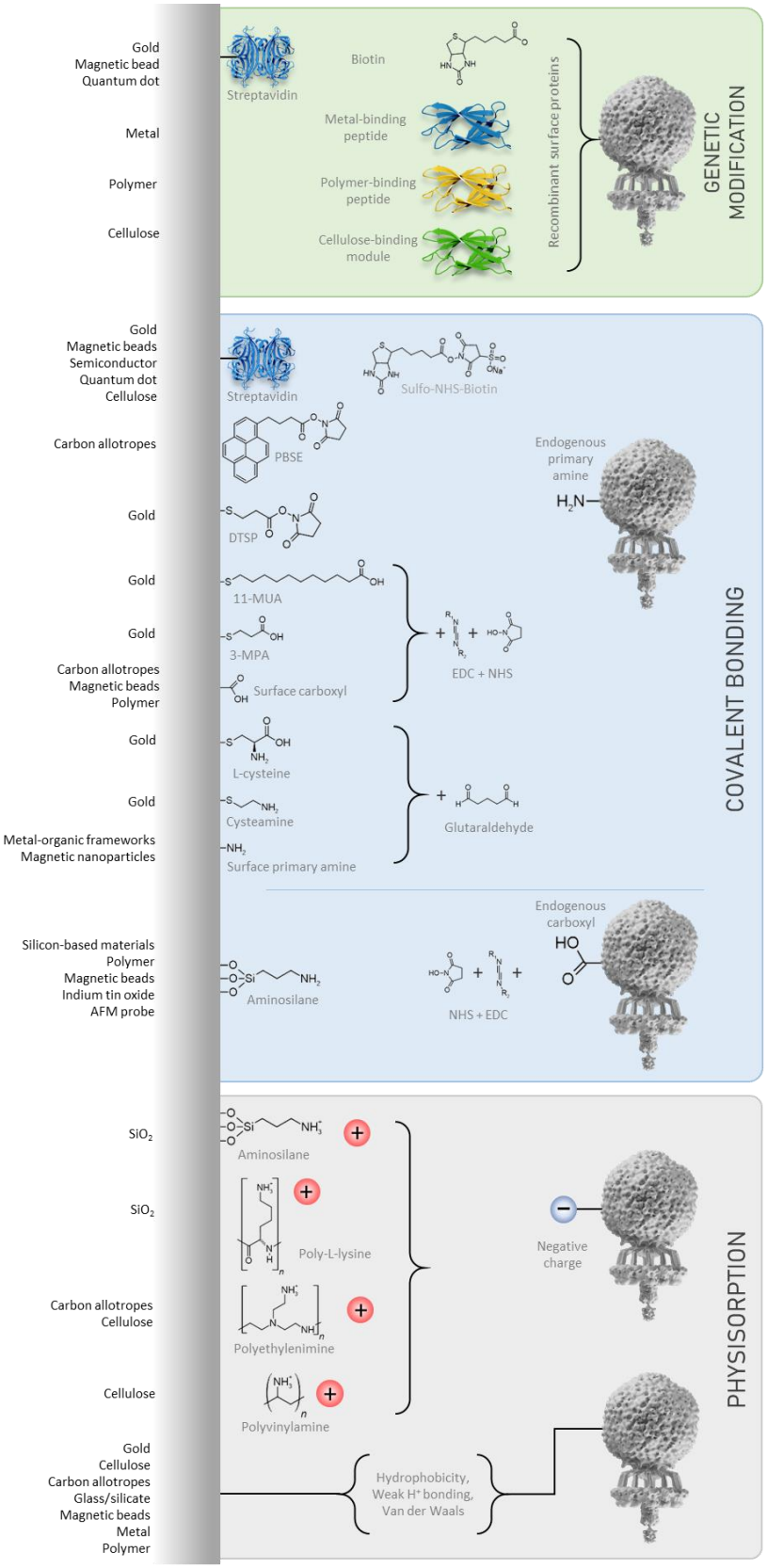

Figure 3.2 Schematic representation of a selection of the most popular bacteriophage immobilization strategiesMethods are broadly grouped into covalent bonding, physisorption, and genetic modification. At left, the substrates that have been demonstrated in the literature with the adjacent immobilization method. Note: bacteriophages are represented by a generic *Podoviridae* but in most cases represent other phage morphologies

The literature concerning phage-functionalization of substrates falls into three main categories, with some overlap:

- Coupling to a transducer for the specific detection of bacteria or other analytes.

  Starting in earnest in 2005 [180], the last 16 years have seen bacteriophages immobilized on biosensors using a variety of transduction mechanisms, towards the detection of a large variety of target analytes including bacteria and their spores [212–217], antibodies [218–221], prostate specific antigen [221–223], enzymes [181,183], cancer biomarkers [224], and glucose [225].

- As a biosorbent layer for species-targeted biocontrol and anti-fouling

  The incorporation of bacteriophages into materials (*e.g.*, food packaging and wound dressing) can confer them targeted anti-bacterial properties which can help reduce the proliferation of bacteria in foodstuffs or surrounding wounds. Such bioactive materials have been demonstrated in food packaging that targets *Listeria* [211,226], *Escherichia coli* [211,226,227], and *Salmonella* [210]. Bioactive fabrics have been demonstrated with specific antimicrobial action against *Pseudomonas aeruginosa* [228] and *E. coli* [229].

- As a structural scaffold for supramolecular nanostructure fabrication

  The tessellated and highly redundant structure of bacteriophage capsids, together with their chemical uniformity and physical monodispersity, also opens up the possibility of bottom-up fabrication of highly ordered supramolecular structures [184,230]. Liquid crystalline bacteriophage films [184,230] have been proposed for use as tissue regenerating scaffolds [231], piezoelectric energy harvesting [232], and colorimetric sensors [233].

Across all applications, the vast majority of papers reviewed demonstrate immobilization of classic phages such as the lytic T4 coliphage, or the temperate M13 and fd phages. However, examples are also to be found of successful immobilization of various other phages of the *Autographiviridae* [218,234–236], *Tectiviridae* [138,237,238], *Herelleviridae* [239], *Leviviridae* [138,239], *Myoviridae* [128,136,138,141,226,237–247], *Siphoviridae* [136,226,228,239,248,249] and *Podoviridae* [128,138,170,239,244,250–254] families.

3.1.3 Viral properties involved in immobilization

When considering the immobilization of bacteriophages on surfaces or particles, we should first consider what properties of the phage, which moieties and/or surface charges, can be modified or leveraged for chemical and/or physical interaction with the surface or intermediate linker molecules (**Figure 3.2**). The vast majority of bacteriophages exhibit an outermost protein layer which encapsulates genetic material on the interior (with the exception of *Cystoviridae*, which encapsulated the capsid in a lipid envelope). Bacteriophage capsids are composed of proteins which are in turn composed of long chains of amino acid subunits, which display primary amine ($-NH_2$) groups on their N-terminus, and carboxyl groups (-COOH) on their C-terminus (**Figure 3.3**). Both the amine and carboxyl groups of polypeptide amino-termini are frequent targets for immobilization chemistry, but in the case of bacteriophages, the termini available for conjugation will be greatly outnumbered by amino acid side chains.

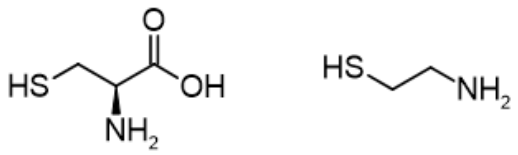

Figure 3.3 Structural formulae of the amino acid L-cysteine (left) and cysteamine (right)

Amino acids vary in the composition of their side chains with some side chains endowing a polarity, charge, or hydrophobic/hydrophilic character, each of which may be leveraged in isolation or in combination for the purposes of conjugation. For example, two amino acids in particular, L-cysteine and methionine, contain sulfhydryl side chains which interact strongly with gold, a common substrate for bio-functionalization. The amino acids lysine, arginine, asparagine, and glutamine feature a second primary amine group on the side chain in addition to their N-terminus.

Each amino acid also has a characteristic isoelectric point which determines the pH below which the side chain is protonated in aqueous solutions. The local hydrophobic character and charge of a phage is the result of an aggregate sum of the local constituent amino acids. The isoelectric point of a bacteriophage dictates the charge it presents to the solution and thus its stability and resilience against aggregation[255–257]. There is significant evidence that tailed bacteriophages – which make up over 95% of described phages [198] – have a net dipole moment, with a negatively charged head and positively charged tail and tail fibers at physiological pH[171,226,258].

The bacteriophage genes that code for amino acids on the outer bacteriophage surface can also be targeted for site-specific genetic engineering and mutagenesis, altering them in order to introduce new functional groups in order to optimize their chemical and/or physical characteristics for the purposes of immobilization [182,225,235,259–268].

To summarize, when developing immobilization strategies, the researcher has at their disposal:

- Primary amine groups (−NH_2), present at the N amino-termini of proteins and in the side chains of lysine, arginine, asparagine, and glutamine
- Carboxylic groups (−COOH), present at the C amino-termini of proteins and in the side chains of aspartic and glutamic acid
- Sulfhydryl side chains (−SH) of the amino acids cysteine and methionine
- The local and overall charge of the phage
- The dipole moment of the phage
- Site-directed genetic engineering of the phage coat

It is starting from this basis that the full suite of immobilization strategies can be derived.

Immobilizing biological entities on surface or nanoparticle substrates can lead to conformational and other changes that impede their original function. When choosing an immobilization strategy, it is important to consider what purpose the phage immobilization is serving. Is the goal to maximize analyte capture itself? Or is it rather to maximize the limit of detection (LOD) of a biosensor? Is the surface to be used for the purpose of biocontrol (*e.g.*, wound dressing or food packaging)? What kind of environment will the phage-functionalized surface be used in? Is it important that the population of phage maintains the same infectivity as its non-immobilized form, or is some loss acceptable? Is it important that the phage be oriented in a given direction relative to the substrate?

The answers to each of these questions places different requirements on the immobilization strategy and optimal phage density. For example, Naidoo *et al.* have found that bacterial capture efficiency only correlates with increasing phage surface density up to a certain threshold, beyond which the capture efficiency actually decreases [128]. However, in a biocontrol context where shedding of phage particles from a substrate may be desirable, this effect may not be problematic and we may indeed aim to achieve a maximal surface density limited only by geometric constraints.

Consideration of the end result is needed in order to optimize the immobilization strategy. Phage density may represent only a proximal measure for a different performance metric of the phage-functionalized substrate. The researcher may indeed aim for lower phage surface densities depending on the application, and one should not necessarily aim to maximize surface density for its own sake.

3.1.4 Scope and organization of the review

This review groups the literature based on immobilization technique, rather than grouping by substrate, phage, or detection scheme (in the case of biosensors). This arrangement makes the particularities and commonalities between immobilization strategies more apparent.

This review does not treat the immobilization of phage-derived proteins (*e.g.*, endolysins or recombinant coat proteins), since this has been treated elsewhere and overlaps with general strategies for protein immobilization, a topic too large for a single review. For an excellent treatment of protein immobilization, see Hermanson [142]. Likewise, this review does not treat phage immobilization on chromatographic columns or microtiter plates, since this falls in the category of phage display literature, thoroughly reviewed in Hust and Lim [269].

The most common substrates are briefly described, as well as the scientific interest in phage-functionalization in each case. Thereafter, the most common and successful immobilization strategies are outlined with reference to their application in the literature, grouped into covalent chemistries, non-covalent or physical methods (*e.g.*, physisorption, electrostatic adsorption, avidin-biotin linkage etc.), and finally genetic modification techniques, which are treated separately since they represent a modification of the bacteriophage itself but facilitate the preceding chemisorptive and physisorptive immobilization strategies.

3.1.5 Oriented immobilization

A phage's host range and ability to replicate is largely based on its ability to specifically recognize cells of its host bacterial strain *via* the phage's receptor-binding domains (RBDs) – epitope-recognizing regions on the phage capsid. This recognition event is a *sina qua non* to initiate phage replication and relies on serendipitous encounters between the RBDs and a bacterial cell surface.

Over 95% of described phages are tailed [198] and thus have an inherent asymmetric, bilateral geometry, having a preferred orientation with regards to attachment to their host cell. For a conjugated phage to retain its binding and replicative capacity, it must be oriented on the surface such that its RBDs are exposed to the environment, and hence any host cells that may be present [270]. Such a tail-upward orientation will hereafter be referred to simply as "oriented" immobilization. Most authors simply accept the lower bacterial capture associated with random phage orientation, relying on immobilization of a sufficiently large number of phages that includes a small subpopulation of serendipitously tail-upward oriented phages. Nevertheless, Nogueira *et al.* recognize that maximizing tail exposure is a key criterion for maintaining immobilized phage infectivity [228]. Similarly, Hosseinidoust *et al.* conclude in an influential review article that the main hurdle to designing efficient phage-based biosensors appears to be controlling the orientation of the immobilized phages [270].

The bacteriophage head presents a net negative charge, while the tail fibers present a net positive charge [258]. Thus, the dipole moment of a phage particle causes the head to be oriented towards a positively charged

surface [171]. In addition to local charge distribution, many phages such as T7, present an overall net negative charge [168,271].

In most circumstances there is a strong entropic preference towards horizontal alignment of tailed and filamentous phages. However, as we shall see, a significant minority of the studies reviewed have taken advantage of the local charge or other properties of bacteriophage capsids to claim oriented immobilization as a result of their protocols (**Figure 3.4**). Frequently, however, insufficient evidence and/or no clear mechanisms are presented to prove oriented immobilization has been achieved. This is partly due to the difficulty in determining the orientation of nanoscale objects, but post-functionalization characterization techniques do exist that can help justify such claims.

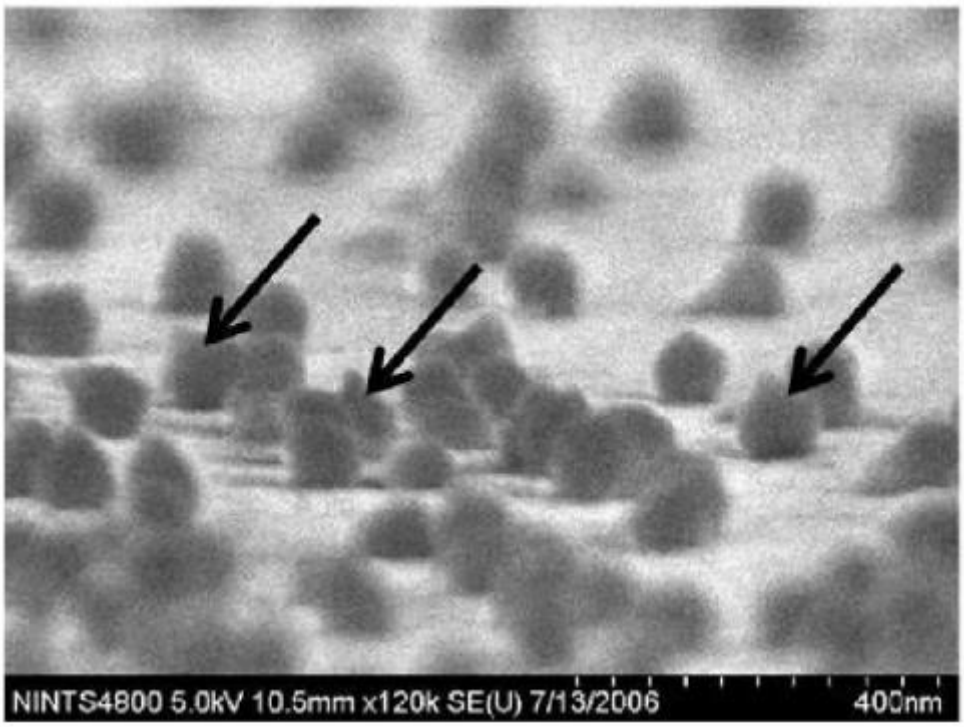

Figure 3.4 Scanning electron micrograph of *in vivo* biotinylated T4 phage, immobilized on a streptavidin-coated gold surface.Arrows indicate phage particles immobilized with a tail-up orientation. Reproduced with permission from *Tolba et al.* [263]. Copyright 2010 American Society for Microbiology.

3.1.6 A note on surface density

A high phage surface density is not the sole criterion for high phage infectivity and/or bacterial capture. For example, Tawil *et al.* found that phages were immobilized on gold with double the density when cross-linked *via* L-cysteine compared to glutaraldehyde, but that no significant difference was found in the bound phages' lytic behavior [254]. Similarly, Leppänen *et al.* rigorously compared infectivity and phage surface density after surface treatments with different combinations of 11-mercaptoundecanoic acid (11-MUA) and (3-aminopropyl)triethoxysilane (APTES), concluding that a higher phage density did not always result in a higher infectivity [272]. Indeed, Naidoo *et al.* achieved an impressive surface density of 199±2 phages/μm^2 but found that – above a value of a 18.9±0.8 phages/μm^2 – higher phage density led to a *reduction* in total bacterial capture [128].

These results suggest that careful consideration and design of the surface functionalization can lead to dramatically improved activity and/or bacterial capture of phage-functionalized surfaces.

3.2 Common substrates

3.2.1 Gold

Gold surfaces are by far the most popular surface for phage functionalization, serving as the substrate in just over half of all papers reviewed on this topic. Gold exhibits ideal properties for functionalization with many biological entities [142], and for bacteriophages the case is no different. Gold is biocompatible, non-oxidizable, readily available, easily cleaned, and its deposition on a variety of substrates is a mature technology [273–275]. Gold also exhibits a very high binding affinity for sulfhydryl (R-SH, aka thiol) groups of around 200 kJ/mol, which also permits easy formation of self-assembled monolayers [275]. Thiol groups are frequently found – or easily introduced – in most target ligands for the purpose of immobilization [275].

Facilitating bioconjugation is the principal motivation behind the deposition of a gold layer on transducers that do not involve the intrinsic properties of gold itself (*e.g.*, magnetoelastic or quartz crystal microbalance (QCM) biosensors, which instead rely on the resonance of an underlying amorphous ferromagnetic material [276] or quartz crystal [277], respectively). However, gold also exhibits ideal properties where its biocompatibility and ease of conjugation is a happy coincidence. Gold features a high density of easily polarizable free electrons – a prerequisite for strong interaction with electromagnetic fields [278] – making it an ideal material for use in surface plasmon resonance (SPR). For SPR, there are effectively only two metals with appropriate properties: gold and silver [107]. While silver actually yields a superior SPR effect, it is less biocompatible and less chemically stable – particularly towards oxidation – compared to gold, and so the latter has become the *de facto* default for SPR biosensors [107,278].

3.2.2 Magnetic beads

Magnetic bead surfaces are a frequent substrate for phage conjugation since, once functionalized, they can be used for immunomagnetic separation (also sometimes referred to as phagomagnetic separation) and concentration of low-titer analytes in order to boost the capture efficiency of biosensor surfaces (Figure 3.5) [234,235,243,250,251,259,279,280]. Briefly, phages specific to a given bacterial strain are immobilized on the beads, which are then mixed with a sample and bind to the target analyte (Figure 3.6). Application of a magnetic field can then be used to concentrate and confine the captured analyte to a given region, for example on the surface of a biosensor. Phage immobilization has been shown for magnetic beads with a variety of surface chemistries including tosyl [250,251], carboxyl [234,236,251,279], streptavidin [235,259,263,281], azide [261], and isothiocyanate-terminated coatings [280].

3.2.3 Carbon allotropes

Carbon allotropes (*e.g.*, graphene, nanotubes) and glassy/vitreous carbon are common components of inks used to fabricate screen-printed electrodes (SPEs). Electrode screen-printing enables cheap, versatile electrodes for use in clinical assays[282], food processing[283], and environmental monitoring [284]. Such electrodes can also be composed of gold, silver, or platinum; but carbon is more typical due to its relatively low cost [285]. The versatility and easy manufacture of SPEs has led to carbon allotropes becoming a target for phage immobilization for the fabrication of biosensors specific to various bacterial strains [241,242,248,286,287], and in one paper a biosensor for West Nile virus-specific IgG [218]. Carbon nanotubes can also be used as an intermediate structure for the immobilization of phages on different substrates, as was demonstrated by Farooq *et al.* for bacterial cellulose matrices for ultra-sensitive and selective electrochemical detection of *Staphylococcus aureus* [134]. Carbon allotrope-specific binding peptides have been discovered that may enable recombinant phage immobilization on such substrates [288–291] (see 3.5.3 Carbohydrate-binding modules below).

3.2.4 Polymers

Phage-functionalization of polymers is of interest since such materials can be formed into antimicrobial wound dressing [80,228], food packaging [211], and biocontrol surfaces resistant to biofilm formation [292]. They also form the

coating of many commercially available magnetic beads [234,236,250,251,279]. Polymers that have been successfully conjugated or co-polymerized with phages include polycaprolactone [228], polymethyl methacrylate (PMMA) [266], polyethersulfone [292], polystyrene [293], polyhydroxyalkanoates [227], polyethylene [294], and poly(3,4-ethylenedioxythiophene) (PEDOT) [222,295,296].

It is interesting to note that a large number of peptides have been discovered that have high binding affinities for specific polymers [297–303], and that such proteins have been expressed on the capsids of recombinant phages to facilitate immobilization [259,263,266].

3.2.5 Cellulose-based materials

A particularly important subcategory of polymers is cellulose and cellulose-derived materials. As the most abundant natural polymer on Earth [304], cellulose features in the phage-functionalization literature because it forms the principal component of paper. With its high porosity, hydrophilicity, chemically inert character, and slight negative charge at neutral pH [229,239], paper lends itself to the fabrication of cheap, mass-produced devices for healthcare [305] and environmental monitoring [306].

Phage-functionalization of paper and cellulose-derived polymers is motivated by the development of antimicrobial food packaging materials [210,211,226], and low cost biosensors [239,307,308]. Phage-containing bio-inks can be printed onto paper substrates, and it has been shown that T4 phages are capable of resisting the shear stress and drying processes involved in industrial printing [309]. It has also been demonstrated that careful consideration of the bio-ink constituents can enable production of bioactive paper that is stable for several days after printing [310]. Anany *et al.* have demonstrated a dipstick assay based on inkjet-printed phages that efficiently captured and infected *E. coli* and *Salmonella* Newport in broth and food matrices [239]. Farooq *et al.* demonstrated phage-functionalization of bacteria-derived cellulose fibers, but *via* intermediate multi-walled carbon nanotubes [134].

There is ample precedent for lateral flow devices that rely on capillary action along capillary beds to channel fluid for the purposes of biochemical analysis, the most well-known of which is probably modern pregnancy tests[311] and more recently covid-19 antigen tests[312]. Such microfluidic paper-based devices may also be combined with electrode screen printing for more elaborate microfluidic electrochemical sensors [311,313]. Phage-derived proteins [314] have been incorporated into lateral flow assays, but to our knowledge in all cases have been immobilized onto intermediate supports (*e.g.*, nanoparticles) rather than the polymer substrate of the device itself. The ability to reliably immobilize phages directly on paper substrates would open new avenues for the development of low-cost, mass-produced bioassays [308].

Some evidence suggests immobilization is more successful if paper has been precoated with polydiallyldimethylammonium chloride (polyDADMAC), a cationic polyelectrolyte which imparts a positive charge to the cellulose fibers and thus electrostatically binding the phage heads [308]. Phage resistance to dry environments can be improved by incorporating gelatin into the deposition ink [310]

When considering cellulose-based substrates, of note is the existence of cellulose binding modules (CBMs) – polypeptides that bind strongly to cellulose [315] and which can be expressed by genetically-engineered phages to facilitate their immobilization on such substrates [259,263].

3.2.6 Silicon-based materials

In this review, phage-functionalization of several materials including silicon nitride [224], optical fibers [316–318], atomic force microscopy probes [319], silica nanoparticles [136,246], and glass [138,170,182,237,260] are all grouped into the category of silicon-based substrates. Such surfaces are typically rendered reactive for immobilization chemistry through amino-silanization [135,136,138,170,182,224,233,237,246,260,272,316,317,319–322].

Optical fiber biosensing is of particular interest since it can exploit the properties of optical biosensing techniques (*e.g.*, SPR), while avoiding drawbacks associated with bulky equipment [316]. Using a smaller sensing element and sample volume can be advantageous in the analysis of small amounts of precious analytes, and can accommodate multiple parallel measurements on adjacent bundled optical fibers [323].

Since the fiber-optic material itself is cheap, this may offer the possibility of disposable, single-use sensors [324,325]. Finally, since the nature of optical fiber geometry means that signal transduction can take place at a physically remote location relative to the optical setup, this form of biosensing enables remote detecting and monitoring capabilities in potentially harsh environments [323], allowing one to bring the sensor to the sample rather than bring the sample to the sensor. Phage-functionalized optical fibers have been demonstrated for the specific detection of E. coli [316–318].

3.3 Covalent methods

3.3.1 EDC/NHS Chemistry

For substrates presenting carboxyl (−COOH) groups – be they endogenous or introduced – a common covalent conjugation method involves the use of the carbodiimide EDC (1-Ethyl-3-(3-dimethylaminopropyl)carbodiimide) to activate the carboxyl groups, creating an unstable ester intermediate [326]. Typically, a separate molecule containing a succinimidal group in the form of NHS (N-hydroxysuccinimide) is then introduced to the surface and supplants the carbodiimide, which is released into the solution. This stabilizes the activated carboxyl group and forms a second NHS-ester intermediate which is more vulnerable to nucleophilic attack from amino groups, in turn priming the NHS to be supplanted by the primary amine of an amino acid [170,326].

When a suspension of amine-containing ligands – such as phages or proteins – is introduced to the sensor surface, a primary amine of the ligand reacts with the NHS (the leaving group) and is then covalently bonded to the surface while the succinimidal group is released into the solution. After ligand binding is complete, the surface may be washed with ethanolamine whose amine groups will react with the remaining activated carboxyl “sites”, which blocks further binding.[326]. In this way, the EDC/NHS solution facilitates amide bonding between carboxyl groups of the surface and amine groups of the ligand [170].

Such EDC/NHS coupling is extremely popular for surface functionalization of gold following introduction of exogenous carboxyl groups (for example by formation of an alkanethiol self-assembled monolayer) [139,140,223,244,327–330], but has also been demonstrated for a variety of carboxylated substrates including glassy carbon electrodes [242], glass [138], magnetic beads [279], and polymers [227,331].

The creation of the second NHS-ester intermediate is not obligatory and in cases where a high yield of conjugated ligands is not crucial, the use of NHS may be omitted entirely. Such EDC-mediated binding has been used to covalently immobilize phages on glassy carbon electrodes [286,287], magnetic microbeads [279], and carboxyl-polystyrene latex beads [293]. However, the addition of even small amount of NHS to an EDC coupling reaction can boost the yield of conjugated ligand by a factor of 20 [332]. NHS activation decreases the water-solubility of the activated carboxylate molecule and for this reason is often instead sold as sulfo-NHS, wherein the charged sulfonate group preserves or increases water-solubility.

One paper made a rigorous comparison of the surface density of immobilized phage BP14 on gold that resulted from different combinations of EDC/NHS with L-cysteine, 11-MUA, and glutaraldehyde cross-linking; finding that cysteine – when combined with 11-MUA and ECD/NHS – gives an incredible 10^3 improvement in phage activity (measured by bacterial lysis) compared to simple physisorption [254].

EDC/NHS can also be used in the other direction: activating the surface carboxyl groups of the phages themselves in order to facilitate grafting to substrates featuring primary amines – be they endogenous or

introduced (*e.g.*, *via* aminosilanization) [135,170,319,333,334]. However, this approach is believed by some researchers to lead to increased blocking of the phage receptors responsible for bacterial capture [138], which seems to have been confirmed in experiment [135,272].

One feature of amide binding is the non-uniform nature of the ligand orientation. Since a ligand typically displays several primary amines, any one of which may react with the activated substrate carboxyl group, this allows a variety of ligand orientations during immobilization. This issue is compounded for very large molecules. On the scale of a bacteriophage, the large number of available primary amines means orientation may be effectively random unless effective mitigation strategies are employed, as discussed below.

Some substrates will already feature carboxyl groups, without the need to introduce a carboxyl intermediate. Such is the case for polyhydroxyalkanoate (PHA), a bacterially produced biopolymer [335] that is currently under investigation as a biodegradable food-packaging. Wang *et al.* have demonstrated that plasma treatment of PHA films results in surface carboxyl groups which can be activated and bound to phages using EDC/NHS, for the purposes of selective bioburden reduction in foodstuffs [227].

Carboxyl-activated magnetic beads are commercially available, for example *Dynabeads MyOne™ Carboxylic Acid* magnetic beads (Invitrogen). Although of proprietary formulation, the manufacturer describes these beads as having a coating of glycidyl ether and a core of highly cross-linked polystyrene with ferromagnetic inclusions. These beads have been employed for the detection of *E. coli* with an LOD as low as 10^3 colony-forming units/milliliter (CFU/mL) by impedimetric [236,279] and linear sweep voltammetry assays [236], as well as a colorimetric scheme based on release of endemic β-galactosidase from lysed analyte cells [234].

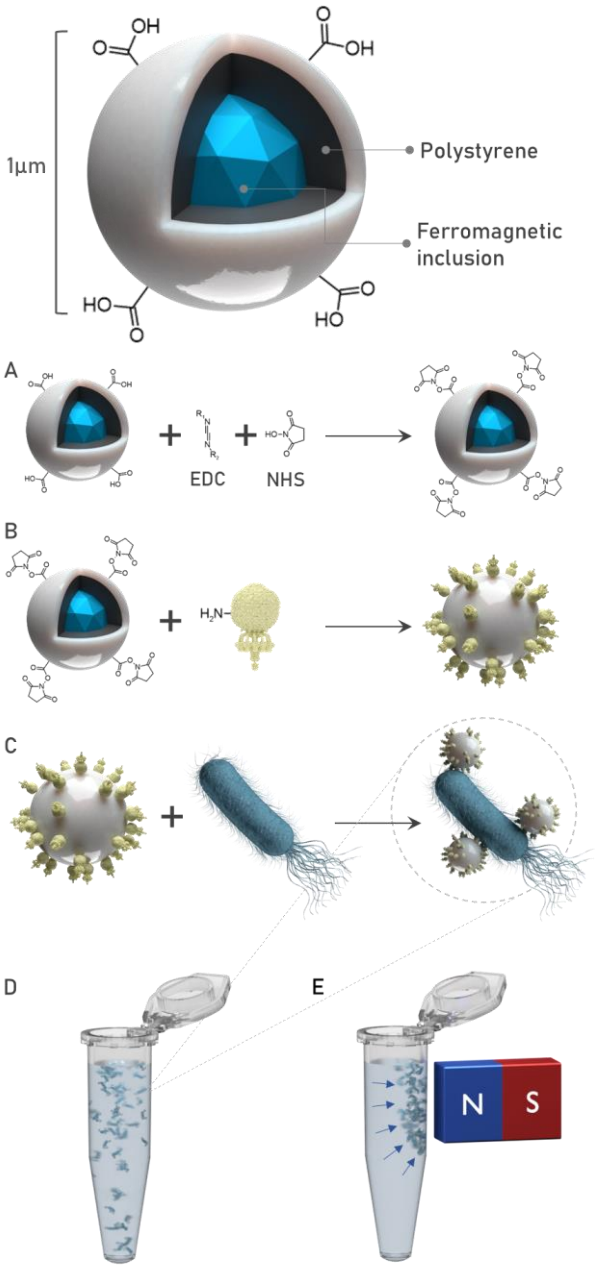

Figure 3.5 Schematic representation of a typical magnetic bead and its use for phagomagnetic separation.(A) A carboxyl-terminated magnetic bead is activated with EDC and NHS, priming it for conjugation. (B) A ligand bearing primary amines, in this case a phage, is mixed with the beads, becoming conjugated to the bead surface through amide bonding. (C) Mixing the functionalized beads with bacteria causes the beads to bind to the surface of any bacteria present. (D) and (E) The bacteria can now be retained in a standard tube while the supernatant is removed, or concentrated near a biosensor transducer surface, by the application of a magnetic field.

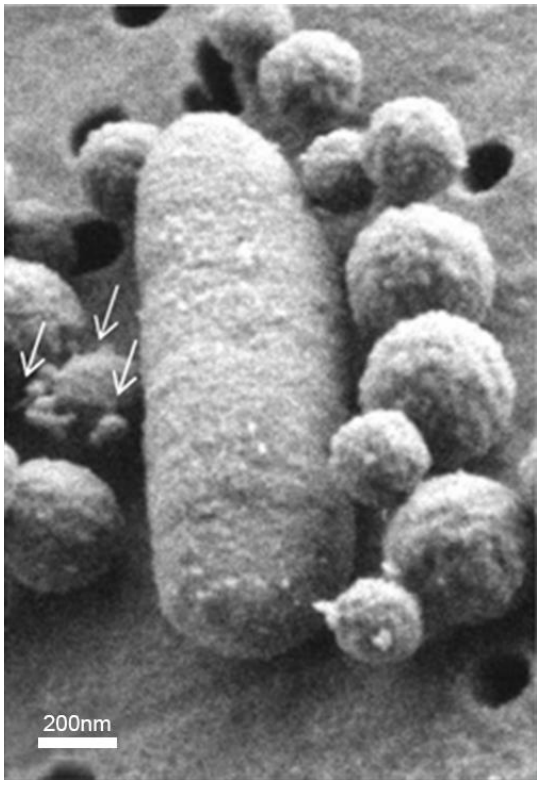

Figure 3.6 Scanning electron micrograph of P22 phages immobilized on carboxyl-activated magnetic beads following magnetic capture of a *Salmonella* bacterium.The arrows indicate the phages immobilized on the magnetic nanoparticles. Reproduced with permission from Laube *et al.* (2014) [69]. Reproduced with permission from Laube *et al.* [69]. Copyright 2013 Springer-Verlag Berlin Heidelberg.

A similar product is that of Ademtech (Pessac, France), in the form of Carboxyl-Adembeads which feature a superparamagnetic core of magnetite, covered with a proprietary styrene-based copolymer which presents carboxyl groups to the solution.[†] Regardless of the magnetic bead product used, in all cases in the literature reviewed, the beads' carboxyl groups are activated by EDC/NHS, exposed to the phage for immobilization, and used for the magneto-separation and subsequent detection of bacteria (*e.g.*, Salmonella [251] or E. coli [234,236,279]) by varying detection mechanisms (**Figure 3.7**).

[†] Personal communication

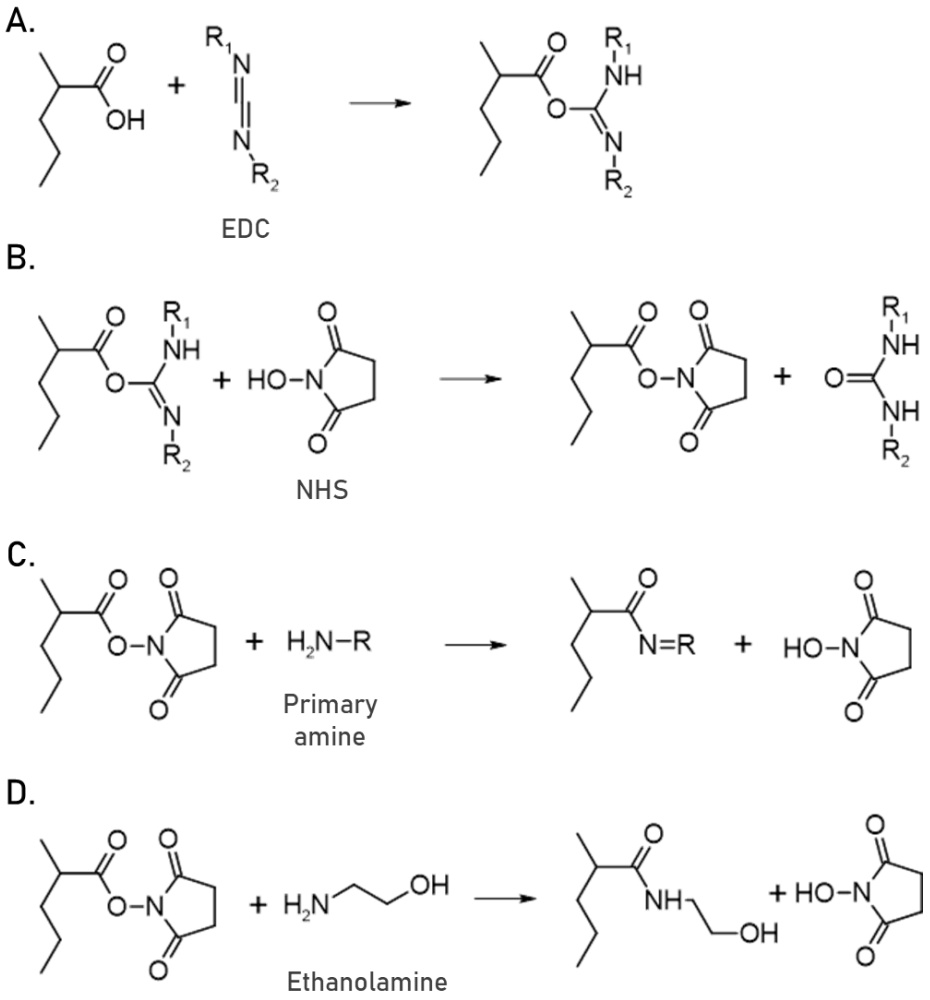

Figure 3.7 The chemical reactions involved in EDC/NHS-mediated ligand conjugation.The carboxyl group (−COOH) is activated with EDC/NHS (A. and B.), and then covalently bonds to the primary amine of the target ligand (C.). The remaining NHS esters are blocked using ethanolamine (D.). Here, R represents any arbitrary radical, in this case a bacteriophage. The side group R_1 is $–CH_2CH_3$ and R_2 is $–(CH_2)_3N+H(CH_3)_2Cl–$. Adapted from Chapter 3 - Surface Plasmon Resonance, Phillips and Cheng [326].

Alternatively, the researcher may have the possibility of grafting carboxyl groups to the substrate themselves. This has been shown for graphene, which can be electrochemically oxidized to produce carboxyl sites, allowing phage-functionalization of glassy [286] and screen-printed carbon electrodes [287]. A similar process has been demonstrated for carboxylated multi-walled carbon nanotubes for the phage-mediated detection of *S. aureus* [134]. There are many advantages of EDC/NHS chemistry that have led to it becoming a staple in the bioconjugation literature. Both EDC and the resultant isourea formed after binding are water soluble, meaning one can avoid organic solvents which could otherwise harm the ligand. The carbodiimide reaction occurs with high yield up to pH 7.5, allowing conjugation at physiological pH which is well-tolerated by most biological ligands. Since carbodiimides such as EDC are what is known as zero-length crosslinkers, no additional chemical structure is introduced between the conjugated molecules after cross-linking [142].

3.3.2 Self-assembled monolayers of thiolated molecules

No discussion of surface immobilization techniques would be complete without mention of thiol-gold bonding, a workhorse of conjugation chemistry. Also known as sulfhydryl groups, thiol moieties are widely exploited for the formation of self-assembled monolayers (SAMs) on soft metal substrates [275], and are regularly employed in the functionalization of planar and nanoparticulate metals – gold in particular – with proteins, antibodies,

and DNA. The most popular thiol-containing molecules are the alkanethiols which feature a sulfhydryl headgroup, an alkane chain of specified length, and a terminal functional group which can be used to introduce carboxyl sites to the substrate, for example (**Figure 3.8**). This stereotypical structure serves as a good model for a brief discussion of SAM formation.

In a classical SAM formation model, a soft metal surface is incubated with a solution of alkanethiol molecules. The strong affinity of the sulfur headgroup for the metal surface leads to an initial "lying-down" configuration of the alkanethiol molecules, chemisorbed to the surface strongly by the metal-sulfur bond of the headgroup but also lightly physisorbed *via* van der Waals interactions between the surface and the alkane chain [336] (**Figure 3.9**).

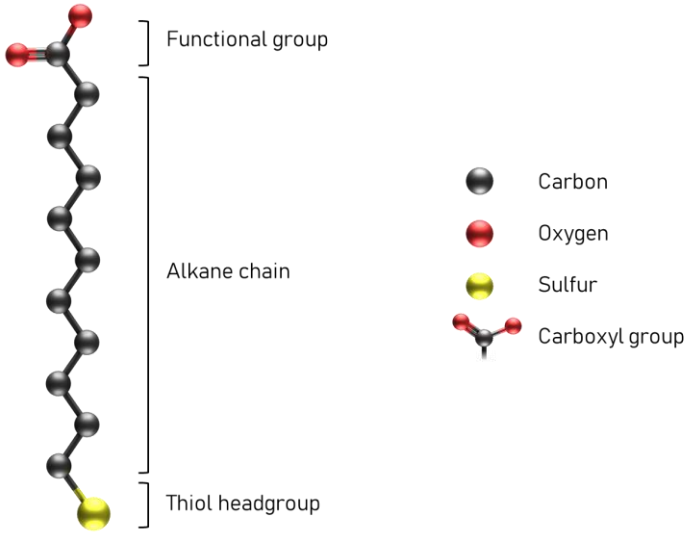

Figure 3.8 Structure of a typical alkanethiol, in this case 11-mercaptoundecanoic acid (11-MUA).Hydrogens have been omitted for simplicity.

Since the sulfur headgroups of arriving conjugate molecules have a higher affinity for the metal surface compared to the hydrocarbon chains, over time the latter are displaced from the surface as more alkanethiol molecules diffuse to and bind with the substrate via the sulfur atom. This gives rise to a phase transition to a "standing up" configuration with a strong entropic preference for upright orientation of the conjugated molecules relative to the surface. Mutual intramolecular van der Waals interactions between the alkane chains stabilize the SAM, resulting in the formation of a closely packed (surface coverage ≈1/3), crystalline monolayer of alkanethiolate molecules [336].

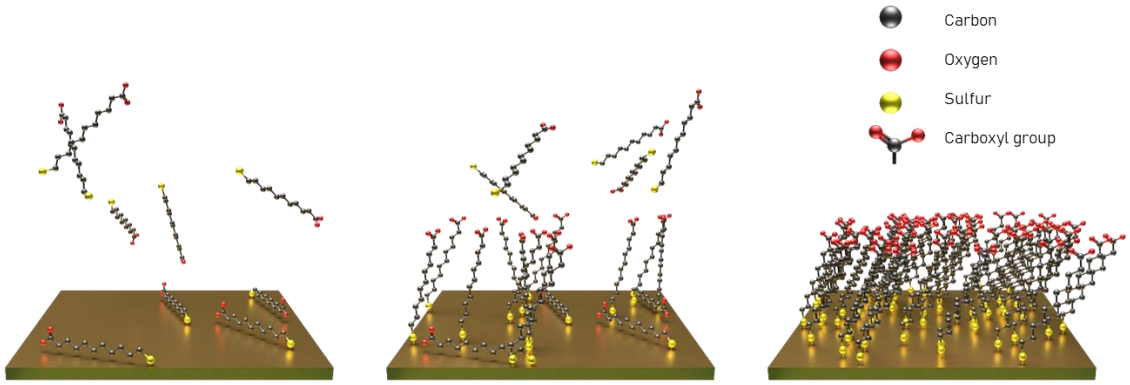

Figure 3.9 Progressive formation of an alkanethiol self-assembled monolayer (SAM) on a gold substrate.Diffusion of alkanethiol from the solution to the surface is followed by binding of the molecule to the gold surface through a strong gold-sulfur bond and also by interactions with the alkane chain, leading to a "lying down" configuration. With increasing incubation duration, more of the molecule diffuses to the surface. As surface density increases, arriving sulfur headgroups compete with and displace the alkane chains on the surface, leading to a "standing-up" configuration. Finally, above a threshold density, intra-molecular forces between the alkane chains stabilize the SAM with the functional groups presented to the solution above

While thiols exhibit high binding affinity for a variety of transition metals (Au, Ag, Cu, Pt, Pd, Ni)[275] and metal alloys, gold's other advantageous properties make it the *de facto* standard substrate for SAM formation and bioconjugation, for reasons discussed above [275].

An advantage of thiol-based immobilization is that the thiol groups readily displace biological contaminants and interferents during adsorption [275]. Furthermore, thiol-based SAMs are known to be stable for periods from days to weeks even in the presence of complex liquid media, as is often the case in biological experiments [275].

Cross-linking molecules containing thiol moieties have been used to immobilize phages of various morphologies on gold surfaces [254,272,327], nanoparticles [330], and plasmonic quasicrystals [252].

Both cysteamine and the amino acid L-cysteine bind to gold through a strong thiol linkage while presenting an amine group which can be cross-linked to primary amines *via* glutaraldehyde (**Figure 3.10**) [137,249,254]. In the case of L-cysteine, a carboxyl group is also present and is available for activation, for example by EDC/NHS [244,249].

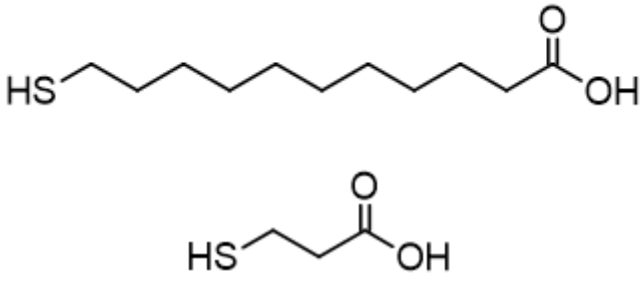

Figure 3.10 Structural formulae of 11-mercapto-undecanoic acid (top) and 3-mercaptopropionic acid (bottom).

11-mercapto-undecanoic acid (11-MUA) is an example of an alkanethiol featuring a long alkane chain terminated at one end by a thiol moiety and on the other end by a carboxyl group (**Figure 3.10**). As is typical for alkanethiols, 11-MUA readily forms SAMs on gold surfaces, presenting carboxyl groups to the solution which may be activated by EDC/NHS [336].11-MUA has been used as a tether molecule to functionalize gold substrates with phages such as M13 to detect peptides by SPR [327]; T4 and BP14 to detect *E. coli* and *S. aureus*

by SPR and impedance measurements [244]; T4 to detect *E. coli* by differential pulse voltammetry (DPV) [139]; and various phages for the detection of *S. aureus* by SPR, and *Bacillus cereus* by ferromagnetoelasticity [140].

As mentioned above, by combining 11-MUA with L-cysteine, Tawil *et al.* were able to achieve a 10^3-fold increase in phage activity relative to simple physisorption [254]. The authors attributed this improvement to the creation of uniform, regularly interspaced depressions in the L-cysteine / 11-MUA monolayer, with a length scale similar to that of the phage head of 36 ± 2 nm, permitting uniform and oriented immobilization of the phages. Another example of a thiol-based linker is 3-mercaptopropionic acid (3-MPA) (**Figure 3.10**). 3-MPA has a similar structure to 11-MUA, featuring terminal carboxyl and thiol moieties, but with a much shorter carbon chain linking them. Sedki *et al.* functionalized glassy carbon electrodes by coating them with 3-MPA-functionalized gold nanoparticles which were then activated with EDC/NHS and conjugated to M13 phages, forming an electrochemical impedance-based bacterial biosensor which achieved an impressive LOD of just 14 CFU/mL [330]. Han *et al.* used a SAM of 3-MPA to immobilize fd phage for detection of prostate specific antigen by differential pulse voltammetry (DPV) at concentrations as low as 3 pg/mL [223].

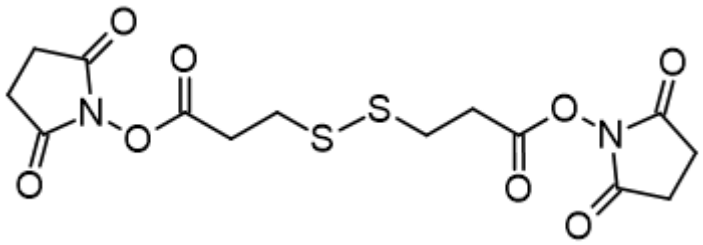

Figure 3.11 Structural formula of dithiobis(succinimidyl propionate).

While 11-MUA and 3-MPA are both examples of monothiols, there also exist dithiol linkers such as dithiobis(succinimidyl propionate), also known as Lomant's reagent, DTSP, or sometimes DSP [142]. DTSP is a homobifunctional NHS ester crosslinking agent, in the form of a homodimer exhibiting both thiol and succinimide moieties, linked by a disulfide bridge allowing SAM-formation on clean gold substrates (**Figure 3.11**). Upon introduction to a gold surface, DTSP cleaves at the disulfide bridge, resulting in two thiolate moieties bonded to the surface, each bound *via* a carboxyl group to a terminal succinimidyl group that is exposed to the solution (**Figure 3.12**). This succinimidyl group is thus available as a binding site for primary amines of a target ligand, as with the EDC/NHS method [337]. Following conjugation, rinsing with ethanolamine blocks further binding of primary amines.

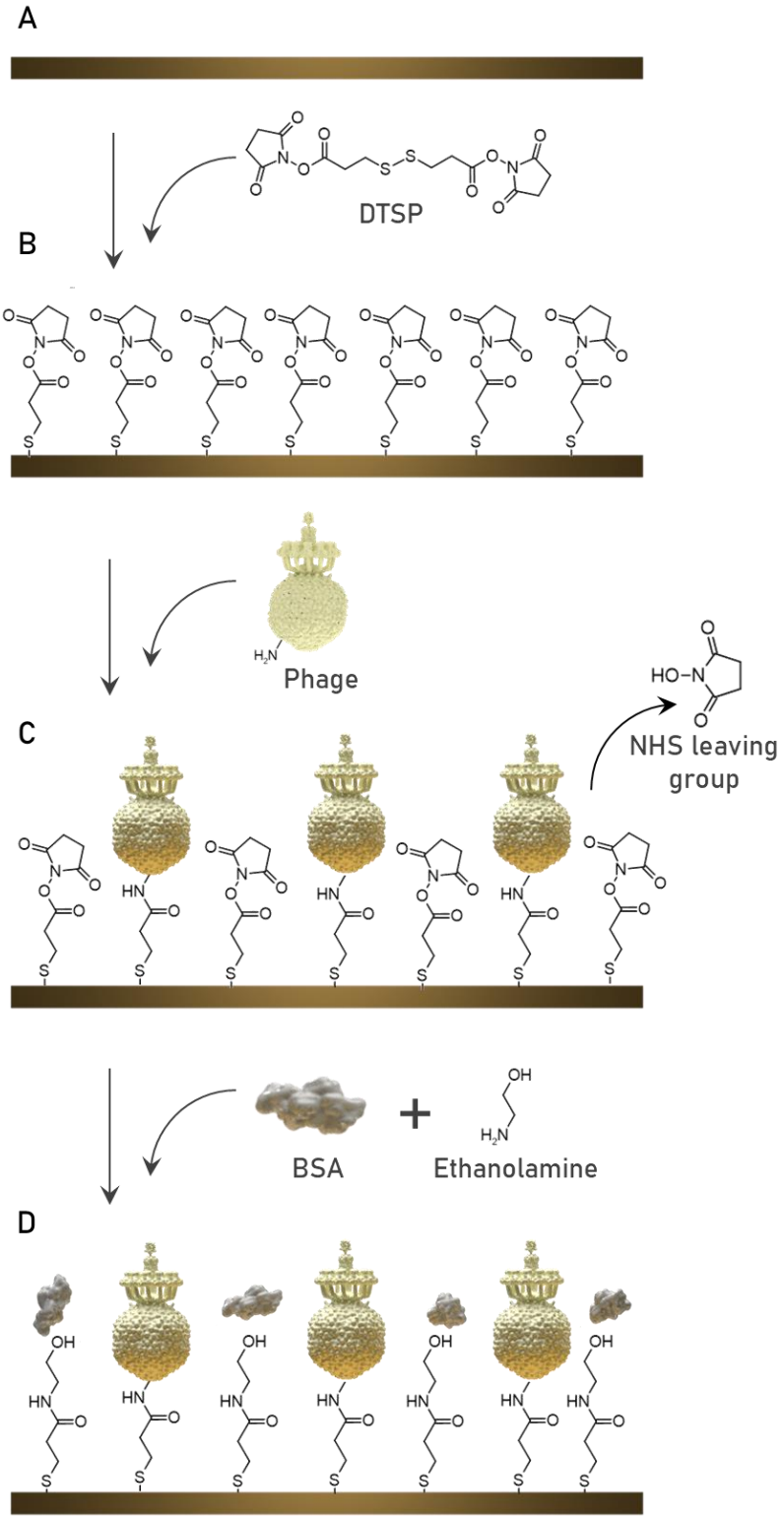

Figure 3.12 Schematic of a generalized protocol for DTSP functionalization and phage-conjugation.(A) A bare gold substrate is cleaned by plasma or otherwise. (B) After incubation on the gold surface, DTSP cleaves at the disulfide bridge and forms a monolayer on the substrate. (C) Sequential introduction of the ligand (phage) followed by ethanolamine results in conjugation of the phage to the surface and blocking of the remaining activated carboxyl sites by ethanolamine. (D) The surface is then incubated with bovine serum albumin (BSA) in order to reduce non-specific binding. Not to scale. Note that immobilization will not always result in a tail-upward orientation as shown.

Arya *et al.* first proposed DTSP for the immobilization of phages in 2011 [337]. By 2012, Naidoo *et al.* were able to leverage DTSP to reach an incredible surface density of 199±2 phages/μm^2. However, they found a threshold surface coverage of 18.9±0.8 phages/μm^2, beyond which higher phage density led to a reduction in total bacterial capture [128]. This result was influential and is widely cited in the phage immobilization literature, with many subsequent papers quoting their results with reference to this "jamming effect". Notable subsequent research by Richter *et al.* combined DTSP with application of an alternating electric field during immobilization to "bake in" a tail-upward orientation of T4 phage as a surface density of 13.64 phages/μm^2 [175]. DTSP has also been used to immobilize T4 [337] and P22 [128] bacteriophages on gold surfaces for detection of *E. coli* [128,175,337] and *Salmonella* Typhimurium [128].

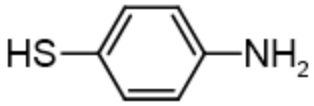

Figure 3.13 Structural formula of 4-aminothiophenol

4-amino-thiophenol (4-ATP) is an aromatic thiol featuring a primary amine moiety (**Figure 3.13**). 4-ATP has been used to immobilize T4 phages on nano-sculptured thin films of silver for detection of *E. coli* by surface-enhanced Raman scattering (SERS) with an LOD of 1.5×10^2 CFU/mL [338]. In this method, glutaraldehyde is used to cross-link primary amines present both on 4-ATP and on the phage capsid (see 3.3.3 Glutaraldehyde below).

In a different approach, Rippa *et al.* deposited and diazotized a SAM of 4-ATP on plasmonic quasicrystals of gold [252]. The diazonium moieties were then available for covalent linkage to the histidyl groups of bacteriophage *Tbilisi*. This SERS-based sensor was capable of detecting femtomolar concentrations of immobilized phages, but this work did not extend the method for the detection of an analyte. The choice of plasmonic quasicrystals is motivated, among other considerations, by the higher spatial density and larger field strengths of electromagnetic hot-spots, enhancing SPR and SERS effect and thus the sensitivity of the sensor.

Horikawa *et al.* made a comparison between carboxy-terminated, aldehyde-terminated, and methyl-terminated SAMs for immobilization of filamentous fd phages on the gold surface of magnetoelastic sensors [339]. The resultant phage surface coverage was found to be 46.8%, 49.4%, 4.2%, and 5.2% for bare gold, carboxy-, aldehyde-, and methyl-functionalized resonators, respectively. This paper is notable in its findings that physisorption can be as performant as activated carboxyl-mediated immobilization. The authors propose that the aldehyde and methyl surface treatments were so effective in *reducing* phage adsorption that they may be employed as "anti-phage surfaces", which may provide the possibility of negative surface patterning using these surface treatments as a form of negative resist.

3.3.3 Glutaraldehyde

Glutaraldehyde – a symmetrical, bireactive compound with an aldehyde (−CHO) at each end – is frequently used as a cross-linker (**Figure 3.14**). The aldehydes can react with an amine to form an imine – a group with a carbon-nitrogen double bond. In this way, glutaraldehyde cross-links amine groups (**Figure 3.14**).

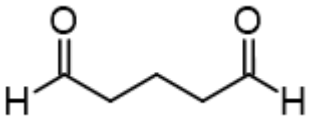

Figure 3.14 Structural formula of glutaraldehyde

Singh *et al.* immobilized L-cysteine and cysteamine on a gold surface *via* their thiol side-chains, and then used glutaraldehyde to cross-link the amine groups of these immobilized species to those exposed on the capsids of wild type T4 phages. The surfaces were then used for the specific capture of *E. coli* EC12 bacteria, as confirmed by scanning electron microscopy (SEM) and X-ray photoelectron spectroscopy (XPS) [137]. Compared to simple physisorption, they found a 37-fold improvement of phage immobilization at 18±0.15 phages/μm^2, resulting in a 9-fold higher bacterial capture density of 11.9±0.2 bacteria/100μm^2.

Similarly, He *et al.* coated interdigitated gold electrodes with L-cysteine before crosslinking *via* glutaraldehyde to phage D29, to form an impedimetric sensor of *Mycobacterium smegmatis* and *Mycobacterium tuberculosis* [249].

Richter *et al.* further developed this technique to achieve some of the most convincing evidence for oriented immobilization in the literature. By combining an alternating electric field with glutaraldehyde cross-linking to a gold substrate, the authors leveraged the permanent dipole moment of T4 phages to yield a tail-outward orientation that is "baked in" at the time of immobilization [175]. This allowed the authors to achieve immobilized phage densities on gold of 13.64 phage/μm^2 and 17.32 phage/μm^2 for oriented and non-oriented layers, respectively. The same paper demonstrated a very low LOD of 10^2 CFU/mL *E. coli* without any pre-enrichment step.

Immobilization chemistries featuring glutaraldehyde have been demonstrated for phage-functionalization of silica-based materials such as optical fibers [316], silicon nitride [224], and silica nanoparticles [246] for the purposes of biodetection and biocontrol, respectively. A widely-cited paper demonstrated glutaraldehyde cross-linking of T4 phages onto long-period gratings etched into optical fiber for the specific detection of *E. coli* with an LOD of 10^3 CFU/mL [316].

Glutaraldehyde has also been used for the creation of bacteriophage-functionalized metal-organic frameworks (MOFs). MOFs – coordination networks with organic ligands [340] – are characterized by an easily tunable size (nano- to micron scale depending on synthesis parameters) [341] and potentially large surface area [247]. An area of active research is the use of MOFs as fluorescent probes for molecular sensing. Bharwaj *et al.* have used glutaraldehyde to create bacteriophage-functionalized MOFs for the detection of *Staphylococcus arlettae* [247] by means of fluorescence and *S. aureus* [240] by photoluminescence-based biodetection. Very low LODs were demonstrated of 10^2 CFU/mL for *S. arlettae* and 31 CFU/mL for *S. aureus*.

In a different approach, Yoo *et al.* demonstrated a variation of glutaraldehyde cross-linking whereby a solution of M13 phages was simply drop cast and allowed to dry on a cysteamine monolayer on gold, then exposed to a glutaraldehyde vapor for three days in order to cross-link the phages [321]. This allowed the study of mouse fibroblast proliferation under the influence of growth factors immobilized to the phages themselves, taking advantage of the phages' self-assembled nanofibrous matrix structure.

In all cases, cross-linking with glutaraldehyde relies on the presence of amine groups on the substrate, which is typically achieved either through amino-silanization of the surface, deposition of an intermediate molecule presenting both thiol and amine moieties (*e.g.*, L-cysteine and cysteamine), or through electropolymerisation, for example of polytyramine [342].

3.3.4 Silane-based self-assembled monolayers

For immobilization on silicate-based materials, a preferred method is silanization of the substrate using alkoxysilanes which act as hetero-bifunctional crosslinkers between inorganic mineral surfaces and organic ligands [135,136,138,170,182,224,237,246,260,272,316,317,319,320,343,344].

Typically, the inorganic surface is treated with a strong oxidizer (*e.g.*, piranha solution or aqua regia) or oxygen plasma to form surface silanol groups which feature dangling hydroxyl (-OH) groups. These hydroxyl groups

will then condensate with the three alkoxy groups on the alkoxysilane[‡], leaving a primary amine bonded to the surface. One can then perform standard amine-immobilization chemistry with these amines, as above (**Figure 3.2**).

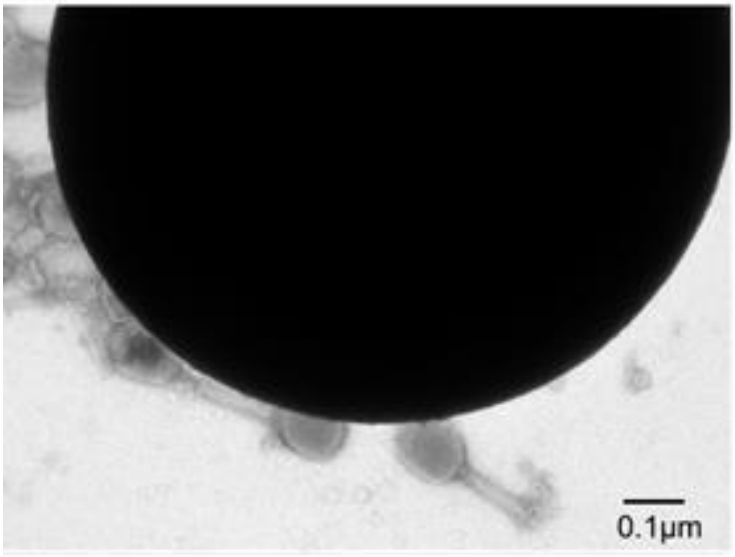

Figure 3.15 Transmission electron micrograph of T4 myovirus covalently immobilized on APTES-functionalized 1 µm diameter silica particles. Reproduced with permission from Bone *et al.* [147]. Copyright 2018 Elsevier Inc.

The most popular alkoxysilanes for phage immobilization are (3-aminopropyl)triethoxysilane (APTES or APTS) and (3-aminopropyl)trimethoxysilane (APTMS) [142]. Alkoxysilanes can be used either for electrostatic or covalent immobilization of proteinaceous ligands (**Figure 3.2**). In covalent bonding, the amine groups of the alkoxysilane react with aldehyde either present on a cross-linker molecule such as glutaraldehyde [224,316,317], or on the phage itself after enzymatic modification to yield a reactive aldehyde as demonstrated by Kwak *et al.* [182]. Alternatively, the phage's endogenous carboxyl groups can be activated by EDC/NHS to facilitate amide bonding with the substrate aminosilane layer [135,170,319] (**Figure 3.15**), although – as explained above – activation of the phage by EDC/NHS can be detrimental to phage infectivity [135,138,272].

In contrast, electrostatic binding with alkoxysilanes relies on the differing isoelectric points of the ligand and the silanized surface, as discussed later in this work in the 'Electrostatic binding' subsection.

Hosseinidoust *et al.* demonstrated covalent immobilization of a variety of phage families through silanization of glass with APTES, achieving a consistent surface density of 4.5 +/- 0.7 phages/µm^2, as calculated from SEM imagery of the surface [138].

Handa *et al.* instead used EDC/NHS to activate the carboxyl groups of the phages themselves, which are then bound to the primary amines of an amino-silanized atomic force microscopy probes [319], and in a separate paper achieved 67% surface coverage of phage P22 on glass substrates [170].

An interesting application of organosilane grafting has been demonstrated for the phage-functionalization of indium tin oxide (ITO) [343,344]. ITO is the most well-known of all transparent conductors – exhibiting exceptional optical transmissivity combined with low electrical resistance [345] – and is seen as a promising material in

[‡] In reality the hydroxy groups will replace between zero and three alkoxy groups in each alkoxysilane. One can even have the terminal amino (−NH_2) group bond with the surface hydroxyl group [519]. Recent research supports a model wherein the silane monolayer is in fact highly cross-linked *via* these remaining alkoxy groups, with only occasional bonds to the surface [520].

biosensing technology [346]. In a pair of papers, Liana *et al.* investigate phage adsorption onto bare, amine, methyl, and carboxyl-functionalized planar and particulate ITO [343,344]. These comparative studies found divergent results between planar and particulate ITO, but a consistent drop in performance was observed with the introduction of amine groups on the substrate compared to carboxylic and hydroxyl groups, suggesting the latter as more promising routes for phage immobilization on ITO.

3.3.5 Miscellaneous covalent techniques

3.3.5.1 Isothiocyanate

Isothiocyanate compounds feature a terminal sulfur atom and a central electrophilic carbon which is susceptible to nucleophilic attack by the primary amines of amino acids, yielding a thiourea linkage with the latter, with no leaving group in the reaction [142]. Isothiocyanates react best at alkaline pH, and it has been demonstrated that by carefully controlling pH during conjugation, it is possible to modify only the N-terminal α-amines while leaving side-chain amines unmodified [347]. Zhang *et al.* functionalized isothiocyanate-terminated magnetic beads for the purposes of phagomagnetic separation in an enzymatic assay for the presence of *E. coli* O157:H7, with a comparatively poor LOD of 4.9×10^4 CFU/mL [280].

3.3.5.2 Electro-deposited polytyramine

Niyomdecha *et al.* demonstrated immobilization of M13 phages using glutaraldehyde cross-linking between primary amines on the phage capsid and the activated primary amine groups of an electrodeposited polytyramine layer on a gold surface, for use as a capacitive biosensor for *Salmonella* [342]. Rinsing with ethanolamine blocks any unoccupied aldehyde groups and reduces non-specific binding following functionalization. The use of electrodeposited polytyramine for immobilization of phages has some precedent, having been demonstrated for enzymes [348], myoglobin [349], and oligonucleotides [350].

3.3.5.3 Tosyl

A toluenesulfonyl (tosyl) is a molecule or group with the formula $CH_3C_6H_4SO_2$ (**Figure 3.16**). Tosyl chloride is used to activate hydroxyl groups on a substrate in nonaqueous conditions, creating a tosyl ester. When subsequently placed in aqueous conditions, this ester can then react with sulfhydryls, amines, and hydroxyls to form thioether, secondary amine, and ether linkages, respectively. This allows the immobilization of proteins either through the primary amino group or sulfhydryl side-groups [142,351]. The tosyl group is an effective "leaving group", since it is easily released during the conjugation reaction.

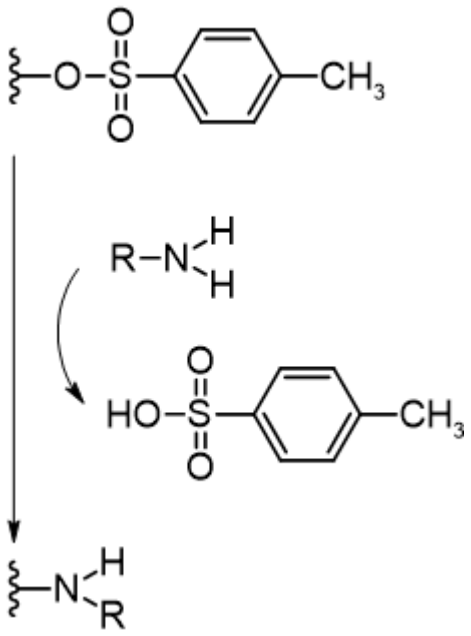

Figure 3.16 Immobilization via a primary amine, facilitated by a tosyl leaving group.

Dynabeads M-280 (Invitrogen) are tosyl-activated, 2.8 µm diameter polystyrene beads which feature superparamagnetic inclusions and an outer polyurethane coating. They have been demonstrated to be capable of immobilizing P22 *Podoviridae* for the purposes of phagomagnetic separation and detection of *Salmonella* in two papers [250,251]. Such methods were capable of reaching an impressive LOD of only 3 CFU/mL [250] and as low as 0.06 CFU/mL if combined with a pre-enrichment step [251].

3.4 Non-covalent & physical methods

3.4.1 Physisorption

Many papers make use of simple "physisorption" which is generally not considered to involve covalent bonding between the phage and the substrate. The simplicity of these methods is appealing since the functionalization operation can be as trivial as cleaning the substrate and then incubating it with a purified phage suspension [143,144,183,318,352–372]. However, physisorption yields a functionalization that is more variable and less robust since the physisorbed phage can detach following changes in ionic strength, temperature, pH, or even high fluid velocities at the substrate surface [270].

There appears to be no clear consensus on the physical mechanism behind physisorption, with many papers proposing several factors which could play a role such as van der Waals forces, hydrophobic bonding, H^+ bonding, or weak covalent bonding between cysteine residues and gold surfaces [355,373].

Several papers present physisorption and electrostatic attachment as synonymous, attributing the binding to charge differences: positively charged surfaces attracting negatively charged phages [135]. Following this convention, electrostatic binding will be presented here as a subcategory of physisorption.

3.4.2 Electrostatic binding

The basis of electrostatic immobilization is to take advantage of the relative charges of the surface and of the ligand to be immobilized. Most phages have a net negative charge and permanent dipole moment at neutral pH [171,226,258]. In the case of T4 and T7 phages, the head acquires a negative charge above a pH of 4 and is thought to be responsible for the overall negative charge of the virion despite the positive charge on the tail fibers [226,271].

Electrostatic immobilization can be achieved by varying the pH of the aqueous environment to control the surface charge of the substrate and/or phage in order to produce favorable conditions for attraction between the two. If there exists a pH at which the surface species present a positive charge while the phage – or even just the phage head – presents a negative charge (*i.e.*,if the isoelectric point of the surface is higher than that of the phage), then the pH of the solution can be tuned to facilitate electrostatic attraction of phage particles [168]. Alternatively, chemical modification of the substrate can also result in a positive surface charge, facilitating phage immobilization without recourse to tuning the pH.

Alkoxysilanes such as APTES and APTMS will present NH_3^+ groups – and thus a positive charge on the substrate – from a neutral pH [246] to as high as 9 [374,375]. This surface charge can then be used to electrostatically attract phages that display a negative charge at the same pH (**Figure 3.17**) [320], and even to achieve oriented immobilization. Cademartiri *et al.* demonstrated such oriented electrostatic immobilization on APTES-modified silica particles, with confirmation of the orientation by transmission electron microscopy (TEM) (**Figure 3.18**) [136]. Furthermore, the authors found a linear correlation between infective phage binding and the magnitude of positive surface charge resulting from varying chemical modification of the substrate.

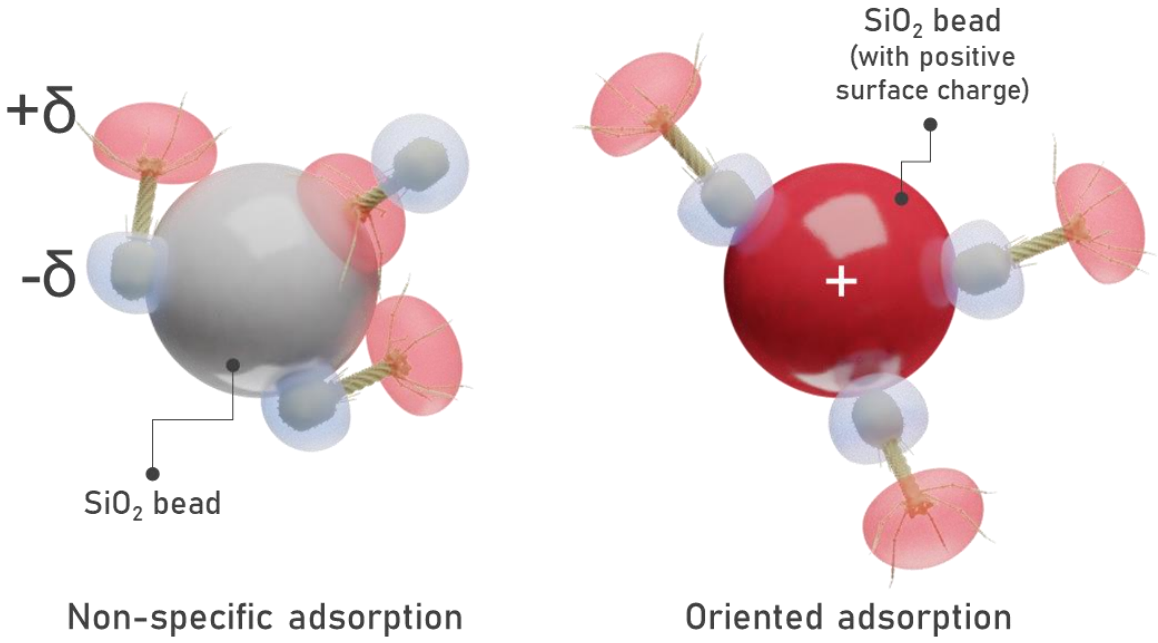

Figure 3.17 Left: A neutral surface charge leads to non-oriented adsorption of phages on silica particles.Right: A polymer layer (*e.g.*, polyvinylamine or polyethylenimine [59]) is protonated at neutral pH, electrostatically binding the phage head, leading to oriented immobilization. Adapted from Cademartiri *et al.* [54]. Adapted with permission from Cademartiri *et al.* [54]. Copyright 2009 Elsevier Ltd.

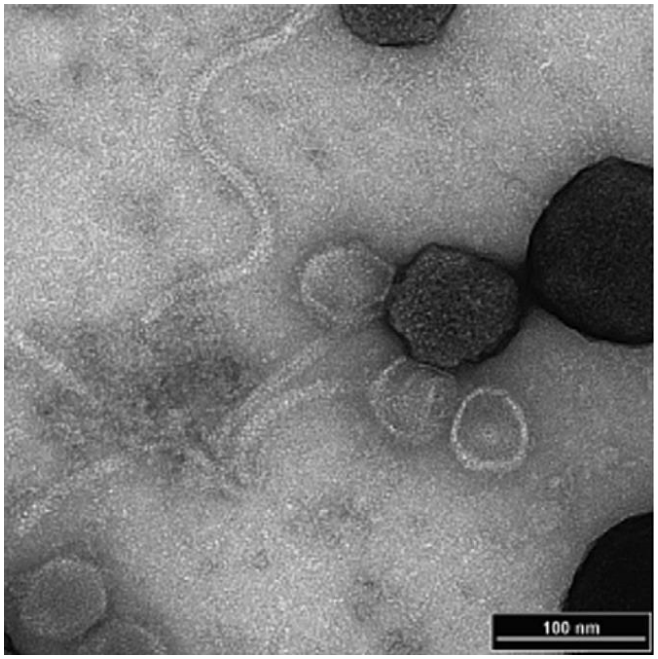

Figure 3.18 Transmission electron micrograph of the siphovirus VB_SenS-AG11 (active against *Salmonella)* electrostatically physisorbed by their heads on cationic, APTES-modified silica particles.Reproduced with permission from Cademartiri *et al.* [54]. Copyright 2009 Elsevier Ltd.

In 2011, Anany *et al.* developed a method for electrostatic immobilization of anti-*Listeria monocytogenes* phages on cellulose membranes that had been chemically modified with the cationic polymer polyvinylamine to present a positive surface charge (**Figure 3.2**) [226]. In 2016 Lone *et al.* employed this technique with anti-*E. coli* O104:H4 phages on alginate beads to produce a bioactive packaging prototype [211].

Similarly, Zhou *et al.* used polyethylenimine (PEI) to impart a positive surface charge to a carbon nanotube (CNT)-modified glassy carbon electrode, for the specific detection of *E. Coli* B [241]. In this case T2 phages were electrostatically oriented by the positive surface charge, while immobilization was achieved through PBSE-mediated conjugation (see 3.4.3 π - π stacking). Vonasek *et al.* similarly used PEI to electrostatically immobilize T7 phages on electrospun cellulose microfibers for biocontrol in the context of food packaging and biomedical applications [229]. More recently, Farooq *et al.* used PEI to phage functionalize CNT-modified bacterial cellulose for the electrochemical detection of *S. aureus* [134].

Poly(diallyl dimethylammonium chloride) or polyDADMAC is a cationic polyelectrolyte that has been used to electrostatically bind T4 phages on paper [308], M13 phages on glass [376], and S13' phages on gold [253]; in the latter case for the specific detection of *S. aureus*.

An alternative strategy to impart a positive charge to the substrate was demonstrated by Richter *et al.* wherein a positive potential was applied to a gold substrate, yielding an oriented physisorbed layer of T4 phages with a density of 14.3 PFU/mL (**Figure 3.19**) [171].

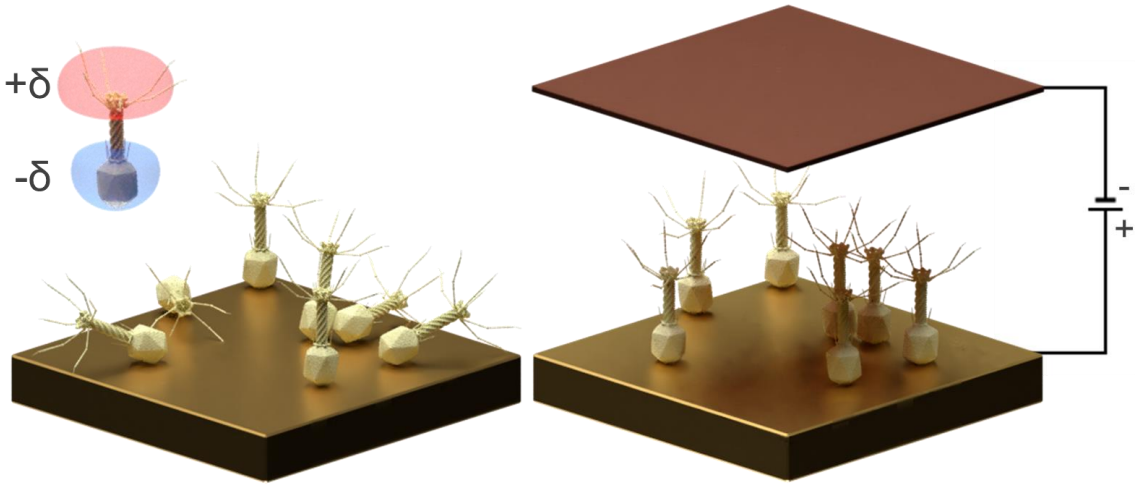

Figure 3.19 Due to the inherent dipole moment of T4 phage particles, an externally-applied electric field orients the phages such that their tail fibers point outward from the substrate.Such an orientation is considered essential for increasing the immobilized phages' infectivity and host capture efficiency. Adapted with permission from Richter *et al.* [78]. Copyright 2015 Elsevier B.V.

In the same paper, Richter *et al.* proposed a model of orientation of bacteriophages based on electrical screening of the substrate surface due to the formation of an electric double layer [171]. Briefly, the Debye length (denoted κ^{-1}) refers to the physical distance in an electrolyte solution over which an electrical potential will decrease by a factor of 1/e. This length is proportional to the inverse square root of the ionic strength of the solution, since it is the mobile charge carriers of the solution which form an electric double layer, screening the electric field that results from the substrate surface potential. Richter *et al.* proposed that when κ^{-1} is larger than the phage, they will align along electric field lines; whereas when κ^{-1} is smaller, the phage orientation occurs instead due to electrostatic interactions (**Figure 3.20**).

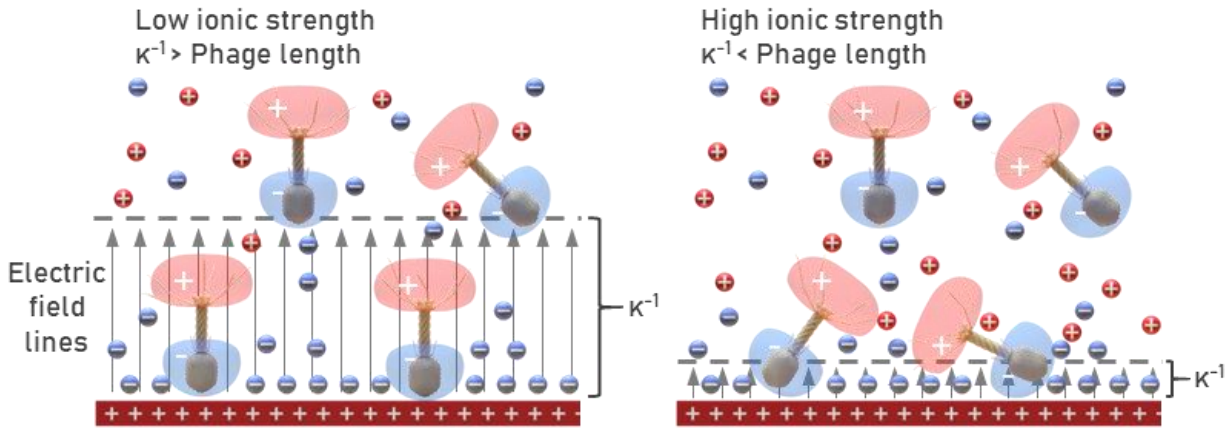

Figure 3.20 The electrostatic binding model proposed by Richter *et al.* [78].At low ionic strength, fewer charge carriers are available to screen the surface charge. This leads to a larger Debye length of the same scale as a phage particle and thus oriented immobilization. Conversely, at high ionic strength the surface charge is more effectively screened, leading to a Debye length smaller than the phage. In the latter case, the phages are still attracted to the substrate due to their overall negative charge, but the immobilization is not appreciably oriented. Adapted with permission from Richter *et al.* [78]. Copyright 2015 Elsevier B.V.

The ionic strength also influences the stability of the phage solution and aggregation of the phages[255–257]. Archer and Liu reported that physisorbed T4 phages are susceptible to aggregation in high ionic strength solutions (>100mM) or low pH [168]. However, the same study observed phage immobilization even on negatively charged surfaces, indicating that interactions other than purely electrostatic attraction might be at play. Confusingly, a different paper found that a relatively high ionic strength of 420 mM NaCl gave the best surface coverage for physisorption of filamentous phage fd [215]. These seemingly contradictory results suggest that phage morphology may play a role in immobilization and aggregative effects of different ionic strengths.

Whatever the mechanism, while simple physisorption of phages has been demonstrated to enable bacterial capture [367], it is not sufficient to prevent phages from migrating on the substrate while in storage or during binding assays [337]. Covalent attachment of phages offers a much stronger bond than simple physisorption, yielding surface functionalization more resistant to phage detachment and resulting in a higher phage surface density [270].

3.4.3 π - π stacking

Zhou *et al.* demonstrated a novel strategy for immobilization of T2 phages on multiwall carbon nanotubes (CNT) on glassy carbon electrodes [241]. First, the CNT are functionalized with polyethylenimine (PEI), which introduces a positive charge to the CNT surface, facilitating tail-outward phage orientation. A hetero-bifunctional molecular tethering agent, 1-pyrenebutanoic acid succinimidyl ester (PBSE) (**Figure 3.21**), is then used to link the phages to the CNT. PBSE features four aromatic rings which interact with CNT sidewalls through π-π stacking [377], and a succinimidyl group which facilitates amide bonding to the phage [241]. Application of a positive potential of +0.5 V *vs.* Ag/AgCl further facilitates oriented phage immobilization.

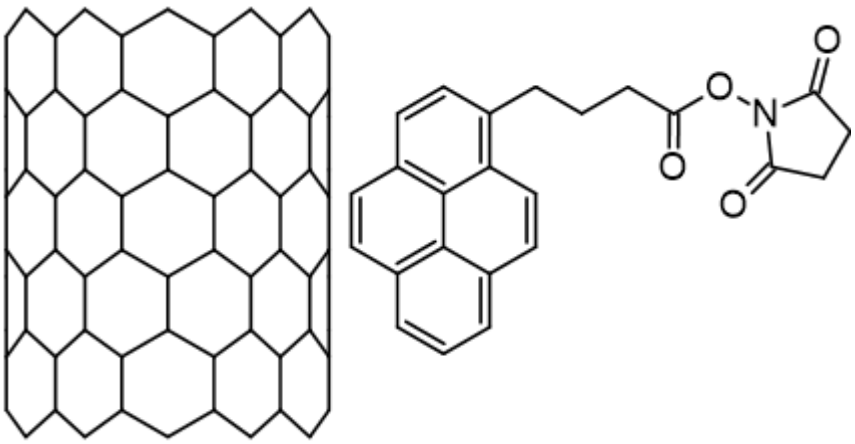

Figure 3.21 Structural formula of 1-pyrenebutanoic acid succinimidyl ester (PBSE), illustrating pi-stacking interactions between the pyrene moiety and a carbon nanotube sidewall

Kim et al. leveraged π- π stacking between the imidazole rings of recombinantly expressed histidine tags on M13 phages (see 3.5 Genetic modification) to achieve a nematically aligned unidirectional bundle structure on the surface of an SPR biosensor [378]. The resultant colorimetric sensor was capable of detecting streptavidin – a surrogate analyte in this work – down to femtomolar concentrations.

3.4.4 Biotinylation

The biotin-avidin bond is one of the strongest non-covalent bonds in nature, with a dissociation constant as low as 10^{-15} M [142]. The binding is also extremely stable, exhibiting high resistance to breakdown by extremes of pH, temperature, or the presence of denaturants or detergents [379]. Avidin is a tetrameric protein, binding up to four biotin molecules simultaneously. These qualities have made the avidin-biotin interaction

particularly useful and widespread in bioconjugation chemistry, and it is frequently used to cross-link biotinylated ligands to one another as well as to substrates.

While avidin is a component of egg-whites, streptavidin is a similar biotin-binding protein of bacterial origin which exhibits superior properties to avidin. The main disadvantage of avidin is its high isoelectric point of 10, presenting a positive charge at neutral pH making it susceptible to non-specific binding to negatively charged components other than biotin, such as cell surfaces for example [142]. This problem is circumvented by instead using streptavidin which has a pI of 5-6, which greatly reduces nonspecific binding due to ionic interactions with non-analyte molecules. For this reason, streptavidin has largely replaced avidin in most (but not all) conjugation protocols.

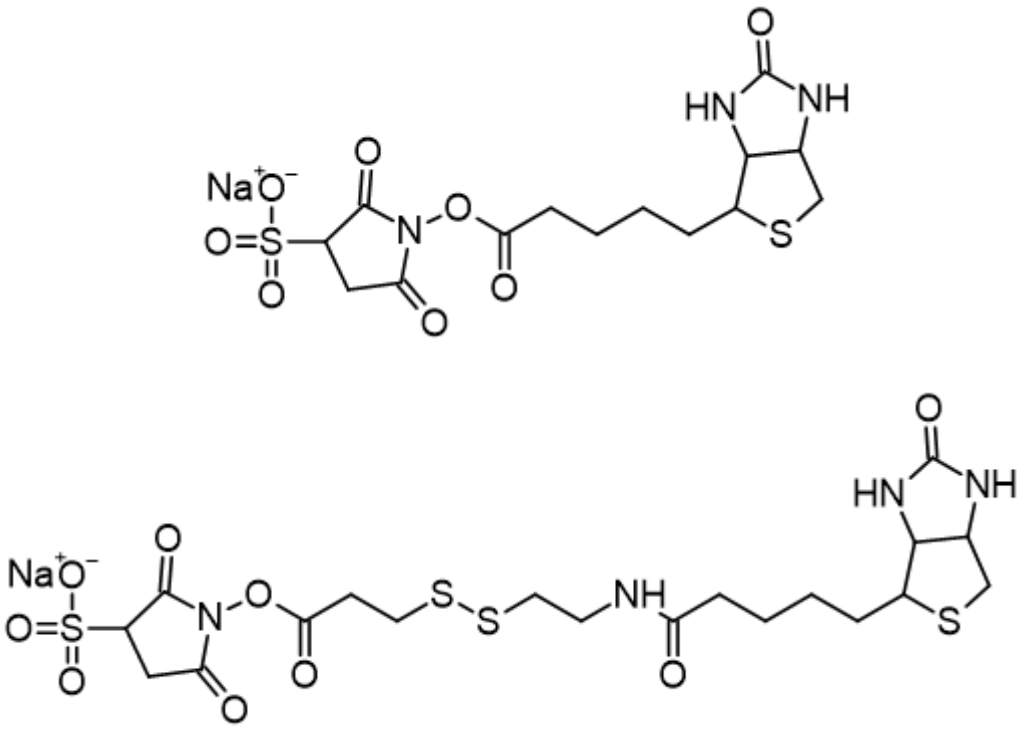

Figure 3.22 Structural formulae of and sulfo-NHS-biotin (top) and sulfo-NHS-ss-biotin (bottom).

The use of streptavidin-biotin heterobifunctional cross-linkers has been demonstrated for phage immobilization using sulfo-NHS-ss-biotin and sulfo-NHS-biotin (**Figure 3.22**). These molecules can participate in an amide bond with the phage capsid – facilitated by a terminal succinimidyl group on one end – tagging the phage with a terminal biotin group which can bind to a streptavidin-functionalized surface. Such covalent biotinylation of the phage was used by Sun *et al.* to immobilize of SJ2 phages on streptavidin-capped magnetic beads to create a biosorbent for the specific capture of *Salmonella* Enteritidis [281].

Sulfo-NHS-ss-biotin differs from sulfo-NHS-biotin in that the former features a spacer to mitigate steric hindrance effects, and a cleavable disulfide bond. This latter molecule has been used by Fernandes *et al.* to biotinylate a gold substrate, which was then crosslinked *via* streptavidin to genetically biotinylated T4 phages [141].

Despite the above successes seen with covalent biotinylation, all immobilization mediated by streptavidin-biotin since 2001 has instead made use of genetic biotinylation (see 3.5.1 Genetic biotinylation).

3.5 Genetic modification

Genetic engineering can be used either as an alternative immobilization strategy in itself or to enhance the above chemi- and physisorption methods. A popular technique in the literature is site-directed mutagenesis, wherein a foreign coding sequence is spliced in-frame into bacteriophage capsid protein genes. This allows the targeted expression of "guest" peptides which are fused to the coat protein and which exhibit an affinity for a given substrate, or onto which a moiety can be conjugated [380]. Since filamentous phages in the Ff class (*e.g.*, fd and M13) typically have several thousand identical, helically-tessellated copies of the pVIII coat protein [381], they are the most frequent examples of genetic modification for the purpose of immobilization [182,225,260,264–267,382], although examples of such modification of T4 [259,261,263,268] and T7 [383] phages are also found.

The popularity of this technique and of the filamentous phages M13 and fd, stems from the success of phage display-based selection and the closely related technique of biopanning [380]. While the 50-residue pVIII protein of filamentous phages are typically modified [380–382] (but also pIII [182]), in the case of phages T4 and T7 it is rather Soc and Hoc proteins of the phage head that are targeted for modification [261,384,385].

A drawback of genetic modification is that the expression of peptides, especially of large size, can interfere with phage assembly and hence its physical and infective properties [168]. Genetic modification can also prove laborious, time-consuming and expensive [268], and for these reasons genetic modification techniques are somewhat marginal compared to physisorption and covalent techniques.

3.5.1 Genetic biotinylation

Several papers demonstrate phage immobilization facilitated by streptavidin/biotin, wherein the biotinylation of the target phages is a result of recombinant expression of a biotin tag rather than the result of chemical modification.

In 2006, Edgar et al. genetically modified T7 bacteriophage to exhibit a small peptide on the major capsid protein, which is then post-translationally biotinylated at a specific lysine residue by the host bacterium's biotin-ligase protein during phage assembly [262]. This allows conjugation to streptavidin-coated quantum dots, resulting in a biosensor with a LOD of as low as 10 bacterial cells/mL.

Gervais et. al demonstrated an impedance-based biosensor by immobilizing T4 phages on streptavidin-coated gold at a density of 4.4 phage/μm^2, with tail-outward orientation enabled by the strategic genetic biotinylation of only the head capsid protein [268]. Phages were found to retain their infectivity, burst size and latent period compared to the wild-type. Attractive features of this method are the retention of infective activity after biotinylation, and the localization of the modified tagged peptide exclusively on the phage head, leading to a 15-fold increase in phage attachment to the gold surface.

Wang *et al.* immobilized a genetically biotinylated T4 phage to streptavidin-terminated magnetic beads, calculating that each bead was on average conjugated to 248 ± 15 phages per 2.8 µm-diameter bead after 12 hours of incubation [235].

3.5.2 Formylglycine

Kwak *et al.* used genetic engineering to introduce a cysteine-containing peptide motif to the pIII coat protein of fd phage, which was converted to formylglycine by formylglycine-generating enzyme (FGE) (**Figure 3.23**). This yields a reactive aldehyde (-CHO) group that is then available for immobilization chemistry, for example to form a Schiff base with primary amines on a silanized substrate surface [182]. As with genetic biotinylation, an advantage of this technique is that the formylglycine modification is site-specific and can be targeted to exclusively modify the pIII coat protein which is displayed at one extremity of filamentous phage fd. This allows

the pVIII coat protein to be preferentially presented to the solution, since the phage is immobilized in an upright orientation [182]. This method has been further developed to enable surface patterning of filamentous phages with 200µm spot size as a template for organic and inorganic materials [260].

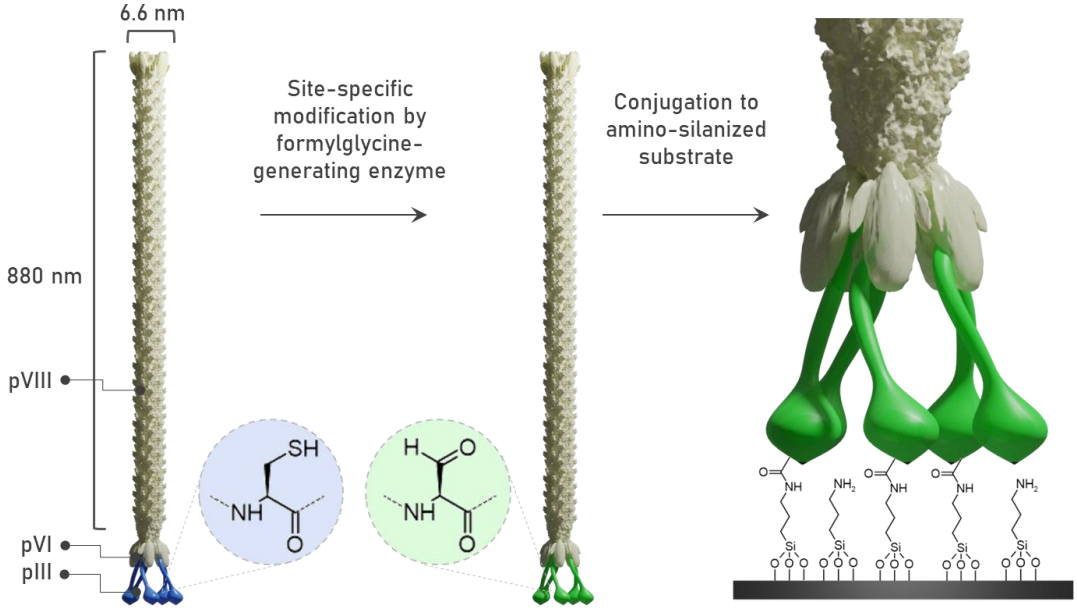

Figure 3.23 Phage immobilization by genetic engineering.Recombinant expression of a specific peptide motif exclusively on the pIII coat protein of an M13 phage enables enzymatic modification of cysteine residues to yield formylglycine and its associated carboxyl side-chains. Formylglycine can then undergo amide bonding with an amino-silanized surface. This oriented immobilization yields a high density of pVIII coat proteins displayed on the substrate. Not to scale. Reproduced with permission from Kwak *et al.* [87]. Copyright 2013 The Royal Society of Chemistry.

3.5.3 Carbohydrate-binding modules

Carbohydrate-binding modules, also known as cellulose-binding modules (CBM), are short protein domains normally found within carbohydrate-active enzymes, that exhibit high affinity for a given substrate. Fusion of phage capsid and CBM genes results in expression of recombinant CBM on the phage capsid. This allows oriented immobilization of the phages on cellulosic substrates such as paper or cellulose beads. Tolba *et al.* demonstrated such modification of T4 phages which, when combined with polymerase chain reaction (PCR), resulted in an assay with a LOD of 800 cells/mL [263]. A similar method allowed immobilization of T4 phages on microcrystalline cellulose beads [259].

3.5.4 Polymer and other binding domains

Short peptides have also been identified that exhibit highly specific affinities against a range of materials. Sawada *et al.* have demonstrated the immobilization of M13 phages on isotactic poly(methyl methacrylate) (it-PMMA) *via* an (it-PMMA)-binding terminal peptide expressed on the pIII coat protein [266]. This result is intriguing since it demonstrates a potentially fruitful avenue for further research. As the same authors point out in another paper [302], similar peptides have been identified that exhibit binding specificity towards targets as varied as metals (silver [386], titanium [387], platinum [388]), metal oxides (iron oxide [389], magnetite [390]), silica [391], semi-conductors [392,393], carbon allotropes (nanotubes [288,289], nanohorns [290], and fullerenes [291]), and various polymers (polystyrene and polyvinyl chloride [297], nano-imprinted methacrylate polymer [298], chlorine-doped polypyrrole [299], PMMA [300], syndiotactic PMMA [301], syndiotactic polystyrene [303]). Thus, the successful demonstration of one of these peptides as a strategy for M13 phage immobilization, presents a compelling case for the use of substrate-specific peptides as a general phage grafting strategy.

3.5.5 Click chemistry

An alternative class of reactions, thus far seldom exploited for phage immobilization, is click chemistry. Click reactions proceeds quickly at room temperature, producing strongly stabilized products and either no byproducts or only water as a byproduct [394]. Click reactions are furthermore highly tolerant to water and in some cases even accelerated in aqueous solutions.

Click chemistry is therefore a popular choice for making carbon−heteroatom bonds in aqueous solutions in a wide variety of chemical and biological applications in drug discovery, chemical biology, and proteomics[395].

An elegant method of phage capsid modification was recently demonstrated by Zurier *et al.* wherein a genetically engineered variant of T4 known as NRGp17 was decorated with a self-assembled cage of 870 small outer capsid (soc) proteins engineered with unnatural, alkynylated amino acids [261]. These alkynes enable oriented immobilization of the phage heads on azide-terminated magnetic beads[396,397] (TurboBeads, Zurich, SUI) *via* click chemistry, creating a biosorbent that can concentrate target bacteria from a very low initial concentration. NRGp17 causes expression of a nanoluciferase (Nluc) reporter enzyme fused to a cellulose-binding module (CBM) [398]. The bioluminescent activity of Nluc serves to transduce the presence of their host *E. coli* into a luminescence signal, while the fused CBM enables immobilization and concentration of the reporter enzyme on a nitrocellulose membrane to improve sensitivity. This assay presents an impressive LOD of <10 CFU *E. coli* in 100 mL of tap water

3.6 Optimization of the immobilized bacteriophage layer

In discussing the targeted immobilization of bacteriophage particles, we must also confront the issue of immobilization of undesirable interferents which will have a significant impact on the quality of the immobilized layer, both during preparation as well as in its final application, be it an immobilized interaction layer on a biosensor transducer or a biosorbent for bio-active food packaging. The purification protocol immediately preceding conjugation can have a large effect on the success, homogeneity, and overall quality of the immobilized phage layer [130], and is thus of critical importance and an integral part of any phage immobilization protocol. Following immobilization, an additional blocking step is often included to prevent off-target immobilization and non-specific binding to the surface.

3.6.1 Phage propagation and purification methods

The process of phage propagation (also referred to as phage amplification) necessarily generates large amounts of bacterial debris (*e.g.*, DNA, peptidoglycans, lipopolysaccharides[127] etc.) which must be separated from the phage particles, since many immobilization techniques will equally – if not preferentially – bind these contaminants to the surface along with the phages of interest [130]. Furthermore, storage of phages in the presence of certain cellular debris can trigger premature ejection of phage genetic material[399–401], potentially rendering the phage inactive. For these reasons, immobilization of phages requires first the isolation of a high-purity, high-titer phage suspension. Typical phage concentrations used for immobilizations range between 10^{10} and 10^{12} plaque-forming units per milliliter (PFU/mL), although some success has been seen with lower infective titers. The lower phage concentrations in this range tend to be biased towards myoviruses such as T4 and podoviruses such as P22, while the higher concentrations are almost exclusively seen in papers using the filamentous phages M13 and fd. The topic of phage purification necessitates a review in its own right, but the main methods will be outlined briefly here.

Dead-end filtration through 0.45µm and 0.2µm pore-size membranes is typically employed[§] – along with differential centrifugation[172] – as an initial first purification step to rid phage suspensions of the largest bacterial debris and leftover culture medium constituents. Differential centrifugation can be used to pellet contaminants brought out of solution using chemical precipitation (*e.g.*, using PEG and/or NaCl)[163,172]. It is

[§] Unfortunately, such filtration can immediately reduce the infectious titer by a factor of 10.

carried out at relatively low centrifugal force of ~5 000 *g*, in larger volumes (between 1 and 1 000 mL), and in simple centrifugation media (typically simply the phage buffer) compared to ultracentrifugation.

In contrast, in density gradient ultracentrifugation (DGU) the components of a sample are fractionated based on their buoyant density. DGU necessitates centrifugation at very high acceleration (>70-80 000 *g* for 4-6 hours is typical [159]), smaller volumes (~6 mL), and the careful selection and preparation of centrifugation media such as CsCl or sucrose[166]. DGU is performant enough to permit the separation of terminated viruses from empty ghost particles [167]. Potential drawbacks of DGU include the high cost of ultracentrifuge equipment, the potential for phage aggregation due to high ionic strength of centrifugation media [168], and the difficulty in harvesting the final product. DGU purification has also been found to lose un-tailed phages [169] and can yield solutions contaminated by – for example – large quantities of host bacterium flagella fragments [128,170]. Despite these disadvantages, the use of DGU has become an established technique for the isolation and purification of virus particles [167,171,173,174].

PEG precipitation – either employed on its own or in conjunction with DGU [166] – is another popular method for concentration and purification of viruses [155–158,163]. PEG, a polymerized form of ethylene glycol (used at various molecular weights [159] but most often at 6 kD [160–163] for phage purification), is employed as a fractional precipitating agent which separates proteins by virtue of their solubility. PEG acts as an inert solvent sponge, reducing water availability. With increasing concentration of PEG the effective protein concentration is increased until solubility is exceeded and precipitation occurs. Thus, larger proteins will precipitate at lower concentrations of PEG and can be separated with differential centrifugation [164,165]. PEG precipitation is considered by some experts to be "*a crude and non-specific technique*" [165].

An alternative suite of purification methods involve various forms of chromatography [178]. Boratynski *et al.* used size-exclusion chromatography (SEC) to produce phage suspensions with endotoxin levels low enough to permit intravenous administration [127]. SEC can also be used as part of a short-turnaround purification protocol, used by Naidoo *et al.* to avoid CsCl DGU and PEG precipitation, giving a total process time of only 3 hours [128]. Recombinant affinity tags expressed on T4 capsids have been used by Ceglarek *et al.* to facilitate affinity chromatography [178]. While elegant, this method relies on genetic modification of each host bacterial strain which may be infeasible for some researchers and applications. Adriaenssens et al. demonstrated anion-exchange chromatography (AEC) for the purification of eleven morphologically distinct phages. The authors concluded that although this method presents easier scalability for industrial-scale throughput compared to CsCl DGU, it requires more laborious optimization of purification at the outset [179].

3.6.2 Surface blocking

Due to their inherent charge – and often their hydrophobicity – proteins have a tendency to spontaneously adhere to surfaces in an aqueous environment. Extremely pure reagents and clean surfaces are a *sine qua non* for well-controlled and reproducible fabrication of biosensors and bioactive surfaces. However, a clean surface is also susceptible to non-specific binding of proteins in aqueous solutions. Off-target binding of interferents can hinder biofunctionalization, obscure the transduction of specific interaction events and decrease the signal-to-noise ratio (SNR) in the case of biosensors, and generally compromise reproducibility, even when phage infectivity is not impacted [237].

For this reason, a common unit operation in phage-functionalization is to follow conjugation with a blocking step, whereby the surface is flooded with an amphiphilic biological species (*e.g.*, casein[171,175], bovine serum albumin (BSA)[286,367]) or synthetic polymer (*e.g.*, PEG[143,402]) or amine-presenting molecule (*e.g.*, ethanolamine[245,328]) that will occupy non-functionalized sites on the surface without impeding the sensitivity of the functionalized sites. In this way, the non-specific binding of proteins – and other components of the sample – is reduced, while specific reactions with the target analyte are (ideally) unaffected. If a researcher

finds that they have trouble with non-specific binding to their phage-functionalized substrate, surface blocking may be an easy first step to boost performance.

PEG and casein have been investigated for surface blocking and have in some cases been found to be more performant than BSA [143,402]. However, incubating with BSA remains – by a wide margin – the most popular strategy for passivation of biofunctionalized surfaces to reduce or even eliminate non-specific binding, due to its low cost and its ease of storage, preparation, and use.

3.7 Conclusion and Remarks

Since the first papers on phage immobilization began to appear at the turn of the century [281,403], a variety of strategies have been developed. By far the most popular single method relies on simple physisorption of phages to the substrate (usually a gold layer) without any chemical modification of the surface, with over one third of papers making use of this method. Although such easily implemented methods may be seductive, physisorbed phages have been shown to easily detach following changes in ionic strength, temperature, and pH at the substrate surface [270], when compared to covalent immobilization.

Covalent conjugation of phages has been demonstrated with a variety of techniques, but three surface modifications in particular dominate: carbodiimide activation of surface carboxyl moieties (*i.e.*, by EDC and NHS); self-assembled monolayer formation of thiol linkers (*e.g.*, 11-MUA, L-cysteine, and DTSP); and amino-silanization (*e.g.*, APTES, APTMS). Together, these chemistries cover half of all the reviewed literature on phage conjugation, and each relies on heterofunctional linkers with at least one terminal functional group (carboxyl (-COOH), or primary amine ($-NH_2$)) that engages in amide bonding with the phage capsid.

Genetic modification-based methods compose a significant minority of the immobilization techniques demonstrated in the literature, being used in about 10% of all papers reviewed. Genetic engineering of phages may prove time-consuming and laborious compared to physisorption or covalent conjugation [268], but may prove practical in some instances. New avenues for immobilization *via* display of recombinant phage coat proteins may be revealed as a result of the discoveries of peptides exhibiting binding specificity for a plethora of substrates including metals[386–388] and their oxides[389,390], silica [391], semi-conductors [392,393], carbon allotropes [288–291], and several polymers [297–303].

The protocols presented in many papers omit a surface-blocking step to prevent non-specific binding, despite ample evidence in the literature that such a step increases sensitivity and overall performance in the case of biosensors. Surface blocking can be as simple as incubating a substrate for 30 minutes in a 1% BSA solution[214,224], which is unlikely to prove too onerous to be incorporated into any workflow.

Regarding the purity of phage suspensions, since the purification protocol immediately preceding immobilization can have a large effect on the success, homogeneity, and overall quality of the immobilized phage layer, researchers may have difficulty replicating and comparing results in the literature where the purification protocol has not been stated explicitly. Many papers do not clearly describe the purification procedure for the bacteriophages used, particularly when these phages have been obtained from collaborators. Historically, a large impediment to the widespread adoption of phage therapy in the west was the lack of standardization of phage preparation procedures or the criteria for purity and potency [47]. In order to facilitate greater reproducibility of results and comparison between studies, the authors of this review would recommend inclusion of any purification procedures in future papers.

In conclusion, phage-functionalization of substrates presents many promising avenues for the development of, *inter alia,* novel bioactive surfaces and specific interaction layers within biosensors. The performance of these phage-functionalized substrates depends on the production of high-purity phage suspensions and careful consideration of the immobilization technique employed.

As the pernicious effects of antimicrobial resistance become more apparent in the 21st century, bacteriophages and adjacent research are well-placed to play an increasing role in biomedical, agricultural, and environmental monitoring applications for many years to come.

Summary tables of covalent, physisorption, and genetic engineering methods for immobilization of phages can be found in **Table A.2**, **Table A.3**, and **Table A.4** of the Annex, respectively.

Chapter 4

Approaching the Geometric Limit of Bacteriophage Conjugation to Gold: Synergy of Purification with Covalent and Physisorption Strategies

Article submitted April 2022

Larry O'Connell[1,2], Pierre R. Marcoux[1], Prisca Perlemoine[1], Yoann Roupioz[2]

[1] Univ. Grenoble Alpes, CEA, LETI, F38054 Grenoble, France

[2] Univ. Grenoble Alpes, CNRS, CEA, IRIG, SyMMES, 38000 Grenoble, France

Keywords: Immobilization, biomaterials, bacteriophage, bioactive surfaces, biosensor, physisorption, electron microscopy

Abstract

Here we report the immobilization of bacteriophages 44AHJD, P68, Remus, and gh-1 by physisorption and covalent cross-linking *via* a series of thiolated reagents: 11-merceptoundecanoic acid (11-MUA), L-cysteine with 11-MUA, L-cysteine with glutaraldehyde, and dithiobis(succinimidyl propionate) (DTSP).

Surprisingly, phage purification protocols showed significant impact on phage immobilization efficiency. Indeed, purification of phages by density gradient (CsCl) ultracentrifugation and centrifugal ultrafiltration was found to have a dramatic determinant effect on the quality of the immobilized layer. Surface densities of 160 ±13.9 phage/μm^2 were observed when careful phage purification was combined with 11-MUA self-assembled monolayer functionalization of the surface.

High-resolution scanning electron microscopy enabled direct confirmation of immobilization, along with calculation of phage densities on the surface, and even resolution of phage capsid substructures.

4.1 Introduction

Bacteriophages (phages) are obligate parasitic viruses that replicate exclusively in the cells of their host bacterium. A phage's host range and ability to replicate is predicated on recognition of its host *via* receptor-binding domains (RBDs) — epitope-recognizing regions on the phage tail fibers. Modification of the phage capsid (either by genetic engineering or post-translationally) can yield engineered tropism towards an increasingly varied collection of analytes in addition to bacteria.[130] The use of phage as an immobilized biosensing layer began in earnest in 2005[180] and has since been demonstrated in combination with a variety of transduction mechanisms towards the detection of a range of analytes including bacteria and their spores [212–217], antibodies [218–221], cancer biomarkers [221–224], enzymes [181,183], and even glucose [225]. Such strategy is motivated by the very high phage specificity, usually associated with high sensitivity, toward target molecular motifs. While some evidence exists that a lower than maximal surface density is optimal for bacterial capture,[128] phage-based biosensing layers targeting other analytes can benefit from the densest possible packing of phages limited only by geometric constraints.

Gold is by far the most common phage-functionalized substrate, used to immobilize a bacteriophage sensing layer in approximately half of the literature.[133] There are several reasons for this. Of the suite of transduction mechanisms available to the biosensor researcher, several of the most popular rely on a gold layer interfaced with an analyte or carrier liquid. Such is the case for biosensors leveraging surface plasmon resonance (SPR) and surface enhanced Raman scattering (SERS), both of which exploit gold's high density of easily polarizable free electrons – a prerequisite for strong interaction with electromagnetic fields.[278] While other transduction methods such as quartz crystal microbalance, magneto-elasticity, magnetoresistance, and magneto-restriction instead rely on an underlying ferromagnetic[276] or quartz layer[277], gold is nevertheless deposited due to its ease of deposition on these materials and its ability to facilitate bioconjugation. Furthermore, gold exhibits high biocompatibility, resistance to oxidation, is easily cleaned, and is efficiently deposited on a variety of substrates[273–275]. Gold also exhibits a high binding affinity (200 kJ/mol) for thiol groups (R-SH), which permits formation of self-assembled monolayers of thiolated cross-linkers.[275] Endogenous thiol groups are also frequently found – or easily introduced – in many ligands for the purpose of conjugation.

Of the existing literature featuring phage immobilization, there have been several strategies demonstrated for conjugation to gold, but only rarely is a comparison made between several different methods or for more than a single phage at a time. This work aims to make an extended comparison between multiple conjugation strategies, apply them for immobilization of several different phages, and investigate the effect of purification protocol on the quality of the resulting phage layer.

The process of phage replication necessarily liberates large quantities of biomaterial from the host bacterium into the surrounding medium. Bacterial DNA, lipopolysaccharide,[127] flagella[128] and other components can all be found in the crude phage lysate even before considering other contaminants that may originate in the bacterial culture medium and labware. Tryptic soy broth, for instance, contains large quantities of free amino acids by design. This material must be removed from the crude phage lysate, separating it from the phages before they can be used for functionalization of substrates. Bacteriophages are unusually large compared to molecular ligands that are normally employed as probe molecules in the biological sciences (*e.g.*, antibodies, oligonucleotides, aptamers etc.). As a result, values for the diffusion coefficient of bacteriophages are typically of the order of 5×10^{-8} cm^2/second,[131] — many orders of magnitude smaller than for these smaller species. The result is that more rapidly diffusing impurities will be preferentially bound to the substrate surface unless removed from phage suspensions.

Many articles incorporating phage immobilization describe rudimentary purification protocols based only on filtration[134] or centrifugation,[135,136] seem to mistakenly make use of trisaminomethane (tris) buffer[137–140] which immediately blocks any activated esters on the surface[141,142]; or trust the purity of a phage suspension

provided by a collaborator.[140,143,144] We posit that insufficient purity of phage suspensions results in competitive immobilization of contaminants left over from the crude phage lysate, which reduces the quality of the final phage layer. We test this hypothesis by using two different phage purification protocols and comparing the resulting immobilized layer.

Lastly, we demonstrate a scanning electron microscopy protocol which allows direct counting of bacteriophage density on substrate surfaces and permits sufficiently high resolution to directly confirm phage layer quality, and even to resolve phage capsid substructures.

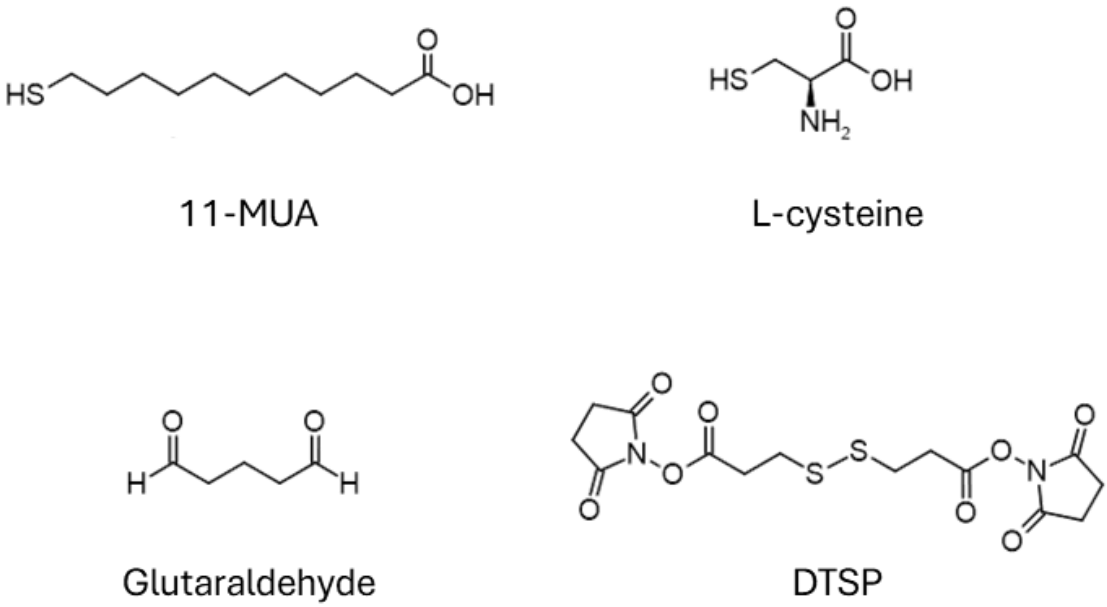

Figure 4.1 Structural formula of 11-mercapto-undecanoic acid (top left), L-cysteine (top right), glutaraldehyde (bottom left), and DTSP (bottom right)

Self-assembled monolayers (SAMs) of thiolated molecules underlie a popular method for conjugation to gold substrates, and are regularly employed in the functionalization of planar and nanoparticulate soft metals with proteins, antibodies, and DNA.[275]

11-merceptoundecanoic acid (11-MUA) is typical of this class of thiolated cross-linker, featuring a thiol headgroup and a terminal carboxyl group (**Figure 4.1**). The amino acid L-cysteine similarly binds to gold through a strong thiol linkage while presenting both a carboxyl and an amine group.[254] Upon introduction to the gold substrate, the strong sulfur-gold bonds of these molecules readily displace biological contaminants,[275] eventually forming a stable SAM, presenting carboxylic functionalities to the bulk.[336] Normally, these carboxyl groups are then activated using the carbodiimide (1-Ethyl-3-(3-dimethylaminopropyl)carbodiimide) (EDC) in combination with N-hydroxysuccinimide (NHS), which together catalyze amide bonding with primary amines of the ligand.[170,326] Cross-linking molecules containing thiol moieties have been used to immobilize phages of various morphologies on gold surfaces,[254,272,327] nanoparticles,[330] and plasmonic quasicrystals.[252]

The amino acid L-cysteine (**Figure 4.1**) binds to gold *via* a strong gold-thiol bond while presenting an amine group which can be cross-linked to primary amines of phage capsids via glutaraldehyde[137,249,254] or tagged with a reactive ester by EDC/NHS.[244,249] L-cysteine has been used to immobilize T4[137,175], D29[249], and M13 phage.[321]

DTSP is an NHS ester cross-linking agent — a homodimer presenting both thiol and succinimide moieties, linked by a disulfide bridge which cleaves during formation of a self-assembled monolayer on gold (**Figure 4.1**). This results in in two thiolate moieties bonded to the surface, each bound via a carboxyl group to a terminal

succinimidyl group that is exposed to the solution.[404] Since the succinimidyl group is already present in the DTSP molecule, no subsequent activation of the surface with EDC/NHS is required. This allows a one-step preparation of the surface before binding with primary amines of a target ligand.[337] DTSP has been demonstrated for the immobilization of P22, NCTC 12673 and T4 phages.[128,175,337]

Physisorption is another appealing technique for phage immobilization due to its apparent simplicity, and has been extensively used for phage immobilization[217,402], employed in approximately a third of all articles on the subject.[133] Physisorbing a bacteriophage layer can be as simple as incubating a thoroughly cleaned substrate with a phage suspension, but yields a bioactive layer that is less robust against changes in ionic strength, temperature, pH, and high fluid velocities at the surface.[270] Despite these drawbacks, physisorption is seen as sufficient for some applications where phage desorption and/or migration on the surface is not problematic. Van der Waals forces, hydrophobic bonding, or weak covalent bonds between cysteine residues and gold surfaces have all been proposed as potential mechanisms underlying physisorption, but there appears to be no consensus as yet.[355,373]

4.2 Materials & Methods

4.2.1 Products and reagents

L-cysteine (97%), glutaraldehyde (Grade I, 50% in H_2O), glycerol (≥99%), 11-MUA (95%), DTSP (99%), agar (Difco), trypticase soy broth (TSB), phosphate-buffered saline (PBS), potassium nitrate (KNO_3), acetone, and ethanol (≥99.9%) were purchased from Sigma-Aldrich (Saint Quentin Fallavier, France) and used without additional purification. CsCl (≥99.9%), 0.9% w/v NaCl solution (OTEC), and 90 mm TSA petri plates were purchased from VWR (France). EDC (≥98%) and sulfo-NHS were purchased from Thermofisher and used as received. Deionized water (DIW; >18 MΩ resistivity) was obtained from an ELGA PURELAB flex dispenser (Veolia Water, France). Polyethylene glycol 6 kDa (PEG-6000) was purchased from Merck (Darmstadt, Germany).

4.2.2 Host bacterium and bacteriophage preparation

Bacterial hosts *Staphylococcus aureus* subsp. *aureus* Rosenbach (ATCC 43300, P68; ATCC 12600, host of phage Remus), and *Staphylococcus aureus* (ATCC BAA-2312, host of phage 44AHJD) were obtained from Microbiologics (Kwik-Stik™ lyophilized strains).

Bacterial host *Pseudomonas putida* (ATCC 12633; host of phage gh-1), phages 44AHJD,[405] P68, Remus,[406] and gh-1[195] were obtained from the *Félix d'Hérelle Reference Center for Bacterial Viruses* of the Université Laval, Quebec, Canada.

Bacterial cultures were routinely prepared in TSB at recommended temperatures for each host: *S. aureus* at 37 °C and *Pseudomonas putida* at 30 °C. Bacteriophage suspensions were routinely prepared using the double layer agar method[99]: 100 µL of overnight liquid precultures of each bacterial host were inoculated into fresh TSB and allowed to proliferate until reaching 10^8 CFU/mL as confirmed by optical density at 550 nm. Then, 200 µL bacterial host and 100 µL bacteriophage suspension (5×10^3 PFU/ml) were inoculated into each of several 15 mL Falcon tubes filled with 5 mL molten agar (TSB prepared with 7.5 g/L agar) at 51.5 °C, vortexed, and poured over 20 mL solidified tryptic soy agar (TSA, 15 g/L agar) in a standard 90 mm petri plate. Plates were then incubated overnight until lysis plaques became confluent in the top agar layer, which was then collected and soaked for 4 h at room temperature in sterile 154 mM NaCl solution in a 50 mL polypropylene tube. Each tube was then twice centrifuged for 20 min 5 500 *g* at 4 °C and the supernatant retained each time. The supernatant was then filtered through a 0.45 µm and then 0.2 µm syringe filter (Millipore, Cork, Ireland).

Each suspension was brought to 0.5M NaCl (35-45 mL depending on the experiment) and 8% w/v PEG-6000 and left at 4 °C overnight. The following day, each suspension was centrifuged for 30 min at 12 000 *g* at 4 °C,

the supernatant removed, and the pellet resuspended in sterile 154 mM NaCl, vortexed, centrifuged 20 min 5 500 *g* at 4 °C and the supernatant retained to produce what are hereafter referred to as *'PEG-purified'* suspensions.

To investigate whether further elimination of contaminants has an effect on the final surface density, some phage suspensions were selected for additional purification.

Following PEG-precipitation, several suspensions were then purified by density gradient ultracentrifugation (DGU) for 2 h at 100 000 *g* at 4 °C on a CsCl step gradient (1.7 g/ml, 1.54 g/mL, and 1.34 g/mL CsCl in DIW) in 5 mL, Open-Top Thinwall Ultra-Clear ultracentrifuge tubes (Beckman Coulter, Villepinte, France) in a SW55Ti swinging-bucket rotor (Beckman Coulter) mounted in an Optima l-90K Ultracentrifuge (Beckman Coulter). Bacteriophages were concentrated at the second visible band from the top and collected with a micropipette tip. CsCl was removed from phage suspensions by repeated centrifugal ultrafiltration (UF) and resuspension in 154 mM NaCl solution using 100 kDa Vivaspin 500 ultrafiltration units (Sartorius), to produce what are hereafter referred to as *'DGU-purified'* suspensions.

All phage suspensions were stored at 4 °C in the dark in 1.5 mL polypropylene Eppendorf-type tubes. Following purification, the infectious titer of phage suspensions was obtained by the agar overlay method,[99] and is reported in units of plaque-forming units per millilitre (PFU/mL).

4.2.3 Preparation of gold substrates

Flat *D*263® glass slides coated with Cr/Au – 1.5 ± 0.5 nm / 55 ± 3 nm were purchased from SCHOTT. Gold-coated slides were cleaved into 15×26 mm sections, the surface rinsed with DIW, ethanol, then once more with DIW. Slides were then dried with argon and plasma cleaned for 3 mins in 0.6 mBar 75:25 oxygen/argon mix at 80% power in a Femto plasma system (Diener electronic, Ebhausen, Germany). The slide surfaces were then left at room temperature to stabilize for at least 24 hours before use.

4.2.4 Preparation of reference lysate suspension

During the lytic phage replication cycle, bacteria are lysed and empty an array of contaminants which may survive the purification process and compete with the phage for immobilization on the substrate.[130] In order to control for this, we propose a control suspension designed to contain any contaminants that may survive the phage purification process but devoid of phage particles.

To this end, an overnight liquid culture of *P. putida* (the host of phage gh-1) was mechanically lysed by exposure to high-intensity ultrasound (US) using a CV33 ultrasound probe connected to a Vibracell 75115 controller, at 30% amplitude and 25% duty cycle. Colony counting after US exposure, carried out previously, established a decimal reduction rate of D_{20}=1.97 minutes with this method (see Annex: Bacterial Decimal Reduction Time Following Ultrasound). The control lysate was thus sonicated for 10 minutes at room temperature to lyse almost all bacteria, but no longer in order to avoid heating or other side effects. The purpose of ultrasound treatment is to generate the same debris as is generated during phage replication but by physical rather than chemical means. The control lysate was then purified by PEG precipitation in an identical way to phage lysates and stored at 4 °C in the dark in a 1.5 mL polypropylene Eppendorf-type tube.

In this way, any interferents are given the same opportunity to adhere to surfaces during the purification process (*e.g.*, exposure to surfaces of plastic labware, tools, filtration membranes etc.) and persist at comparable concentration until use in immobilization experiments. Such a solution is hereafter referred to as the 'ultrasound control lysate'.

4.2.5 Bacteriophage immobilization

4.2.5.1 11-MUA, and 11-MUA with L-cysteine

11-MUA was dissolved in ultrapure ethanol to a concentration of 50 mM. Cleaned gold-coated slides were functionalized with 11-MUA to form a self-assembled monolayer by soaking overnight at room temperature. Immediately before use, gold-coated slides were rinsed with ultrapure ethanol, dried with compressed air, and activated with a 100 mM EDC 25 mM NHS aqueous solution for 30 minutes at room temperature to activate the carboxyl groups of the 11-MUA SAM. The surface was then rinsed with DIW, dried with compressed air, and immediately drop-cast with 1 µL droplets of each phage suspension supplemented with 10% w/v glycerol (titer of phage suspensions varied between 10^8-10^{11} PFU/mL). Phage suspensions were incubated with the surface overnight at room temperature in a humid environment inside a desiccator loaded with saturated KNO_3 solution (to produce 95% relative humidity) and rinsed with DIW the following day. Each slide-phage pair was produced in duplicate. Addition of glycerol has been found to be a crucial step to prevent drying of deposited droplets. Deposition of small volumes not only allows one to use precious phage stocks sparingly, but also permits the arrayed immobilization of different phage species in adjacent, closely-spaced regions on the same substrate (*e.g.*, for the purpose of phage-based biochips).[404]

For 11-MUA with L-cysteine slides, the process was identical except the slide surfaces were additionally incubated with 50 mM L-cysteine aqueous solution overnight at 40 °C, then rinsed with deionized water and dried before 11-MUA incubation.

4.2.5.2 L-cysteine with glutaraldehyde

Gold-coated slide surfaces were incubated with 50 mM L-cysteine aqueous solution overnight at 40 °C, then rinsed with DIW. The slides were then soaked in glutaraldehyde 2% v/v in PBS for one hour at room temperature. Slides were rinsed thoroughly with PBS, dried, and immediately drop-cast with 1 µL droplets of each phage suspension (10% w/v glycerol, 10^8-10^{11} PFU/mL), incubated overnight at room temperature in a humid chamber (95% relative humidity), and rinsed the following day. Each slide-phage pair was produced in duplicate.

4.2.5.3 DTSP

Gold slides were soaked in a 2 mg/mL solution of DTSP in high-purity acetone in a covered glass dish sealed with parafilm to minimize solvent evaporation. After 24 hours at room temperature, the slides were rinsed with acetone, dried with compressed air, immediately drop-cast with 1 µL droplets of each phage suspension (10% w/v glycerol, 10^8-10^{11} PFU/mL), incubated overnight at room temperature in a humid chamber (95% relative humidity), then rinsed the following day with DIW. Each slide-phage pair was produced in duplicate.

4.2.5.4 Physisorption

No preparation of slides was made prior to physisorption other than rinsing and plasma cleaning, as detailed above. Gold-coated slides were drop-cast with 1 µL droplets of each phage suspension (10% w/v glycerol, 10^8-10^{11} PFU/mL), incubated overnight in a humid chamber at room temperature, and rinsed the following day with DIW. Each slide-phage pair was produced in duplicate.

4.2.6 Scanning electron microscopy

In order to evaluate the surface density of immobilized phages, scanning electron microscopy (SEM) was carried out on gold substrates functionalized by each strategy. In order to avoid charging effects during imaging, a ~4 nm thick layer of carbon was deposited on the gold slides using a Safematic CCU-010 HV compact coating unit (Zizers, Switzerland), at 3×10^{-5} mBar, with the sample mounted at stage height 6. The surface was observed in a Zeiss Ultra 55 scanning electron microscope under a 2 kV acceleration voltage and working distance in the range 4-10 mm. Images were taken with two secondary electron detectors, one mounted inside the chamber, the other an "in-lens" detector mounted inside the column. The in-lens detector yields more topographical contrast, since the signal from the chamber walls is excluded. At least three images were taken

at distant locations within each functionalized region in order to provide an accurate measure of the phage density that results from each strategy.

4.3 Results & Discussion

4.3.1 Initial comparison shows superiority of 11-MUA with ultracentrifugation, and ultrafiltration

Since a large variety of phage immobilization methods have been proposed in the literature, we sought to investigate a selection of strategies for the immobilization of the three phages gh-1, P68, and Remus. Gold-coated slides were chemically functionalized and drop cast with purified phage and ultrasound control suspensions, producing different permutations of immobilization strategy and phage.

Following immobilization and rinsing, functionalized gold slides were observed by SEM to obtain a direct measurement of immobilized phage density on the substrate surfaces (**Figure 4.2**) as well as a qualitative measure of the level of contaminant immobilization. Additionally, SEM measurements of phage surface density allowed us to assess the level of aggregation on the surface. When purified by PEG/NaCl precipitation, phages P68, Remus, and gh-1 were immobilized with a range of surface densities of 0.2 - 11.5 phage/μm^2 (**Figure 4.3**), which is comparable with typical densities seen in the literature.[133] 11-MUA and DTSP yielded the best and similar results, despite involving a two-step and one-step surface activation protocol, respectively. L-cysteine, when combined with 11-MUA, rather than enhancing the immobilization level, instead seemed to inhibit phage conjugation relative to the use of 11-MUA alone. While L-cysteine + 11-MUA had equivalent performance to L-cysteine + glutaraldehyde, the latter was found to increase the wettability of the substrate, rendering it hydrophilic and making it difficult to deposit small droplets.

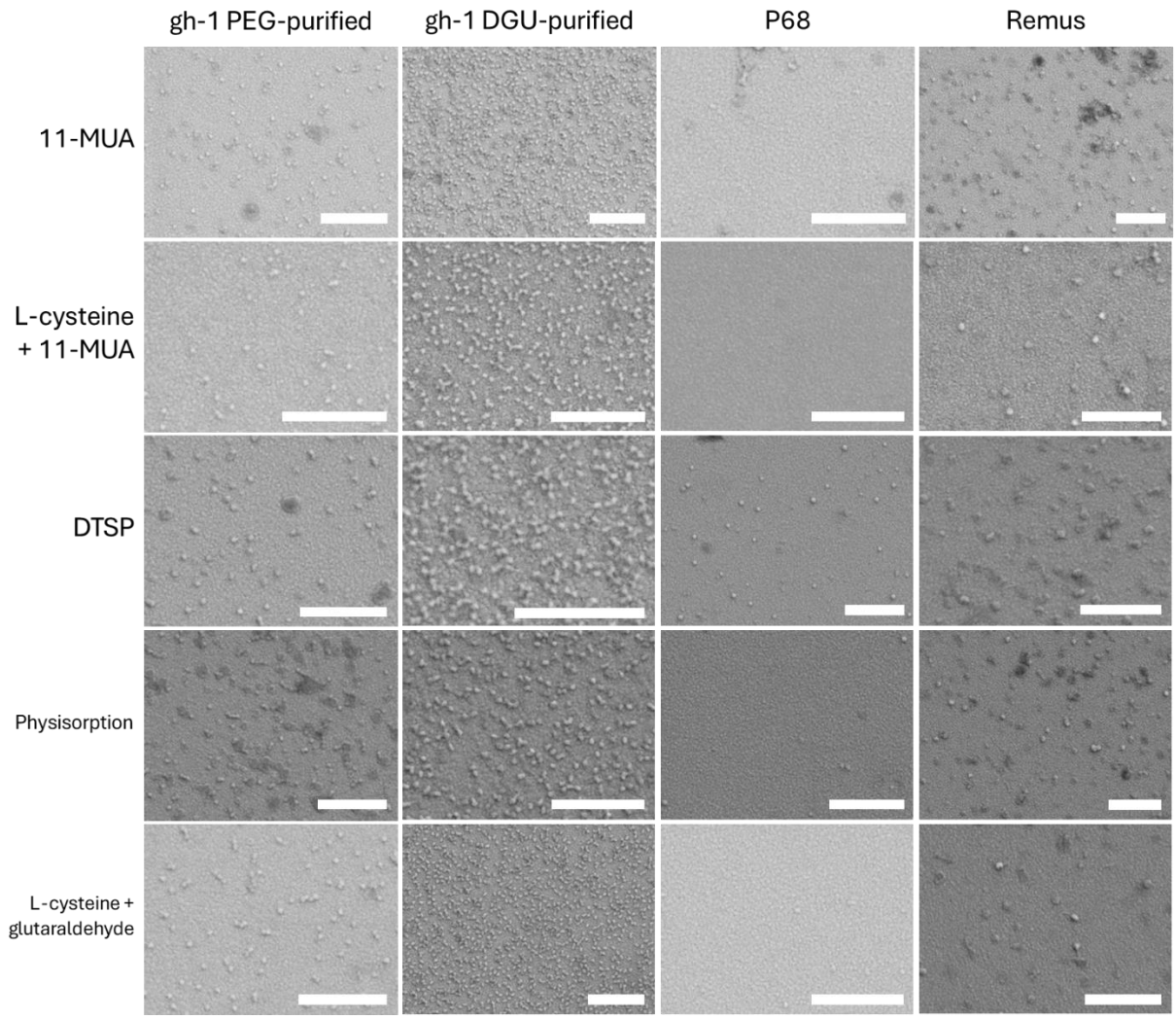

Figure 4.2 Representative scanning electron micrographs of gold substrate surfaces functionalized by various strategies (rows) and with various bacteriophage (columns).Scale bars indicate 1 µm.

We hypothesized that insufficient purification of phage suspensions compromises the quality and density of the immobilized phage layer, as smaller molecular weight contaminants may survive the purification process and diffuse more quickly than phage to the substrate surface, where they are immobilized and block sites for phage conjugation. To test this hypothesis, phage gh-1 was further purified by DGU and ultrafiltration with a 100 kDa molecular weight cut-off membrane. These additional purification steps produced gh-1 phages that have been selected first by size as the filtrate (0.2 µm filtration), then by solubility (PEG precipitation), then by buoyant density (DGU), and finally again by size as the retentate (UF).

The additional steps of ultracentrifugation and ultrafiltration yielded a dramatic rise in surface density of between 5.2 and 16.5 times more gh-1 phage on the surface, reaching 93.4 ±5.3 phage/µm^2 when immobilized using 11-MUA (**Figure 4.3**). We attribute this to the removal of smaller molecular weight contaminants.

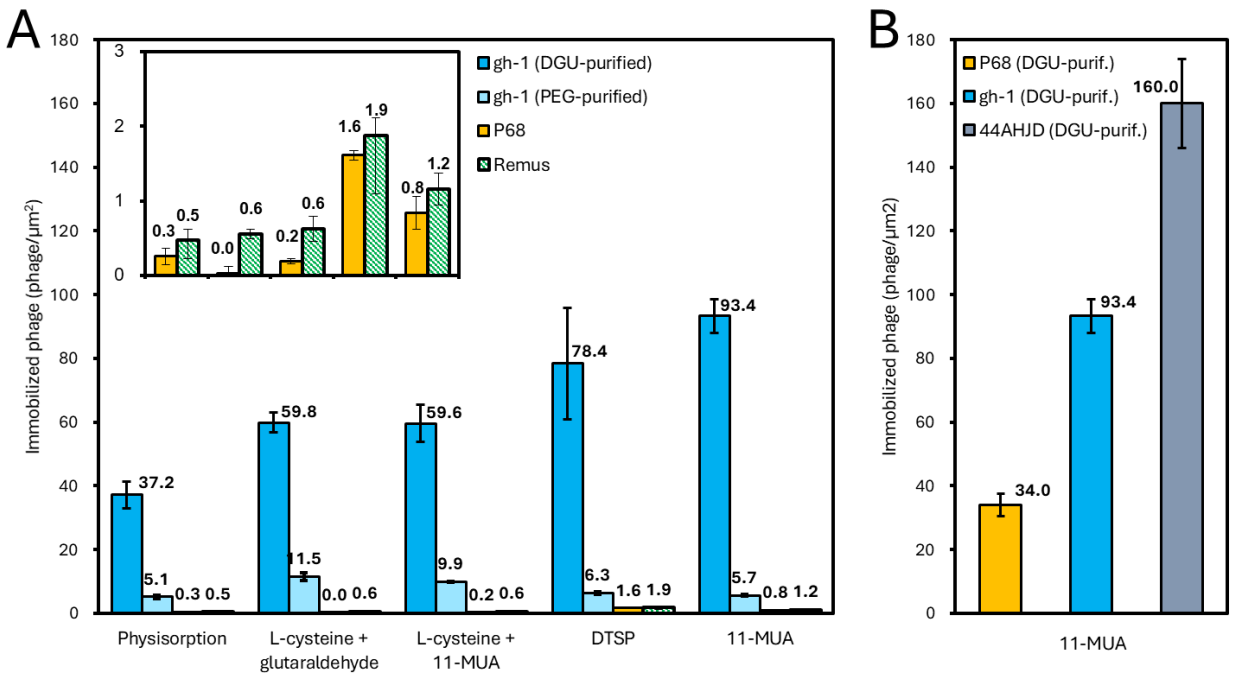

Figure 4.3 Characteristics of phage functionalized surfaces.A: Surface density as observed by scanning electron microscopy on gold substrates of immobilized phage gh-1 purified by ultracentrifugation (blue), and PEG precipitation-purified phages gh-1 (light blue), P68 (yellow), and Remus (hatched green). Inset shows detail of much smaller surface density values for P68 and Remus after immobilization with the same chemistries. B: Surface density on gold substrates of immobilized phages P68 (yellow), gh-1 (blue), and 44AHJD (grey); after purification by PEG/NaCl precipitation followed by density gradient ultracentrifugation and centrifugal ultrafiltration. Error bars indicate standard deviation.

The UF step, initially conceived as an alternative method to dialysis to remove CsCl left over from ultracentrifugation, may have contributed significantly to the removal of contaminants with smaller molecular weight than the bacteriophages. Although filtration at 0.2 µm is frequently performed at some point in phage purification protocols,[133] we posit that since UF allowed selection of phages as *retentate* rather than phages as filtrate, it is uniquely effective for elimination of contaminants that normally compromise the final phage layer.

Aside from phage density, another important metric is the level of uncontrolled binding of material of the same length scale as phages. Careful attention to microscope parameters (see 4.3.3 High-resolution scanning electron microscopy) allowed close inspection of the surface by SEM., assessment of the quality of the bound phage layer and revealed differences in the binding of flat, circular, pancake-like material. Taking PEG-purified gh-1, for example, while the surface densities may be similar for physisorption, L-cysteine, and L-cysteine + glutaraldehyde-functionalized surfaces, it appears from our observations that physisorption results in significant amounts of these flat, circular contaminants on the surface.

This makes intuitive sense, since physisorption is expected to bind material less discriminately from the phage lysate through a variety of mechanisms, whereas the active ester and aldehyde-presenting chemistries should preferentially bind primary amines.

4.3.2 Developing 11-MUA immobilization

Inspired by the surprisingly high phage density and low level of contaminants that resulted from the PEG/DGU/UF purification in combination with 11-MUA, we next wanted to confirm the replicability of this protocol in the immobilization of several phages in addition to gh-1. In a subsequent experiment, we purified

several phages by PEG/DGU/UF and focused exclusively on the 11-MUA chemistry. DGU, although performant for the podoviruses used in this study, resulted in significant loss of the myovirus Remus, with an infectious titer of only 2×10^5 PFU/mL following purification compared to 10^9-10^{11} PFU/mL for other phages. For this reason, the PEG/DGU/UF and 11-MUA protocol was extended to a new phage 44AHJD in addition to gh-1 and P68. Phages were purified with the PEG/DGU/UF sequence and immobilized by 11-MUA as before.

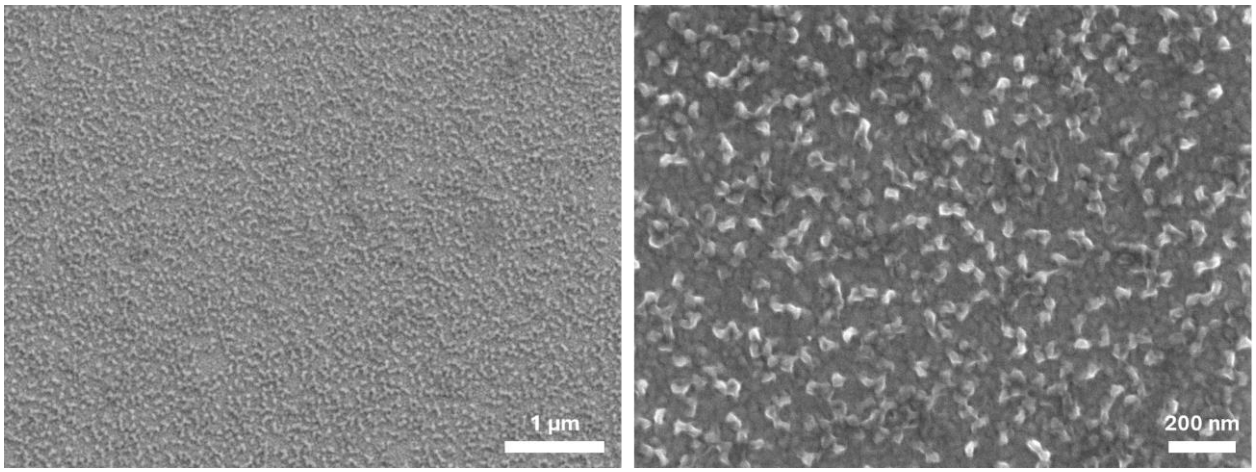

Figure 4.4 Scanning electron micrographs of a region heavily coated with phage 44AHJD to a density of 160 ±13.9 phage/µm^2, observed using the chamber secondary electron detector (left) and a zoom on the phage particles themselves, observed using the in-lens detector which provides more topographical contrast. Phages appear as a homogenous monolayer of 75 nm-diameter particles, in agreement with values indicated in the literature.[407]

An extremely high density of 160 ±13.9 phage/µm^2 was achieved for phage 44AHJD (**Figure 4.4**). Furthermore, the immobilized layer was observed to be homogenous over millimetre length scales, with no significant aggregation of the particles evident in SEM. The close packing of phage on the surface necessitated the use of the in-lens detector — which gives superior topographical contrast — in order to distinguish adjacent particles. Excluding phage multilayers (shown to attain 1100 phage/µm^2 by Yang *et al.*[219]), the authors are aware of only one other paper that credibly claims immobilization approaching a similar density on gold substrates. Immobilization of phage P68 with a density of 34 ±3.4 phage/µm^2 was also demonstrated with the same protocol.

The infectivity of phages immobilized by 11-MUA was confirmed by the observation of a zone of lysis surrounding the gold slide surface in a bacterial lawn of the host of the immobilized phage (see Annex: Proof of Phage Infectivity Following Immobilization **Figure A.9**).

4.3.3 High-resolution scanning electron microscopy

Following immobilization of phages purified by DGU, phage surface density frequently reached a level that made adjacent particles difficult to distinguish. It is also important to note that the evaporated gold forms a polycrystalline layer with granules on the order of 50 nm. Since phages themselves have a diameter of approximately the same scale as these granules, distinguishing the two can prove difficult unless attention is paid to the imaging conditions.

The SEM analysis parameters used in this work allowed sufficient resolution to resolve individual phage particles on the surface and, furthermore, different protein complexes within the phage. **Figure 4.5** shows gh-1 particles immobilized on the surface, with their capsid and tail fibers visible with an apparent prolate

spheroid geometry (See Annex: Observed Bacteriophage Morphology), while **Figure 4.6** shows the tail tube and baseplate of phage Remus.

Traditionally, TEM has been favoured over SEM for observation of phages due to their small size and the superior resolution afforded by TEM. Since phages are composed of non-conducting proteins, the prevailing dogma is that they are not resolved by SEM due to charge accumulation effects. For these reasons, comparable SEM images to the present work are rare. Tolba et. al. used SEM to prove oriented immobilization of T4 phages, but the extended tails that are characteristic of myoviruses were not present in the images.[263] Our work showed that high-resolution imaging of surface immobilized phages is feasible, even permitting the observation of the myovirus baseplate. Furthermore, this method can be used to prepare multiscale imagery showing the immobilized phage layer *in situ* on the functionalized substrate.

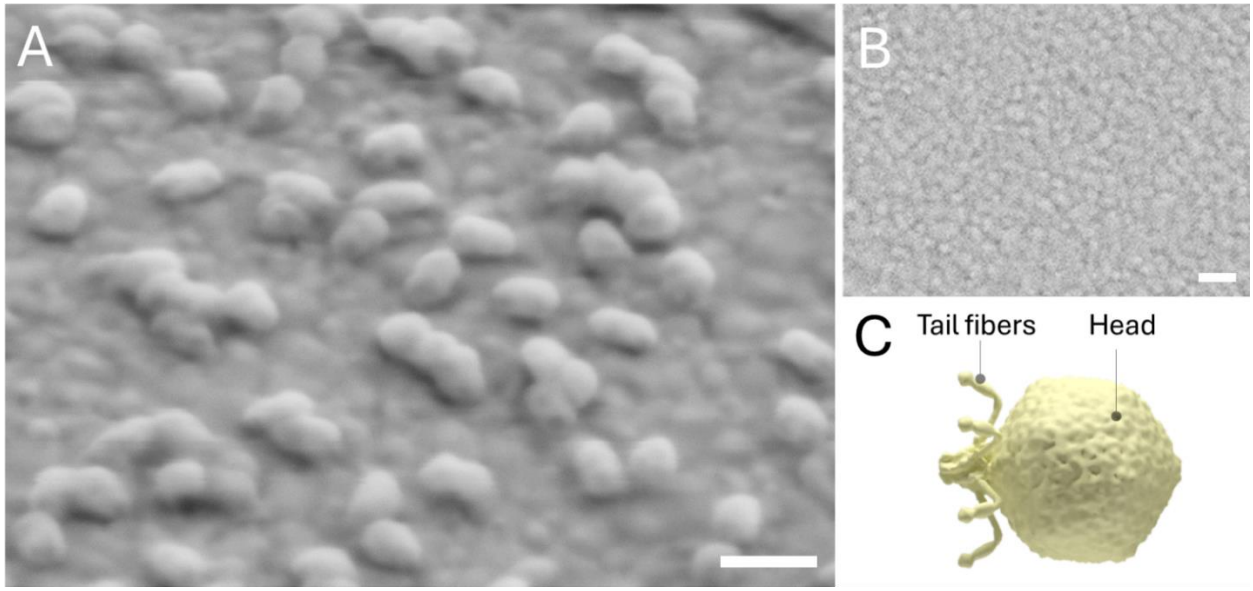

Figure 4.5 A: Scanning electron micrograph of bacteriophage gh-1, purified by density gradient ultracentrifugation and immobilized in this region with a density of 119.8 ±6.1 phage/μm^2 on a gold substrate via a self-assembled monolayer of 11-mercaptoundecanoic acid.B: Inset shows a reference surface without phage. C: Shows an illustration of the morphology of a generic podovirus based on structures of the T7 head and tail complexes as resolved by cryo-electron microscopy.[408,409] Scale bars indicate 100 nm.

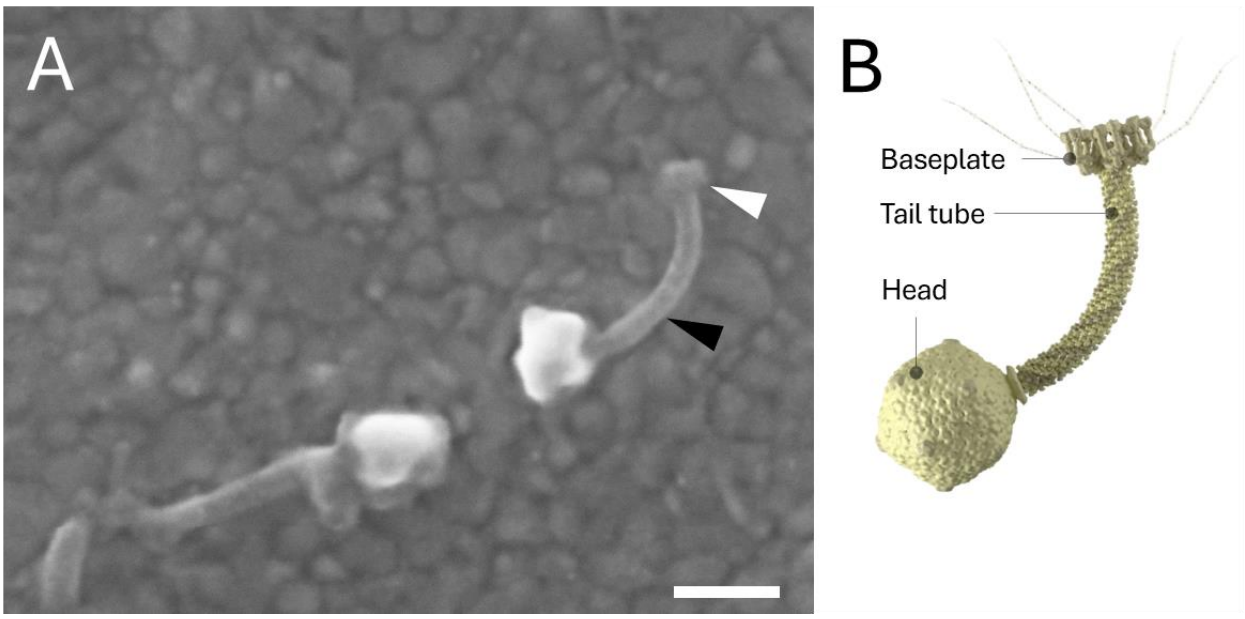

Figure 4.6 A: High-resolution scanning electron micrograph of two Remus bacteriophages of the myoviridae family, immobilized via DTSP cross-linker to a gold substrate.The baseplate (white arrow) and tail tube (black arrow) are clearly visible. The tail tube is approximately 23 nm in diameter. B: An illustration of a generic myovirus assembled from protein various protein structures.[410–412] Scale bar indicates 100 nm.

4.3.4 Overviewing chemical routes for phage immobilization and phage surface densities

Considering the phage surface densities achieved in this work, a brief comparison with the literature is warranted, although a full treatment of the topic of phage immobilization strategies can be found elsewhere.[133] **Figure 4.7** collects the results and immobilization methods published in the literature, which demonstrated phage functionalization while also specifying the phage titer used to functionalize the surface together with the final surface density achieved. Comparing outcomes in this way, the phage densities attained in our work places our protocol among the most performant in the literature (note the log scale of phage surface density in **Figure 4.7**). Additionally, the importance of high-titer suspensions is immediately clear, with increasing phage titer correlating with high density in the final immobilized layer. The optimal density of 19 phage/μm^2 observed by Naidoo *et al.* for bacterial capture by phage T4,[128] for example, can be seen to normally require a phage suspension of at least 10^{10} PFU/mL if not 10^{11} PFU/mL or higher, depending on immobilization strategy. In comparison, our method attained almost double this density — 34 ±3.4 phage/μm^2 — from a phage titer of only 6.1 ±0.4 × 10^9 PFU/mL in the case of P68.

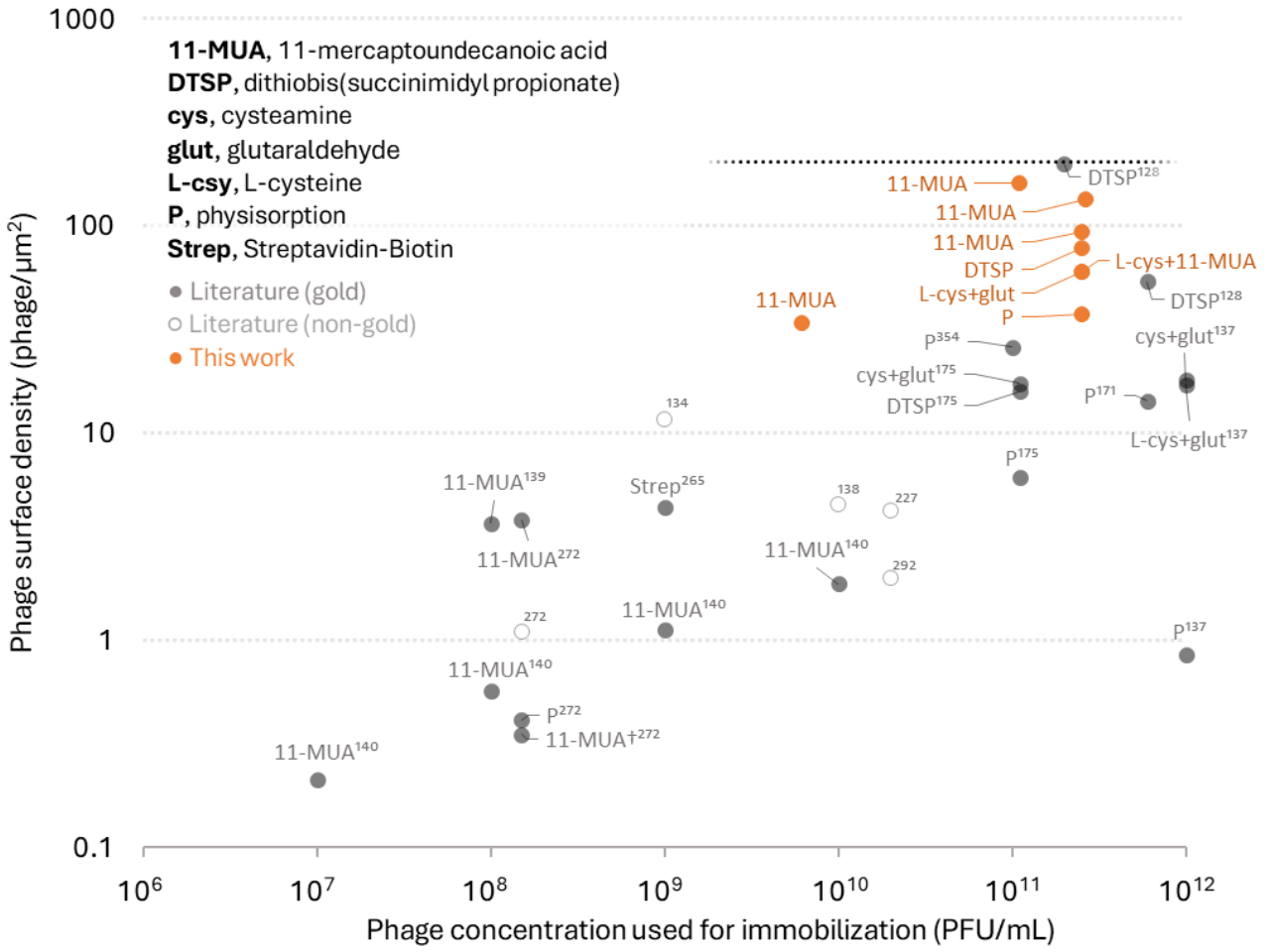

Figure 4.7 Semi-log scatter plot comparing the densities achieved in this work (orange) to values extracted from the literature. Superscripts indicate the article from which each datapoint is extracted. Dashed line indicates the theoretical maximum possible density for 75nm-diameter spheres (See Annex: Calculation of the Theoretical Limit to Bacteriophage Packing in a 2D Plane).
† Indicates that activation of carboxyl groups with EDC/NHS was omitted.

In many papers, physisorption is shown to result in poor densities of immobilized phage for a given concentration of phages incubated with a gold surface. This trend was replicated in our own observations, where physisorption yielded the lowest surface density regardless of phage and purification method. Moreover, physisorption was observed to bind contaminants with a higher surface coverage than other immobilization methods. In our work, as in others, self-assembled monolayers of thiolated molecules DTSP and 11-MUA yield the highest surface densities of any immobilization technique.

As demonstrated above — and highlighted previously by other authors[130] — the phage purification protocol that precedes immobilization can have an outsized effect on the density, homogeneity, and quality of the immobilized layer. This is revealed when we correlate the final surface densities that result from the most common and/or performant purification protocols used in the literature: ultracentrifugation, PEG precipitation, filtration, and chromatography (See annex **Figure A.1**).

When DGU is incorporated into the purification protocol, higher surface densities are achieved, although rarely above 20 phage/µm^2. When DGU and chromatography have been combined, higher densities have been claimed (199 ±2 phage/µm^2), although such values were calculated from SEM imagery that was insufficiently resolved to observe individual phage particles.[128] In our work, we achieved comparable densities to the highest demonstrated in the literature (between 34-160 phage/µm^2), confirmed by high-resolution microscopy, and

without the use of size-exclusion chromatography. We attribute the success of our own technique to the inclusion of a final ultrafiltration step. While size-exclusion chromatography allows separation of phages from smaller MW contaminants that elute more slowly,[128] ultrafiltration similarly removes smaller MW contaminants while preserving phages in the retentate. While it is important to remove contaminants of the same or larger length scale as phage, we posit that the improvements seen with both size-exclusion chromatography and ultrafiltration are due to the removal of the smallest MW components of the crude phage lysate.

The PEG/DGU/UF/11-MUA protocol presented in this work, combining the removal of small MW contaminants with the binding performance of a thiolated SAM, potentially presents the advantage of requiring less volume of parent phage stock to functionalize a given surface area of substrate. Or, conversely, this protocol may allow immobilization of phages that prove difficult to amplify to a titer high enough to be immobilized with other methods.

Among the various phage purification methods, ultracentrifugation in particular requires a significant up-front capital investment in equipment as well as maintenance. Following DGU with a relatively inexpensive ultrafiltration step may permit substantial savings of high-purity phage stock that can be costly to produce.

While Naidoo *et al.* proposed the existence of a "jamming" surface density of T4 phages beyond which bacterial capture is inhibited,[128] certain applications may benefit from immobilizing phages at the highest possible density. For example, in the case of a biosensing layer of immobilized biosensing phages with engineered tropism towards analytes other than bacteria, the optimal density may indeed be much higher than such a jamming density.

A hexagonally close-packed array of spheres in two dimensions yields a packing efficiency (*i.e.*, surface coverage) of 91%.[413] From a purely geometric standpoint, assuming 75 nm-diameter spherical particles (the same diameter as the icosahedral capsids of 44AHJD and Remus[407]), ideal close packing would result in a theoretical maximum surface monolayer density of 205 phage/μm^2 (See Annex: Calculation of the Theoretical Limit to Bacteriophage Packing in a 2D Plane). In reality, many factors — such as non-spherical morphology, random orientation, interparticle forces etc. — reduce the effective maximum attainable density of a phage monolayer. This approximate calculation is informative however, serving to contextualize the performance of immobilization strategies relative to a theoretical limit. As shown in this work, we have approached this geometric limit with a density of 160 ±13.9 44AHJD phage/μm^2.

4.4 Conclusion

In this work we compared physisorption and different covalent methods for immobilization of phages 44AHJD, P68, Remus, and gh-1 on planar gold. High surface densities were confirmed by scanning electron microscopy. Upstream purification of bacteriophages was demonstrated to have a profound effect on density of the immobilized layer, with PEG-precipitation-purified suspensions yielding 0-11.5 phage/μm^2 but higher densities of 34-160 phage/μm^2 achieved when PEG-precipitation was combined with ultracentrifugation and ultrafiltration. Such a high density is close to the theoretical geometric limit.

Phage density is not the sole criterion by which we should judge the quality of the immobilized layer, and different levels of contaminants were observed on the surface depending on strategy, with physisorption in particular exhibiting a high density of adsorbed contaminants.

A self-assembled monolayer of 11-MUA performed the best of all strategies despite requiring an additional activation step by EDC/NHS compared to DTSP. Glutaraldehyde was found to significantly modify the wettability of the surface, which could make it unsuitable if one is hoping to confine ligands to a small region on the substrate (*e.g.*, protein microarray). Inclusion of the ultrasound lysate supported the conclusion that virus-like particles observed on the surface were indeed phages (See Annex: A7 Observed Bacteriophage

Morphology **Figure A.10**), and we propose that inclusion of a similar control may prove useful in validation of phage functionalization protocols. Scanning electron microscopy was demonstrated to offer sufficient resolution to observe immobilized phage layers, with oblique imaging and use of an in-lens detector found to improve contrast and permit direct counting of phages on the surface and resolution of phage sub-structures.

In conclusion, a bacteriophage-functionalized gold layer can easily approach the geometric limits of surface density when cross-linked to the surface with 11-MUA if special consideration is paid to upstream purification of the phage suspensions. As we confront an uncertain future with increasingly widespread antimicrobial resistance in the coming decades, bacteriophages represent a promising and versatile tool with which to confront these challenges. Well-characterized and repeatable production of phage-functionalized substrates will only prove increasingly relevant.

Chapter 5

Container Material Dictates Stability of Bacteriophage Suspensions: Light Scattering & Infectivity Measurements Reveal Mechanisms of Infectious Titer Decay

Published article in Journal of Applied Microbiology (2022)
DOI: 10.1111/jam.15581

Larry O'Connell[1,2], Yoann Roupioz[2], Pierre R. Marcoux[1]

[1] Univ. Grenoble Alpes, CEA, LETI, F-38054 Grenoble, France

[2] Univ. Grenoble Alpes, CNRS, CEA, IRIG, SyMMES, F-38000 Grenoble, France

Keywords: Bacteriophage, colloidal stability, aggregation, virus adsorption, nanoparticle tracking analysis, infectious titer, phage stability, plaque counting

Abstract

Aims: To measure the infectious titer (IT) decay rate for various bacteriophages as a function of storage container material. Additionally, parallel light scattering and infectious titer measurements reveal distinct mechanisms for IT loss, depending on phage.

Methods and Results: Suspensions of bacteriophages 44AHJD, P68, and gh-1 were stored in various labware. IT of each suspension was repeatedly measured over the course of two weeks. Large variability in IT decay was observed, with >4 log10 loss in glass and low-binding polypropylene. Incubation of polymer containers with Bovine Serum Albumin (BSA) resulted in a consistent reduction in IT decay. Aggregation state of phage suspensions was studied by nanoparticle tracking analysis (NTA), revealing highest aggregation in glass-stored suspensions and lowest after storage in BSA-treated containers.

Conclusions: Glass and "low-binding" containers may aggravate IT decay while BSA treatment may present an easy mitigation strategy. IT vs. NTA titer diagrams highlight the importance of phage inactivation in combination with aggregation.

Significance and Impact of the Study: Container material is a significant determinant of bacteriophage IT decay. It is therefore essential to confirm IT following storage and tailor choice of phage storage containers accordingly. Aggregation of phages and adsorption onto labware surfaces are not the only mechanisms accounting for IT loss, but also biological instability.

5.1 Introduction

Bacteriophages (phages) have been employed in a remarkable variety of applications[133] including *in vivo* treatment of pathogenic bacteria[89], as a vaccine vector[414], and as surrogates for the study of eukaryotic viruses in water remediation facilities[256,415] and SARS-CoV-2 survival in microdroplets[416]. In each of these contexts it is essential to understand any changes in particle size and concentration that may occur; be it through aggregation, inactivation, adsorption onto labware surfaces, or some other effect that causes an evolution of the measured infectious titer. This is especially true in a clinical context involving preparation and administration of phage preparations, since regulatory agencies standardize therapeutic doses based on the number concentration of phage ml^{-1} of such suspensions. So-called magistral preparations can have infectious titer on the order of 10^{10}-10^{12} PFU ml^{-1}[417], before being diluted to 10^5 – 10^7 PFU ml^{-1} for administration to a patient[64,418,419].

Infectious titer (IT) is measured through the observation and counting of lysis plaques in a host bacterial lawn in soft agar[420]. IT decay during storage or processing can have profound effects on downstream applications if the reduction is not mitigated or compensated for. In a published clinical trial, a failure to take into account a decay of infectious titer of phage suspensions resulted in patients receiving a dose of 10^2-10^3 PFU ml^{-1} instead of the intended 10^6 PFU ml^{-1}, due to an unanticipated 3 $\log_{10}$ drop in IT of phage preparations over the course of 15 days in storage[64]. In wastewater remediation, over-estimation of the viral elimination capability of water purification processes may result from reduction in infectious titer and/or aggregation of phage which inadvertently increases filtration performance[256]. In survival studies of SARS-CoV-2 virus in respiratory droplets, aggregation of bacteriophage (employed as surrogate viral particles) is recognized as a potential confounding factor for interpretation of survival estimates[416].

Recently, it was revealed that exposure to common labware can lead to a drastic reduction of bacteriophage infectious titer on timescales ranging from days to mere hours[205]. Three mechanisms can cause the observed IT losses: adsorption onto labware surfaces, virion aggregation in the aqueous phase, and finally virus inactivation. These phenomena have important implications, not only for future phage research, but also in retrospect when considering findings of past publications that may have failed to control for such an effect. As a result, there is now interest in treatment of container surfaces[421] and optimization of phage buffer composition[422] to mitigate loss of infectious titer.

The present work explores the phenomenon of phage infectious titer loss in common glass and polymer labware, extending the investigation to three new phages that have not been previously investigated. Furthermore, in addition to standard counting of lysis plaques, light scattering analysis of virus suspensions was performed. Nanoparticle tracking analysis (NTA) reveals the aggregation state of phage suspensions as a function of storage container material and was compared to changes in infectious titer as measured by the drop cast method[423]. Finally, pre-incubation of container surfaces with amphiphilic protein bovine serum albumin (BSA) is demonstrated as a simple and effective method for significantly reducing IT loss. Scanning electron microscopy was performed on container surfaces in order to assess the level of phage surface adsorption.

5.2 Materials and methods

5.2.1 Host bacterium and bacteriophage preparation

Bacterial hosts *Staphylococcus aureus* subsp. *aureus* Rosenbach (ATCC 43300; host of phage 44AHJD) and *Staphylococcus aureus* (ATCC BAA-2312; host of phage P68) were obtained from Microbiologics (Kwik-Stik™ lyophilized strains). *Pseudomonas putida* (ATCC 12633; host of phage gh-1), phages 44AHJD[405], P68, and gh-1[195] were obtained from the *Félix d'Hérelle Reference Center for Bacterial Viruses* of the Université Laval, Quebec, Canada. All three phages used in this work are lytic, non-enveloped members of the *Podoviridae* family. Electron microscopy has indicated a 75 nm icosahedral head for both 44AHJD and P68 with a short, non-contractile tail of ~27 nm in length for 44AHJD and ~40 nm in length for P68.[407] Phage gh-1 features a 50 nm icosahedral head with a ~10 nm tail.[195]

Bacterial cultures were routinely prepared in recommended media. *S. aureus* ATCC 43300 was cultured in Soybean Casein Digest Broth TSB (Sigma-Aldrich, Saint Quentin Fallavier, France) at 37 °C; *S. aureus* ATCC BAA-2312 in ATCC Medium 3 (See Solutions) at 37 °C; *Pseudomonas putida* in ATCC Medium 18 at 30 °C.

Bacteriophage suspensions were routinely prepared using the soft overlay agar method[99]. 100 µl of overnight liquid precultures of each bacterial host were inoculated into fresh medium and allowed to proliferate until reaching 10^8 CFU ml^{-1} as confirmed by optical density at 550 nm. Then, 200 µl bacterial host and 100 µl bacteriophage suspension (5×10^4 PFU ml^{-1} for 44AHJD, 5×10^3 PFU ml^{-1} for P69 and gh-1) were inoculated into 15 ml falcon tubes filled with 5 ml molten agar (TSB prepared with 7.5 g l^{-1} agar (Sigma-Aldrich, Saint Quentin Fallavier, France)) at 51.5 °C, vortexed, and poured over 20 ml solidified tryptic soy agar (TSA, 15 g l^{-1} agar) in a standard 90 mm petri plate (VWR, France). Plates were then incubated overnight until lysis plaques became confluent in the top agar layer, which was then collected and soaked for 4 h at room temperature in sterile 154 mmol l^{-1} NaCl solution (OTEC, VWR) in a 50 ml polypropylene tube. Each tube was then twice centrifuged for 20 min 5500 *g* at 4 °C and the supernatant retained each time.

Each suspension was brought to 0.5 mol l^{-1} NaCl and 8% w/v polyethylene glycol 6 kDa (Merck, Darmstadt, Germany) and left at 4 °C overnight. The following day, each suspension was centrifuged for 30 min at 12108 *g* at 4 °C, the supernatant removed, and the pellet resuspended in sterile 154 mmol l^{-1} NaCl, vortexed, centrifuged 20 min 5500 *g* at 4 °C and the supernatant retained.

Deionized water (>18 MΩ resistivity) was obtained from an ELGA PURELAB flex dispenser (Veolia Water, France). Phage suspensions were then purified by ultracentrifugation for 2 h at 100,000 *g* at 4 °C on a CsCl (VWR) step gradient (1.7 g ml^{-1}, 1.54 g ml^{-1}, and 1.34 g ml^{-1} CsCl in deionized water) in 5 ml, Open-Top Thinwall Ultra-Clear ultracentrifuge tubes (Beckman Coulter, Villepinte, France) in a SW55Ti swinging-bucket rotor (Beckman Coulter) mounted in an Optima l-90K Ultracentrifuge (Beckman Coulter). Bacteriophages were concentrated at the second visible band from the top and collected with a micropipette. CsCl was removed from phage suspensions by repeated ultrafiltration and resuspension in 154 mmol l^{-1} NaCl using 100 kDa Vivaspin 500 ultrafiltration units (Sartorius).

5.2.2 Container preparation

Sterile 10% w/v BSA stock solution was prepared by dissolving 100 mg BSA (Sigma-Aldrich, Saint Quentin Fallavier, France) in 10 ml 154 mmol l^{-1} NaCl solution followed by filter sterilization through a 0.2 µm syringe filter (Millipore, Cork, Ireland). This stock solution was diluted to 0.1% w/v BSA before use.

Clear 2 ml borosilicate glass vials (Wheaton, Dutcher. Reference 048398) were autoclaved six days before use and stored in a sterile hood at room temperature. These tubes were chosen due to their low levels of extractables and low potential for leaching of contaminants into the phage suspension. 1.5 ml polypropylene

(PP) tubes (Eppendorf, VWR) were autoclaved >48 h before use. 1.5 ml low protein-binding polypropylene (PP LoBind) tubes (Protein LoBind, Eppendorf, VWR) were autoclaved >48 h before use. Sterile 15 ml polystyrene (PS) tubes (Falcon, UGAP, France. Reference 2515477) were used without any prior treatment. To produce BSA-treated containers, 1.5 ml polypropylene tubes (autoclaved >48 h before use) and 15 ml polystyrene tubes were incubated upright overnight at 4 °C with 0.1 % BSA solution. The following morning, all tubes were inverted to coat the upper interior surface for a further 6 h. PP+BSA and PS+BSA tubes were then emptied and rinsed thoroughly with 154 mmol l^{-1} NaCl and emptied shortly before addition of phage suspensions.

5.2.3 Serial dilution of phage suspensions

For each container type, each of the three phage suspensions were serially ten-fold diluted ten times, producing 10^{-1} to 10^{-10} dilutions. For suspensions stored in glass, PP, and PP+BSA containers: suspensions were diluted 100 µl in 900 µl 154 mmol l^{-1} NaCl. For suspensions stored in 15 ml PS and PS+BSA containers: suspensions were diluted 1 ml in 9 ml 154 mmol l^{-1} NaCl due to the larger tube size.

5.2.4 Phage titer enumeration

Infectious titer was measured using the drop cast method: a bacterial lawn was prepared by inoculating 200 µl of an overnight liquid preculture of each bacteriophage's respective host into 5 ml of molten agar at 51.5 °C (tryptic soy broth containing 7.5 g l^{-1} agar) and then poured over 20 ml solid TSA (15 g l^{-1} agar) in a standard petri dish. Once the bacterial agar layer cooled and solidified for a few minutes, 10 µl drops of each phage dilution were placed on the bacteria-inoculated agar layer. The droplets are allowed to dry before incubating the plates at the appropriate temperature for each host. Phage lysis plaques were then counted manually after a few hours and then a second time the following day. This two-step counting is performed since lysis plaques can overlap with each other and become indistinguishable if left for too long while counting too early results in late-starting plaques being missed. All phages used in this work produced well-defined, clear plaques, which facilitated counting. Phage suspensions were titered at the following timepoints: after 5 min (*i.e.*, immediately after the initial dilution), 24 h, 48 h, 1 week, and 2 weeks.

Since it has been demonstrated that agitation of phage suspensions can have a strong effect on titer decay[424,425], care was taken to vortex all tubes an identical duration of only 5 seconds prior to plating. All tubes were stored upright in the dark at 4 °C in between measurements. A correction factor was applied to the observed count of lysis plaques to compensate for overlap bias[426,427] (See Annex: Calculation of Experimental Uncertainty in Plaque-counting Experiments).

5.2.5 Nanoparticle tracking analysis

Nanoparticle tracking analysis (NTA) was carried out using a Nanosight NS300 (Malvern Pananalytical Ltd., Malvern, United Kingdom) fitted with a 488 nm laser module and a sCMOS detector. Samples were diluted with 154 mmol l^{-1} NaCl to produce suspensions of 10^{8}-10^{9} particles ml^{-1}, and the dilution factor noted. Each sample was injected by syringe pump into the analysis chamber and measured five times with each measurement lasting 60 s, according to the manufacturer's protocol. All suspensions were analysed with a consistent camera level of 16 and detection threshold of 10. Preliminary data processing was performed using NTA Analytical software (v3.4.4). Violin plots were produced using the violins.m function[428] in MatLab R2021a (v9.10). This data representation presents smoothed vertical histograms of size spectra, each inset with a box-and-whisker plot displaying the median, lower and upper quartiles, and the minimum and maximum of the distribution[429].

5.2.6 Contact angle measurements

Contact angle measurements were performed on replicates of all containers using a GBX Digidrop (Tallaght, Ireland). Replicates of all containers were freshly prepared precisely as before, dried with compressed air, broken into small sections, placed on the Digidrop stage, and had 1.5 µl deionized water dispensed on the

surface with a micropipette. All contact angle images were analysed using the Contact Angle plugin implemented in the FIJI distribution of ImageJ v1.53c[430].

5.2.7 SEM

Scanning electron microscopy (SEM) was performed on a selection of containers. Each container was cut open to expose the interior surface. In order to avoid charging effects during imaging, a ~4 nm layer of carbon was deposited on the tube interiors using a Safematic CCU-010 HV compact coating unit (Zizers, Switzerland), at 3×10^{-5} mBar, with the sample mounted at stage height 6. The surface was observed in a Zeiss ultra 55 scanning electron microscope under a 2 kV acceleration voltage and 4-10 mm working distance.

5.2.8 Statistical Analysis

A separate Kruskal-Wallis H test was performed for each phage to determine if storage container had an influence on proportion of infectious titer remaining after 14 days of storage.

5.3 Results

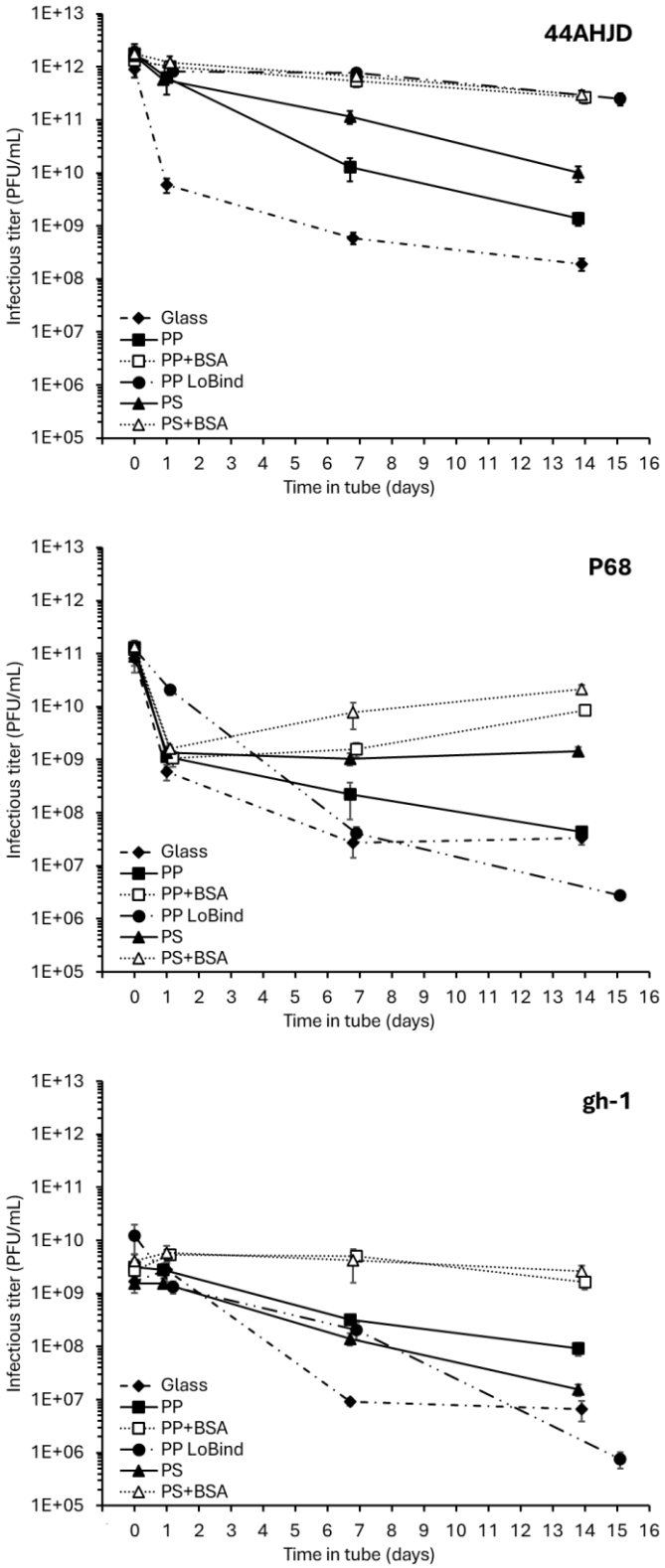

Figure 5.1 Semi-log plots of decay of infectious titer for bacteriophages 44AHJD (top), P68 (center), and gh-1 (bottom); after storage for various durations at 4 °C in glass (◆), polypropylene (■), BSA-treated polypropylene (□), low-binding polypropylene (●), polystyrene (▲), and BSA-treated polystyrene (△) containers.For clarity, the infectious titer at day 2 is not shown, but can be found in the Annex in **Table A.6**.

As purified bacteriophage suspensions are routinely processed and stored from days to months in polymer and glass labware before use, infectious titers of highly purified phage preparations were measured in this work at intervals over the course of two weeks, revealing a time-dependency of infectious titer decay as a function of container material. Glass, polystyrene, polypropylene, and low-binding polypropylene were studied, since use of these materials is common practise in microbiology labs worldwide. All phage suspensions were constituted with pyrogen-free, 0.2 µm-filtered, sterile saline (0.9% w/v NaCl solution (OTEC, VWR)). Addition to the buffer of tris and divalent cations was avoided in order to render the results more universally applicable, considering the variety of phage buffers commonly used in microbiology labs. Furthermore, phage stability exhibits large variation depending on solution composition[422]. Addition of PEG or other protectants was avoided in order to isolate the effects of container surface interaction with the three phages studied.

A dramatic drop in infectious titer was observed for all three phages stored in almost all containers except those treated with BSA (**Figure 5.1**). These results are summarized in Table S1. Storage in glass vials results in significant loss of infectious titer for all three phage: 3.67 $\log_{10}$ loss of 44AHJD, 3.4 $\log_{10}$ loss of P68 and 2.4 $\log_{10}$ loss of gh-1. Titer decay progresses very quickly for phages 44AHJD and P68, but in the case of gh-1 remains comparatively stable for the first two days before showing similar exponential decay. Storage in PP resulted in over 3.11 $\log_{10}$ loss of 44AHJD and 3.47 $\log_{10}$ loss of P68 but resulted in less dramatic loss of 1.54 $\log_{10}$ of gh-1. Incubation of PP with BSA improved retention relative to untreated PP by between 1.31 and 2.40 $\log_{10}$, depending on phage. Low protein-binding PP tubes, marketed under the name 'Protein LoBind', resulted in dramatically different IT decay depending on phage, with only 0.8 $\log_{10}$ loss of 44AHJD, but 4.65 $\log_{10}$ loss of P68 and 4.22 $\log_{10}$ loss of gh-1. In the latter case of P68 and gh-1, PP LoBind resulted in the most significant loss of all containers tested. PS resulted in less loss than PP for 44AHJD and P68 but was worse than PP when used to store gh-1. Similar to the result obtained with PP, incubation of PS with BSA appears to improve retention by between 1 and 1.8 $\log_{10}$ relative to untreated PS. The IT of 44AHJD decreased significantly more slowly in containers other than glass, where very rapid decay was observed. In the case of P68, IT drops homogenously and most rapidly in glass, PS and BSA-treated containers in the first two days before stabilizing. However, the titer of P68 stored in PP and PP LoBind did not stabilize, even after two weeks of storage. In contrast, the IT of gh-1 evolves more slowly than P68 but comparably to 44AHJD. In PP and PS treated with BSA, the titer remained stable at approximately the initial titer (less than 0.22 $\log_{10}$ loss) for the duration of the experiment. After an initial loss of IT, by day 14 phage P68 exhibited a rebound of 1.13 $\log_{10}$ in PS+BSA and 0.9 $\log_{10}$ PP+BSA compared to their value after one day in storage.

The Kruskal-Wallis H test revealed that the resulting infectious titer loss was statistically different, depending on the storage container, with H= 47.5, 33.1, and 33.1 for 44AHJD, P68, and gh-1, respectively; the p-value was less than 0.001 for all three phages.

Infectious titer determination for three separate phages in six different containers involves a significant overhead in terms of both laboratory waste and manual counting to be performed. Despite the economies afforded by the drop-cast method used[423] over the double layer agar method[99], approximately 15,000 individual plaques were counted from 2,500 individual drop cast assays. In order to limit the waste produced and increase the statistical significance of the results of plaque counting experiments, a strategic guess was made at each timepoint regarding the likely infectious titer, and in most cases three or four dilutions were plated rather than the full set of ten serial dilutions. For example, the 10^{-1} to 10^{-4} dilutions contain far too many plaques to be countable, and the higher dilutions from 10^{-9} to 10^{-10} were too dilute for P68 and gh-1 to produce even a single lysis plaque. Plating more replicates of a selection of dilutions permitted 16 drop cast assays in each petri dish, typically with between four and six replicates of each dilution per dish.

Following observation of IT loss in plaque counting experiments, it was hypothesized that this loss could be due to some combination of inactivation, aggregation, and/or adsorption on the container walls. In order to

compare the infectious titer with the aggregation state and particle concentrations of phage suspensions following storage, particle size distributions were produced by nanoparticle tracking analysis (NTA). NTA involves the tracking of individual nanoparticles in order to analyse their Brownian motion and evaluate their volume concentration[431]. From the observed motion of the particles, the diffusion coefficient and hence hydrodynamic radius can be inferred. NTA was performed at the end of the experimental sequence for all three phages in all six container types (18 suspensions total, **Figure 5.2**). NTA produced size distributions that indicate a very high level of aggregation of 44AHJD and P68 suspensions stored in glass, and intermediate aggregation of P68 and gh-1 in PP LoBind containers, as indicated by heavily skewed distributions and large increases in the mean and median particle size relative to other containers (**Figure 5.2**). BSA-treatment of PP and PS containers yields distributions with consistently smaller particle size for all phages except 44AHJD in PP+BSA, where moderate broadening of the distribution was observed. Suspensions of gh-1 stored in PP and PP+BSA showed the highest monodispersity of all samples. Infectious titer of gh-1 stored in PS was too low for NTA measurement, which requires at least 10^7 particles ml^{-1}. Plotting 90^{th} percentile particle diameter (P_{90}) against infectious titer loss after two weeks in storage (**Figure 5.3**), a correlation between aggregation and IT loss is revealed — driven particularly by glass containers — with a power law fit yielding an R^2 value of 74 %. However, inclusion of total particle concentration paints a more intricate picture of IT loss.

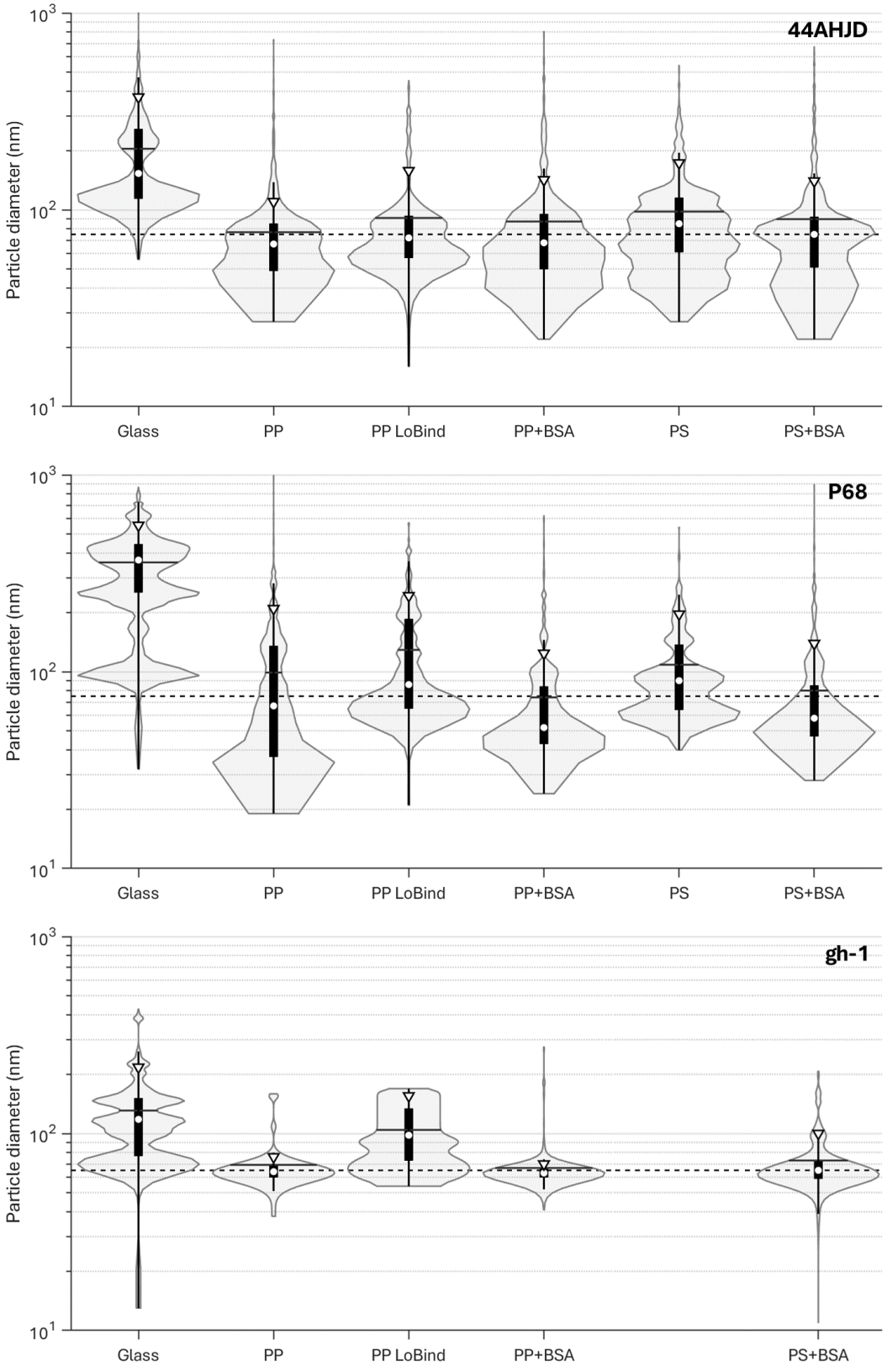

Figure 5.2 Semi-log violin plots of particle size distributions obtained by nanoparticle tracking analysis (NTA) of suspensions of 44AHJD (top), P68 (centre), and gh-1 (bottom); following two weeks of storage in each container.The width of each plot indicates the relative proportion of particles of that diameter within each distribution respectively. The median (○), mean (solid horizontal bars), and P_{90} (▽) are indicated in each distribution. Dashed horizontal line indicates the capsid diameters as determined for 44AHJD and P68 by Vybiral *et al.* (2003); and for gh-1 by transmission electron microscopy.

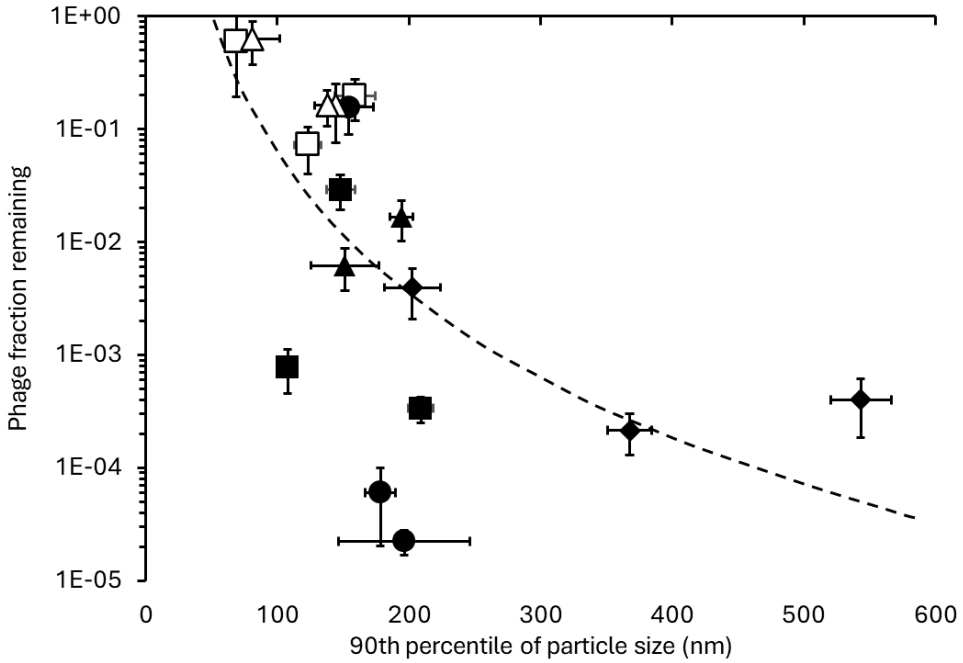

Figure 5.3 Semi-log scatter plot of 90th percentile of particle diameter (as observed by nanoparticle tracking analysis) vs. remaining fraction of initial infectious titer (as measured by plaque counting) after storage for two weeks in glass (◆), polypropylene (■), BSA-treated polypropylene (□), low-binding polypropylene (●), polystyrene (▲), and BSA-treated polystyrene (△) containers.A power law fit (R^2=74%) is indicated with a dashed line.

A distinction must be made between infectious titer and the concentration of viral particles in a phage suspension. The infectious titer is a measure of the presumed viral load of a parent suspension, as calculated from the observed count of lysis plaques produced in plaque-counting methods, together with the dilution factor of the plated sample. Plaque-counting methods are incapable of detecting empty phages or distinguishing between a single phage and aggregates of multiple phage particles. In contrast, nanoparticle tracking analysis reveals the hydrodynamic radius and optical scattering properties of individual particles, with little discrimination between viable phages, empty phages, phage aggregates, or contaminants.

In this work, both adsorption, aggregation, and inactivation are likely to occur in parallel, with the balance between these phenomena varying based on container material. We propose a model by which tandem plaque counting and NTA measurements can be interpreted to reveal the nature of infectious titer loss, as shown in **Figure 5.4**. Depending on three variables — infectious titer (PFU ml^{-1}), particle concentration (PC; particles ml^{-1}), and aggregation state (P_{90})— we can make inferences about the causes of IT decay. Log_{10} discrepancies in the ratio of infectious titer to total particle concentration are shown by diagonal contours. For example, a datapoint at the 10^{-3} contour indicates a suspension in which a small minority of only one in 10^3 particles is infectious. Pure phage aggregation should result in the same number of lysis plaques being produced as the number of particles detected in NTA, since each particle aggregate will initiate a single lysis plaque despite being composed of multiple phage particles. Such aggregation — in the absence of phage inactivation — produces a data point along the identity line in the PC/IT plots of **Figure 5.4**. Phage adsorption to container walls will similarly yield a datapoint along the identity line since the ratio of infectious to total particles in the bulk remains the same. In order to disambiguate between adsorption and aggregation, we must consider the particle size distribution which is also measured by NTA. Datapoint diameters in **Figure 5.4** have been scaled to correspond to the 90th percentile particle diameter (P_{90}; nm) for each suspension. P_{90} is a

more reasonable proximal measure for phage aggregation than mean or median diameter, since this value takes into account the disproportionate contribution of large aggregates to titer loss (a single 500 nm aggregate could contain hundreds of phages). Datapoints near the identity line in **Figure 5.4** can be interpreted as indicating aggregation if they feature a large P_{90}, or adsorption if they feature a small P_{90}, since in both cases they result in a reduction of PC commensurate with reduction in IT. In contrast, pure phage inactivation manifests as a decrease in the infectious titer that is independent of the number of particles measured by NTA, since inactivated phages are still observable by NTA. Inactivation is thus indicated by vertically downward movement in the PC/IT plot.

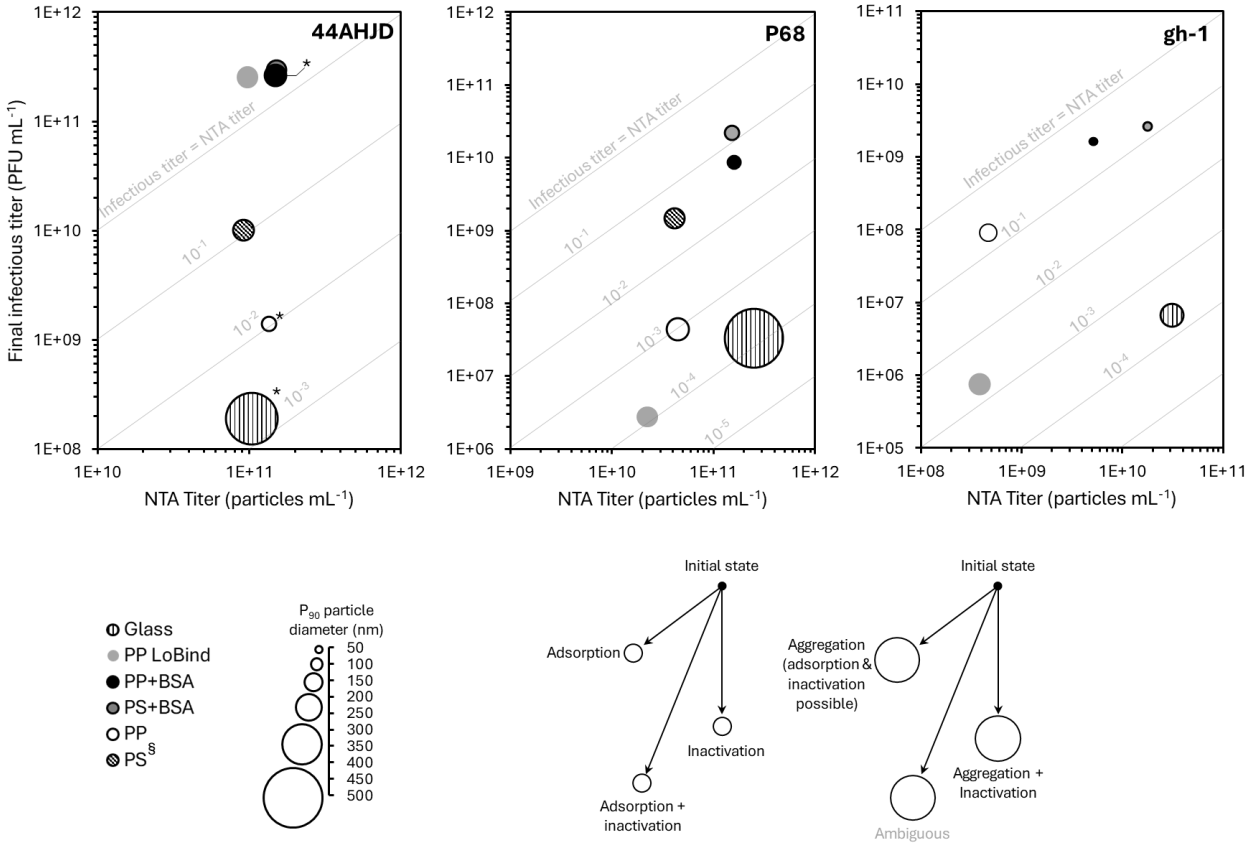

Figure 5.4 Log-log bubble plots of total particle concentration (x-axis; as measured by nanoparticle tracking analysis) vs. final infectious titer (y-axis; as measured by plaque counting) for all three phages after two weeks in storage in various containers.Datapoint diameters are scaled based on the 90th percentile of particle diameter (*i.e.*, P_{90}) for that suspension as observed by nanoparticle tracking analysis. Diagonal contour lines represent the ratio of concentration of total particles to infectious particles (*i.e.*, suspensions on the 10^{-n} contour feature one infectious particle for every 10^{n} particles). Infectious titers at t=0 were 8.9-18×10^{11} PFU/mL (44AHJD), 8.3-13.4×10^{11} PFU/mL (P68), and 1.35-12.5×10^{10} PFU/mL (gh-1).

§PS-stored gh-1 was too low titer for NTA analysis.
*Indicates containers that were also analyzed by SEM.

Finally, it should be pointed out that if the P_{90} increases significantly (indicating aggregation) then datapoints become ambiguous because of two effects. Firstly, aggregation will mask adsorption since both phenomena reduce the PC and IT proportionately (diagonal movement along contour). Secondly, aggregation will mask inactivation, since it is not possible to observe if a lysis plaque is initiated by a single phage or multiple phages within an aggregate. For this reason, there remains some ambiguity in the contribution of inactivation and

adsorption when large P_{90} datapoints occur, which necessitates analysis by other means (*e.g.,* SEM of container surfaces to ascertain level of adsorption).

The PC/IT plot for 44AHJD shows an almost vertical alignment of data points for all containers, with low levels of aggregation for all containers except glass. The close lateral clustering of all 44AHJD datapoints around ~10^{11} particles mL^{-1} suggests that IT loss was mainly driven by inactivation in polymer containers, with the exception of glass containers where a large P_{90} value indicated a strong contribution of aggregation in glass. Adsorption appeared to be less of a driver of IT loss of 44AHJD compared to other phages, which is consistent with the existence of a saturation density on the container surface[205] that is quickly satisfied for 44AHJD which was the highest-titer suspension. Finally, blocking PP and PS surfaces with BSA resulted in datapoints nearest the top right of the PC/IT plot for 44AHJD, indicating a reduction of both inactivation and adsorption, consistent with a blocking of interaction with the polymer surface by a BSA adlayer.

In contrast, several insights allow us to infer that a combination of adsorption and inactivation dominated during storage of P68 and gh-1 in polymer (PP, PS, and PP LoBind) containers. Firstly, pure adsorption results in datapoints along the identity line of the PC/IT plot, which is what was observed for gh-1 stored in PP.

Movement towards the bottom-left of PC/IT plots — if not accompanied by an increase in P_{90} — indicates a combination of adsorption and inactivation, since the total particle number (both infective and not) is decreasing (diagonal movement along contour), and also the fraction of particles that are infective is decreasing (vertical downward movement). This combination of adsorption and inactivation was observed for P68 and gh-1 stored in PP LoBind.

As observed with 44AHJD suspensions, storage in glass appears to have a very different effect on P68 and gh-1 compared to storage in polymer containers. This is indicated by the position of glass-stored datapoints towards the right-hand side of PC/IT plots of gh-1 and P68. While a small P_{90} indicates inactivation of gh-1 in glass, a larger P_{90} indicates significant aggregation of P68.

While NTA analysis yielded peaks of 36-56 nm for 44AHJD and 32-62 nm for P68, respectively (**Figure 5.2**) both phages are quoted in the literature as having a 75 nm isometric head[407]. A possible explanation for this discrepancy is that the NTA software assumes a spherical particle in its calculation of the diameter[204]. Departure of phage geometry from an ideal sphere may account for the difference in diameter between the literature and observed in this work by NTA.

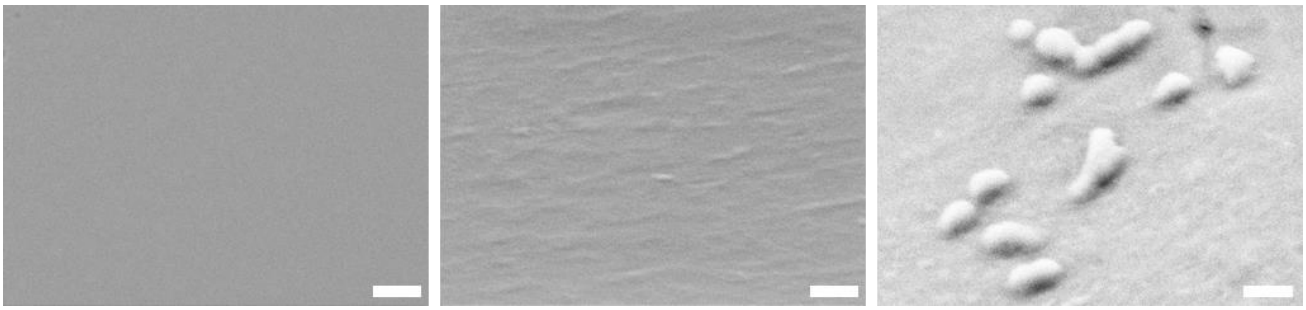

Figure 5.5 Scanning electron micrographs of glass container inner surface (left), polypropylene (centre), and BSA-treated polypropylene (right).Glass was overall much smoother than either bare or BSA-treated polypropylene. In comparison, bare polypropylene appears rougher, and BSA-treated surfaces were rougher still. Increasing surface roughness correlated with improved retention of infectious titer. Scale bars indicate 200 nm.

Following NTA measurements, it was hypothesized that glass was preferentially inducing both aggregation and inactivation, while PP was mainly leading to inactivation with some absorption, and PP+BSA was merely slightly adsorbing phage. In order to investigate the level of phage adsorption on container surfaces, SEM analysis was performed on the inner surfaces of glass, polypropylene, and BSA-treated polypropylene

containers that had been used to store phage 44AHJD (**Figure 5.5**). These surfaces were selected since analysis of all containers would be impractical, yet these three surfaces should elucidate the mechanisms underlying infectious titer loss and validate our interpretation of PC/IT plots. All glass and untreated PP surfaces observed were shown to be free of particles resembling phages. In the case of PP+BSA, however, adsorbed phage-like particles were observed with a density of 0.44 ± 0.08 phage μm^{-2}. The observed titer loss from the suspension stored in this container, if due entirely to adsorption, should result in phages present on the container walls with a surface density of between 0.1-2 phage μm^{-2}, which agrees with our interpretation of the PC/IT plots that IT loss of this suspension in this container is driven by absorption, since the data point is found near the identity line with a small P_{90} value. Increased surface roughness was observed on PP+BSA surfaces, intermediate roughness on PP, and very low roughness on glass.

Recent publications posited a correlation between wettability of labware material and modulation of stability of phage suspensions stored in them[205,421]. Richter *et al.* found that an increase in container surface contact angle resulted in a transition to instability above a threshold of 95°, which the authors propose as a heuristic to approximately judge suitability of labware for phage storage. In an attempt to replicate these results for the containers in this study, and furthermore to investigate if the same correlation holds for BSA-treated surfaces, contact angle measurements were carried out on identically prepared containers to those used to store phage suspensions. The results of water contact angle measurements are summarized in Table S2. Immobilization of BSA on the PP and PS layers is partly confirmed by the observed modification of the surface wetting properties of these surfaces relative to their untreated forms. Incubating PS and PP tubes with BSA overnight was shown to result in an increase in the hydrophilic character of these materials and thus a decrease in the contact angle in each case (decrease of -25.2° for PP and -35.4° for PS). Furthermore, BSA treatment seems to bring both the PP and PS hydrophilicity to a similar level, as evidenced by the fact that they exhibit more similar contact angles after treatment (difference of 4.8°), than beforehand (difference of 15°).

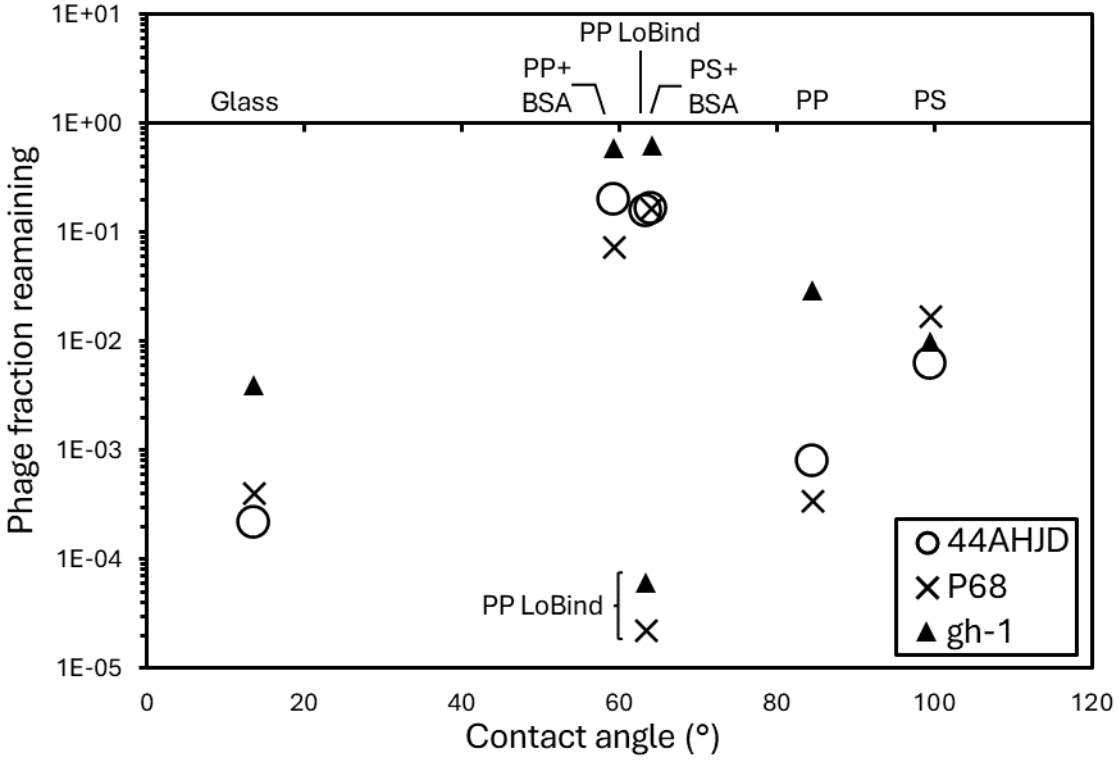

Figure 5.6 Semilog scatter plots of the fraction remaining of original infectious titer as a function of container contact angle after 14 days' storage at 4 °C of phages 44AHJD (○), P68 (×), and gh-1 (▲); in glass, polypropylene, BSA-treated polypropylene, low-binding polypropylene, polystyrene, and BSA-treated polystyrene.

Phage 44AHJD appears to show good stability for PP+BSA, PS+BSA, and PP LoBind —materials whose contact angles are clustered in the range (59.3-64.1°). 44AHJD was the only phage to experience an increase in stability when stored in PP LoBind. In comparison, P68 and gh-1 experienced over 3 $\log_{10}$ more IT loss in PP LoBind tubes. Plotting the contact angle against the drop in infectious titer, we see no clear correlation between contact angle and phage stability (**Figure 5.6**). We also see that BSA-treated surfaces result in a very similar level of titer decay, regardless of the underlying polymer. While PP containers result in significantly different levels of IT loss depending on phage, the loss in PP+BSA and PS+BSA is more clustered compared to all other containers.

5.4 Discussion

NTA and plaque counting form complementary, tandem measurements, which together reveal richer insights into the evolution of the phage suspension titer and aggregation state, compared to either technique alone. NTA yields individual particle information across statistically significant sample sizes[191] and has been demonstrated for the study of bacteriophage[192,193] and viral suspensions[190,194]. In contrast, dynamic light scattering (DLS) yields ensemble averages of diffusion coefficients (and extrapolated distributions of hydrodynamic radius). While DLS is an established technique for analysis of nanoparticle dispersions, it can struggle to give interpretable results for suspensions with significant polydispersity. NTA thus presents advantages over DLS in the study of bacteriophage suspensions, particularly in cases where aggregation is suspected, and yields more granular data.

A naïve interpretation of the drop cast plaque assay would show a simple reduction in infectious titer, obscuring the root cause. Complementing plaque counting measurements with NTA and SEM reveals that the causes of IT decay are manifold, with contributions from aggregation, inactivation, and adsorption depending on container material, with aggregation particularly severe in the case of glass containers. Storage in glass and PP LoBind containers resulted in the most dramatic reduction in IT, and in the case of glass correlated with a skew towards larger particle diameter. In the case of untreated PP, PS, and PP LoBind, the reduction in titer was not commensurate with increased aggregation and so is more likely attributable to inactivation of phages or adsorption on container walls. For instance, in the case of P68 in PP LoBind, only one particle in 10^4 is still infectious after two weeks, while P_{90} is low , highlighting the major role of inactivation. Our results demonstrate the value of NTA as a complementary measurement to traditional plaque assays to interrogate aggregation state of phage suspensions. Without such information, one is essentially "flying blind" when drawing conclusions from plaque counting methods, with regards to the nature of infectious titer loss.

Recent work by Richter *et al.* has shown that choice of container material is an important determinant of stability of bacteriophage suspensions in storage[205]. Inspired by this result, we attempted to replicate the same results with three phages of a different morphology. While Richter *et al.* observed a strong correlation between contact angle and titer loss, we have observed no clear correlation between contact angle and IT decay across a variety of container material and surface treatments. We observed dramatic titer loss in polypropylene containers, which has been shown to be a consistently unsuitable material with regards to phage stability[205,421,422]. Contrary to our expectations, substituting standard polypropylene with low protein-binding formulations exacerbated the problem, resulting in IT loss of 4.65 and 4.22 $\log_{10}$ loss of phages P68 and gh-1, respectively. In fact, IT in PP LoBind containers did not stabilize even by the end of the two-week experiment, and so IT loss is likely to progress further following storage for longer durations. In contrast, the observed retention of IT in the case of phage 44AHJD in PP LoBind containers indicates that choice of container material must be tailored to each phage and that contact angle is not a consistent determinant of phage

stability. We also observed significant and the most rapid IT loss in glass containers, in contradiction to previous research wherein storage in glass was observed to result in almost no detectable drop in infectious titer[205]. However, the work of Richter *et al.* examined only phage T4, a myovirus with very different morphology to the three podoviruses presented in this work, which could explain these divergent observations since phage morphology can be a determinant of stability[432]. Furthermore, our results replicate the findings of Lytle *et al.* who also demonstrated loss of IT following exposure to glass, although the authors were unable to reveal the nature of the observed IT loss.[432]

Instead of a correlation between contact angle and IT decay, we instead saw a correlation between surface roughness and IT loss, as detailed below. SEM analysis of container interior surfaces allowed us to investigate the role of surface adsorption in IT loss of phage 44AHJD in glass, PP and PP+BSA containers. The observed titer loss from the suspension, if due entirely to adsorption, should result in phage present on these container walls with a surface density of between 0.1-2 phage μm^{-2}. In the case of PP+BSA, adsorbed particles were indeed observed with a density of 0.44 ± 0.08 phage μm^{-2}, validating our interpretation of IT/PC plots as indicating that adsorption dominates in these containers. Particles resembling phage were not found on the surfaces of glass or PP containers, which implies that phage were either inhomogeneously deposited on the surface with a very high concentration in regions other than those observed by SEM, or that adsorption is not a significant contributor to IT decay.

Previous studies show that inactivation of phages in suspension is related to the available surface area of the air-water interface, where extrusion of the phage capsid hydrophobic domains into the air phase causes the proteins to denature[424]. Interaction with this interface is insufficient to explain the difference in phage titer loss in our work, however, since the ratio of the liquid phase volume to air-water interface area was very similar between glass and polypropylene containers despite large differences in IT decay rate. Thompson and Yates observed the same inactivation of phage in polypropylene containers as in our work[433] but attributed inactivation not to the air-water interface but rather to the triple-phase-boundary (TPB) where air, liquid, and container tube wall phases intersect[434]. However, this inactivation effect depends on a hydrophobic tube wall, which is not the case in our glass and PP LoBind containers, which also exhibited the worst phage stability. Furthermore, we observed no correlation between IT loss and the ratio of the length of the TPB to volume (L_{TPB}/V), as proposed by (Thompson and Yates, 1999). Since no significant deposits of phage were found on glass and PP surfaces, we consider aggregation or inactivation to be more likely explanations for the observed reduction in IT in containers other than PP+BSA. This leaves two possibilities: either contact with the surface directly induces inactivation and/or aggregation, or material leaches from the surface to induce the same effects in the bulk.

If material leaches into the bulk from the container material and causes phage aggregation/inactivation, the same should be true in the case of BSA-treated containers. Furthermore, Richter *et al.* effectively excluded the possibility of leachables as a major contributor to IT decay in their own containers[205], and we do not consider this to be a plausible explanation in our work either since any leachables should still be able to diffuse through an adsorbed BSA layer and induce IT loss, which was not observed. Finally, glass containers — which resulted in some of the worst IT loss — are not expected to be capable of releasing material into the bulk. This leaves contact interactions between phage and the surface itself as the most likely explanation of IT decay that was observed in this work.

With the potential explanations of adsorption, interactions with the air-water interface and/or triple-phase-boundaries, and no correlation with hydrophobicity of the container walls, we hypothesize that an additional causative factor of IT loss is container surface nanotopography. Nanoscale surface topography has been found to modulate aggregation of various proteins including amyloid-β peptides on polystyrene[435] and amylin on silicon oxide[436], with increasing surface smoothness correlated with more rapid aggregation. Co and Li recently provided a model for understanding this phenomenon, showing in Monte Carlo simulations that an increase

in roughness slows amyloid fibril formation[437]. Kam *et al.* have found that nanotopography of polystyrene and polypropylene was a greater determinant of water contact angle than chemical composition[438], while Nie *et al.* observed that the increase in wettability of plasma-treated polypropylene is coincident with a change to smoother surface topography[439]. Our SEM analysis of glass, PP and PP+BSA containers revealed the surface topography of glass to be significantly smoother than that of PP and PP+BSA. This indicates a correlation between increasing surface roughness and increasing phage stability in our experiments. Our findings are consistent with the observed modulation of aggregation by surface nanotopography that has been established in the literature for proteins, but should be compared with an observation of the opposite effect for bacteriophages of a different myovirus morphology[440]. While the work of Dika *et al.* showed the lowest level of adhesion on glass surfaces, the study did not control for surface material while varying roughness, and furthermore did not observe a monotonic correlation between roughness and phage adhesion. In any case, we do not attribute IT loss in glass containers to adhesion but rather to aggregation. For these reasons we do not find the findings of Dika *et al.* to be incompatible with our hypothesis of a correlation between roughness and aggregation.

Richter *et al.* found that plasma treatment of polypropylene containers reduced IT decay, attributing this to an increased hydrophilicity of the surface. However, such an explanation is in contradiction both to our work and to the findings of Wang *et al.* who observed almost no adsorption of T4 phage on polyhydroxyalkanoate surfaces with a wetting angle of 96.83°, but *increased* adsorption following plasma-treatment and an associated decrease in the contact angle to 14.96°[227]. This latter result is more consistent with our own observation of significant IT decay in glass vials which had a contact angle of 13.6°. Further supporting a hypothesis of nanotopographical modulation of phage stability, Wdowiak *et al.* demonstrated that coating of container surfaces with gold—polyoxoborate nanocomposites prevented adsorption of phages on polypropylene labware[421]. As in the earlier work of Richter *et al.* this protective effect was similarly attributed to modification of the wettability. However, the proposed nanocomposite treatment also significantly altered the nanotopography of the polypropylene surface, and the authors report an increasing phage protection effect with increasing deposition, and presumably a commensurate increase in surface roughness.

We propose that both water contact angle and nanotopography have an influence on phage aggregation. Indeed, Richter *et al.* show that the "safe" tubes seem to be those whose surface topography exhibited the highest spatial frequency, as revealed by AFM analysis[205]. Furthermore, that paper showed that increased mixing and higher temperature had the effect of increasing IT decay. It is possible that this increase was due to increased lateral diffusion of phage on the container walls, which is normally impeded by nanoscale roughness (and thus leads to slower IT decay) which can be overcome by agitation and thermal motion and result in the formation of aggregates which either remain on the surface or migrate back to the bulk[441]. A nanotopography dependence of IT loss is consistent with our own observations, since untreated PP was observed to have a higher nanoscale roughness than glass, resulting in IT decay that was *delayed* relative to glass but continued even after two weeks of storage, while PP+BSA was observed to have the highest roughness and lowest IT loss.

One of the most striking results from phage enumeration experiments was the improvement in infectious titer retention after treatment of PP and PS labware with BSA. This supports the hypothesis that pre-saturating the surface with protein can protect against loss of infectious titer. Our findings can be compared with those of Lytle *et al.*, who found that inclusion of calf serum in phage suspensions prevented IT loss of several podovirus phages following exposure to vinyl, latex and glass[432] and reduced adhesion to nitrocellulose and polysulfone membranes[442]. Although calf serum is a more complex additive than pure bovine serum albumin, both our work and that of Lytle *et al.* show a protective effect when protein is allowed to adhere to labware surfaces. Rossi et al. found that addition of BSA to a phage suspension can induce an increase in infectious titer as BSA displaces phage adsorbed on clay particulate surfaces[425]. A similar effect may explain the increase of IT after

an initial decrease in the case of phage P68 stored in PP+BSA and PS+BSA containers. Our findings indicate that incubating protein with the surface is sufficient to impede phage loss, negating the necessity to add protectant directly to the phage suspension, which could have important implications for pharmaceutical compatibility of phage preparations. It is possible that BSA remains loosely bound to the container surface and subsequently leaches back into the suspension, either interacting with phages themselves in such a way that prevents infectious titer loss, or perhaps migrating to the air-water interface to block free phage from interacting with the air phase[433]. However, all BSA-treated containers were thoroughly rinsed several times before introduction of phage, and were not subsequently exposed to detergent, heat or changes in salinity or pH which may lead to solubility or conformational changes that could cause BSA to desorb. We conclude, then, that the protective effect of BSA may rely on reducing contact between phage and the bare container surface. Further work is necessary to establish the level of BSA leaching from the surface back into the bulk in order to elucidate the nature of the protective effect of BSA.

In this work, we have shown that phage infectious titer drops rapidly in common labware, partly replicating results recently presented in the literature, but finding that storage in glass and low-binding polypropylene labware induced the most rapid and drastic loss of infectious titer of phage suspensions. We propose that several phenomena — adsorption, aggregation, and inactivation — are at play simultaneously, and that the balance between them depends on the nanotopography and/or material composition of the container surface, supporting this hypothesis with comparison between infectious titer and particle size distributions generated by NTA.

NTA was demonstrated as a valuable, complementary measure of the total particle concentration and aggregation state of phage suspensions, revealing the multifaceted nature of infectious titer loss. Water contact angle measurements of container interior surfaces did not yield a correlation between wettability and phage titer stability for any of the three phages studied, contradicting recently published results. Further work is needed to correlate a full characterization of container material surface energy (*i.e.*, more thorough than only the sessile drop method with deionized water) with infectious titer loss of exposed phage suspensions.

Pre-incubation of container surfaces with bovine serum albumin was demonstrated as a simple and effective method to significantly reduce infectious titer loss. Scanning electron microscopy was performed on container surfaces in order to assess the level of phage surface adsorption, suggesting that adsorption accounts for infectious titer decay in PP+BSA containers, while aggregation and inactivation were more important determinants of phage stability in glass and polypropylene containers.

The observed loss of infectious titer has important implications for fundamental research on phage and their use in biomedical applications. Further investigation into the modulation of infectious titer loss by container material and surface topography could yield phage-optimized storage protocols and contribute to consistency and repeatability in phage research.

Chapter 6

Ultrafast and Multiplexed Bacteriophage Susceptibility Testing by Surface Plasmon Resonance and Phase Imaging of Immobilized Phage Microarrays

Published article in *Chemosensors* (2022)
DOI: 10.3390/chemosensors10050192

Larry O'Connell [1,2], Ondrej Mandula [1], Loïc Leroy [2], Axelle Aubert [1], Pierre R. Marcoux [1,*] and Yoann Roupioz [2]

[1] Univ. Grenoble Alpes, CEA, LETI, F38054 Grenoble, France

[2] Univ. Grenoble Alpes, CNRS, CEA, IRIG, SyMMES, 38000 Grenoble, France

Keywords: surface plasmon resonance imaging; phase imaging; phage susceptibility testing (PST); phage therapy; personalized cocktail; *Staphylococcus aureus*; phage microarray

Abstract

In the context of bacteriophage (phage) therapy, there is an urgent need for a method permitting multiplexed, parallel phage susceptibility testing (PST) prior to the formulation of personalized phage cocktails for administration to patients suffering from antimicrobial-resistant bacterial infections. Methods based on surface plasmon resonance imaging (SPRi) and phase imaging were demonstrated as candidates for very rapid (<2 h) PST in the broth phase. Biosensing layers composed of arrays of phages 44AHJD, P68, and gh-1 were covalently immobilized on the surface of an SPRi prism and exposed to liquid culture of either *Pseudomonas putida* or methicillin-resistant *Staphylococcus aureus* (i.e., either the phages' host or non-host bacteria). Monitoring of reflectivity reveals susceptibility of the challenge bacteria to the immobilized phage strains. Investigation of phase imaging of lytic replication of gh-1 demonstrates PST at the single-cell scale, without requiring phage immobilization. SPRi sensorgrams show that on-target regions increase in reflectivity more slowly, stabilizing later and to a lower level compared to off-target regions. Phage susceptibility can be revealed in as little as 30 min in both the SPRi and phase imaging methods.

6.1 Introduction

6.1.1 Antimicrobial Resistance

The proliferation of multi-resistant bacteria is having an increasing and profound impact on health outcomes worldwide, with recent data reporting an overwhelming burden of 1.27 million deaths in 2019 attributable to bacterial antimicrobial resistance [1].

Within this context, alongside the possibility of discovery of novel classes of antimicrobials and stewardship of known molecules, phage therapy is enjoying increasing interest as a plausible alternative to classical antibiotics, which may in the near future form the basis of a new treatment paradigm for bacterial infections [64,89].

The host range of a phage depends on several factors but most strongly on its ability to specifically recognize and bind to cells of host bacterial strains via receptor-binding domains on the phage capsid [83]. Because of this specific binding, phages have a narrow host range that is species- or even strain-specific. This constrained spectrum of action presents an advantage in that an administered phage targeting a given pathogen need not disturb the normal commensal flora of the patient [84]. However, this narrow host range also presents challenges that must be mitigated, namely that screening must be performed to ascertain the susceptibility of a given bacterial pathogen to a range of candidate phages in order to develop a cocktail personalized to each patient, composed only of phages to which the pathogen is susceptible.

Of the different morphologies and lifecycles exhibited by phages, only some are appropriate for phage therapy. Temperate phages must be avoided since lysogeny can confer virulence factors to the host bacteria via genetic transduction, increasing their pathogenicity [88]. Lytic phages are thus preferred since they are immediately lethal to their host bacteria and are less likely to enable horizontal gene transfer or induce superinfection immunity [89]. For these reasons, phages must be characterized and vetted on the above criteria (inter alia) before being incorporated into a library as suitable therapeutic agents [88].

6.1.2 Phage Susceptibility Testing

In order to facilitate a partial or wholesale transition from traditional antimicrobials to phage therapy, new tools are needed for rapid and multiplexed screening of large libraries of candidate phages in order to provide a personalized phage to each patient. Up to 100 different lytic phages may have to be screened to find active phages on the patient's bacterial isolate [443]. More typically, between 5 to 10 different phages are tested either in isolation or in various permutations as a cocktail, over a range of 5 to 9 concentrations, which places a requirement of high multiplexing capacity on any potential PST method.

Currently, the most frequently exploited methods for PST rely on phage–bacteria co-culture since, of the methods available, liquid culture lysis is the technique that appears to be the most easily extensible to scalable automation. Lysis culture assays can be carried out in industry-standard microdilution transfer plates [100], which can feature as few as six and as many as several hundred individual wells. This method also permits combinatorial assays to establish phage synergy or antagonism through a kind of pair-wise checkerboard assay [101]. Several works have demonstrated the use of plate readers adapted to monitor optical density of bacteria–phage co-culture [102,104,105].

However, these techniques rely on a spectrophotometric or colorimetric change that reveals phage replication with long time to results, ranging from 2 to 6 h [104,444]. Furthermore, to the authors' knowledge, there is no work yet describing the use of such methods for parallel comparison of phage–host affinity, as proposed in this work.

More recently, wide-field lens-free imaging has been leveraged to accelerate PST and even detect phage-resistant bacterial microcolonies with a time to results of only 3 h [420]. While such a method significantly

reduces time to results, it has not yet been demonstrated in a scalable way that would be extensible to parallel screening of many phages within the same assay.

The aim of this work is to demonstrate a proof-of-concept parallel, multiplexed SPRi-based phage susceptibility screening assay. To this end, a biosensing layer featuring an array of different candidate phages is covalently immobilized on a gold surface and produces a measurable surface plasmon resonance signal correlated with interactions between immobilized phages and bacterial cells introduced to the sensor surface (**Figure 6.1**A). Monitoring of the interaction in real time of each of a large array of phages with a challenge bacterial strain would reveal those that are suitable for inclusion in a phage cocktail against that strain. In this sense, the envisaged assay would take the form of a single-use SPRi consumable, in analogy to convenience of commercially available antibiotic susceptibility systems.

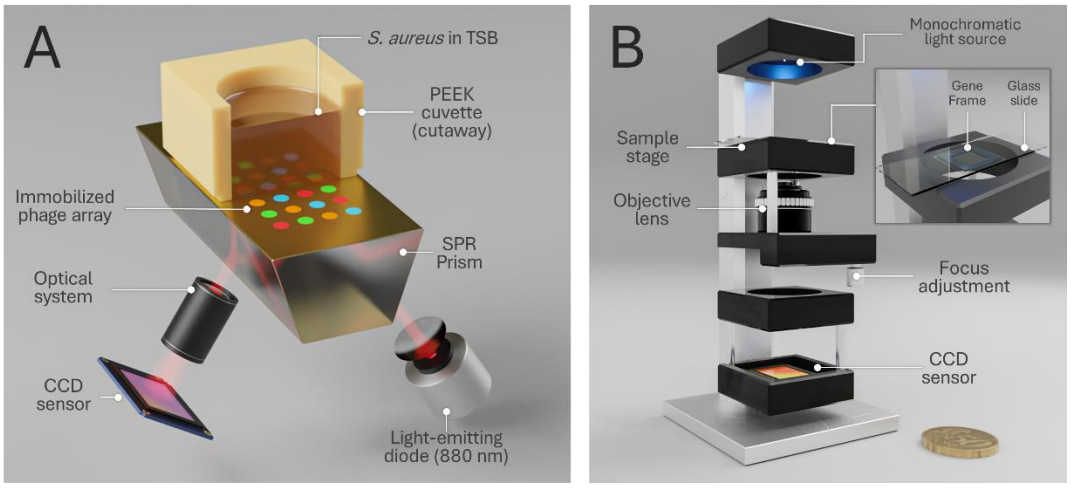

Figure 6.1 (**A**) A schematic illustration of the SPRi prism, functionalized with an immobilized array of phages, shown interfaced with a cutaway of the PEEK cuvette containing liquid cultures of the challenge strain *Staphylococcus aureus*. (**B**) A schematic illustration of the phase imaging microscope. Mounted on the sample stage is a co-culture of phage gh-1 and *P. putida*, sandwiched between a microscope cover slip, a gas-impermeable Gene Frame, and a microscope slide.

6.1.2.1 Surface Plasmon Resonance

Surface plasmon resonance sensing relies on the coupling of light to surface plasmons and allows the transduction of physical binding phenomena on the sensor surface into an optical signal. A key strength of SPR is its high sensitivity to changes in the refractive index within the ~100 nm penetration depth of the sensor surface and exclusion of contributions beyond this region, allowing even small mass uptake of 10–0.01 pg/mm^2 of proteinous material to yield a measurable signal [107].

Surface plasmon resonance imaging (SPRi) builds on the strength of SPR by imaging the entire surface of a sensor (1–2 cm^2) that can be functionalized with many different ligands, simultaneously monitoring the interaction of each functionalized region in a single, parallel, multiplexed assay [109,110]. SPRi has been demonstrated for the specific detection—and potentially even identification and typing—of challenge bacteria using arrays of immobilized antimicrobial proteins [111]. In contrast to state-of-the-art PST methods involving optical measurements of bacteria/phage co-culture in multiwell plates, SPRi arrays can feature many hundreds to thousands of probes arrayed on a single sensor surface.

To the authors' knowledge, this work represents the first time SPRi has been exploited for PST. A 2019 review of phage isolation and characterization techniques made no mention of SPR-based methods of PST [97], and the authors are aware of no such precedent in the literature.

The use of surface plasmon resonance for PST necessitates the localized, addressable immobilization of phages on the sensor surface, a task which is far from trivial [133,404]. We thus tested an alternative optical PST method, in parallel with SPR experiments, based on label-free digital holography.

6.1.3 Phase imaging

Optical label-free techniques have been demonstrated to be effective for non-destructive characterization of bacterial pathogens, phenotypic identification [445] and viability assays [446], not only at the level of colonies [447] and microcolonies [448], but also down to the scale of single-cells [449]. In particular, imaging of phage plaques with wide-field lens-less techniques was recently reported to enable rapid solid-phase phage susceptibility testing with time to results as low as 4h20 for anti-*Staphylococcus aureus* phage and 2h20 for anti-*Klebsiella pneumoniae* phage [420]. In this case, a wide field-of-view (FoV) of 3.3 cm^2 was necessary to observe a sufficient number of lysis plaques. Considering instead PST in the broth phase, it may be advantageous to sacrifice FoV to gain resolution, with a view to imaging single cells, counting them directly, and even visualizing individual lysis events. For this reason, phase imaging experiments were performed with phage gh-1 and its host *P. putida*, in parallel with surface plasmon resonance experiments, to investigate bacterium–phage interaction at the single-cell scale. Phase imaging techniques, such as Zernike phase contrast, differential interference contrast, or digital holography microscopy, allow observation of non-absorbing or poorly absorbing objects such as individual cells immersed in nutritive medium. Bringing the sample slightly out of focus creates well-contrasted interference fringes in the image plane that emphasizes cells but degrades image quality due to diffraction. Post-acquisition analysis of images allows one to recover accurate imagery of bacterial cells and carry out precise monitoring of biomass over the entire FoV.

6.2 Materials & Methods

6.2.1 Materials

Glycerol (≥99%), 11-mercaptoundecanoic acid (11-MUA, 95%), agar (Difco), bovine serum albumin (BSA), ethanolamine (≥99.5%), trypticase soy broth (TSB), potassium nitrate (KNO_3), and ethanol (≥99.9%) were purchased from Sigma-Aldrich (Saint Quentin Fallavier, France) and used without additional purification. CsCl (≥99.9%), 0.9% *w/v* NaCl solution (OTEC), and 90 mm tryptone soy agar (TSA) Petri plates were purchased from VWR (France). 1-Ethyl-3-(3-dimethylaminopropyl)carbodiimide (EDC) (≥98%) and sulfo-N-Hydroxysuccinimide (sulfo-NHS) were purchased from Thermofisher and used as received. Deionized water (DIW; >18 MΩ resistivity) was obtained from an ELGA PURELAB flex dispenser (Veolia Water, France). Polyethylene glycol 6 kDa (PEG-6000) was purchased from Merck (Darmstadt, Germany).

6.2.2 Host bacterium and bacteriophage preparation

Bacterial host *Pseudomonas putida* (ATCC 12633; host of phage gh-1) and phages 44AHJD [405], P68, and gh-1 [195] were obtained from the *Félix d'Hérelle Reference Center for Bacterial Viruses* of Université Laval, Quebec, Canada. Bacterial hosts *Staphylococcus aureus* subsp. *aureus* Rosenbach (SA1; ATCC 43300, host of phage 44AHJD@SA1) and *Staphylococcus aureus* (SA2; ATCC BAA-2312, host of phages 44AHJD@SA2 and P68@SA2) were obtained from Microbiologics (Kwik-Stik™ lyophilized strain).

Bacterial cultures were routinely prepared in TSB at recommended temperatures for each host: *S. aureus* at 37 °C and *P. putida* at 30 °C. Phage suspensions were routinely prepared using the double-layer agar method [99]: 100 µL of overnight liquid precultures of each bacterial host were inoculated into fresh TSB and allowed to proliferate until reaching 10^8 colony-forming units per mL (CFU/mL) as confirmed by optical density at 550 nm. Then, 200 µL bacterial host and 100 µL phage suspension were inoculated into each of several 15 mL Falcon tubes filled with 5 mL molten agar (TSB prepared with 7.5 g/L agar) at 51.5 °C, vortexed, and poured over 20 mL solidified tryptic soy agar (TSA, 15 g/L agar) in a standard 90 mm Petri plate. Plates were then incubated overnight until lysis plaques became confluent in the top agar layer, which was then collected and soaked for

4 h at room temperature in sterile 154 mmol NaCl solution in a 50 mL polypropylene tube. Each tube was then twice centrifuged for 20 min 5500× *g* at 4 °C, and the supernatant was retained each time.

Rigorous purification of phage suspensions is an essential step and was achieved using a combination of PEG/NaCl precipitation, ultracentrifugation, and ultrafiltration. Each suspension (35–45 mL) was brought to 0.5 mol NaCl and 8% *w/v* PEG-6000 and left at 4 °C overnight to precipitate the phages. The following day, each suspension was centrifuged for 30 min at 12,000× *g* at 4 °C, the supernatant removed, and the pellet resuspended in sterile 154 mmol NaCl, vortexed, centrifuged 20 min 5500× *g* at 4 °C and the supernatant was retained.

Suspensions were then further purified by density gradient ultracentrifugation for 2 h at 100,000× *g* at 4 °C on a CsCl step gradient (1.7 g/mL, 1.54 g/mL, and 1.34 g/mL CsCl in DIW) in 5 mL, Open-Top Thinwall Ultra-Clear ultracentrifuge tubes (Beckman Coulter, Villepinte, France) in a SW55Ti swinging-bucket rotor (Beckman Coulter) mounted in an Optima l-90K Ultracentrifuge (Beckman Coulter). Phages were concentrated at the second visible band from the top and collected with a micropipette. Finally, CsCl and small-molecular-weight contaminants were then removed from phage suspensions by twice repeated centrifugal ultrafiltration and resuspension in 154 mmol NaCl solution using 100 kDa Vivaspin 500 ultrafiltration units (Sartorius).

All phage suspensions were stored at 4 °C in the dark in 1.5 mL polypropylene Eppendorf-type tubes. Following purification, the infectious titer of phage suspensions was obtained by the agar overlay method [99] and is reported in units of plaque-forming units per milliliter (PFU/mL). Phages capable of using several bacterial strains as their hosts are appended with the abbreviation of the host used—44AHJD amplified with SA1 is referred to as 44AHJD@SA1, while 44AHJD amplified with SA2 is referred to as 44AHJD@SA2, etc.

6.2.3 Substrate preparation

Gold-coated SPR prisms were purchased from Horiba (SPRi-Biochips™, Horiba Scientific, Palaiseau, France). The gold surface of the prism was rinsed with DIW, ultrapure ethanol, then once more with DIW. The prism was then dried with argon and plasma cleaned for 3 min in 0.6 mBar 75:25 oxygen/argon mix at 80% power in a Femto plasma system (Diener electronic, Ebhausen, Germany). The prism surface was then left at room temperature to stabilize for at least 24 h before use.

6.2.4 Bacteriophage immobilization

11-MUA was dissolved in ultrapure ethanol to a concentration of 50 mmol. The cleaned gold surfaces of SPR prisms were functionalized with 11-MUA to form a self-assembled monolayer (SAM) by soaking the entire SPR prism overnight at room temperature. Before phage immobilization, the prisms were rinsed with ultrapure ethanol, dried with compressed air, and submerged in a 100 mmol EDC, 25 mmol sulfo-NHS aqueous solution for 30 min at room temperature to activate the carboxyl groups of the 11-MUA SAM. The surface was then rinsed with DIW, dried with compressed air, and immediately deposited with phage suspensions—154 mmol NaCl supplemented with 10% *w/v* glycerol with an infectious titer of 6×10^9 PFU/mL for P68 and 10^{11} PFU/mL for other phages. Addition of glycerol has been found to be a crucial step to prevent drying of small deposited droplets, permitting the arrayed immobilization of different phage species in adjacent, closely-spaced regions on the same substrate [404].

In this work, SPR prisms were spotted either manually or using a microarrayer deposition system. Robot-assisted spotting was carried out using a method described elsewhere [404]. Briefly, the prism is mounted in an automated microarrayer system (OmniGrid Micro, Genomic Solutions Inc., Irvine, CA, USA) fitted with a 350 µm-diameter stylus (Xtend, LabNEXT Inc., West New York, NY, USA). A total of 100 µL of each phage suspension was loaded in a standard PCR tube, retrieved by the stylus, and a volume of approximately 10 nL was deposited on the prism surface, producing circular phage-functionalized regions 500–600 µm in diameter. For manually

spotted prisms, a micropipette was used to drop cast 1 µL droplets of each phage suspension on the prism surface.

For both deposition methods, phage suspensions were incubated with the surface overnight at room temperature in a humid environment inside a chamber loaded with saturated KNO_3 solution (95% relative humidity) and rinsed with DIW the following day. Before the surface plasmon resonance imaging, the prism was immersed in 100 mmol ethanolamine aqueous solution for 30 min followed by 1 mg/mL BSA aqueous solution for 10 min in order to block the surface against non-specific binding, then rinsed thoroughly with DIW. The prism surfaces were at no point allowed to dry once phages had been immobilized, since this is known to inactivate many species of phage [270,450].

6.2.5 Phage-bacteria interaction monitoring by surface plasmon resonance imaging

The monitoring of immobilized phage interactions with bacteria was performed using a commercial SPRi device (SPRiLab, Horiba Scientific, Orsay, France) placed in an incubator at either 33.5 °C or 37 °C depending on the experiment. The SPRi prism was interfaced to a PEEK cuvette, which permitted the introduction of an analyte to the sensor surface (**Figure 6.1**A). The cuvette was filled with sterile TSB and plasmon curves recorded for all functionalized regions of the sensor surface. The cuvette opening was covered with labfilm to prevent evaporative concentration of the analyte.

Exponential-phase cultures of *P. putida* and *S. aureus* in TSB were pelleted by centrifugation at 5500× *g* at room temperature for 5 min, resuspended in fresh TSB, centrifuged and resuspended a second time in TSB to a concentration of either 10^6 or 10^9 CFU/mL, and then a volume of 1 mL was introduced to the sensor surface with one strain in each chamber. Reflectivity shifts were then recorded, with images taken every six seconds.

6.2.6 Phase imaging

We used a custom phase imaging microscope setup (**Figure 6.1**B) in an inverted configuration that has been described elsewhere in the work of Mandula et al. [451]. Briefly, a bright field of 20×, 0.4 numerical aperture, infinity-corrected, dry objective (Motic) with f = 50 mm tube lens creates a magnified image of the sample on a CMOS chip (IDS UI-1490SE-M-GL). A blue LED (450 nm, CREE) coupled to a multi-mode fiber (400 µm diameter, Thorlabs) placed at 5 cm above the sample provides a semi-coherent illumination in transmission geometry.

A chamber was made by sandwiching a Gene Frame (1 cm × 1 cm, 250 µm thick, Thermofisher) between a standard microscope slide and cover slip, forming a volume of 25 µL (**Figure 6.1**B). A co-culture of phage gh-1 and *P. putida* was mixed (10^8 phage/mL and 10^7 bacteria/mL), and 20 µL was immediately introduced into the Gene Frame chamber.

The slide and chamber were placed on the sample stage and inverted with the coverslip facing the objective. The inner surface of the coverslip covered with sedimented bacteria was deliberately placed ~5 µm out of focus to create better contrast between bacteria and the background. A time-lapse was recorded over 80 min at 30 s intervals.

6.2.7 Data analysis

SPRi reflectivity data were captured using SPRiView (v3.1.2) and processed using MatLab R2021a (v9.10). Regions of interest (ROIs) were manually selected during initialization of the SPRi experiment, chosen to correspond to the phage-functionalized regions of the surface. The reflectivity signal was averaged across the area of each ROI. A one-minute rolling average (i.e., mean of 20 data points) was then taken of the resultant traces. No blank subtraction or drift correction was necessary to reveal the phage–host interactions.

In phase imaging experiments, time-lapse imagery was processed to detect individual bacteria using Laplace of Gaussian detection with an estimated blob diameter of 3 µm, using ImageJ plugin TrackMate [452].

6.3 Results

6.3.1 SPR

In order to investigate interactions between sensor surfaces and challenge bacterial strains, phages were immobilized in a 10 × 6 rectilinear array using a microarrayer system [404], and the array was exposed to TSB containing methicillin-resistant *S. aureus* (SA1, host of 44AHJD@SA1) to demonstrate susceptibility screening of a clinically relevant pathogen (i.e., a member of the ESKAPE group of pathogens [9]). A moderate concentration of bacteria of 10^6 CFU/mL was introduced to the surface to represent a reasonable concentration of analyte comparable to that likely to be available in a clinical setting.

In order to compare the response of several phages with varying levels of affinity to the challenge strain, four candidate phages were immobilized in separate regions: an *off-target* phage gh-1, which is incapable of replicating with SA1 as its host, an *on-target* phage 44AHJD@SA1, which is capable of replicating with SA1, and two additional candidate phages—P68@SA2 and 44AHJD@SA2—which had both been amplified with a different species of *S. aureus* (SA2; ATCC BAA-2312) than the challenge strain SA1. The purpose of including P68@SA2 and 44AHJD@SA2 is that we may expect them to have an intermediate affinity for the challenge bacteria, between that of gh-1 and 44AHJD@SA1, due to evolutionary pressure on receptor-binding domains during phage amplification

The results of previous experiments indicate that the purification and immobilization protocol used in this work consistently yields homogenous, high-purity, high-density (90–160 phage/μm^2) phage monolayers from suspensions of phages gh-1 and 44AHJD (unpublished results). This arraying method allows several replicates of each phage to be immobilized on the surface and demonstrates the extensibility of the proposed technique to arrays of many dozens or hundreds of phages.

Plotting the reflectivity shifts revealed that the reflectivity of on-target regions (i.e., regions where a phage is exposed to its host) increased most slowly and stabilized to a lower value (**Figure 6.2**, dashed orange line) compared to off-target (black line) and intermediate regions (solid orange and blue lines). Interestingly, the sensorgram revealed a spread of responses, which reflects the expected affinity of each phage for the challenge bacteria. While 44AHJD@SA1 exhibited the strongest response (slowest reflectivity increase), 44AHJD@SA2 showed the next strongest response, which correlates well with its reduced (but non-zero) ability to use this bacterial strain as a host. Continuing the pattern, P68@SA2 is another phage that uses a related *S. aureus* strain as its host and exhibited the next strongest response after 44AHJD@SA2. Phages 44AHJD@SA2 and P68@SA2 are the product of several rounds of amplification on SA2; it may be that these immobilized phages exhibit an increased affinity for the SA2 strain as a result of selective pressure on the host-determining regions of the phage receptor-binding domains.

Finally, phage gh-1 is entirely incapable of replicating on the challenge strain, and we observed the weakest response from this phage. Nevertheless, we see an increase in reflectivity in these regions. We attributed this to the increase in concentration of bacteria in the cuvette above the off-target regions as bacteria sedimented across the entire sensor surface as the experiment progresses.

Considering the first derivatives of the sensorgrams (See annex **Figure A.2**), we observed that on-target regions peaked with a lower rate of change in reflectivity compared to all other regions. Despite the difference in peak rate of change, the first derivatives of sensorgram traces of both on and off-target regions all peaked within 25 min of one another.

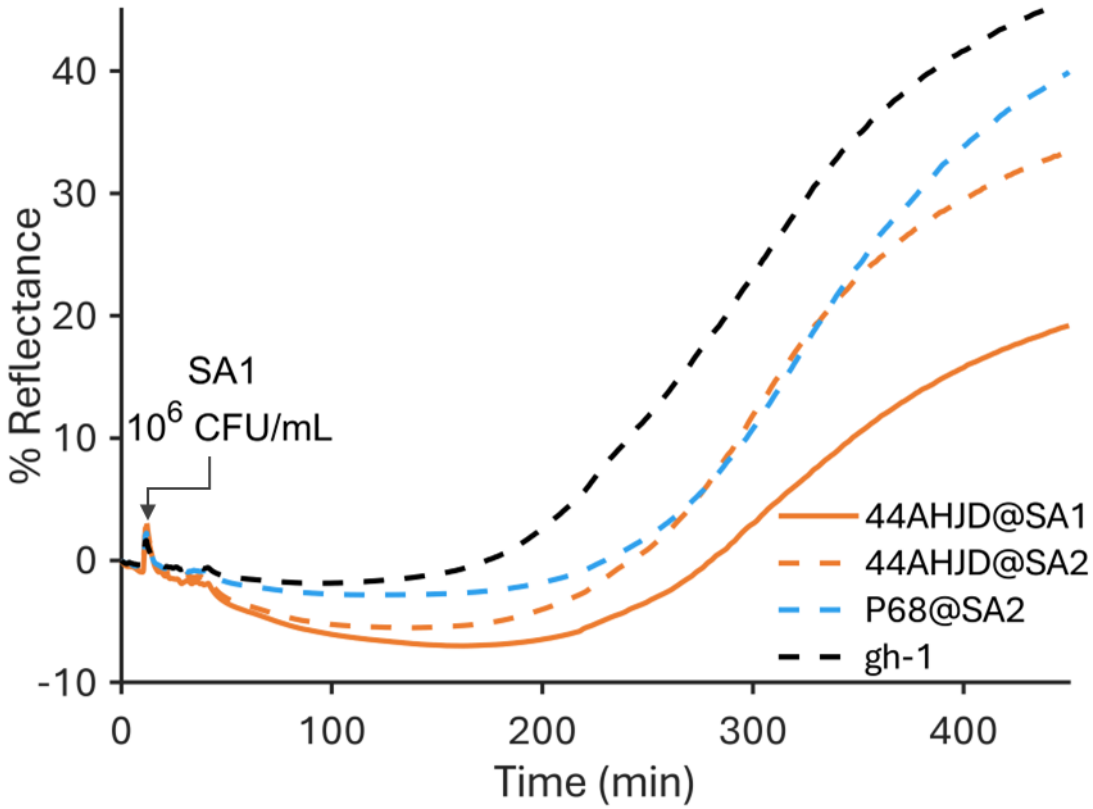

Figure 6.2 Sensorgram showing the SPR responses of regions functionalized with phages 44AHJD@SA1 (solid orange lines), 44AHJD@SA2 (dashed orange lines), P68@SA2 (blue lines) and gh-1 (black lines) when exposed to *S. aureus* SA1.Traces show a one-minute rolling average (i.e., mean of 20 data points).

In order to validate the above result through cross-comparison of phage interactions with two separate bacterial hosts, phages were again immobilized, this time in duplicate arrays on the sensor surface, with each duplicate array exposed to one of two chambers containing TSB inoculated with either *P. putida* (host of gh-1) or *S. aureus* (SA1, host of 44AHJD@SA1).

Again, we observed the same effect where the reflectivity levels of on-target regions increased most slowly and stabilized to a lower value compared to off-target regions (**Figure 6.3**). This effect is especially clear in the first derivative of the reflectivity (See annex **Figure A.3**), where the signals of off-target regions increase immediately in response to the introduction of bacteria and reach a higher peak (at 25 and 29 min for gh-1 + *S. aureus* and 44AHJD@SA1 + *P. putida*, respectively), while on-target regions lag behind and reach a lower peak value and do so later (at 119 and 86 min for gh-1 + *P. putida* and 44AHJD@SA1 + *S. aureus*, respectively) compared to the first derivative of off-target regions. The specific response of phages to their host is revealed within in the first 30 min after introduction of bacteria at a high concentration of 10^9 CFU/mL.

In addition, the response time of the sensor was shortened relative to the previous experiment, with the inflection points of off-target sensorgram traces occurring at 26 min for gh-1 exposed to S. aureus and 29 min for 44AHJD@SA1 exposed to *P. putida*, approximately 10 times faster than in the first experiment after injection of SA1 where all curves peaked around 315 ±10 min. We attribute this faster result to the much higher concentration of bacteria in the second experiment of 10^9 CFU/mL, compared to 10^6 CFU/mL in the first.

While *P. putida* is a motile bacterium [453], *S. aureus*—barring special circumstances—is non-motile [454]. For this reason, the sedimentation of *S. aureus* onto the sensor surface is likely to progress more rapidly than for *P.*

putida, having the effect of facilitating increased interaction between *S. aureus* and the sensor surface. This may account for the more rapid development of reflectivity under the *S. aureus* chamber in this experiment.

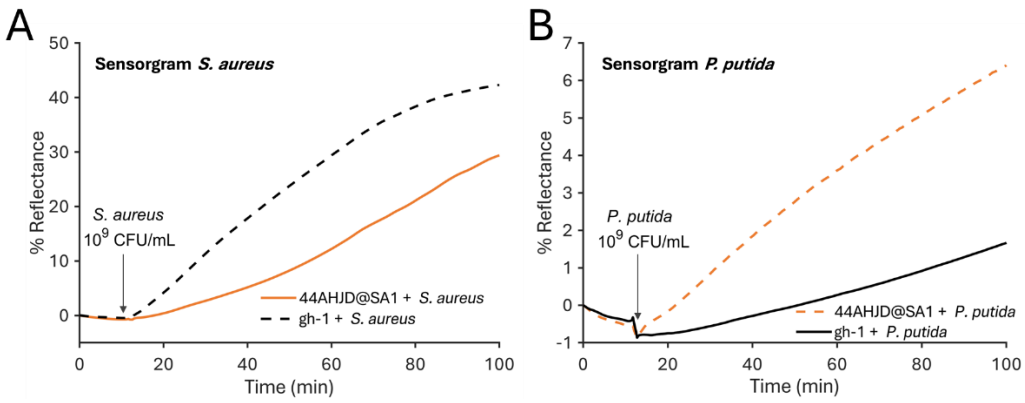

Figure 6.3 Sensorgrams showing the SPR responses of regions functionalized with phages 44AHJD@SA1 (orange lines) and gh-1 (black lines) when exposed to *S. aureus* (**A**) or *P. putida* (**B**).Traces show a one-minute rolling average (i.e., mean of 20 data points).

Since this second type of experiment exposed identically phage-functionalized regions to two different challenge strains during the same experiment, the relative SPR responses of each phage are directly comparable. Several potential sources of experimental variability are controlled for in this two-chamber setup. Firstly, any variation in the upstream processing of the substrate (e.g., cleaning, chemical activation, etc.) is controlled for since all phages are immobilized on the same surface. Phage titer can be unstable in aqueous suspensions, which brings the risk that otherwise identical substrates prepared on different days may be incubated with phage suspensions with different aggregation states and/or infectious titers [125,205]. Any differences in the phage response between the two chambers can reliably be considered to originate in the divergent response of each phage to each challenge strain, providing strong preliminary support for the feasibility of the proposed method of susceptibility testing.

The phage–host pairs in this work were chosen to include bacteria-featuring membranes with very different characteristics. While *S. aureus* is Gram-positive, *P. putida* is Gram-negative, and so the two types of cells differ significantly in cell wall composition. The receptor of phage gh-1 is known to be lipopolysaccharide [186], which is present in *P. putida* but absent in the Gram-negative *S. aureus*.

In contrast, podoviridae infecting *S. aureus* are known to require the presence of teichoic acid in the bacterial surface in order to absorb to their host [455]. Teichoic acid is present in the cell wall of *S. aureus* but absent in that of Gram-negative *P. putida*. For these reasons, we consider it to be a reasonable conclusion that the observed lack of activity in off-target phage/host pairs is well correlated with an inability of phages to bind to cells of the off-target bacterial strain.

6.3.2 Phase imaging

In order to explore PST at the scale of single cells, phase imaging experiments were performed to observe bacterial lysis due to phage replication, over a population of several thousand cells within the FoV (**Figure 6.4**A). Computational reconstruction was carried out to permit imaging of scattering centers (i.e., bacteria) 200 µm below the observation plane, coinciding with the lower surface of the Gene Frame chamber, on the glass cover slip. **Figure 6.4**C shows the number of detected bacteria over time, when gh-1 phages are present, on the upper glass surface (red curve, observation plane) and on the lower glass surface (green curve, reconstructed image). For the first 35 min, the number of detected bacteria is observed to increase due to exponential division (**Figure 6.4**B), reaching a peak after 35 min. The increase is slightly larger on the lower

surface (red curve) as the lower glass slide collects bacteria that sediment. A shallow decrease is followed by a steep drop at 39 min with the fastest decrease at 43 min. In a 20 min interval from 35 min to 100 min, the number of bacteria drops by 94%, coinciding with widespread phage-induced lysis. Larger, out-of-focus features in the background of these images are due to motile bacteria outside of the focal plane of the microscope. In the control experiment without phages, similar curves are shown in **Figure 6.4**D, plotting biomasses on the upper and lower surfaces: they both reveal a continuous increase throughout the experiment. Once again, the increase in biomass is slightly larger for the red curve corresponding to the lower surface because of the sedimentation of bacteria.

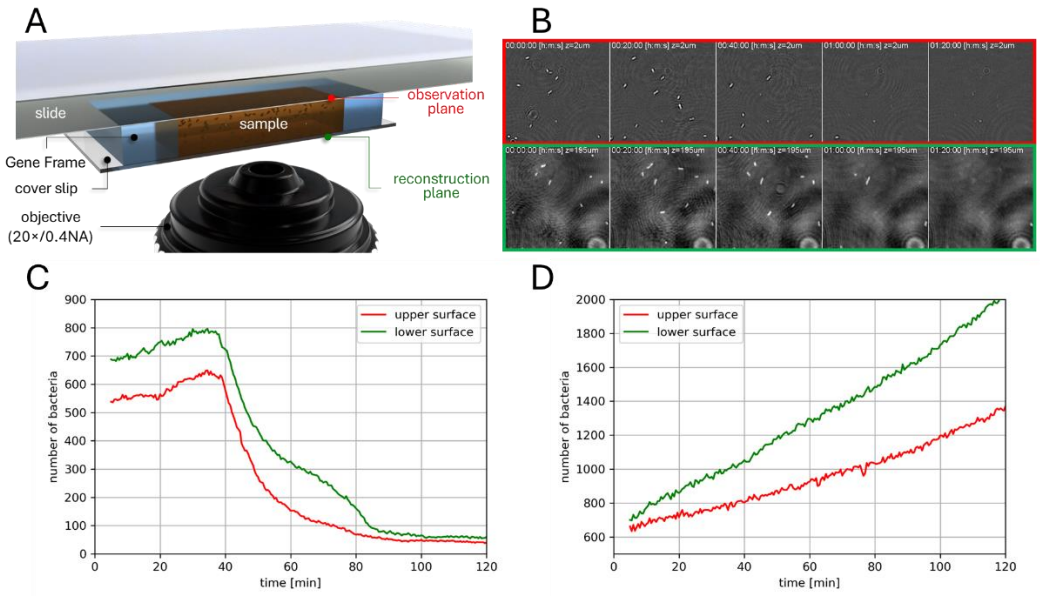

Figure 6.4 (**A**) Schematic of the optical setup for phase imaging of phage–bacteria interactions.The position of the glass slide was adjusted such that its upper surface was coincident with the observation plane. Images can be reconstructed in any plane within the volume enclosed by the Gene Frame, e.g., on the surface of the lower glass slide. Not to scale. (**B**) A sequence of 100 µm × 100 µm regions of interest extracted from the time-lapse of the observation plane (top row) and in the reconstructed image in the plane of the lower surface (bottom row). (**C**) Total number of bacteria vs. time in presence of gh-1 bacteriophages on the observation plane (red) and on the reconstructed plane (green). (**D**) Total number of bacteria vs. time (negative control without phages) on the observation plane (red) and on the reconstructed plane (green).

Interestingly, bacteria can be observed to continue growing and dividing up until lysis, indicating that the cellular metabolism is not entirely diverted toward phage synthesis.

While the large FoV brought by our system enables the continuous monitoring of thousands of cells (**Figure 6.5**B), a thorough investigation of a given cell as a function time reveals that the phage-induced lysis follows a three-step process (**Figure 6.5**A). First, the degradation of peptidoglycan through endolysins is not visible, until the infected cell loses its bacillus shape and becomes a spheroplast [456,457]. At this stage, the outer and inner membrane still exist and take a round shape due to osmotic pressure. In the final stage of the lytic process, membranes disappear. Interestingly, phase imaging allows sufficient contrast to allow the observation of the bacterial debris that remains on the glass surface following phage lysis.

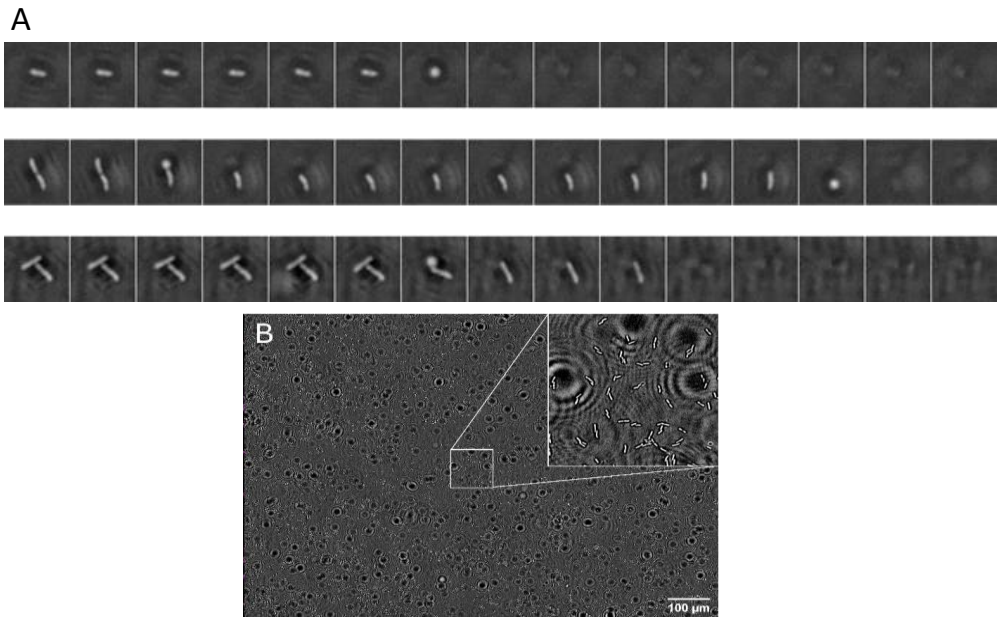

Figure 6.5 (**A**) Time-lapse sequences in three regions of interest, illustrating the different phases of lysis resulting from phage replication. (**B**) The entire FoV of our system (1.1 mm × 0.8 mm) with bacteria observed on the inner surface of the coverslip (bright rods) covering the gene frame chamber. Inset shows a magnified region of interest of 100 µm × 100 µm.

6.4 Discussion

A 2014 report by the World Health Organization [4] makes it increasingly clear that we must decrease our reliance on profligate and prophylactic administration of antibiotics in order to limit the proliferation of antimicrobial resistance genes. In order to enable new treatment paradigms in the context of healthcare and agribusiness, novel methods such as SPRi and phase-imaging PST may prove to be indispensable tools.

This work demonstrates a proof-of-concept SPRi-based method of rapid, multiplexed phage susceptibility testing. Specific responses of immobilized phages to their host are revealed as a lag in reflectivity increase. High concentrations of analyte bacteria (10^9 CFU/mL) can yield results within 30 min compared to several hours with state-of-the-art susceptibility testing methods.

Phage microarraying allows addressable immobilization of an array of dozens up to hundreds of different phage strains on the same surface [404]. Array pitch of 800 µm is consistently achievable with this technique, potentially permitting as many as 400 spots on the ~290 mm^2 surface area available on prisms used in this work, even before further refinement of the deposition parameters.

While covalent immobilization of phages via thiolated SAMs is a popular method [133], phage stability in this conjugated state is still an unknown. The challenge of variable phage stability may impact the interpretability of SPR sensorgram curves since differences in sensor response may originate in differences in the quality and density of the immobilized phage layer rather than differences in phage affinity. In this experiment, phages were immobilized within 24 h before use in SPRi experiments. Stability experiments are required to establish the reproducibility of SPRi-based PST with a larger variety of substrate-immobilized phages, and if the method presented in this work is compatible with long-term storage of the functionalized prism.

An alternative to SPRi PST was investigated in the form of phase imaging of phage-induced bacterial lysis. This method allows us to observe bacterial susceptibility within a physically compact region with a surprisingly

simple apparatus and without the need for labelling bacteria or covalent immobilization of phage on a sensor surface.

Further development of SPRi and phase-imaging-based PST is needed to scale up throughput to screening of hundreds of candidate phage strains.

Chapter 7

Rapid Fabrication of Interdigitated Electrodes by Laser Ablation with Application to Electrokinetically Enhanced Surface Plasmon Resonance Imaging

Article submitted May 2022

Larry O'Connell[1,2], Brice Poirier[3], Oleksii Bratash[2], Charlène Plénière[2], Loïc Leroy[2], Yoann Roupioz[2], Pierre R. Marcoux[1]

[1] Univ. Grenoble Alpes, CEA, LETI, F38054 Grenoble, France

[2] Univ. Grenoble Alpes, CNRS, CEA, IRIG, SyMMES, 38000 Grenoble, France

[3] Y.Spot, CEA, F38054 Grenoble, France

Keywords: Fabrication, laser ablation, rapid prototyping, dielectrophoresis, electro-osmosis, antimicrobial peptides, surface plasmon resonance, biosensing

Abstract

Significance: Dielectrophoresis, electro-osmosis, and other electrokinetic effects are frequently used in a variety of applications but necessitate patterning of electrodes on sensor surfaces. This typically requires a cleanroom and time-consuming, expensive, and arcane lithography and etching procedures.

Aim: To demonstrate the applicability of commercial laser direct writing equipment for rapid patterning of electrodes into gold layers on glass substrates, particularly with application to producing electrokinetically active plasmonic sensors.

Approach: A commercial printed circuit board prototyper was used to pattern interdigitated electrode (IDE) arrays into the surface of gold-coated slides and off-the-shelf surface plasmon resonance (SPR) prisms. The electrode geometries resulting from different patterning parameters were characterized by profilometry and

electron microscopy. The patterned surfaces were then employed for trapping and electro-kinetic manipulation of bacteria, and finally for sensing of bacteria by SPR imaging.

Results: Fabrication of an IDE array can be completed in as little as 12 seconds, with longer fabrication times permitting superior geometry and minimum feature size of 15 µm. The patterned IDEs were capable of concentrating bacteria and controlling their position on the sensor surface as a function of applied frequencies. SPR was demonstrated to detect specific interactions between bacteria and immobilized antimicrobial peptides.

Conclusions: Laser direct writing is demonstrated as a feasible, cleanroom-free alternative to more lengthy lithography methods, permitting very rapid fabrication and prototyping of IDEs, which are compatible with active plasmonic sensing and bacterial detection.

7.1 Introduction

Interdigitated electrodes – intermeshed, individually addressable planar electrodes – have been demonstrated in a wide variety of applications including biosensing[458,459], cell-sorting[460], diagnostics[461], and petrochemistry[462]; making use of transduction mechanisms either inherent to the electrodes themselves (*e.g.*, impedance[461,462] or capacitance based methods[463–465]) or in adjacent transducers near which the IDEs concentrate an analyte by electrokinetic mass transport.[466,467]

When employed for mass transport, IDEs can leverage electrokinetic effects such as dielectrophoresis (DEP), alternating current electro-osmosis (ACEO), and the electro-thermal effect (ETE) to concentrate and displace particulate matter in a carrier liquid as a function of the frequency and amplitude of oscillating electrical signals applied to the opposing electrodes.[466,467]

Due to the polyvalent nature of IDEs, they are incorporated into a large variety of different devices. As a result, it is common practise for researchers to fabricate the IDEs themselves in order to tailor the micro-patterned surfaces to their specific application.[462,464–466,468]

Traditionally, fabrication of electrodes necessitates some or all of: deposition of the electrode material and adhesion layers onto a suitable substrate, fabrication of a hard mask, and deposition of photoresist followed by lithography and associated wet or dry etching techniques.[469–472] Such methods are time-consuming, expensive, and incompatible with rapid iteration of component design, slowing the pace of research and obligating researchers to handle etchant chemicals and perform lengthy lithography processes and other steps which require skills that may be unrelated to their scientific training.

Increasingly, there is interest in more rapid processes for producing patterned surfaces. Alternative methods that have been demonstrated include inkjet printing,[473] fused deposition modelling,[474] and laser ablation of printed circuit boards (PCBs).[475] Although intriguing results have been obtained with these methods, each suffers from various drawbacks including poor pattern reproduction, large minimum feature sizes, large variability that depend on fabrication parameters etc.

Furthermore, use of unorthodox materials to form the IDEs may prove incompatible with popular bioconjugation methods such as thiol-gold immobilization[133,275], introducing complication downstream of the IDE fabrication.

First proposed by Tender *et al.* [476], laser direct writing (LDW) has only rarely been exploited for the fabrication of IDEs, despite the advantage that LDW can surpass the achievable resolution offered by conventional photolithography of gold.[477] However, fabrication of IDEs by laser ablation has so far necessitated construction of a custom optical setup, typically by channelling laser output *via* a dedicated optical bench through adapted microscope objectives.[476,477] While elegant, this method substitutes lengthy fabrication protocols with the

necessity to develop a custom optical system, negating any time-saving and recreating the problem of obligating experimenters to develop skills orthogonal to their research.

In order to improve the turn-around time for rapid prototyping of IDEs, here is presented a patterning method based on laser ablation of a deposited metal layer on glass substrates by a commercial PCB prototyper. This method retains the time-saving benefits of LDW, without the need to develop a custom optical setup.

In order to demonstrate the compatibility of the fabricated IDEs with biosensing, they were first employed for mass concentration of bacteria in a microfluidic circuit, then the same geometry was patterned into a surface plasmon resonance imaging (SPRi) sensor functionalized with antimicrobial peptides (AMPs) (**Figure 7.1**).

SPR is a popular technique for label-free, real-time monitoring of surface phenomena, transducing mass-uptake at a sensor-analyte interface into an optical signal.[107] SPR imaging builds on the strength of SPR by observing the entire surface of a sensor that has been functionalized with many different ligands, simultaneously monitoring the interaction of each functionalized region in a single, parallel, multiplexed assay.[109,110] SPRi has been demonstrated for the specific detection of bacteria using arrays of immobilized AMPs.[111] However, the time-to-results with this method was long, taking several hours to reveal interactions between AMPs and challenge bacteria.

Recently, there is increasing interest in enhancement by electrokinetic mass transport of plasmonic sensors including SPR[478], localized SPR[479], and optical fiber SPR sensing[480]. The work of Costella *et al.* and Avenas *et al.* demonstrated a form of active plasmon SPRi sensing on IDE arrays but stopped short of chemical functionalization of the surface for specific sensing.[466,467] Terao developed this technique for the monitoring of specific interactions between immunoglobulin G (IgG) and sensor-immobilized anti-IgG antibodies.[471]

To the authors' knowledge, this work represents the first time that LDW has been used to rapidly fabricate electrodes directly into an SPR sensor; and furthermore, the first time electrokinetic SPR imaging (EK-SPRi) has been demonstrated for parallel, multiplexed sensing with multiple probes of a clinically relevant, antibiotic-resistant strain of *Staphylococcus aureus*.

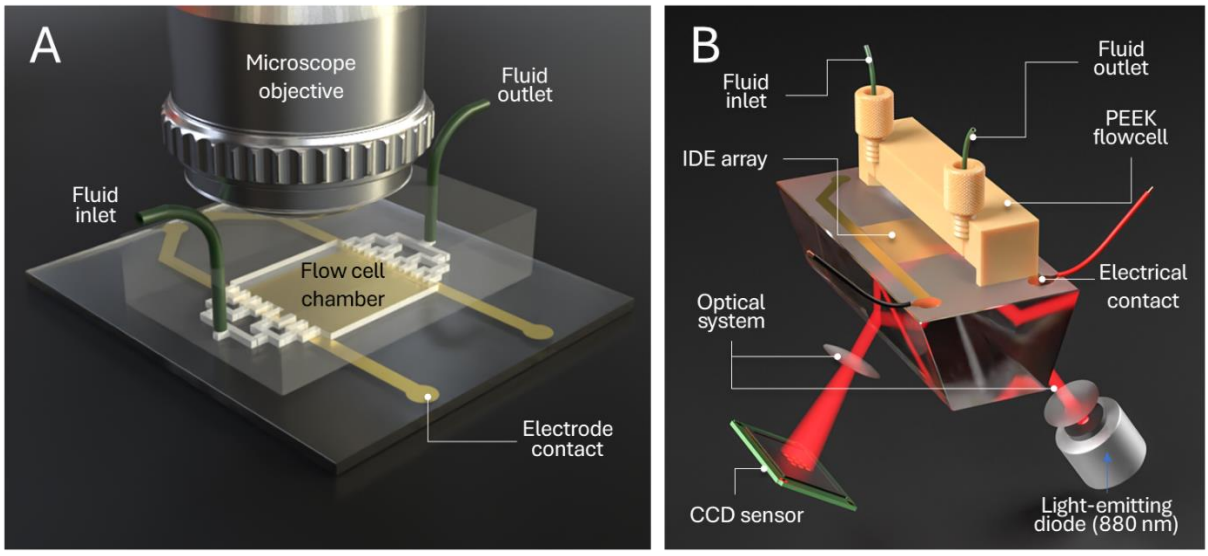

Figure 7.1 (A) An illustration of the electrotrapping experimental setup.An interdigitated electrode array was patterned into the surface of a gold-coated slide, interfaced with a PDMS flow cell, and observed by microscope. (B) Illustration of the electrokinetic SPR imaging system in the Kretschmann configuration with a cutaway of the flow cell.

7.2 Materials & Methods

7.2.1 Purchased materials

Dimethylformamide (DMF), dimethyl Sulfoxide (DMSO), ethanol (≥99.9%), glycerol (≥99%), phosphate-buffered saline (PBS), polydimethylsiloxane (PDMS; Sylgard 184), poly(ethylene glycol) methyl ether thiol (PEG-800), potassium nitrate (KNO_3), and trypticase soy broth (TSB) were purchased from Sigma-Aldrich (Saint Quentin Fallavier, France) and used without additional purification. 0.9% w/v NaCl solution (OTEC) was purchased from VWR (France). Deionized water (DIW; >18 MΩ resistivity) was obtained from an ELGA PURELAB flex dispenser (Veolia Water, France).

7.2.2 Peptide synthesis

Magainin was synthesized by Smart Bioscience (Saint Égrève, France) using a standard Fmoc solid-phase method described elsewhere.[111] The remaining peptides were synthesized by the 9-fluorenylmethoxycarbonyl/tert-butyl (Fmoc/tBu) strategy on RINK-amide resins on a Syro II peptide synthesizer (Biotage), followed by purification by reverse phase HPLC. Purity of synthesized proteins was confirmed by high-performance liquid chromatography and electrospray ionisation mass spectrometry. While magainin is conjugated *via* an L-cysteine amide on the C-terminus, the remaining peptides are instead conjugated *via* 3-mercaptoproprionic acid (3-MPA) on their N-terminus. Further information on antimicrobial peptides can be found in **Table A.8**.

7.2.3 Bacterial culture

Bacterial strain *Pseudomonas putida* (ATCC 12633) was obtained from the *Félix d'Hérelle Reference Center for Bacterial Viruses* of Université Laval, Quebec, Canada. Bacterial strain *S. aureus* subsp. *aureus* Rosenbach (ATCC 43300) was obtained from Microbiologics (Kwik-Stik™ lyophilized strains). Bacterial cultures were routinely prepared in TSB at recommended temperatures for each host: *S. aureus* at 37 °C and *P. putida* at 30 °C.

7.2.4 Preparation of gold substrates

Flat *D*263® glass slides coated with Cr/Au – 1.5 ± 0.5 nm / 55 ± 3 nm were purchased from SCHOTT and cleaved into 30×26 mm sections. Gold-covered SPRi biochips were purchased from Horiba Scientific (Palaiseau, France).

7.2.5 Rapid fabrication by laser ablation

Gold slides and prisms were both patterned in the same manner using a ProtoLaser S4 printed circuit board prototyper (LPKF, Garbsen Germany), which was initialized at least 20 minutes before use to allow the laser to reach stability.

Laser power was set to 5 W for hatching and 9 W for contouring. Both hatching and contouring were performed with a pulse frequency of 160 kHz. Insulation width was maintained at 15 µm. Several laser patterning parameters were varied in order to find the optimal conditions for reproduction of the smallest possible features of a pattern design. Parameters varied included the hatching overlap (10, 15, 20, or 25 µm), repetition of beam passes (1, 2, or 3 passes), and the direction of the beam (concentric, parallel, or perpendicular to the electrode axis).

The pattern design features 54 electrodes fingers, 27 connected to each of two separate opposing busbars (See annex **Figure A.4**). The busbar width was 1 mm to minimize voltage drop across this part of the circuit. The electrodes overlapped by 7.7 mm of their total 8 mm length. As well as varying fabrication parameters, the pattern design was also varied to include different electrode widths (30, 50, or 100 µm) and electrode separations (15, 20, 30, 40, and 50 µm).

After optimization of the patterning parameters, the best settings were used to produce electrokinetic SPRi prisms (EK-SPRi prisms)

7.2.6 Electron microscopy

In order to evaluate the fidelity to pattern designs and efficacy of removal of gold from ablated regions, scanning electron microscopy (SEM) was carried out on substrates produced by different patterning parameters. The surfaces were observed using a Zeiss Ultra 55 scanning electron microscope under a 2 kV acceleration voltage and working distance in the range 5-10 mm. Images were obtained with either an "in-chamber" secondary electron (SE) detector or an "in-lens" detector mounted inside the column, yielding greater topographical contrast.

7.2.7 Profilometry

Profilometry measurements were performed on patterned surfaces using a DektakXT profilometer equipped with a 12.5 µm-radius stylus applying a 3 mg stylus force. Measurements were taken both perpendicular and parallel to the electrode axes.

7.2.8 Simulation

Clausius–Mossotti (CM) factors were calculated using the software tool myDEP[481] for a range of carrier liquid conductivities and electrical field oscillation frequencies, using a two-shell cell model.[467]

7.2.9 Electrokinetic trapping and concentration

A microfluidic flow cell was produced by pouring vacuum-degassed PDMS over a stainless-steel mould, followed by curing at 80 °C for 90 minutes. The fabricated flow cell consisted of an inlet and outlet, each subdivided into 16 channels using 4 layers of T-junctions on either side of a main chamber 200 µm in height (**Figure 7.1**A). This geometry allows an homogenous flow of analyte through the chamber and thus over the IDE array.

The high reflectivity of the gold electrodes necessitated observation from above (*i.e.*, from the side of the PDMS circuit). However, the thickness of the PDMS necessitated a larger working distance than would be possible with a microscope objective that would permit the magnification needed to observe trapping of individual cells. To circumvent this, the patterned slide was interfaced with the PDMS flow cell and mounted in a microscope permitting single-cell resolution (× 500-600 magnification) over the width of one electrode finger while permitting a working distance longer than the thickness of the PDMS layer (**Figure 7.1**A).

Using a syringe pump (KDS 250 Nanoliter 4, KD Scientific), a flow rate of 0.4 mL/min was used to fill the PDMS circuit with bacterial suspensions, and a reduced flow rate of 0.1 mL/min during electrokinetic experiments. The salt concentration of the carrier liquid was varied between 1.54 mmol and 154 mmol NaCl (*i.e.*, physiological saline). Signals were applied between the IDE array contacts, controlled by a signal generator, and monitored using an oscilloscope (waveRunner 64Xi, Teledyne LeCroy). The resulting behaviour of bacterial cells during application of signals was observed and recorded by the microscope camera (Sony α7S).

Imagery was transcoded from Apple ProRes 422HQ using Davinci Resolve v17.4.3, with each frame extracted as a RGB colour TIFF. Frames were then processed by ImageJ (v1.53f51) to perform background subtraction and contrast adjustments.

7.2.10 Immobilization of peptides on electrokinetic prisms

The patterned gold surfaces of EK-SPRi prisms were rinsed with DIW, ethanol, then once more with DIW. EK-SPRi prisms were then dried with argon and plasma cleaned for 3 mins in 0.6 mBar 75:25 oxygen/argon mix at 80% power in a Femto plasma system (Diener electronic, Ebhausen, Germany) and the surface left to stabilize for 24 hours at room temperature.

The surface of each EK-SPRi prism surface was then functionalized with peptides using a protocol described elsewhere.[111] Lyophilized peptides were resuspended (Magainin in DMSO, others in PBS supplemented with 5% w/v glycerol) at 1-2 mmol and stored at −80 °C. 20 µL aliquots of peptides were sonicated for 10 minutes in an ultrasound bath to disaggregate them, then centrifuged for 2 000 *g* for 20 seconds at room temperature. Peptides were then diluted to 100 µmol by addition of aqueous solution of 15% w/v DMF, 15% w/v glycerol to make a final volume of 20 µL. Peptide suspensions were then once more centrifuged as before, sonicated a further 5 minutes as before, then centrifuged again before deposition on the prism surface.

The surface texture created by laser patterning caused deposited droplets to spread across the surface by capillary action. To permit localized functionalization, the EK-SPRi prisms surface was partitioned into sections by application of silicon grease using the edge of a microscope cover glass, creating a hydrophobic barrier on the surface to yield eight separated regions available for functionalization. 1 µL of each peptide suspension was pipetted onto a different region and the suspensions incubated with the prism surface for 18 hours at 25 °C in the dark in a humid environment inside a desiccator loaded with saturated KNO_3 solution (to produce 95% relative humidity).

The following day, the prism surface was rinsed with DMF then DIW. The prism was then dried with argon and immediately covered with 2 mmol PEG-800 aqueous solution and incubated for 2 hours at 25 °C in the dark in a humid chamber, blocking the surface. The prism was then rinsed with once more with DIW, dried with argon, and stored in air in a 50 mL Falcon tube in the dark at 4 °C for 24 hours before use.

7.2.11 Peptide-bacteria interaction monitoring by surface plasmon resonance imaging

The detection of immobilized AMP interaction with bacteria was performed using a commercial SPRi device (Horiba Scientific, Orsay, France) placed in an incubator at 30 °C. The SPRi chip was interfaced with a PEEK flow cell to allow interaction with the bacterial suspension (**Figure 7.1**B). The biochip surface was illuminated from below with polarized and collimated 880 nm light from a light-emitting diode. Monitoring of binding was performed using a CCD camera (Dolphin F-145B, Allied Vision, Stadtroda, Germany) with a fixed working angle of 52.78°.

An exponential-phase culture of *S. aureus* was pelleted by centrifugation at 5 500g at room temperature for 5 minutes, resuspended in 1.54 mmol NaCl solution to a concentration of 10^9 CFU/mL, centrifuged and resuspended a second time in 1.54 mmol NaCl, then adjusted to various concentrations between 10^6 – 10^8 CFU/mL and introduced to the sensor surface with a flow rate of 4 µL/s. Images were taken every six seconds.

In order to facilitate mass transfer to the surface, the frequencies established in earlier electro-trapping experiments were applied to the EK prism contacts. First, a signal of 100 kHz 5 V_{pp} is applied for 10 s to facilitate mass transport of bacteria from the analyte suspension (pDEP interval). Then, a signal of 10 kHz 5 V_{pp} is applied for a further 10 s in order to move any captured bacteria to the center of electrode fingers (ACEO interval). Finally, no signal was applied for 40 seconds to allow bacteria to interact with immobilized AMPs (interaction interval). These signals were applied in sequence of five cycles after each injection of bacteria and the SPR signal allowed to stabilize for 10 minutes to reveal any mass uptake on the electrode surfaces.

7.2.12 Data analysis

SPRi reflectance images were recorded with an SPRiLab SPR imager (Horiba Scientific, Palaiseau, France). Data were treated using SPRiView (v3.1.2) and processed using MatLab R2021a (v9.10). Regions of interest (ROIs) were manually identified during initialization of the SPRi experiment, chosen to correspond to the phage-functionalized regions of electrode centers of the surface.

Since the ROIs exhibited plasmon curves with different slopes at the chosen working angle (See annex **Figure A.6**), it was not appropriate to directly compare the changes in reflectivity between different ROIs but rather the shift in the plasmon curve corresponding to the reflectivity change. In order to calculate the plasmon curve shift, a B-spline was fitted to the plasmon curves observed at the beginning of the SPR experiment. This fit was then used to convert changes in reflectance to the real plasmon curve shift, expressed in degrees.

A one-minute rolling average of plasmon angle shift (*i.e.*, a mean of 10 data points) was plotted for analysis of interactions between AMP and bacteria. All curves were offset to zero approximately one minute prior to injection of bacterial suspensions, and corrected for baseline drift.

7.3 Theory

7.3.1 Principle of dielectrophoresis

Dielectrophoresis (DEP) is a phenomenon whereby particles in an electrolyte medium will experience a nett motive force in response to an inhomogeneous electrical field. For a homogenous particle, the time-averaged DEP force on a particle of radius *r* due to an electric field gradient $\nabla|E^2|$ is given by[482]:

$$\langle \vec{F}_{DEP} \rangle = 2\pi r^3 \varepsilon_0 \varepsilon_m Re\{CM(\omega)\} \nabla \left|\vec{E}\right|^2 \qquad (1)$$

Where ε_0 is the permittivity of free space, ε_m is the permittivity of the medium, and $Re\{CM(\omega)\}$ refers to the real component of $CM(\omega)$ — the *Clausius-Mossotti* (CM) *factor* as a function of ω, the angular frequency of oscillation of the electrical field.

Crucially, the force is proportional to the gradient of the square of the electric field but not on its polarity. This permits us to leverage DEP to concentrate bacteria from the bulk onto the electrode borders by applying an alternating current with a frequency that yields a positive CM factor.

For a given electrical field oscillation frequency, the sign of the CM factor depends strongly on the medium conductivity, the particle's geometry, and its electrical permittivity. **Figure 7.2** shows the balance of forces on a homogenous, spherical particle in an electric field gradient. When the particle is more polarizable than the surrounding medium, the resulting force is towards the region of high field gradient, a regime known as positive dielectrophoresis (pDEP). Conversely, a less polarizable particle than the surrounding medium experiences negative dielectrophoresis (nDEP) — a force away from the region of high field gradient.

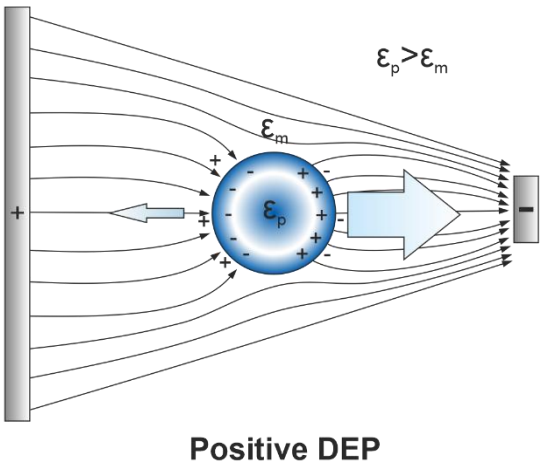

Figure 7.2 Schematic representation of positive dielectrophoresis for an homogenous, spherical particle in an electric field gradient. A particle that is more polarizable than the medium experiences a force towards the region of high electric field gradient.

While **Figure 7.2** depicts the case for a spherical and homogenous particle, the CM factor for a bacterium is more complicated since the cell is composed of a series of cell membranes enclosing a cell cytosol. Two bacterial strains were used in this work — *P. putida* and *S. aureus*. Although *S. aureus* is Gram-positive and so differs in cell wall composition compared to Gram-negative, *P. putida*; in practice the convention is to neglect the intermediate layer of Gram-negative bacteria from calculations of the CM factor since it is only 2 nm thick. This permits the use of a more simple, two-shell model for both bacteria, specifying a separate conductivity (σ) permittivity (ε) for each region of the cell.

In order to predict the correct signals to apply to the IDE array in order to manipulate bacterial cells, the software tool myDEP[481] was used to calculate the CM factor for *S. aureus* and *P. putida* over a range of carrier liquid conductivities and electrical field oscillation frequencies from 1 kHz to 1 GHz (**Figure 7.3**). A positive CM factor — and thus pDEP — was obtained in the frequency range 1 kHz to 100 MHz when the carrier had a conductivity lower than 0.2 S/m, which corresponds to an NaCl concentration of 17.1 mM or lower.

This provides a basis to estimate the experimental conditions necessary to facilitate pDEP and hence concentration of bacteria on the electrodes.

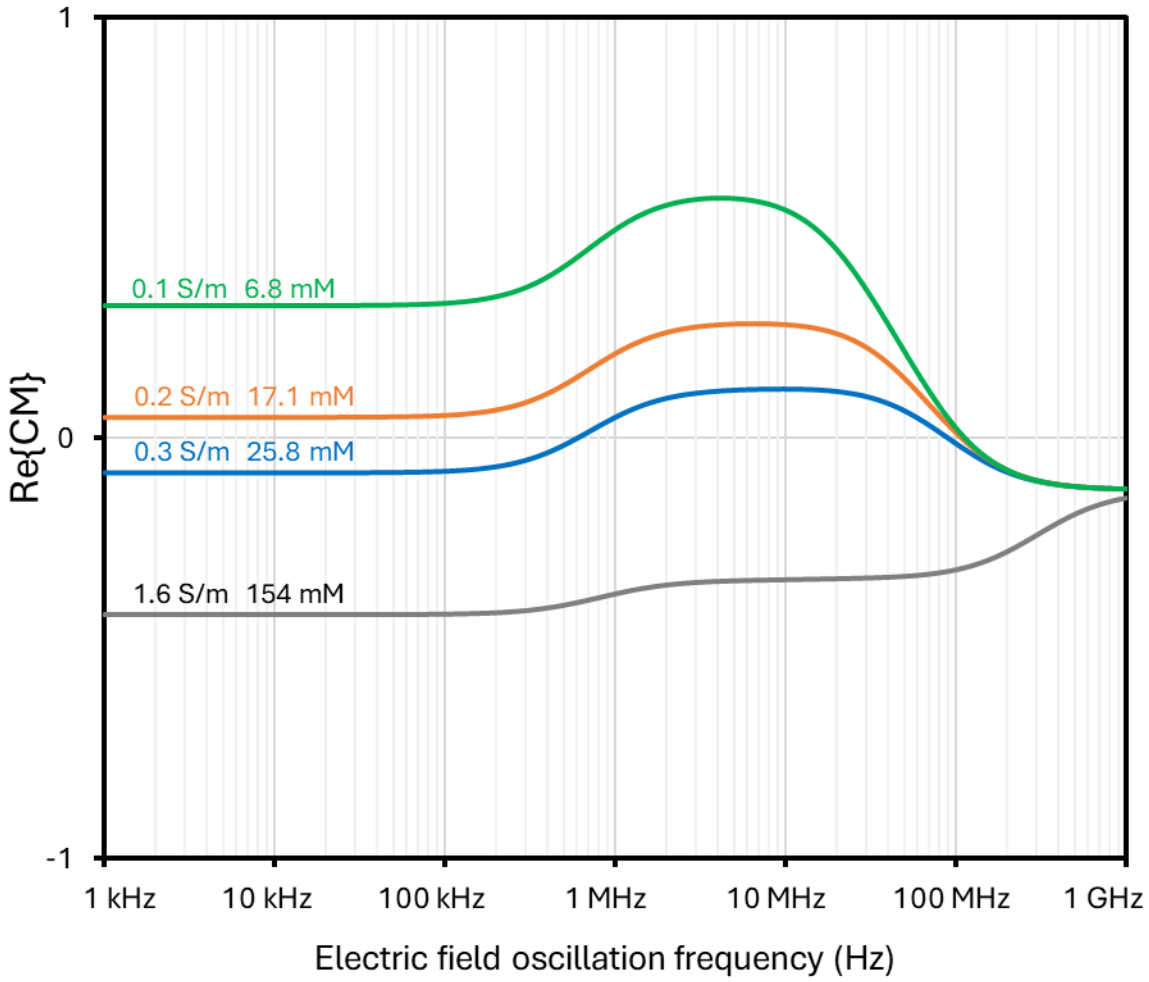

Figure 7.3 The Clausius-Mosotti (CM) factor, as calculated at a range of frequencies for various medium conductivities assuming a two-shell bacterium model and assuming a negligible volume fraction of the carrier liquid is occupied by suspended cells.An NaCl concentration of 17.1 mM (orange line) yields a positive CM factor over the entire frequency range from 1 kHz to 100 MHz, and thus permits a positive dielectrophoretic force on bacteria.

7.3.2 Principle of alternating current electro-osmosis

In contrast to DEP — which acts on the cells directly — ACEO acts on the carrier liquid itself, creating a current of ions perpendicular to the long axis of the electrode fingers which entrains the carrier fluid — and in turn any suspended particles — *via* drag forces.[483]

A solid surface immersed in an electrolyte presents a given surface potential V_0 and thus spontaneously develops an electric double layer. When a rapidly changing potential is applied between two adjacent electrodes, the surface does not discharge everywhere simultaneously, leading to a tangential component of the electric field $\vec{E}_{||}$. Non-hydrated, charged ions of the medium in the double layer are accelerated by this electric field, away from electrode borders and towards the electrode center.[483]

Ramos *et al.* gave an expression for the fluid velocity $\vec{v}$ across the electrode surface as a function of $\vec{E}_{||}$, the charge density of the double layer σ_q, and the viscosity η:[484]

$$\vec{v} = \frac{\vec{E}_{||}\sigma_q}{\kappa\eta}$$

The fluid velocity thus depends on both the conductivity and the frequency of electric field oscillation. In order to leverage the ACEO effect, a non-zero minimum conductivity is required and the signals applied to the electrodes must be within the frequency interval permitting ACEO.

7.4 Results

7.4.1 Electrode patterning

In order to optimize IDE fabrication, electrodes were fabricated with various parameters, imaged by SEM, and compared based on several figures of merit including fidelity to the original CAD design, minimal electrode width and separation, and presence of residual metal in ablated regions or redeposition on un-patterned regions.

Initial patterning attempts made use exclusively of the 'contouring' tool with a concentric path, which specifies a beam route that hugs the periphery of unablated regions and uses a moderate power of 9 W compared to the device's maximum of 12 W, which is normally reserved for milling through the entire substrate thickness.

SEM analysis of these initial patterning experiments revealed that the CAD pattern was reproduced on the surface with reasonable fidelity with an electrode width of 110 µm and electrode separation of 37 µm (**Figure 7.4**a and b). Furthermore, gold was effectively removed from between the electrodes. Electrical isolation of the IDEs was later confirmed with a multimeter, which showed no short circuit between opposing electrodes. This first result was all the more interesting since patterning with these settings took approximately 12 seconds.

However, artifacts were observed in certain regions of the IDE array where the pattern geometry necessitated a tight turning circle of the beam path (**Figure 7.4**a and b). At the electrode extremities, in between the end of each electrode and the opposing busbar, the concentric contouring tool failed to remove the metal and instead produced a repeated oval motif of resolidified material (**Figure 7.4**b). The concentric contouring also failed to remove material at "corners" in the beam path (**Figure 7.4**a). Also, although the CAD design specified flat electrode tips, the electrode fingers took on a rounded shape and greater width than the CAD design (**Figure 7.4**b). We attributed this to an overshoot of the beam as the device attempted to round the corner at the end of each electrode.

While the metal in between the electrodes was observed to be entirely removed, the electrode borders seem to be subject to pure melting rather than ablation[485], with surface tension of the transiently molten metal forming a 2-4 µm-wide ridge during resolidification.

To explore the possibility of improving electrode geometry and push the resolution limits of the device, subsequent experiments explored the use of multiple repetitions and alternative beam paths. Since it has been shown that reduction of electrode width and separation improves sensitivity with some transduction methods (*e.g.*, impedance[461,486] capacitive sensors[487]), we sought to find the limit of minimum feature size producible with laser ablation in order to demonstrate the wide applicability of this method to a variety of sensor types.

Following the contouring tool with a 'hatching' tool resulted in improved electrode geometry. The hatching tool used a lower power of 5 W and specifies a rastering beam path that proceeds line-by-line across the substrate surface, activating the laser only when over a region marked for ablation by the software. Electrodes of width as thin as 15 µm can be achieved in this way (**Figure 7.4**d), much smaller than the 50 µm minimum conductor trace width specified by the manufacturer. However, due to the overshoot problem, the electrode bulges to ~20 µm for the last 200 µm of the electrode length.

Rather than a minimum electrode width, the limiting factor with this device was found to be the finite minimum width of the ablated region. The software of this device (tool library version 0.3.11) will not translate hatching overlap of smaller than 15 µm to the substrate, and instead fails to remove material between electrodes with these settings. Setting the hatching instead to 20 µm is necessary to yield the minimum observed electrode separation of 35 µm. This is reasonable since the manufacturer specifies a minimum focused beam diameter of 20 ± 2 µm.

A poor result was produced when repetitions of two or three passes were specified, since slight variation in the substrate/beam alignment between passes resulted in unpredictable removal of material from the electrode fingers (**Figure 7.4**c). It was unclear whether this was due to uncontrolled movement of the substrate relative to the stage, or rather poor translational precision of the stage actuators.

Surprisingly, an improvement was observed when using a hatching path that rastered perpendicularly rather than parallel to the electrode axis (See annex **Figure A.5**). It was expected that a parallel beam path (*i.e.*, following the electrode axis) would provide superior results, but instead was found to ablate a wider region and lead to more deposition of metal on un-patterned regions. This may be because a parallel beam path results in the ablation being initiated in adjacent regions consecutively within 6.25 µs, which is of the same order of magnitude as the time scale of heat dissipation out of the focal volume of the laser[488], which may result in energy input into metal that is still molten from ablation of an adjacent region. In contrast, if using a perpendicular beam path, immediately adjacent locations between electrodes are not removed consecutively and instead have time to reach thermal equilibrium with the bulk of the substrate before the next beam pass. We posit that redeposition of gold on un-patterned regions was minimized when a perpendicular (**Figure 7.4**f) instead of parallel hatching path was used (**Figure 7.4**e) because molten metal had an opportunity to cool before return of the beam.

Regardless of tool settings, the formation of a ridge persisted at the electrode boundary as a result of ablation of adjacent metal (**Figure 7.4**e and f), accompanied by a modified surface texture due to transient melting and resolidification (**Figure 7.4**f, black arrow).

Finally, optimal settings were found that resulted in efficient removal of gold from the glass, minimized redeposition of ablated material, and produced consistent electrode widths. For subsequent SPR experiments, IDE arrays were produced 85 µm width electrodes with 45 µm spacing (**Figure 7.4**g).

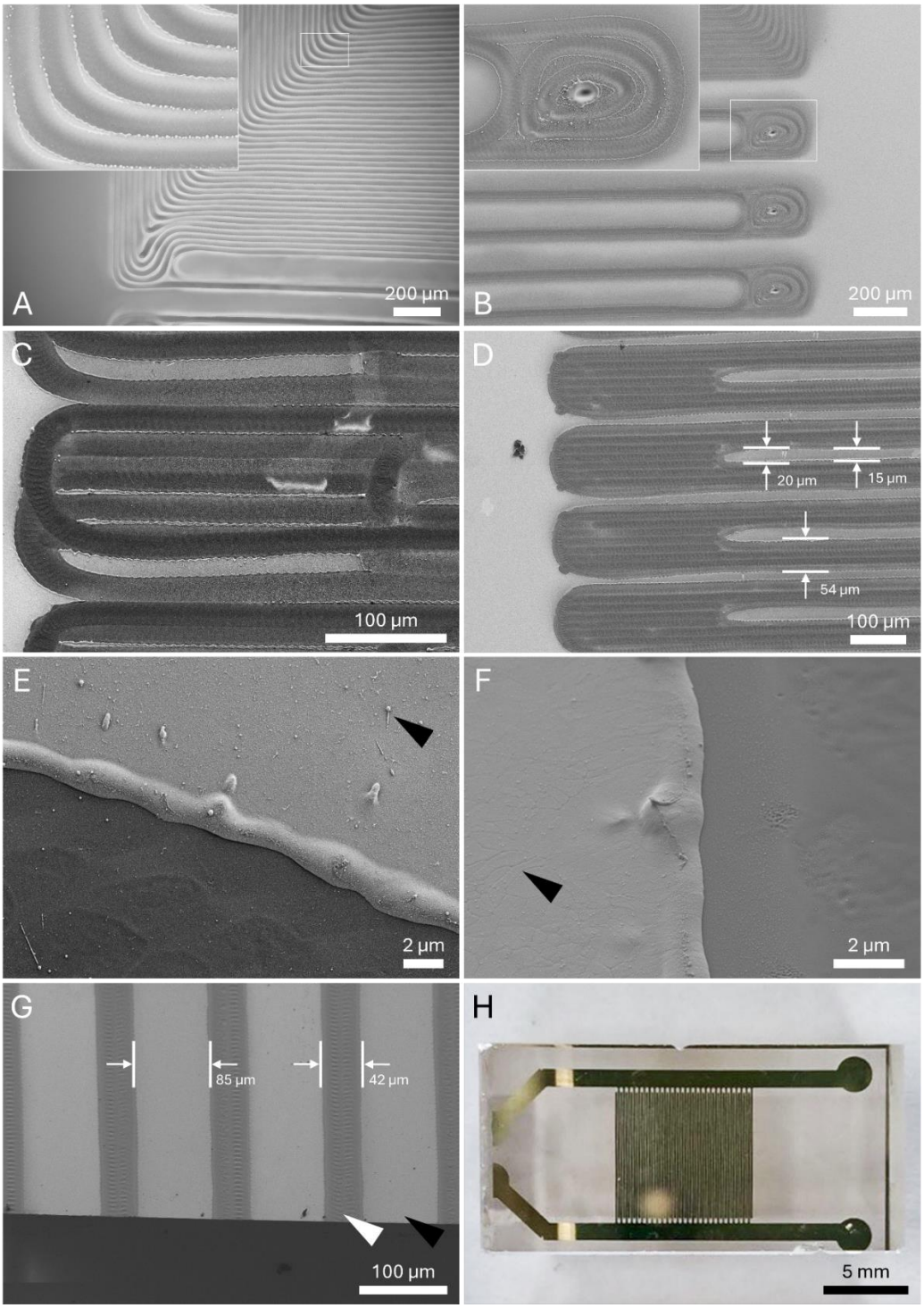

Figure 7.4 Collage of scanning electron micrographs of IDE arrays resulting from various patterning parameters.(A) Far from the electrode fingers, the concentric contouring path leaves residual metal on the surface where successive passes fail to overlap. Inset shows that this phenomenon is most pronounced in regions where the beam path exhibits high curvature. (B) The concentric contouring path also fails to completely remove metal between the end of each electrode and the opposing busbar. Inset shows detail of the repeating oval motif of resolidified metal. (C) Multiple repetitions of the contouring and hatching paths are poorly superimposed, leading to a failure to transfer the design to the substrate. (D) Combining a contouring pass with a parallel hatching pass can produce electrodes with a width as thin as 15 µm. (E) Electrode boundaries exhibited a raised profile up to 300 nm above the surface and extending up to 4 µm into un-patterned regions. Redeposition of removed metal was observed in surrounding areas (black arrow). (F) Use of a perpendicular hatching path reduced deposition in un-patterned regions but did not mitigate the increased metal thickness at the boundaries. (G) An edge-on cross-sectional view of uniform electrodes of 85 µm width (black arrow) and 42 µm separation (white arrow), fabricated for use in subsequent surface plasmon resonance experiments. (H) A typical patterned SPRi prism that results from laser ablative patterning.

7.4.2 Profilometry

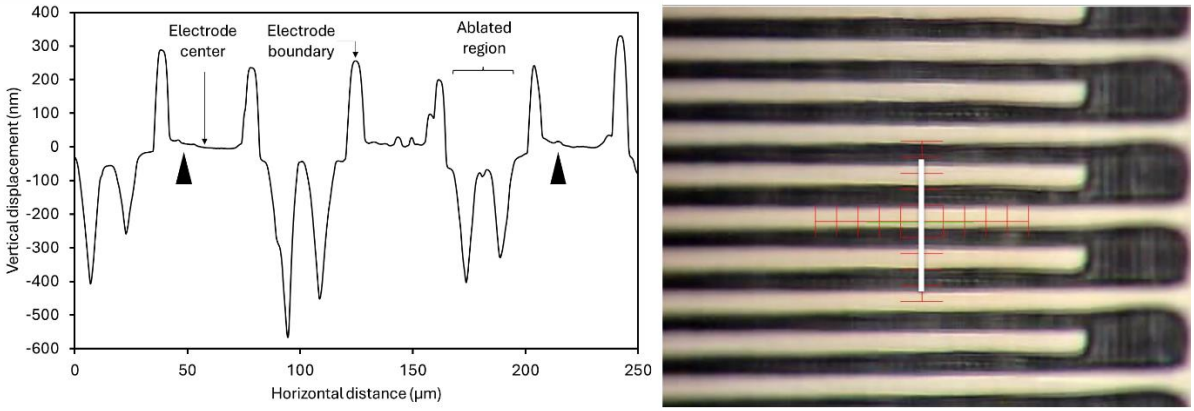

Figure 7.5 Left: Profilometry analysis of a patterned gold-covered slide, showing the profile perpendicular to the electrodes.Black arrows indicate a small increase in metal layer thickness that extends approximately 15 µm from the boundary towards the electrode center. Note the different scales on the x and y axes, which greatly exaggerates the vertical displacement. Right: Optical microscopy of the region measured. The location of the measured profile is indicated (white line).

In order to obtain a more quantitative picture of the patterned surfaces, profilometry was performed on a patterned slide with 50 µm-wide electrodes. The electrode boundaries were observed to rise approximately 300 nm above the surface, a significant departure from the 56.5 nm nominal thickness of the original metal layer (**Figure 7.5**). While profilometry appears to indicate that the boundary ridge of 8 µm width, this is not in agreement with SEM imagery of the same regions (**Figure 7.4**e and f). It is likely that the width measured by profilometry was an artifact stemming from a convolution of this surface feature with the 12.5 µm-radius stylus tip, giving an erroneous result for the lateral dimension of the ridge. Instead, we conclude that the vertical displacement of up to 300 nm obtained by profilometry is reliable, while the lateral width of the boundary ridge should instead be measured from electron micrographs (**Figure 7.4**e and f), indicating a ~3 µm-thick ridge 300 nm in height.

Also observed was a region that extends ~15 µm into the electrode with a smaller departure from nominal thickness of ~20 nm (**Figure 7.5**, black arrows). Favouring electrodes with a width larger than ~50 µm allows rapid fabrication of electrodes with a central region with nominal metal layer thickness unaffected by the ablation process.

In between the electrodes were observed the same repeating circular motif as in SEM, originating from the firing pattern of the laser which removes some glass material below the gold layer to a depth of 200-600 nm. For the purposes of IDE fabrication, the removal of some glass is not deemed to be problematic since this region is not active for surface plasmon resonance nor is it targeted for functionalization.

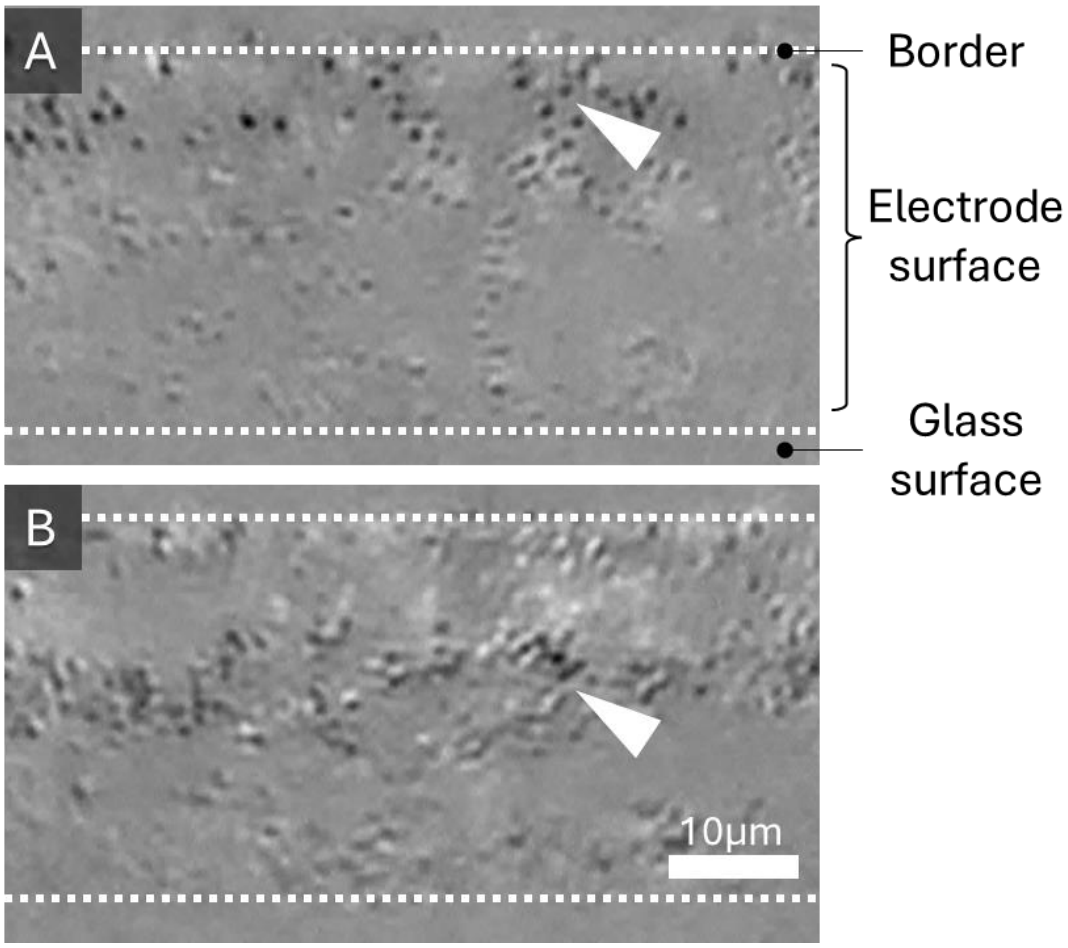

Figure 7.6 (A) Upon introduction of the *P. putida* and application of alternating electrical signals to the electrode contacts, bacteria (white arrows) were observed to be concentrated at the electrode borders or (C) displaced to the electrode centers, depending on the applied frequency.

7.4.1 Electrotrapping

In order to confirm the ability of the patterned electrodes to concentrate bacteria from the carrier liquid by pDEP and displace them to the electrode centers using ACEO, a glass slide featuring a patterned IDE array was interfaced with a microfluidic circuit and exposed to *P. putida* at a concentration of 10^8 CFU/mL in carrier liquid of varying ionic strength (0.15 – 15.4 mmol NaCl).

Electrotrapping experiments were performed with *P. putida* as a surrogate for *S. aureus* since the latter is a biosafety level 2 (BSL-2) organism, which prohibits manipulation in lower BSL facilities. Use of *P. putida* simplified manipulation during optimization of applied signals.

Informed by calculations of the CM factor, signals of up to 14 V peak-to-peak (V_{pp}) and frequency between 5 kHz 200 kHz were applied to the electrode contacts and the resulting movement of bacteria observed by optical microscopy.

In this frequency interval, both pDEP and ACEO are expected to occur in superposition, but the balance between them was found to vary depending on the applied frequency. At 100 kHz and above, bacteria were observed to be congregate on the electrode borders within one second. Reducing the signal towards 10 kHz was found to progressively alter the balance of pDEP and ACEO forces, permitting the displacement of bacteria towards the center of the electrode (**Figure 7.6**).

The combination of this amplitude and range of frequencies has been shown in similar conditions not to result in electrochemical oxidation of the electrodes.[471]

7.4.2 SPRi

In order to validate the sensing ability of the EK-prisms, an SPRi prism surface was double functionalized, first by patterning to create an IDE and then chemically by covalent immobilization of an array of five AMPs with known affinity to *S. aureus* (the challenge bacteria): bactenecin[489] and a bactenecin derivative[490], cecropin A-melittin[491], penetratin[492], and magainin[493].

A suspension of *S. aureus* was resuspended in 1.54 mmol NaCl solution and introduced to the sensor surface using a microfluidic flow. Following application of signals to the IDE array, a persistent plasmon resonance angle shift was observed on regions functionalized with AMPs, indicating mass uptake on the surface (**Figure 7.7**). The degree of shift increased with increasing concentration of bacteria in the range 10^6-10^8 CFU/mL. Application of alternating current to the IDE array results in a transient change in the reflectivity, most likely to Joule heating.

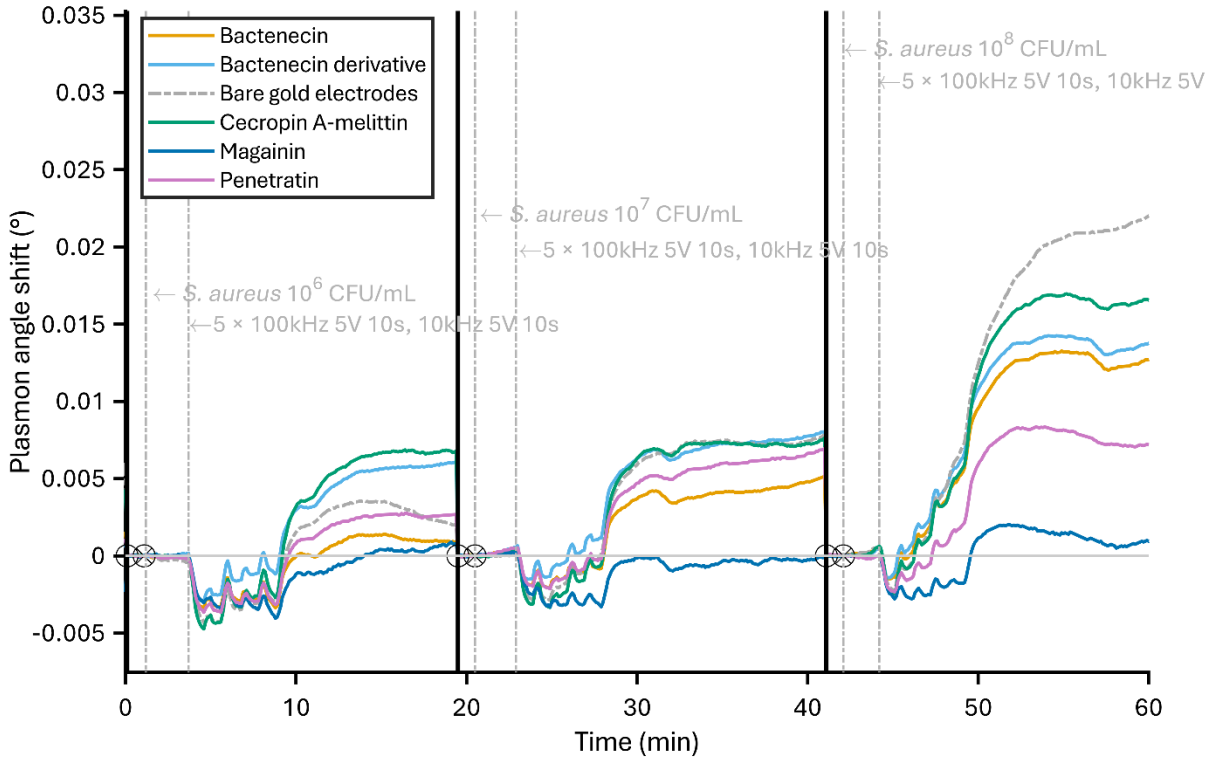

Figure 7.7 Surface plasmon resonance sensorgrams showing the response of patterned sensor surfaces, functionalized with antimicrobial peptides, to injections of *S. aureus* at 10^6, 10^7, and 10^8 CFU/mL.Following each injection of bacteria, five cycles of the following sequence are applied to the surface electrodes: 100 kHz 5 V_{pp} 10 s then 10 kHz 5 V_{pp} 10 s. Sensorgrams represent a one-minute rolling average and have been offset to zero (×) and baseline drift corrected (◯) before each injection. Each trace is a mean of 16-20 replicate regions, depending on immobilized species.

Bactenecin and penetratin regions were observed to monotonically increase in signal with increasing bacterial concentration. In contrast, magainin was found to interact very little to the presence of this strain of MRSA, in agreement with the findings of Pardoux *et al.*[111] Interestingly, the bactenecin derivative and cecropin A-melittin hybrid regions appear to yield similar signals upon injection of 10^6 and 10^7 CFU/mL, but increase significantly after injection of 10^8 CFU/mL.

Aside from the SPR response to injection of bacteria, significant modification of the plasmon curve was observed from the beginning of the experiment for the patterned electrodes relative to an unpatterned surface. The center of electrodes exhibited a plasmon curve with a useable linear region between 51° and 53°, while the electrode borders did not yield a plasmon effect within the range of angle swept by the SPR device (**Figure 7.8**). This marks a significant change to the plasmon curve relative to the unpatterned gold surface, which instead presents a reflectance minimum around 58° under the same experimental conditions (See annex **Figure A.6**).

Surface plasmon propagation length is about 25 µm for 800 nm light. This places a limit on the spacing of electrodes, but only in the direction parallel to plasmon propagation.[107] This necessitates orienting the electrodes parallel to the direction of incident light.[494]

This observation is consistent with the increased thickness of electrode borders observed in SEM and profilometry. For the purposes of SPRi sensing, this did not present an issue since the borders are expected to interact with bacteria only during the pDEP interval. During the ACEO interval, bacteria are instead brought to the electrode centers, where plasmon resonance allows monitoring of surface phenomena at the chosen working angle.

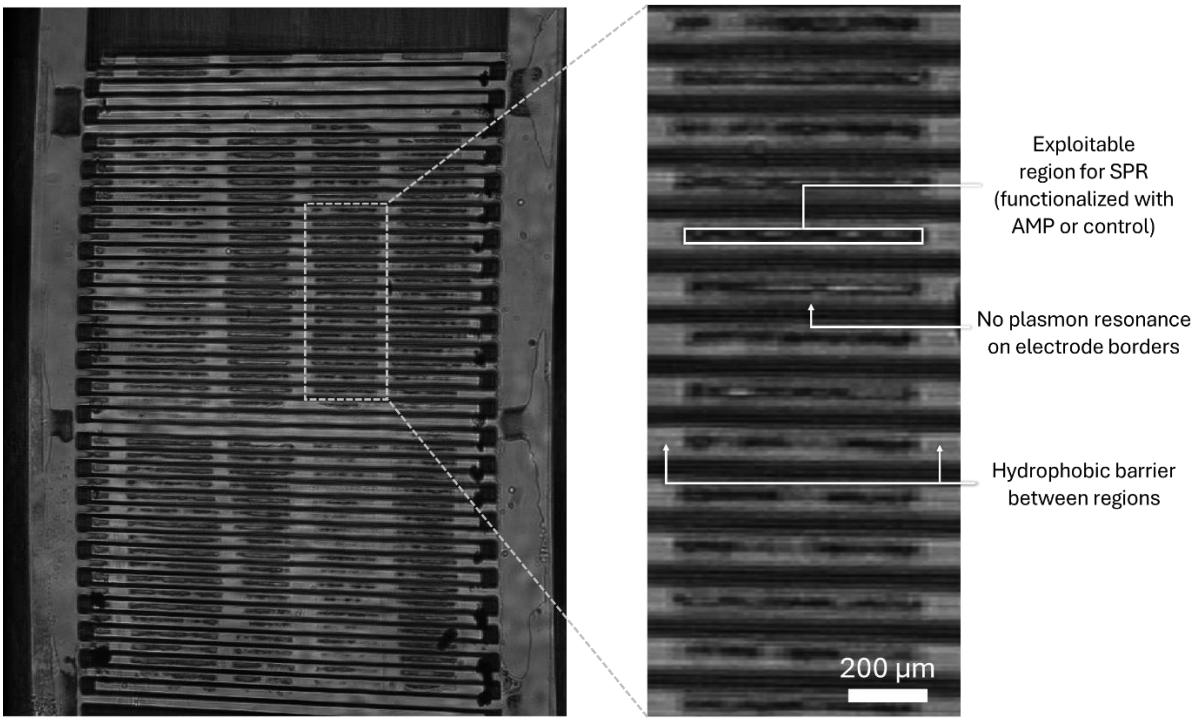

Figure 7.8 Left: The fabricated IDE array as observed by SPRi. Hydrophobic areas form a grid which delineate regions functionalized with different peptides. Right: Detail of one region, showing the plasmon resonance effect only in the center of each electrode.

7.5 Discussion

While laser ablation has been exploited for patterning of electrodes previously[476,477], the applicability of this method to the wider scientific community has to date been limited due to the hurdle of developing a custom optical setup. The advent of commercial LDW solutions democratizes access to this form of rapid prototyping, at least in terms of the skills required if not from a financial perspective. The presented method presupposes access to a PCB prototyper, which represents a significant up-front capital investment. Yet, in comparison to the cleanroom infrastructure, lithography equipment and chemical handling training necessary for traditional IDE fabrication methods, the purchase and maintenance of a PCB prototyper may still present cost savings in addition to the significant reduction in demands on a researcher's time.

While this work demonstrated the compatibility of laser patterning of IDE arrays with plasmonic biosensing, the results are presented as an alternative to traditional fabrication methods for these structures more generally. Due to a reliance on coupling of photons to surface plasmon polaritons, the SPR sensing method demonstrated in this work places especially stringent requirements on electrode smoothness and geometry, which may not apply for other applications of IDE arrays such as capacitive and impedimetric sensing. If the artifacts observed with only a contouring pass are not deemed problematic for a given application, an IDE array can be patterned in a gold surface in as little as 12 seconds with our method, which is difficult to improve upon even with the most rapid of alternative strategies. Electrodes of width 15 µm and larger can be easily achieved with this method, while retaining compatibility with popular gold-thiol conjugation chemistry.[133]

In this work, no attempt was made to modify the device control software, yet there are surely improvements to be made on our results if software-level limitations can be relaxed, for example by removing minimum allowable hatching overlaps.

These patterning results should be compared with IDEs produced by other rapid fabrication methods. One proposed alternative to lithography is inkjet printing of nanoparticles, as demonstrated by Tran *et al.*[473] While this method presents advantages such as being non-lithographic, maskless, and vacuum-free — the resulting electrode geometry was of much poorer quality than with our method, yielding much larger boundary ridges 40 µm in width and 42 nm thicker than the electrode center. Inkjet printing also necessitated a post-deposition curing step which had a strong determinant effect on the conductivity, potentially introducing unwanted variability. Furthermore, the printer struggled to reproduce edges that were not aligned with the printhead direction, for example with curved boundaries. In comparison, the ability of the PCB prototyper beam to follow contours of the design geometry has an advantage since it does not introduce pixelation into the resulting pattern in the substrate, which may more faithfully reproduce curved or diagonal features.

Gaál *et al.* demonstrated IDE fabrication using fused deposition modelling (FDM) of graphene-doped thermoplastic.[474] While this method was rapid and produced IDEs in only six minutes, the electrodes are quite large in all dimensions with a thickness, width, and separation all on the order of 1 mm.

A further advantage of the method presented in this work is its feasibility not only for rapid prototyping, but also a moderate level of scalability to small volume production. Once a desired design has been identified, a single user can produce hundreds of patterned substrates in an afternoon with minimal changes to their workflow.

For example, with little regard for conserving material, we were able to create three different IDE array patterns, each with many different electrode spacings, into a single gold-coated microscope slide in as little as 10 minutes. By far the longest part of the fabrication workflow involved specifying the patterns in a CAD program, which can also be done in minutes.

SPRi prisms of the type used in this work are relatively expensive with a cost on the order of €100 per unit. For this reason, it is common practise to instead functionalize a cheaper gold-coated slide, which is then interfaced

using an index matching gel with an un-metallized prism that is permanently mounted in an SPR device.[107] As shown in this work, the laser ablation method is compatible with both types of consumable.

During electro-trapping experiments, the observed progressive movement of bacteria towards the center of electrodes as applied frequency was reduced from 100 kHz to 10 kHz conforms with the frequency dependence of electro-osmotic velocity, which is maximal around 1 kHz and decreases almost to zero between 1 kHz and 100 kHz.[483]

The choice of 1.54 mmol NaCl as the carrier fluid was four-fold: it permitted a minimum mobile charge carrier density to enable ACEO[483], to yield pDEP within the desired frequency range, to minimize hypo-osmotic shock to the bacteria, and finally to minimize the oxidation of the gold film as a result of the applied alternating current.[471]

SPRi has previously been demonstrated for the specific detection of bacteria using arrays of immobilized antimicrobial peptides.[111] However, the time-to-results with this method was long, taking several hours to reveal interactions between AMPs and challenge bacteria.

We improved on this method by removing the diffusion limitations to SPR assay sensitivity.[466] This work directly showed detection of *S. aureus*, a realistic target analyte by virtue of its antibiotic resistance and status as a clinically relevant member of the ESKAPE group of pathogens.[9] A set of AMPs with known affinity to the challenge bacteria were chosen: bactenecin[489] and a bactenecin derivative[490], cecropin A-melittin[491], penetratin[492], and magainin[493]; and were immobilized using a method previously demonstrated elsewhere.[111]

The results of this work should be compared with previously demonstrated incorporation of electrokinetic mass transport into plasmonic sensors. A pair of articles have described a form of SPRi on an IDE arrays but stopped short of (bio)chemical functionalization of the electrodes for specific sensing.[466,467] Terao *et al.* recently demonstrated an electrokinetically active SPR sensor for the specific monitoring of molecular interactions, but dedicated the entire sensor surface to one probe and did not extend the technique to multiplexed SPRi.[471] The ability to monitor interactions between immobilized AMPs and bacteria with the patterned IDE array demonstrates the compatibility of this method of fabrication with SPRi sensing.

7.6 Conclusion

In this work we demonstrated the feasibility of leveraging commercial laser ablation equipment for rapid fabrication of micro-scale electrodes, yielding electrode widths from 111 µm down to 15 µm and electrode separation as small as 35 µm with total fabrication times as short as 12 seconds for a substrate area of 1 cm^2, with a potential for scaling to a very large surface area limited only by the 229×305 mm working area of the prototyper. It is a single-step, mask-free, and vacuum-free technique that requires no curing step or cleanroom infrastructure. Since no photolithography is performed, there is no danger of residual photoresist remaining on the surface which could otherwise adversely affect the surface characteristics and interfere with (bio)chemical functionalisation.[133]

The method was then exploited for patterning of IDE arrays directly into gold-coated slides and off-the-shelf SPRi prisms. The patterned substrates were shown to be capable of electrokinetic mass transport of bacteria by dielectrophoresis and manipulation of the cells on the sensor surface by alternating current electro-osmosis.

The IDE arrays were then biofunctionalized with an array of various antimicrobial peptides and used to demonstrate for the first time the multiplexed biosensing of *S. aureus* by electrokinetic surface plasmon resonance imaging.

The fusion of rapid prototyping, electrokinetic manipulation, and plasmonic sensing represents an intriguing integration of mature and nascent technologies and opens up promising avenues for a new generation of electrokinetically active SPR sensors.

Chapter 8

Conclusions & Outlook

8.1 Summary

In this work, a novel bacteriophage susceptibility testing modality was proposed, based on SPR monitoring of interactions between immobilized phage and challenge strains of bacteria.

SPR exhibits high sensitivity within the penetration depth of an evanescent field (a few hundred nanometers) which necessitates immobilization of probes at a metal-analyte interface. The cultivation of phages involves the lysis of host bacteria and the generation of large amounts of debris which must be separated from the phages before immobilization chemistry can be performed on them, an exercise that proved to be far from trivial.

Several methods were explored for purification of phage gh-1, including ultrafiltration, density gradient ultracentrifugation, PEG-precipitation, and tangential flow filtration. The comparison was made based on figures of merit such as a high level of infectious titer, low aggregation of phages, and consistent removal of contaminants from the phage lysate. While no one method satisfied all criteria, a combination of these methods was found to yield highly pure and monodisperse phage suspensions that retained their infectivity.

A review of the phage immobilization literature informed the selection of a set of strategies that were explored for the immobilization of phages on gold substrates. After comparing the results of different immobilization methods, the tried-and-tested thiolated self-assembled monolayer was shown to produce a dense, homogenous layer of infective bacteriophages on gold substrates.

This immobilization chemistry was then employed for the micro-arraying of multiple phages on the surface of a sensor exploiting SPR for parallel, multiplexed monitoring of phage-host interactions. This SPR sensor was shown to reveal specific interactions between phage 44AHJD and its host *S. aureus*; and between phage gh-1 and its host *P. putida*.

During the course of experimentation, it was noticed that phage titer unexpectedly dropped while in storage, occasionally leading to failures in phage culture or functionalization of substrates. A large-scale, multi-week experiment was carried out to investigate the root cause of this phenomenon. Complementary plaque-counting measurements and nanoparticle tracking analysis of phage suspensions revealed new insights into multi-modal loss of infectious titer due to adsorption, inactivation, and aggregation — which was found to vary as a function of container material.

In the interest of improving the sensitivity of plasmonic sensing, a novel SPR sensor was conceived, which featured an embedded interdigitated electrode array (IDE) to permit electrokinetic mass transport of analyte to the sensing region. To produce IDE arrays on SPRi prisms, a novel rapid prototyping method was developed based on laser ablation with a commercial printed circuit board prototyper. The resulting electrokinetic SPR (EK-SPR) sensor was demonstrated for the detection of *S. aureus* by leveraging the affinity of an immobilized array of antimicrobial peptides.

8.2 Outlook

8.2.1 Future of the SPR phagogram

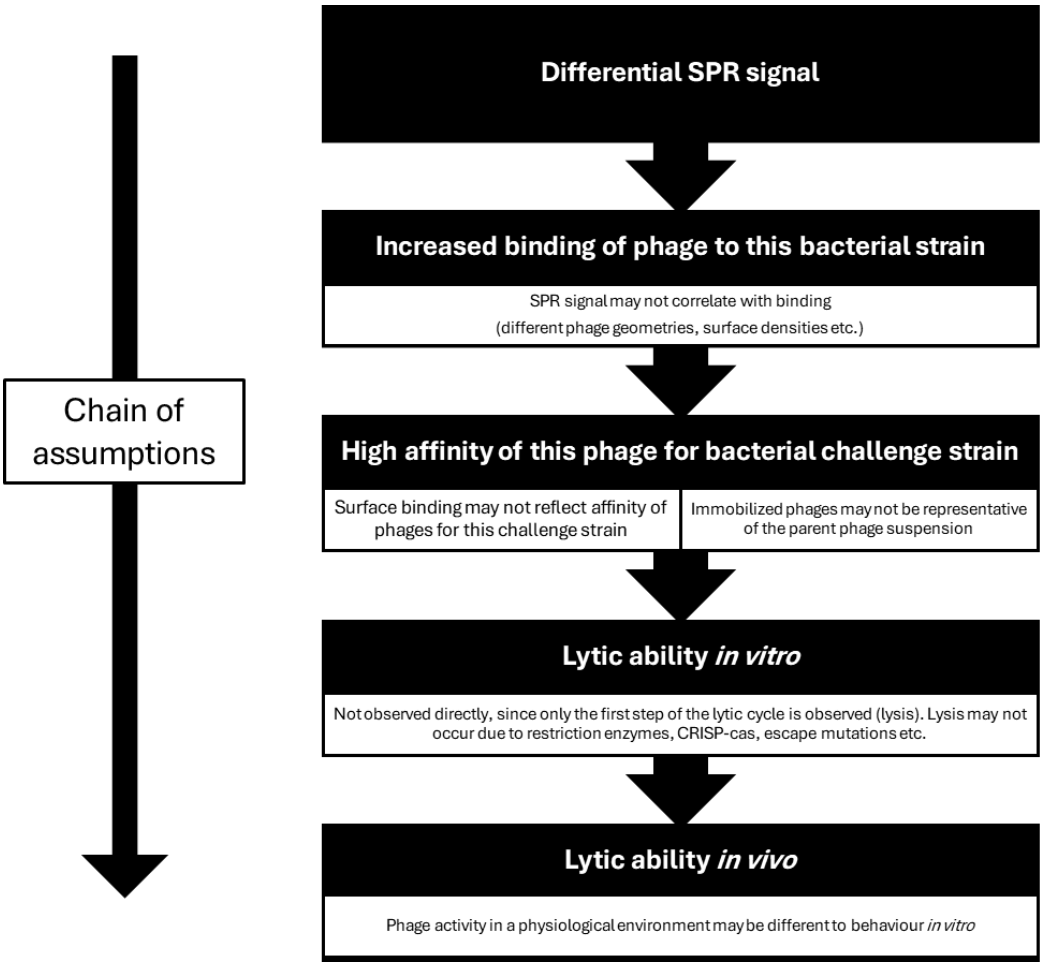

Figure 8.1 The chain of assumptions linking the SPR signal to phage susceptibility *in vivo*.Each step represents a proximal measure of the following quantity. Potential confounding factors in interpretation of the SPR phagogram are detailed in the inset of each step.

While a proof-of-concept of the SPR phagogram was demonstrated in this work, some limitations of the method should be considered. The SPR phagogram relies on the transduction of the interaction of the phage receptor-binding domains with structures of the exterior of the host bacterial cell. The host range of the immobilized phage is thus inferred from a difference in reflectivity relative to regions functionalized with a different phage. However, binding of the host bacterium is only the first step in the lytic cycle. Phage replication can be interrupted by a number of host defense mechanisms (*e.g.*, the CRISPR-Cas system, restriction enzymes etc.)[88,207] and so it is difficult to directly infer lytic capability from initial binding (**Figure 8.1**).

This may lead to false positive results, where a bacterial strain appears to be susceptible to a given phage but is in fact resistant. Such false positives would have an obvious impact on clinical outcomes for patients inadvertently treated with ineffective phage.

A potential improvement on the SPR phagogram would more directly link the successful lysis of bacteria to a measurable signal, while retaining the ability to monitor phage-host interactions for an array of many different candidate phages in a physically compact form. A technology that may enable such an improvement to the phagogram is lens-fee imaging.

8.2.2 Lens-free microscopy for phage susceptibility testing

A recent publication details the use of wide-field, lens-less imaging for the purposes of PST.[420] In this method, a monochromatic point light source is used to illuminate a bacterial lawn inoculated with lytic phages, which is placed in close proximity to a CMOS sensor. Lysis of the bacteria is detected as the appearance of transparent regions in the bacterial lawn, which can yield a phage susceptibility result in three hours, a substantial improvement in time-to-results compared to current PST methods (see 1.3 State of the art).

Experiments developing this concept were pursued as part of this PhD. A method was conceived which permits the monitoring of an array of phage-host interactions with a lens-free microscopy system. Promising preliminary results with a proof-of-concept device yielded a phage susceptibility result in as little as 90 minutes with room for improvement after further optimization of the concept. Since a patent application is currently in preparation on the basis of this work, it was not possible to describe these experiments in this manuscript due to confidentiality.

8.2.3 Rapid fabrication and electrokinetically active plasmon sensing

Recent publications speak to the active interest in improving plasmonic sensing by leveraging electrokinetic effects.[466,467,471] The laser patterning method demonstrated in this work removes barriers to development of the EK-SPR concept. Further optimization of the laser ablation method is very likely to result in further improvements to the quality of the resulting IDE arrays. Altering the beam power and other parameters may avoid the formation of a boundary ridge or changes in metal crystallinity which could yield more surface area available on the EK-SPR sensor surface for the immobilization of probes.

Addition of multiple electrical contacts in the electrode array design would permit the creation of different electrical regimes on the sensor surface, potentially permitting dielectrophoretic cell-sorting of different components of a complex analyte to different regions of the sensor surface (*i.e.*, de-complexification).[495,496] Using the example of blood testing, tailoring of the carrier liquid conductivity and applied electrical signal could, for example, allow one to use a single EK-SPR sensor to selectively study interactions with only the erythrocyte subpopulation in one region,[497,498] leucocytes in a different region,[499,500] circulating tumor cells in another,[501] and so on. Such capability would have obvious applications in lab-on-a-chip and micro total analysis systems (μTAS).

8.2.4 Future technologies

Looking farther afield, we can anticipate the disruptive contributions that new technologies may bring in the coming decades.

8.2.4.1 Protein structure prediction

Arguably one of the most underappreciated yet revolutionary technologies available to the biologist is now the graphical processing unit (GPU) and the closely related tensor-processing unit (TPU).[502] GPUs and TPUs are electronic circuits specialized for the rapid execution of mathematical operations related to the manipulation of large matrices of values. This specialization has enabled the development of artificial neural networks, which form the foundational basis for machine learning and artificial intelligence. The ability of a neural

network to make predictions is predicated on the manipulation and representation of statistical weightings as arrays of values in large matrices, which is why advances in GPU/TPU manufacturing and computer science have enabled incredibly rapid progress of machine learning in a variety of domains. One such example is the challenge of protein structure prediction.

In 2021, Alphabet's subsidiary DeepMind published a pair of articles in *Nature* describing *AlphaFold*, a computational protein-folding model based on machine-learning.[503,504] Given only the constituent amino acid sequence, AlphaFold can predict the structure of a protein in a matter of minutes with unprecedented accuracy that matches and often surpasses empirical methods. Training of the AlphaFold neural network required the equivalent of 200 GPUs[**] running for several weeks and resulted in a computational model that has now revealed the structures of 98.5% of the approximately 20 000 proteins expressed by humans, as well as 350 000 proteins for 20 additional model organisms.[503,504]

DeepMind has recently partnered with the European Molecular Biology Laboratory's European Bioinformatics Institute to make these structures available to researchers through the *AlphaFold Protein Structure Database*.[505]

8.2.4.2 In silico phage susceptibility testing

The pertinence of the advent of computational models like AlphaFold to the field of phage therapy is the potential for *in silico* phage susceptibility screening.[506] The ability to predict the structure of phage-encoded proteins may one day permit the prediction of host range partially or entirely in software. Inroads are already being made in this direction.

AlphaFold has already been demonstrated for topology prediction of phage RBD contact residues, indicating the potential of this method in the study of host-binding mechanisms.[507]

Leite *et al.* demonstrated how machine-learning can enable a model for computational prediction of phage-host interactions, based on feature extraction from genomes of known positive phage-host pairs.[508] The authors further posited the possibility of training such an algorithm directly on the respective genomes, bypassing the need for feature extraction.

In a similar vein, a recent article in Scientific Reports details the development of phage-bacteria infection networks (PBINs)[509] to individually evaluate interactions between 2 877 bacterial strains with a library of 899 candidate phages.[124] Algorithms were then trained and used to predict the correct choice of the phages that enabled an optimized phage cocktail of minimum size. In this parallelized, combinatorial approach, 52 688 phage-host permutations were studied in software. The authors of the study collated 50 empirically derived datasets to train their algorithm.

Computational PST techniques such as these potentially enjoy the benefits of both batch and parallel PST (discussed in 1.5 Phage-phage Interference Necessitates Parallel Phage Susceptibility Testing) since the algorithms can allow the prediction of phage-phage synergy and antagonism which can act to broaden or narrow the host range and efficacy of a cocktail.[510] While these works did not make use of molecular modelling of interactions between host-range determining regions and bacterial receptors, it sets the scene for the exploitation of advances made in protein-folding and bioinformatics to facilitate exploration of *in silico* methods for PST. However, until such methods can attain a selectivity and sensitivity comparable to *in vitro* techniques, some form of *in vitro* PST will remain necessary and this need may be met by SPR, lens-free, or some other form of parallel, multiplexed PST.

[**] A bank of 128 tensor processing unit cores (TPUs) was exploited for this study.

8.3 Conclusions

As this manuscript can attest, phage biology is an intriguing area of study. Researchers working with phages benefit from nano-assembly processes which are surely the envy of nanotechnology researchers laboring to synthesize other nanostructures. One merely mixes a small amount of precursor (phage) with a liquid culture of host bacterium, leaves the mixture unsupervised for a few hours and returns to reliably find on the order of one hundred trillion (10^{14}) replicates of the desired nanoparticle. The raw materials are cheap, and new phage strains can be sourced relatively easily from the environment.

These self-assembling entities can then be used to detect a large variety of materials.[133] They can be used to prevent spoiling of our food,[211,226,511] corking of our wine,[512] and to kill the bacteria that make us sick. They can be coaxed to express viral proteins on their surface to produce potent vaccines,[414] or even attack eukaryotic viruses directly.[513] We can exploit them to harvest electrical energy[232] and help regenerate our own injured tissue.[231] Phages seem to present a platform for innovation that is limited only by our own ingenuity, and the above list is poised to expand as more researchers come to appreciate the potential of the humble phage.

Annexes

A1 Version francaise

Dans ce manuscrit, une nouvelle modalité de test de susceptibilité aux bactériophages est proposée. Elle est basée sur le suivi par SPR des interactions entre des phages immobilisés et des souches bactériennes.

La SPR est une technique ayant une sensibilité élevée dans le domaine de la profondeur de pénétration d'un champ évanescent (quelques centaines de nanomètres), ce qui nécessite l'immobilisation de sondes à une interface métal-analyte. La culture des phages nécessite la lyse des bactéries hôtes et la génération de grandes quantités de débris qui doivent être séparés des phages avant que des réactions chimiques entrainant leur immobilisation puissent être effectuées. Il convient de noter que cette tâche s'est avérée loin d'être triviale.

Plusieurs méthodes ont été explorées pour la purification du phage gh-1, notamment l'ultrafiltration, l'ultracentrifugation à gradient de densité, la précipitation au PEG et la filtration à flux tangentiel. La comparaison a été effectuée sur la base de facteurs de mérite tels qu'un titre infectieux élevé, une faible agrégation des phages et l'élimination complète des contaminants du lysat de phage. Bien qu'aucune des méthodes mentionnées ne réponde simultanément à tous ces critères, leur combinaison a permis d'obtenir des suspensions de phages très pures et monodispersées tout en conservant leur infectivité.

Une revue de la littérature sur l'immobilisation des phages a mené à la sélection d'un ensemble de stratégies qui ont été explorées pour l'immobilisation des phages sur des substrats en or. Après avoir comparé les résultats de différentes méthodes d'immobilisation, il a été démontré que l'utilisation d'une monocouche auto-assemblée thiolée produisait une couche dense et homogène de bactériophages infectieux sur des substrats à base d'or.

Cette chimie d'immobilisation a ensuite été utilisée pour la micro-implantation de plusieurs phages sur la surface d'un capteur exploitant la SPR pour le suivi parallèle et multiplexé des interactions phage-hôte. Ce capteur SPR a mis en évidence des interactions spécifiques entre le phage 44AHJD et son hôte *S. aureus*, et entre le phage gh-1 et son hôte *P. putida*.

Au cours de l'expérimentation, il a été remarqué que le titre des phages chutait de façon inattendue pendant la phase de stockage, ce qui entraînait parfois des échecs dans la culture des phages ou la fonctionnalisation des substrats. Une expérience à grande échelle, sur plusieurs semaines, a été menée pour étudier la cause profonde de ce phénomène. Des mesures complémentaires de comptage de plaques et une analyse de suivi des nanoparticules dans les suspensions de phages ont permis de mieux comprendre la perte multimodale du titre infectieux due à l'adsorption, à l'inactivation et à l'agrégation. Il a été confirmé que celle-ci varie en fonction du matériau constituant le récipient.

Afin d'améliorer la sensibilité de la détection plasmonique, un nouveau capteur SPR a été développé. Il comporte un réseau d'électrodes interdigitées (IDE) intégré pour permettre le transport électrocinétique de masse allant de l'analyte vers la région de détection. Pour produire des réseaux d'électrodes interdigitées sur

des prismes SPRi, une nouvelle méthode de prototypage rapide a été mise au point, basée sur l'ablation laser avec un appareil commercial de prototypage de circuits imprimés. L'efficacité du capteur SPR électrocinétique (EK-SPR) ainsi produit a été démontrée pour la détection de S. aureus, en exploitant l'affinité d'un réseau immobilisé de peptides antimicrobiens.

A2 Miscellaneous Figures

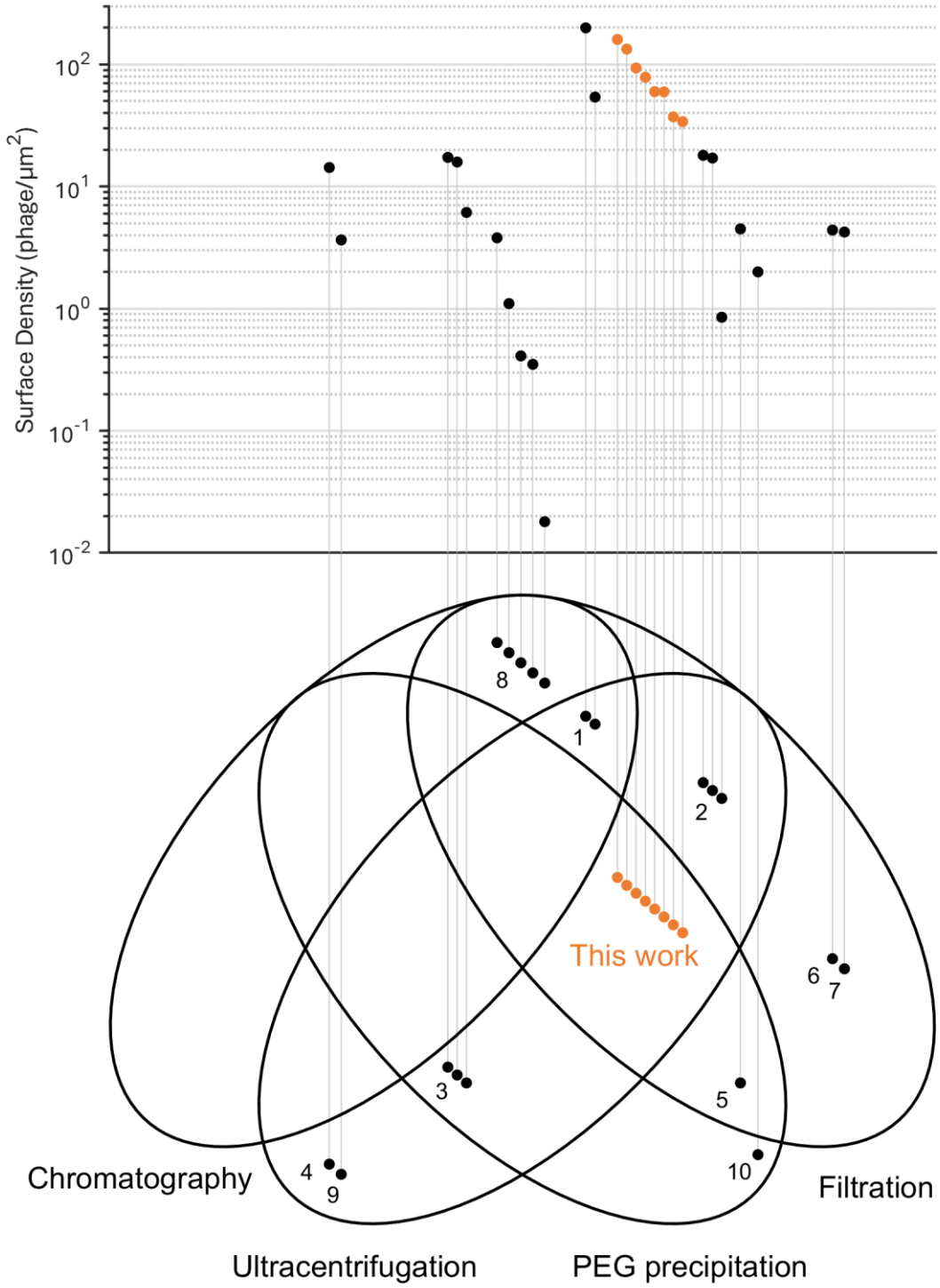

Figure A.1 A 4-set Venn diagram compares the purification methods used in prior publications (references 1-10 in figure), correlated with density of the resulting immobilized phage layer.

(1)Naidoo, R.; Singh, A.; Arya, S. K.; Beadle, B.; Glass, N.; Tanha, J.; Szymanski, C. M.; Evoy, S. Surface-Immobilization of Chromatographically Purified Bacteriophages for the Optimized Capture of Bacteria. Bacteriophage 2012, 2 (1), 15–24. https://doi.org/10.4161/bact.19079.

(2) Singh, A.; Glass, N.; Tolba, M.; Brovko, L.; Griffiths, M.; Evoy, S. Immobilization of Bacteriophages on Gold Surfaces for the Specific Capture of Pathogens. Biosens. Bioelectron. 2009, 24 (12), 3645–3651. https://doi.org/10.1016/j.bios.2009.05.028.

(3) Richter, Ł.; Bielec, K.; Leśniewski, A.; Łoś, M.; Paczesny, J.; Hołyst, R. Dense Layer of Bacteriophages Ordered in Alternating Electric Field and Immobilized by Surface Chemical Modification as Sensing Element for Bacteria Detection. ACS Appl. Mater. Interfaces 2017, 9 (23), 19622–19629. https://doi.org/10.1021/acsami.7b03497.
(4) Richter, Ł.; Matuła, K.; Leśniewski, A.; Kwaśnicka, K.; Łoś, J.; Łoś, M.; Paczesny, J.; Hołyst, R. Ordering of Bacteriophages in the Electric Field: Application for Bacteria Detection. Sensors Actuators B Chem. 2016, 224, 233–240. https://doi.org/10.1016/j.snb.2015.09.042.
(5) Hosseinidoust, Z.; Van De Ven, T. G. M.; Tufenkji, N. Bacterial Capture Efficiency and Antimicrobial Activity of Phage-Functionalized Model Surfaces. Langmuir 2011, 27 (9), 5472–5480. https://doi.org/10.1021/la200102z.
(6) Gervais, L.; Gel, M.; Allain, B.; Tolba, M.; Brovko, L.; Zourob, M.; Mandeville, R.; Griffiths, M.; Evoy, S. Immobilization of Biotinylated Bacteriophages on Biosensor Surfaces. Sensors Actuators, B Chem. 2007, 125 (2), 615–621. https://doi.org/10.1016/j.snb.2007.03.007.
(7) Wang, C.; Sauvageau, D.; Elias, A. Immobilization of Active Bacteriophages on Polyhydroxyalkanoate Surfaces. ACS Appl. Mater. Interfaces 2016, 8 (2), 1128–1138. https://doi.org/10.1021/acsami.5b08664.
(8) Leppänen, M.; Maasilta, I. J.; Sundberg, L. R. Antibacterial Efficiency of Surface-Immobilized Flavobacterium-Infecting Bacteriophage. ACS Appl. Bio Mater. 2019, 2 (11), 4720–4727. https://doi.org/10.1021/acsabm.9b00242.
(9) Xu, J.; Zhao, C.; Chau, Y.; Lee, Y. K. The Synergy of Chemical Immobilization and Electrical Orientation of T4 Bacteriophage on a Micro Electrochemical Sensor for Low-Level Viable Bacteria Detection via Differential Pulse Voltammetry. Biosens. Bioelectron. 2020, 151 (June 2019), 111914. https://doi.org/10.1016/j.bios.2019.111914.
(10) Ma, W.; Panecka, M.; Tufenkji, N.; Rahaman, M. S. Bacteriophage-Based Strategies for Biofouling Control in Ultrafiltration: In Situ Biofouling Mitigation, Biocidal Additives and Biofilm Cleanser. J. Colloid Interface Sci. 2018, 523, 254–265. https://doi.org/10.1016/j.jcis.2018.03.105.

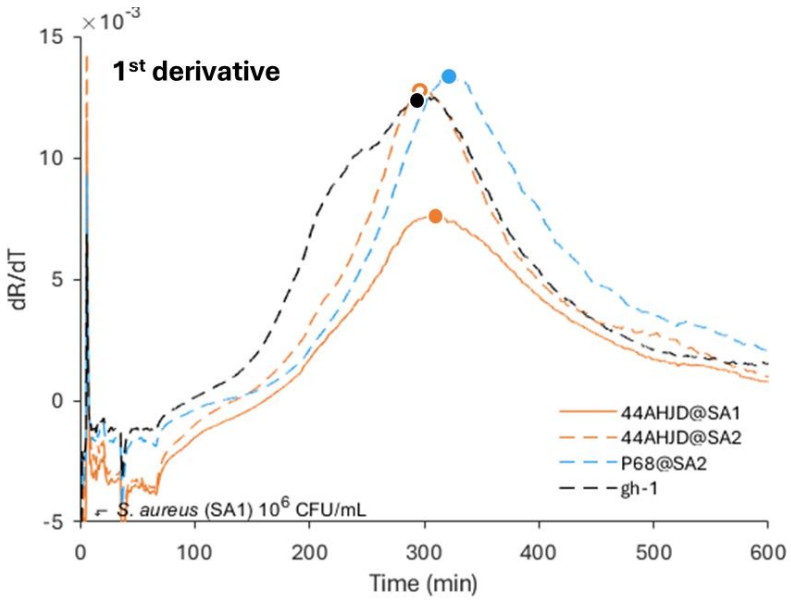

Figure A.2 First derivatives of SPR responses of regions exposed to *S. aureus* SA1.On-target response of 44AHJD@SA1 to its host is indicated with a solid line. The maximum of the first derivative is indicated in each case (●). Traces show a one-minute rolling average (i.e., mean of 20 data points).

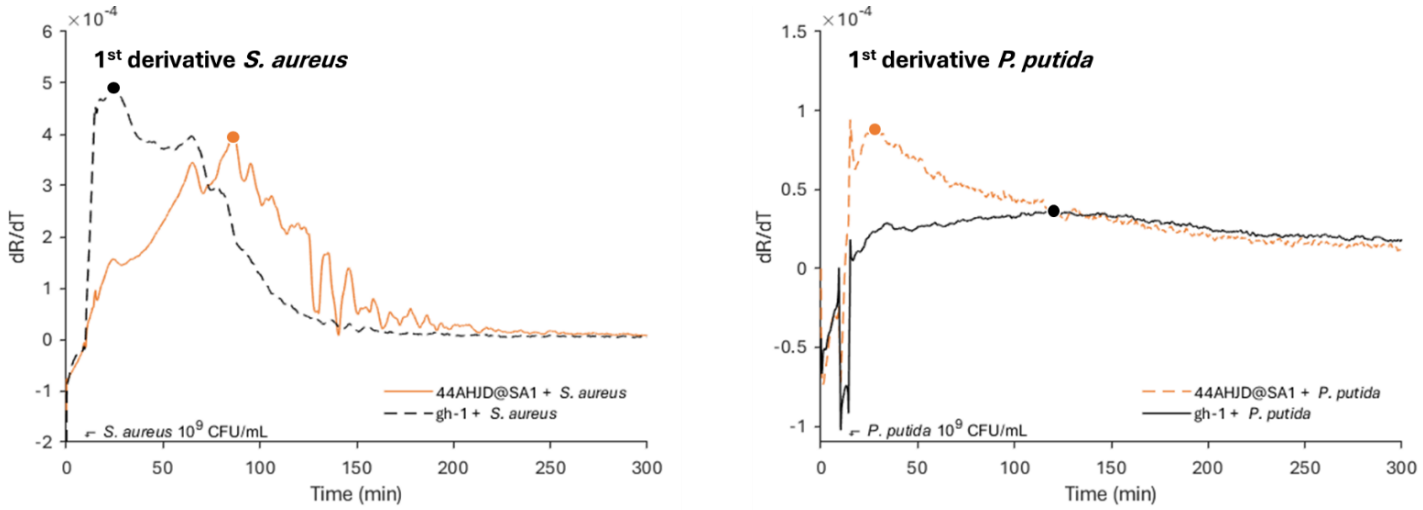

Figure A.3 First derivatives of SPR responses of regions exposed to *S. aureus* and *P. putida*.Responses of each immobilized phage to its host is indicated with a solid line, while response to non-host bacteria is indicated with a dashed line. The maximum of the first derivative is indicated in each case (●). Traces show a one-minute rolling average (i.e., mean of 20 data points).

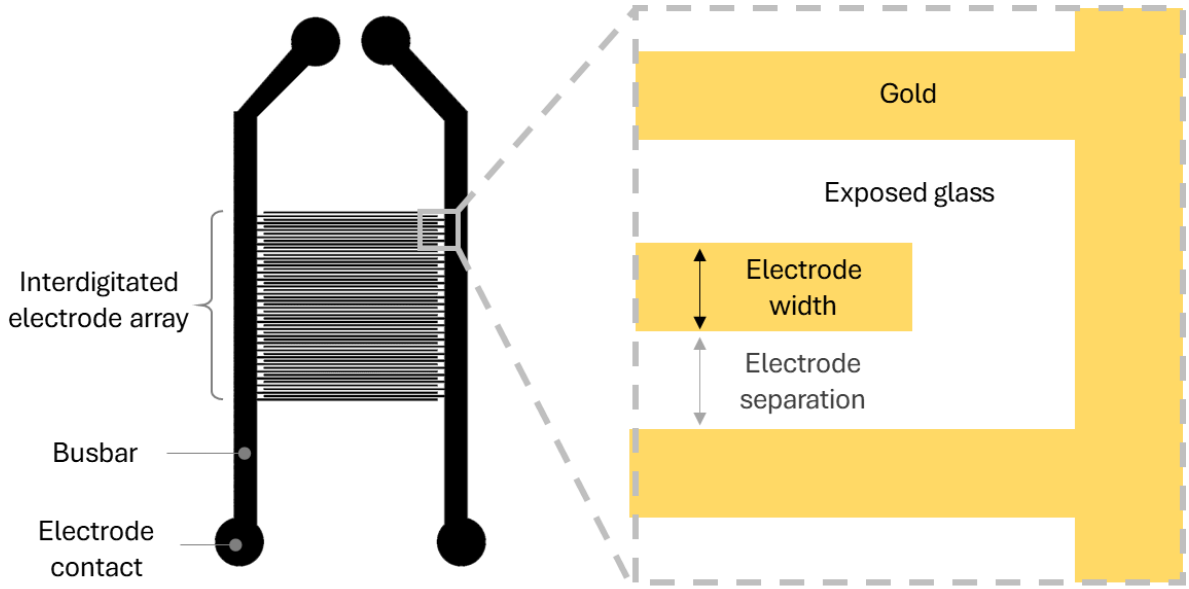

Figure A.4 Schematic of the pattern transferred to the substrate surface by laser patterning, featuring an array of 54 intermeshed electrodes of variable width and separation.

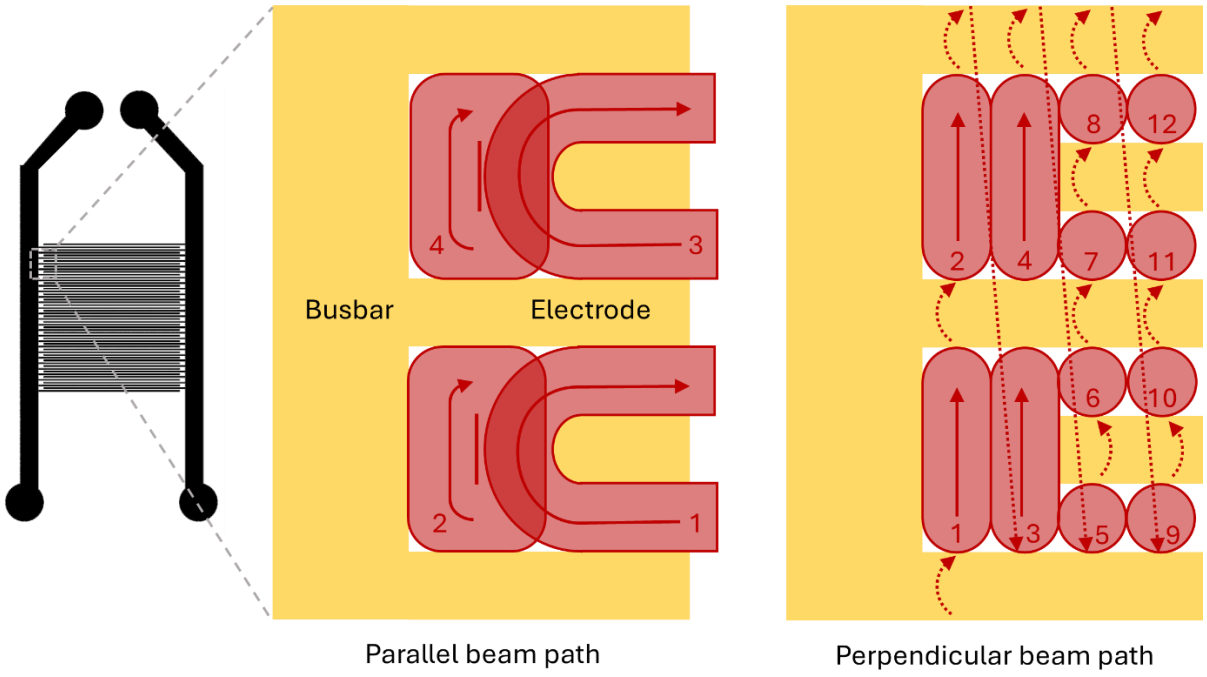

Figure A.5 Comparison of the parallel and perpendicular beam paths used in this work, so-named for the beam path orientation with respect to the long axis of electrode fingers.Numbers indicate the hypothetical order that each region would be exposed to the beam and are for illustrative purposes only. A parallel beam path was initially used but produced poor reproduction of the desired pattern. Surprisingly, a perpendicular beam path produced superior results.

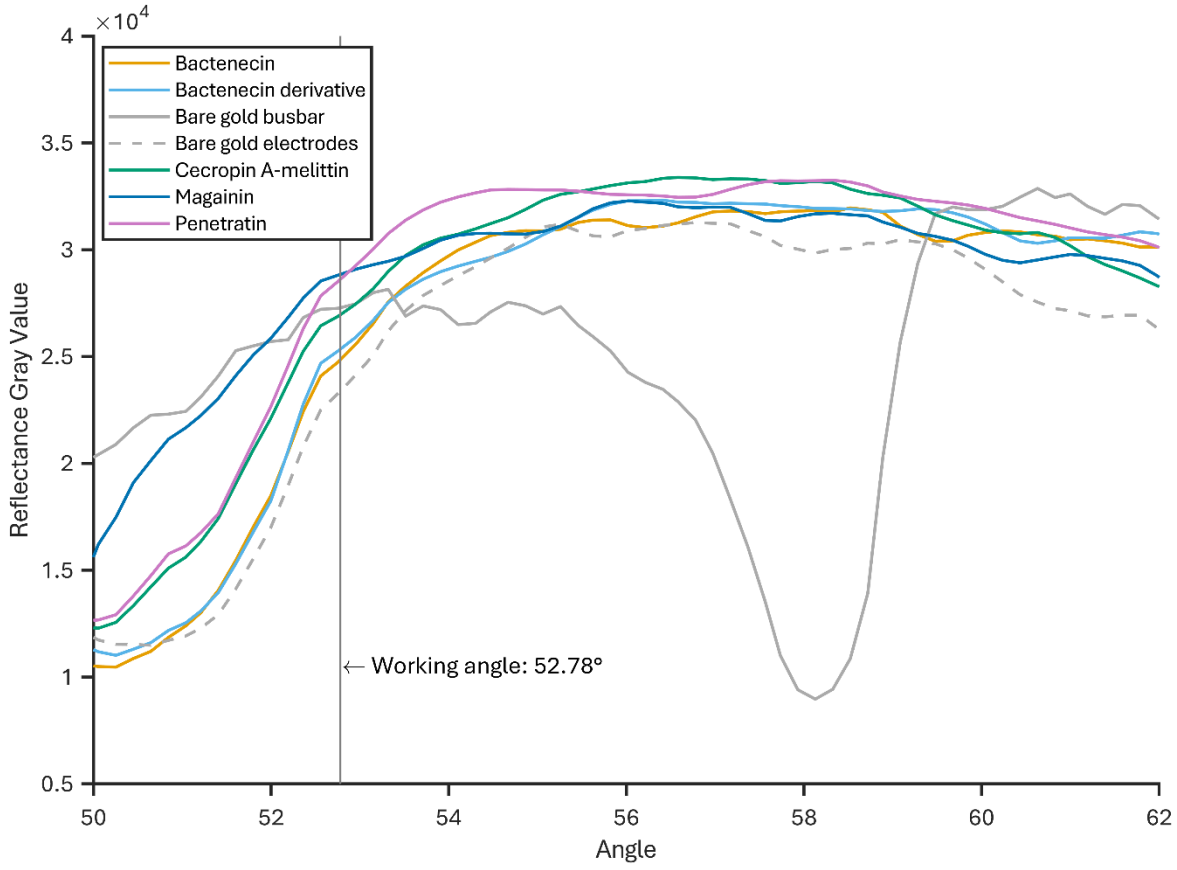

Figure A.6 Plasmon curves for all species. Each curve (except the gold busbar) is a mean of 16-20 replicate regions, depending on species.The reflectance minimum was strongly shifted relative to the un-patterned bare gold busbar surface (solid grey line).

A3 Solutions

The composition of ATCC Medium 3, recommended by the ATCC for culture of *S. aureus* ATCC BAA-2312 and used in this work, was as follows:

- ATCC Medium: 3 Nutrient Agar/Broth
  - Beef Extract 0.6 g
  - Peptone 1 g
  - Agar 1.6 g
  - Distilled water 200 ml

A4 Calculation of the Theoretical Limit to Bacteriophage Packing in a 2D Plane

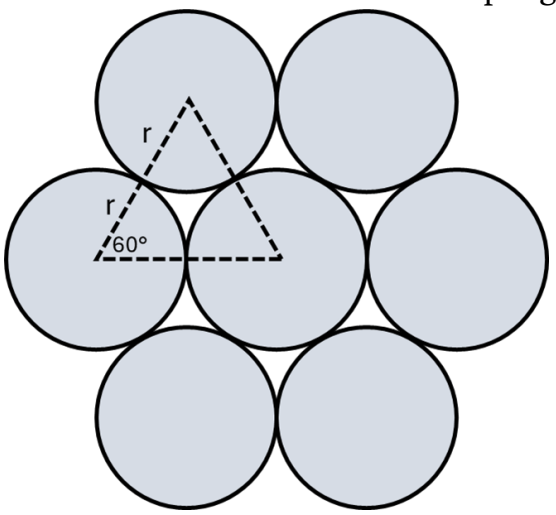

Figure A.7 Hexagonally close-packed spheres on a two-dimensional plane.

An array of spheres in two dimensions can be packed with a maximum density in a hexagonal close-packed arrangement as shown in **Figure A.7**. Taking advantage of the 6-fold symmetry of the hexagonal unit cell, and excluding the edges of the 2D array, the region enclosed by an equilateral triangle connecting the centres of 3 adjacent spheres reflects the proportion of the entire surface occupied by the sphere. The total area of the equilateral triangle is given by:

$$A_{\Delta} = \frac{\sqrt{3}}{4}(2r)^2$$

The area where the triangle overlaps with spheres is 3 times one 6th of the area of one circle:

$$A_{\diamond} = 3 \times \frac{A_{\circ}}{6} = \frac{\pi r^2}{2}$$

The ratio of these two values gives the surface coverage, also known as the *packing efficiency* or *packing fraction*:

$$\frac{A_{\diamond}}{A_{\Delta}} = \frac{\pi}{2\sqrt{3}} = 90.69\%$$

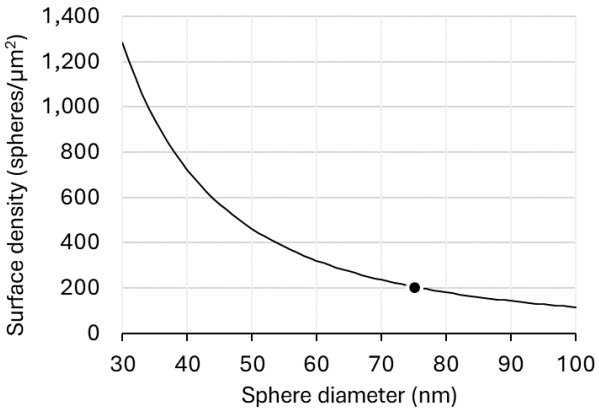

Figure A.8 Maximum theoretical density of hexagonally close-packed spheres in two dimensions, with the value for a 75 nm-diameter sphere indicated (●).

Taking this classic result together with the fact that 1μm^2 is equivalent to 10^6 nm^2, we have an equation for the maximum density of spheres of radius *r* (in nm) that can be arranged in a 2D plane with no overlap:

$$\text{Density (phage/}\mu\text{m}^2) = 10^6 \times 90.69\% \times \frac{1}{\pi r^2}$$

Which yields a curve relating the diameter of spherical particles and the maximum theoretical density at which they can be arranged on a two-dimensional surface (**Figure A.8**).

A5 Proof of Phage Infectivity Following Immobilization

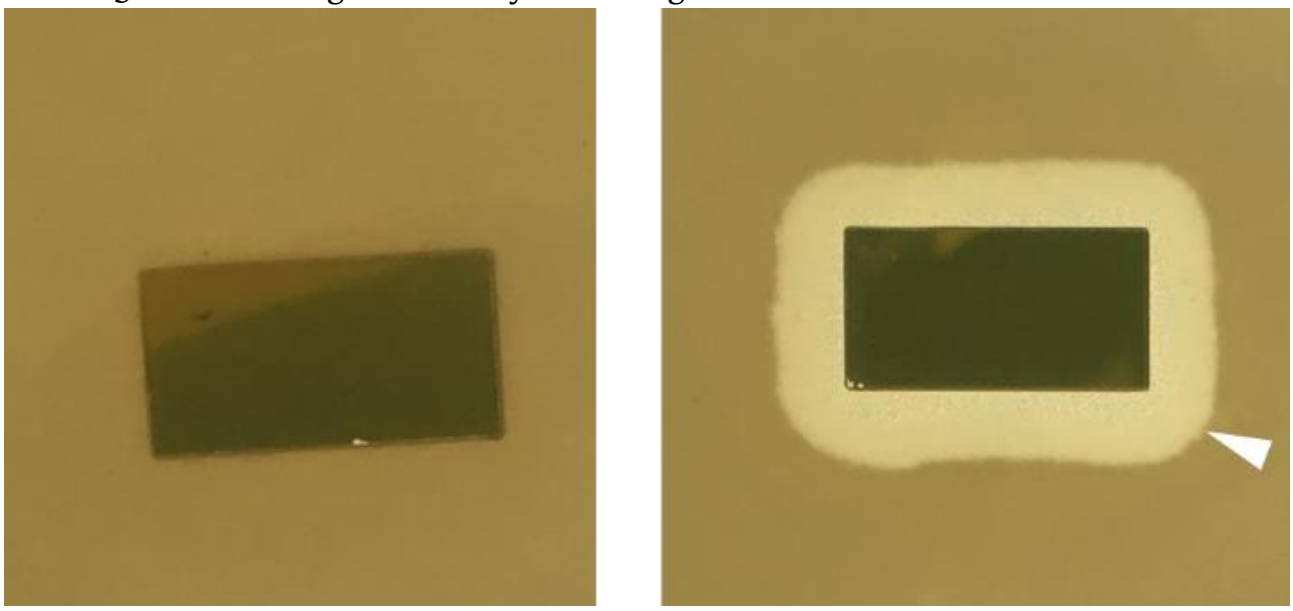

Figure A.9 A zone of lysis (white arrow) appears in a bacterial lawn of *Pseudomonas putida*, surrounding a gold-coated slide functionalized with bacteriophage gh-1, cross-linked to the surface via 11-MUA (right). A control slide (left) shows no evidence lysis.

In order to demonstrate that phage particles remain infective following 11-MUA cross-linking to gold, gh-1 functionalized gold-coated slides and unfunctionalized controls were placed face-down on a layer of TSA inoculated with exponential phase *P. putida* (ATCC 12633; host of phage gh-1) and incubated at 30°. The following day, appearance of a zone of lysis around only the phage-functionalized gold-coated slide demonstrated that the phage remained infective (**Figure A.9**)

A6 Transmission Electron Microscopy of Phage Suspensions

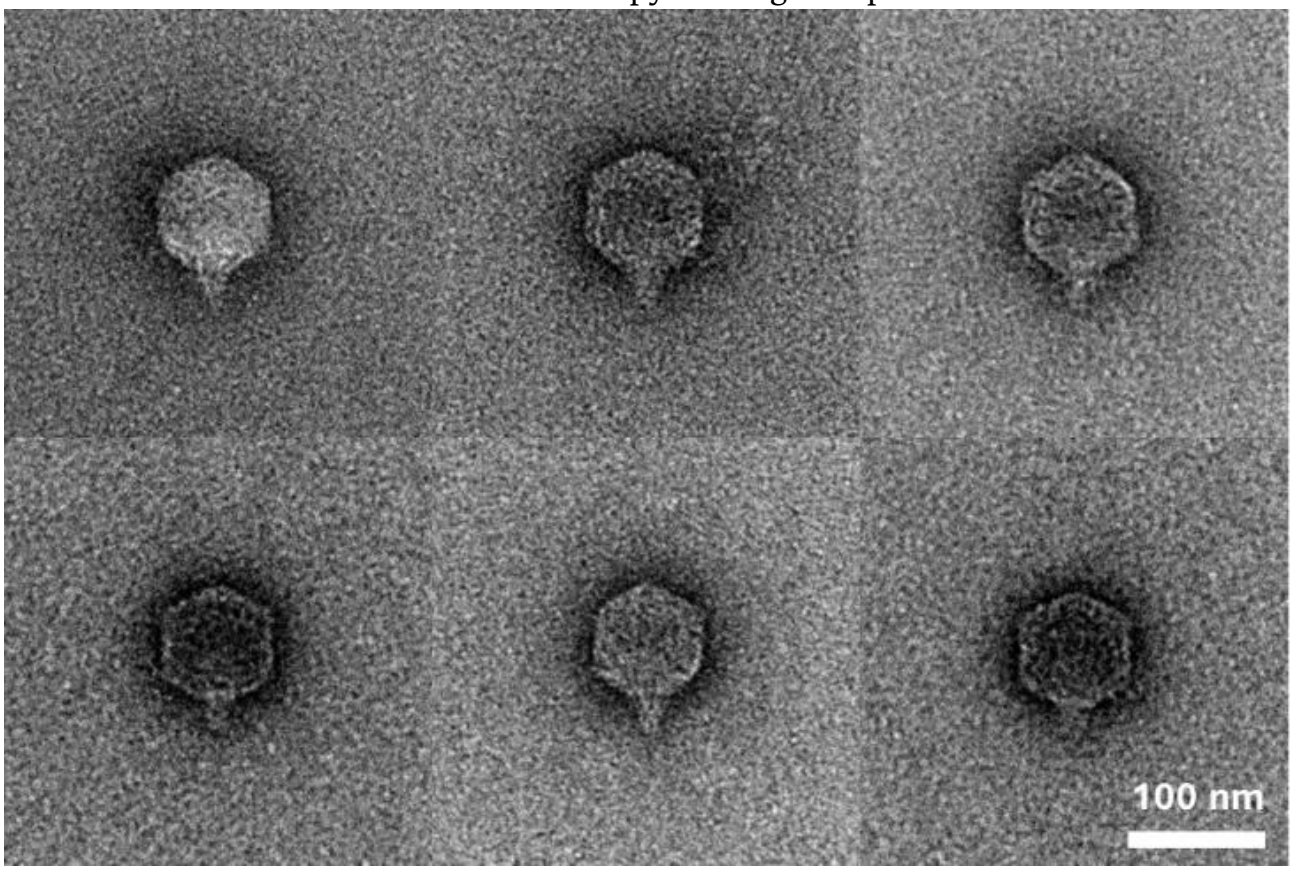

Figure A.10 A collage of transmission electron micrographs of gh-1 bacteriophages, purified by density gradient ultracentrifugation.The icosahedral capsid and tail fibers are visible.

In order to compare bacteriophage morphology observed by scanning electron microscopy (SEM) with a complementary observation by transmission electron microscopy (TEM), selected phage suspensions were analyzed by TEM at the Institut de Biologie Structurale (IBS), Grenoble; according to the negative stain-mica-carbon flotation technique. Phages were adsorbed to the clean side of a carbon film on mica, stained with uranyl acetate (AcUr) $UO_2(CH_3COO)_2 \cdot 2H_2O$ at 2% in distilled water (pH 4.2-4.5), and transferred to a 400-mesh copper grid. Images were taken under low dose conditions (<10 $e^-/Å^2$) with defocus values between 1.2 and 2.5 µm on a Tecnai 12 LaB6 electron microscope at 120 kV accelerating voltage using a Camera Gatan Orius 1000 CCD.

A7 Observed Bacteriophage Morphology in Scanning Electron Microscopy

SEM imagery of immobilized gh-1 phage revealed a surprising prolate spheroid geometry that was not expected from transmission electron micrographs of similarly synthesized suspensions (**Figure A.10**). A possible explanation for this is that bacterial ribosomes were mistakenly purified from the phage lysate instead of bacteriophage and were then immobilized on the substrate.

As a prokaryote, *P. putida* (the host of phage gh-1) features 70S ribosomes, composed of a larger 50S subunit and a smaller 30S subunit, together forming a ~25 nm-diameter macromolecule.[11] Bacteria downregulate ribosomal activity by dimerizing 70S ribosomes into an inactive 100S ribosomal complex.[12,13] This dimerized structure, when considered with a diameter of the same order of magnitude as that of the particles observed on the surface, suggests the possibility that ribosomes were accidentally immobilized rather than phage. Furthermore, bacterial cells are known to house thousands of ribosomes per cell, compared to the burst size of “only” 103 gh-1 particles generated for each lysis event.[14] We may then expect to see as much as an order

of magnitude more ribosomes than phage present in the crude lysate, which must be separated from the phage during purification.

However, the 50S and 30S subunits have a buoyant density of 1.67 and 1.63 g/mL, respectively, while that of gh-1 is much lower at 1.45 g/mL.[15,16] We would thus expect ribosomes to be present in the band that formed below the 1.54g/mL region, while the phage remain above, effectively separating the two populations. All fractions of the CsCl density gradient were recovered and titered separately by the agar overlay method.[17] The second white band from the top was consistently shown to have at least 1 $\log_{10}$ higher concentration of phage than the next most concentrated fraction, indicating this to be the correct fraction to select for purified phages. If the particles observed on the surface were ribosomes, this would imply that they were concentrated in the same fraction as phage but then exclusively immobilized by all methods tested, including physisorption which binds somewhat indiscriminately.

Furthermore, transmission electron micrographs do not yield particles that resemble ribosomes either in the purified phage lysate or ultrasound control lysates. Since ribosomes are present in bacterial cytosol, they should also be liberated by mechanical lysis of the bacteria. However, suspected phage particles of the type observed by SEM are entirely absent from regions incubated with the ultrasound control lysate, which would not be the case had ribosomes been purified.

For these reasons, we conclude that the particles observed on the surface by SEM were not bacterial ribosomes.

An alternative explanation is that the observed particles are denuded tail and core complexes, which somehow were separated from the main capsid in very significant numbers. However, the observed diameter of the particles is too large for this to be plausible.

Comparable *scanning* electron microscopy images to the present work are rare, since transmission electron microscopy is typically favored in the study of bacteriophages due to their small size and the superior resolution afforded by TEM. We lack comparable structural data for gh-1, but genetic analysis reveals its close resemblance to T7.[18] The majority of published electron microscopy images do not resolve the tail fibers of phage T7, even though they have been shown to exist,[19] arrayed around the tail complex with six-fold symmetry on wild-type T7.[20]

From this information we can reasonably conclude that, just like the closely related phage T7, gh-1 has tail fibers which are not resolved by TEM but which are visible in SEM. Deposition of a 4 nm carbon layer was required to allow imaging, which may have the effect of decorating the thin tail fibers with a carbon layer, rendering them visible in SEM imagery.

It is on the basis of the above information that we conclude that the particles observed on gold-coated slide surfaces are indeed immobilized, whole, infective bacteriophage particles.

A8 Bacterial Decimal Reduction Time Following Ultrasound Exposure

An overnight culture of *P. putida* was placed in a 10mL beaker, covered with labfilm to prevent contamination of the ultrasound chamber by aerosolized bacterial culture, and a CV33 ultrasound probe was immersed. The probe was connected to a Vibracell 75115 controller and operated at 30% amplitude and 25% duty cycle. The sonication was judged to effectively agitate and homogenize the sample, so the beaker was left in place and sampled using a micropipette immediately after the end of the appropriate sonication cycle.

A 100 µL sample was taken at three time points (t=0s, 60s, and 660s), serially ten-fold diluted seven times, then plated in duplicate on TSA plates before being incubated overnight at 30C. The following day, colonies were counted in order to calculate the decimal reduction rate of with this setup for future experiments. Fitting

of an exponential curve to the observed bacterial concentration (R^2=0.994) yielded the exponential survival rule:

$$\frac{N_t}{N_0} = 0.6762\, e^{-0.97t}$$

where N_0 and N_t are the bacterial concentration at zero time and time t, respectively. The decimal reduction time D_{20} is related to the survival rate parameter by[21]:

$$\mathrm{D}_{20} = -\frac{\ln\left(\frac{0.1}{0.6762}\right)}{k} = 1.97 \text{ minutes}$$

A9 Calculation of Experimental Uncertainty in Plaque-counting Experiments

Experimental error in lysis plaque counts can be significant. Estimates range from 10-20%[514,515] to as high as 50%[516]. We calculated the uncertainty in infectious titer measurements in terms of three quantities: overlap bias, uncertainty in the serial dilutions, and uncertainty in the plated volume.

Lysis plaques are randomly distributed across the agar surface and may mutually overlap with a probability that increases commensurately with plaque size and density in the bacterial lawn. This overlap bias will lead to under-counting of plaques that are separated by less than a minimum separation distance (*g*), taken in this work as half of the radius of the average plaque. In a pair of papers, Howes and Fazekas de St Groth describe a relation correcting for overlap bias between the observed plaque count (*N*) and true plaque count (*Q*)[426,427]:

$$Q = -\tfrac{1}{K}\ln(1 - KN) \quad (1)$$

where *K* is an assay constant defined in terms of *g*, and the diameter of the region covered by the deposited droplet (*D*):

$$K = \tfrac{4g^2}{D^2} \quad (2)$$

For each phage, spot and plaque diameters were measured across several petri dishes, and the results collated to produce assay constants according to equation 2 (Table A.1). Using equation 1, this assay constant was then used to obtain the true plaque count (*Q*). The variance in the true plaque count (σ_Q^2) can be calculated from the variance in the observed plaque count (σ_N^2) by the relation[427]:

$$\sigma_Q^2 = e^{2KN} \cdot \sigma_N^2$$

Table A.1 Summary of spot diameters, plaque diameters, and assay constants (K) for each phage.

Phage	Average spot diameter (mm)	Average plaque diameter (mm)	K
44AHJD	10.01 (n=6)	0.52 (n=6)	0.0027
P68	12.99 (n=4)	1.54 (n=11)	0.014
gh-1	12.30 (n=5)	1.68 (n=5)	0.018

Data shown are the mean of n replicates.

The concentration of phage and all contaminants in the parent suspension (C_0) is related to the concentration of the nth dilution (C_n) by the dilution factor:

$$C_0 = C_n \times \text{Dilution factor of n}^{\text{th}} \text{ serial dilution}$$

For suspensions serially diluted in glass, PP, and PP+BSA containers, the dilution factor of the first serial dilution is expected to be 10 relative to the parent dilution, since 100µL of the parent suspension was diluted with 900µL of diluent. The concentration of phage (and contaminants) in the first serial dilution (C_1) relative to the concentration of the parent suspension (C_0) can be given in terms of the pipetted volumes of parent suspension (V_{100}=100 µl) and diluent (V_{900}=900 µl):

$$C_1 = C_0 \times \frac{V_{100}}{V_{100} + V_{900}}$$

However, due to finite tolerance of the micropipette, there is a variance associated with both the 900 µl volume of diluent dispensed ($\sigma^2_{V_{900}}$) and 100 µl volume of the parent suspension sampled ($\sigma^2_{V_{100}}$). Since these measurements are uncorrelated, the variance in the concentration of the first serial dilution ($\sigma^2_{C_1}$) is given by[517]:

$$\sigma^2_{C_1} = \sigma^2_{C_0}\left(\frac{\partial C_1}{\partial C_o}\right)^2 + \sigma^2_{V_{100}}\left(\frac{\partial C_1}{\partial V_{100}}\right)^2 + \sigma^2_{V_{900}}\left(\frac{\partial C_1}{\partial C_{V_{900}}}\right)^2$$

Evaluating the partial derivatives yields:

$$\frac{\partial C_1}{\partial C_0} = \frac{V_{100}}{V_{100} + V_{900}} = \frac{1}{10}$$

$$\frac{\partial C_1}{\partial V_{100}} = C_0 \frac{V_{900}}{(V_{100} + V_{900})^2} = \frac{9}{10000} C_0$$

$$\frac{\partial C_1}{\partial V_{900}} = -C_0 \frac{V_{100}}{(V_{100} + V_{900})^2} = \frac{-1}{10000} C_0$$

Substituting the values for the partial derivatives gives the variance of the concentration of the first serial dilution in terms of the variance in the volume of sample and diluent:

$$\sigma^2_{C_1} = \frac{\sigma^2_{C_0}}{100} + {C_0}^2 \cdot \sigma^2_{V_{100}} \cdot \left(\frac{9}{10000}\right)^2 + {C_0}^2 \cdot \sigma^2_{V_{900}} \cdot \left(\frac{-1}{10000}\right)^2 \quad (3)$$

Note that for the first serial dilution, assuming a homogenous distribution of phage particles within the parent sample, the variance term for the concentration of the parent suspension ($\sigma^2_{C_0}$) is zero, and the first term will disappear when calculating $\sigma^2_{C_1}$.

We can then generalize equation 3 to an expression for the variance in the concentration of the nth serial dilution ($\sigma^2_{C_n}$) when diluting 100 µl sample with 900 µl diluent:

$$\sigma^2_{C_n} = \frac{\sigma^2_{C_{n-1}}}{100} + {C_{n-1}}^2 \cdot \sigma^2_{V_{100}} \cdot \left(\frac{9}{10000}\right)^2 + {C_{n-1}}^2 \cdot \sigma^2_{V_{900}} \cdot \left(\frac{-1}{10000}\right)^2 \quad (4)$$

We took the error in measurement of a 900 µl volume using a 1000 µl (nominal volume) micropipette ($\sigma^2_{V_{900}}$) to be ±20 µL, and the error in measurement of a 100 µL volume using a 200 µL (nominal volume) micropipette ($\sigma^2_{V_{100}}$) to be ±4 µl [518]. Using equation 4, these values yield an uncertainty of ±4.1% in the dilution factor of the first dilution relative to the parent, increasing to ±13.0% for the 10th serial dilution (**Figure A.11**). For

suspensions serially diluted in PS and PS+BSA containers, an identical estimation of the error applies, although the larger volumes involved (100 µl sample in 900 µl diluent for the 1st serial dilution, followed by 1 mL sample diluted in 9 mL diluent for subsequent dilutions) result in a lower value of the uncertainty, increasing to ±8.7% for the 10th serial dilution (**Figure A.11**).

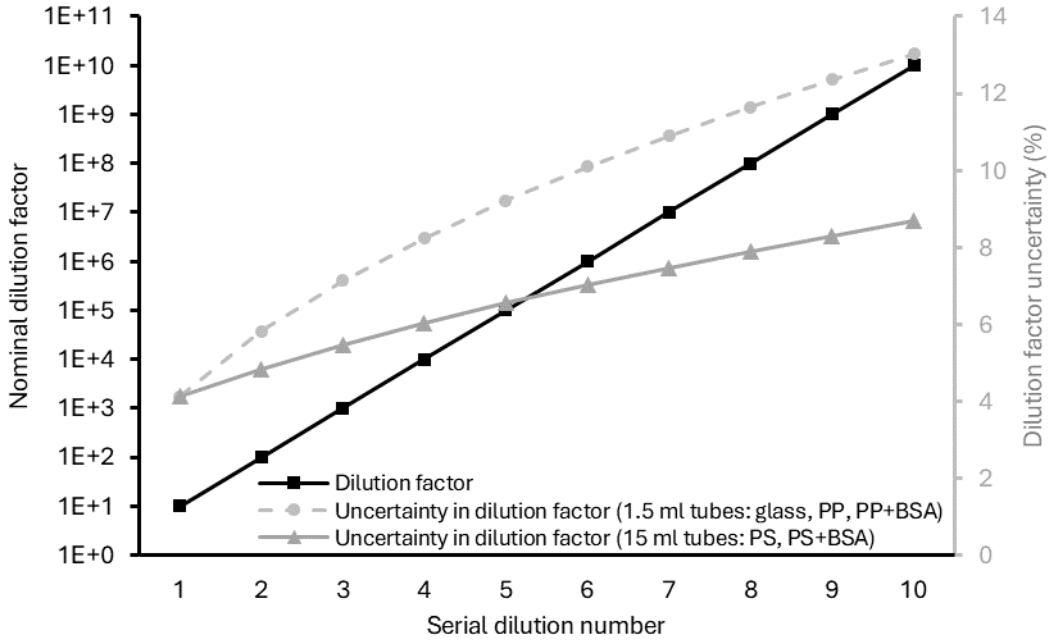

Figure A.11 Semilog plot showing nominal dilution factor (■) and propagation of uncertainty in dilution factor relative to the parent suspension for glass, PP, and PP+BSA containers (●); and PS and PS+BSA containers (▲), as a function of serial dilution number.

Following serial dilution, a droplet with a nominal volume of 10 µl is sampled from each suspension and deposited on the agar layer, introducing an additional source of uncertainty. We took the variance in measurement of a 10 µl volume using a 20 µl (nominal volume) micropipette ($\sigma_{V_{10}}^2$) to be ±0.4 µl[518].

The infectious titer of the parent suspension (IT) dilution is found by multiplying the overlap-bias corrected plaque count (Q), the dilution factor, and the plated volume (nominally 10 µl) by 100 to obtain the titer in units of PFU /mL.

$$IT = Q \cdot \frac{1000}{V_{10}} \cdot \text{Dilution factor} = Q \cdot \frac{1000}{V_{10} C_n}$$

To obtain the variance in the infectious titer of the parent suspension (σ_{IT}^2), we must propagate the variances of the plated volume (V_{10}), corrected count of plaques (Q), and the dilution factor ($1/C_n$):

$$\sigma_{IT}^2 = \sigma_Q^2 \left(\frac{\partial IT}{\partial Q}\right)^2 + \sigma_{V_{10}}^2 \left(\frac{\partial IT}{\partial V_{10}}\right)^2 + \sigma_{C_n}^2 \left(\frac{\partial IT}{\partial C_n}\right)^2$$

Evaluating the partial derivatives yields:

$$\frac{\partial IT}{\partial Q} = \frac{100}{C_n}$$

$$\frac{\partial IT}{\partial V_{10}} = \frac{-10Q}{C_n}$$

$$\frac{\partial IT}{\partial C_n} = \frac{-100Q}{C_n^2}$$

Substituting the values for the partial derivatives gives the variance of the infectious titer of the parent sample in terms of the variances in Q, V_{10}, and C_n:

$$\sigma_{IT}^2 = \sigma_Q^2 \left(\frac{100}{C_n}\right)^2 + \sigma_{V_{10}}^2 \left(\frac{-10Q}{C_n}\right)^2 + \sigma_{C_n}^2 \left(\frac{-100Q}{C_n^2}\right)^2$$

The uncertainty in the infectious titer (σ_{IT}) is simply the square root of the variance and is the value represented by error bars in all figures of this work, unless otherwise stated.

$$\sigma_{IT} = \sqrt{\sigma_Q^2 \left(\frac{100}{C_n}\right)^2 + \sigma_{V_{10}}^2 \left(\frac{-10Q}{C_n}\right)^2 + \sigma_{C_n}^2 \left(\frac{-100Q}{C_n^2}\right)^2} \quad (5)$$

A10 Protein Structures used in Illustrations

- Structural analysis of PRD1
  PDB ID: 1W8X
  Abrescia, N.G.A. *et al.* (2004) Insights into Assembly from Structural Analysis of Bacteriophage Prd1. Nature 432: 68

- PRD1 vertex protein P5
  PDB ID: 1YQ8
  Merckel, M.C. *et al.* (2005) The structure of the bacteriophage PRD1 spike sheds light on the evolution of viral capsid architecture. Mol Cell 18: 161-170

- Atomic models of P1, P4 C-terminal fragment and P8 fitted in the bacteriophage phi6 nucleocapsid reconstructed with icosahedral symmetry
  PDB ID: 6HY0
  Ilca, S.L. *et al.* (2019) Multiple liquid crystalline geometries of highly compacted nucleic acid in a dsRNA virus. Nature 570: 252-256

- Cryo-electron microscopy structure of the hexagonal pre-attachment T4 baseplate-tail tube complex
  PDB ID: 5IV5
  Taylor, N.M. *et al.* (2016) Structure of the T4 baseplate and its function in triggering sheath contraction. Nature 533: 346-352

- CryoEM single particle reconstruction of prolate head of bacteriophage T4
  EMD ID: 6323
  Sun, L. *et al.* (2015) Cryo-EM structure of the bacteriophage T4 portal protein assembly at near-atomic resolution in Nat Commun 6, 7548

- Fitting of gp18M crystal structure into 3D cryo-EM reconstruction of bacteriophage T4 extended tail
  PDB ID: 3FOH
  Aksyuk *et al.* (2009) The tail sheath structure of bacteriophage T4: a molecular machine for infecting bacteria in EMBO J 28(7):821-9

- Structure of native bacteriophage P68
  PDB ID: 6Q3G
  Hrebík *et al.* (2019) Structure and genome ejection mechanism of Staphylococcus aureus phage P68 in Sci Adv. 16;5(10):eaaw7414

- Structure of the bacteriophage C1 tail knob protein, gp12
  PDB ID: 4EO2
  Aksyuk *et al.* (2012) Structural investigations of a Podoviridae streptococcus phage C1, implications for the mechanism of viral entry in Proc.Natl.Acad.Sci.USA 109: 14001-14006

- Localized reconstruction of tail-spike of bacteriophage P68
  PDBJ ID: EMD-4450
  Hrebík *et al.* (2019) Structure and genome ejection mechanism of Staphylococcus aureus phage P68 in Sci Adv. 16;5(10):eaaw7414

- Capsid model of M13 bacteriophage virus from Magic-angle spinning NMR and Rosetta modeling
  PDB ID: 2MJZ
  Morag, O. *et al.* (2015) The NMR-Rosetta capsid model of M13 bacteriophage reveals a quadrupled hydrophobic packing epitope in Proc Natl Acad Sci USA 112: 971-976

- Crystal structure of Bovine Serum Albumin
  PDB ID: 3V03
  Majorek *et al.* (2012) Structural and immunologic characterization of bovine, horse, and rabbit serum albumins in Mol. Immunol. 52: 174-182

A11 Tables

Table A.2 Covalent phage immobilization techniques

								Purification								
Substrate	**Paper Category**	**Immobilization Category**	**Surface treatment**	**Phage**	**Phage morphology (geometry)**	**Analyte/Host**	**Detection scheme (if biosensor)**	**Centrifugation**	**Ultracentrifugation**	**Solvent precipitation**	**PEG precipitation**	**Filtration**	**Dialysis**	**Chromatography**	**Limit of detection (if biosensor)**	**Phage surface density**
AFM probe	Fundamental research	Amino-silanization	APTMS + EDC / NHS	P22	Podoviridae (Short-tailed)	N/A	AFM	✓	✓						N/A	40 PFU/μm^2
Cellulose Magnetic bead	Fundamental research, detection	Streptavidin / biotin*	Streptavidin / biotin Cellulose-binding module	T4†	Myoviridae (Long-tailed)	*E. coli*	Magnetic separation + qPCR								800 CFU/mL (with PCR)	84 - 98%
Glass/silicate	Biocontrol	Amino-silanization	APTES + EDC / NHS	PRD1 P22 PR772 MS2 T4	Tectiviridae, Podoviridae, Leviviridae, Myoviridae (Icosahedral, short-tailed, long-tailed)	*E. coli* *S.* Typhimurium	N/A	✓			✓				N/A	4.5 PFU/μm^2
Glass/silicate	Capture	Amino-silanization	APTES + EDC / NHS	PRD1 T4	Tectiviridae, Myoviridae (Icosahedral, long-tailed)	*S. enterica*	N/A	✓			✓	✓			N/A	?
Glass/silicate	Detection	Amino-silanization*	APTMS + EDC / NHS	P22	Podoviridae (Short-tailed)	*S.* Typhimurium	N/A	✓				✓			?	67%
Glass/silicate	Fundamental research	Amino-silanization, Amino-silanization + electrostatic physisorption*	APTES + EDC / NHS	T4	Myoviridae (Long-tailed)	*E. coli*	N/A	✓							N/A	16 PFU/ particle
Glass/silicate	Structural	Amino-silanization	APTES	fd†	Inoviridae (Filamentous)	*E. coli*	N/A	✓			✓				N/A	?
Glass/silicate	Structural, detection	Electropolymerization	PEDOT	M13	Inoviridae (Filamentous)	Antibody	Resistive								20×10^-9 M	?
Glassy carbon electrode	Detection	Amide bond	EDC	T4	Myoviridae (Long-tailed)	*Salmonella*	EIS	✓				✓			10^4 CFU/mL	?
Glassy carbon electrode	Detection	Amide bond	EDC / NHS	PaP1	Myoviridae (Long-tailed)	*P. aeruginosa*	ECL								56 CFU/mL	?
Glassy carbon electrode	Detection	Electropolymerization	Pyrrole-alkyl ammonium	T7	Autographiviridae (Short-tailed)	Antibody	Amperometric	✓			✓				36 pg/mL	?
Gold	Capture, detection	Thiol SAM	DTSP	T4 P22 NCTC 12673	Myoviridae, Podoviridae (Long-tailed, short-tailed)	*E. coli* *S.* Typhimurium	SPR							✓	?	18.9 PFU/μm^2

Gold	Capture, detection	Thiol SAM + amide bond, Thiol SAM + crosslinker*	L-cysteine L-cysteine + glutaraldehyde 11-MUA 11-MUA + EDC/ NHS L-cysteine + 11-MUA + EDC/NHS	BP14	Podoviridae (Short-tailed)	*S. aureus*	SPR, SEM	✓			✓		N/A	19 ng/mm²
Gold	Detection	Amide bond	Carboxymethylated dextran + EDC / NHS	M13	Inoviridae (Filamentous)	*E. coli* *Salmonella*	SPR			✓			1.3×10^7 CFU/mL	?
Gold	Detection	Electropolymerisation + crosslinking	Polytyramine + glutaraldehyde	M13	Inoviridae (Filamentous)	*Salmonella*	Capacitive						200 CFU/mL	?
Gold	Detection	Thiol SAM	DTSP	T4	Myoviridae (Long-tailed)	*E. coli*	SPR	✓	✓		✓	✓	7×10^2 CFU/mL	57 ng/mm²
Gold	Detection	Thiol SAM	Sulfo-LC-SPDP	PVP-SE1	Myoviridae (Long-tailed)	*S.* Enteritidis	Magnetoresistive						3–4 cells/sensor	?
Gold	Detection	Thiol SAM + amide bond	11-MUA + EDC / NHS	BCP8-2	Herelleviridae (Long-tailed)	*Bacillus cereus*	Ferromagnetoelastic						?	5.51 phages/µm²
Gold	Detection	Thiol SAM + amide bond	11-MUA + EDC / NHS	M13	Inoviridae (Filamentous)	ET101 protein	SPR						?	?
Gold	Detection	Thiol SAM + amide bond	3-MPA + EDC / NHS	fd	Inoviridae (Filamentous)	Prostate-specific antigen	DPV						3 pg/mL	?
Gold	Detection	Thiol SAM + amide bond	3-MPA + EDC / NHS	M13	Inoviridae (Filamentous)	*E. coli*	EIS	✓		✓			14 CFU/mL	?
Gold	Detection	Thiol SAM + amide bond	L-cysteine + 11-MUA + EDC / NHS	T4 BP14	Myoviridae, Podoviridae (Long-tailed, short-tailed)	*E. coli* *S. aureus*	SPR, ECIS	✓			✓		10^3 CFU/mL	?
Gold	Detection	Thiol SAM + amide bond	NHS thioctic ester	M13	Inoviridae (Filamentous)	Antibody	EIS, QCM						6.6×10^-9 M	1100 PFU/µm²
Gold	Detection	Thiol SAM + amide bond	NHS thioctic ester	M13	Inoviridae (Filamentous)	Antibody	EIS			✓			20×10^-9 M	?
Gold	Detection	Thiol SAM + amide bond	NHS thioctic ester	M13	Inoviridae (Filamentous)	Prostate-specific antigen Antibody	EIS, QCM						120×10^-9 M	?
Gold	Detection	Thiol SAM + amide bond*	11-MUA + EDC / NHS	T4	Myoviridae (Long-tailed)	*E. coli*	DPV	✓	✓				14 ± 5 CFU/mL	3.65 PFU/µm²
Gold	Detection	Thiol SAM + crosslinker	L-cysteine + glutaraldehyde	D29	Siphoviridae (Long-tailed)	*M. tuberculosis*	Piezoelectric	✓	✓				10^3 CFU/mL	?
Gold	Detection	Thiol SAM + crosslinking	Cysteamine + glutaraldehyde	M13†	Inoviridae (Filamentous)	NIH3T3 mouse fibroblasts	SPR						1000 cells	?
Gold	Detection	Thiol SAM + crosslinking	L-cysteine + glutaraldehyde	D29	Siphoviridae (Long-tailed)	*M. smegmatis* *M. tuberculosis*	QCM	✓	✓				10^3 CFU/mL	?
Gold	Detection	Thiol SAM + crosslinking*	Cysteamine + 1,4-phenylene diisothiocyanate	T4	Myoviridae (Long-tailed)	*E. coli*	CV, LSV, EIS, LAMP						8×10^2 CFU/mL (impedimetric) 10^2 CFU/mL (LAMP)	?

Gold	Detection	Thiol SAM + crosslinking*	DTSP Cysteamine + glutaraldehyde	T4	Myoviridae (Long-tailed)	*E. coli*	Confocal microscopy	✓	✓		✓		✓		10^2 CFU/mL	13.64 - 17.32 PFU/µm²
Gold	Detection	Thiol SAM + streptavidin / biotin*	Sulfo-NHS-SS-biotin + streptavidin / biotin	T4†	Myoviridae (Long-tailed)	*E. coli*	ECIS	✓				✓			?	4.4 PFU/µm²
Gold	Detection, fundamental research	Thiol SAM	carboxy-terminated SAM aldehyde-terminated SAM methyl-terminated SAM	fd-tet	Inoviridae (Filamentous)	Microbeads	Magnetoelastic								3.6×10^5 beads/mL	5.2 - 49.4%
Gold	Fundamental research, capture	Thiol SAM + crosslinking	Histidine + glutaraldehyde L-cysteine + glutaraldehyde Cysteamine + glutaraldehyde	T4	Myoviridae (Long-tailed)	*E. coli*	SPR	✓	✓			✓		✓	N/A	18 PFU/µm²
Gold	Structural	Electropolymerization	PEDOT	M13	Inoviridae (Filamentous)	Prostate-specific antigen	N/A								N/A	7.2 µg/cm²
Gold (plasmonic quasicrystal)	Fundamental research	Thiol SAM	4-ATP	Tbilisi	Podoviridae (Short-tailed)	*Brucella abortus*	SERS	✓		✓		✓	✓		?	?
Gold Glass/silicate	Fundamental research, biocontrol	Amino-silanization Thiol SAM + amide bond	11-MUA + EDC / NHS (on gold) APTES (on glass)	FL-1	Myoviridae (Long-tailed)	*Flavobacterium columnare*	N/A					✓	✓	✓	N/A	0.5 PFU/µm²
Indium tin oxide	Biocontrol	Amino-silanization	APTES APTES + succinic anhydride Octadecyltrimethoxysilane	T4	Myoviridae (Long-tailed)	*E. coli*	N/A								N/A	?
Indium tin oxide	Fundamental research	Amino-silanization	APTES APTES + succinic anhydride Octadecyltrimethoxysilane	T4	Myoviridae (Long-tailed)	*E. coli*	N/A								N/A	~25 - 200 PFU/µm²
Magnetic bead	Capture	Crosslinking*	Bissulfosuccinimidyl suberate	P100 (Listex)	Myoviridae (Long-tailed)	*L. monocytogenes*	N/A								N/A	?
Magnetic bead	Capture, detection	Amide bond	Carboxyl-activation + EDC / NHS Tosyl-activation	P22	Podoviridae (Short-tailed)	*Salmonella*	Magnetic separation + optical reporter	✓	✓			✓	✓		19 CFU/mL (without preenrichment) 0.06 CFU/mL (with pre-enrichment)	1650 PFU/bead
Magnetic bead	Capture, detection	Amide bond	EDC / NHS	T4	Myoviridae (Long-tailed)	*E. coli*	Magnetic separation + impedimetric	✓		✓		✓	✓		10^3 CFU/mL	?
Magnetic bead	Capture, detection	Amide bond	EDC / NHS	T7	Autographiviridae (Short-tailed)	*E. coli*	Magnetic separation + LSV								10^5 CFU/mL	?
Magnetic bead	Capture, detection	Amide bond	EDC / NHS	T7	Autographiviridae (Short-tailed)	*E. coli*	Colorimetric	✓							1×10^4 CFU/mL (without preenrichment) 10 CFU/mL (with pre-enrichment)	1871 PFU/bead

Magnetic bead	Capture, detection	Misc.*	Tosyl-activation	P22	Podoviridae (short-tailed)	*Salmonella*	Magnetic separation + PCR	✓	✓			✓	✓	3 CFU/mL (with PCR)	2000 PFU/bead
Magnetic bead	Capture, detection	Thiol SAM	Isothiocyanate	O157-IOV-4	?	*E. coli O157:H7*	Magnetic separation + colorimetric	✓	✓		✓	✓		4.9×10^4 CFU/mL	?
Metal-organic framework	Detection	Crosslinking	Glutaraldehyde	?	?	*S. arlettae*	Fluorescence	✓	✓			✓		10^2 CFU/mL	?
Metal-organic framework	Detection	Crosslinking*	Glutaraldehyde	?	Siphoviridae (Long-tailed)	*S. aureus*	Photoluminescence quenching	✓		✓	✓	✓		31 CFU/mL	?
Optical fiber	Detection	Amino-silanization + crosslinking	APTES + glutaraldehyde	T4	Myoviridae (Long-tailed)	*E. coli*	SPR	✓		✓				10^3 CFU/mL	?
Optical fiber	Detection	Amino-silanization + crosslinking	APTES + glutaraldehyde	T4	Myoviridae (Long-tailed)	*E. coli*	Optical mode interference	✓				✓		10^3 CFU/mL	?
Polycaprolactone	Biocontrol	Amide bond*		vB_Pae_Kakheti25	Siphoviridae (Long-tailed)	*P. aeruginosa*	N/A							N/A	1 phage per 118 nm
Polyethersulfone	Biocontrol	Amide bond*	EDC / NHS	T4	Myoviridae (Long-tailed)	*E. coli*	N/A	✓			✓			N/A	2 PFU/µm^2
Polyhydroxyalkanoate	Fundamental research, capture	Amide bond	EDC / NHS	T4	Myoviridae (Long-tailed)	*E. coli*	N/A	✓				✓		N/A	4.24 PFU/µm^2
Polystyrene latex beads	Detection	Amide bond	EDC / NHS	M13	Inoviridae (Filamentous)	*P. aeruginosa*	Micro-Raman spectroscopy							10^3 CFU/mL	?
Screen-printed carbon electrode	Detection	Amide bond	EDC	?	Siphoviridae (Long-tailed)	*S. arlettae*	EIS	✓				✓		2 CFU	?
Screen-printed carbon electrode	Detection	Crosslinking	Glutaraldehyde	Gamma phage	Siphoviridae (Long-tailed)	*B. anthracis spores*	Impedimetric							10^3 CFU/mL	?
Silica nanoparticle	Fundamental research, biocontrol	Amino-silanization + crosslinking Amino-silanization + electrostatic Physisorption*	APTMS AEAPTMS + glutaraldehyde	?	Siphoviridae (Long-tailed)	*S. aureus*	N/A	✓	✓			✓		N/A	?
Silicon Nitride (Si3N4)	Detection	Amino-silanization + crosslinking	APTES + glutaraldehyde	?	?	Cancer biomarkers	Potentiometric							?	?
Silver	Detection	Thiol SAM + crosslinking	4-ATP + glutaraldehyde	T4	Myoviridae (Long-tailed)	*E. coli*	SERS	✓				✓		1.5×10^2 CFU/mL	?

N/A Not applicable

% Surface coverage

† Phage was genetically engineered

*** Oriented immobilization**

Table A.3 Physisorptive phage immobilization techniques

								Purification								
Substrate	**Paper Category**	**Immobilization Category**	**Surface treatment**	**Phage**	**Phage morphology (geometry)**	**Analyte/Host**	**Detection scheme (if biosensor)**	**Centrifugation**	**Ultracentrifugation**	**Solvent precipitation**	**PEG precipitation**	**Filtration**	**Dialysis**	**Chromatography**	**Limit of detection (for biosensors)**	**Phage surface density**
Carbon nanotubes	Detection	Electrostatic Physisorption*	Polyethylenimine	?	?	*S. aureus*	CV, DPV	✓		✓					3 CFU/mL	11.7 PFU/μm^2
Carboxymethylcellulose (paper)	Detection	Amide bond*		StyM-AG6 SenS-AG11 LmoM-AG20 EcoM-AGl0 T4 MS2 rV5 AG2A vB_SnwM CGG4-1	Myoviridae, Herelleviridae, Siphoviridae, Leviviridae, Podoviridae (Long-tailed, icosahedral, short-tailed)	*E. coli* O157:H7 *E. coli* O45:H2 *Salmonella* *L. monocytogenes*	qPCR	✓				✓			10−50 CFU/mL	0.01 PFU/μm^2
Cellulose	Biocontrol	Electrostatic Physisorption*	Cibacron Blue F3GA Polyethylenimine Chitan	T7	Autographiviridae (Short-tailed)	*E. coli*	N/A								N/A	?
Cellulose	Biocontrol	Electrostatic Physisorption*	Polyvinylamine	LinM-AG8 LmoM-AG13 LmoM-AG20 EcoM-HG2 EcoM-HG7 EcoM-HG8 (LISTEX P100 commercial cocktail)	Myoviridae (Long-tailed)	*L. monocytogenes* *E. coli* O104:H4	N/A								N/A	?
Cellulose	Biocontrol	Electrostatic Physisorption*	Polyvinylamine	T4 EcoM-AG2 SboM-AG3 LinM-AG8	Myoviridae, Siphoviridae (Long-tailed)	*L. monocytogenes* *E. coli* O157:H7	N/A	✓							N/A	?
Cellulose	Biocontrol	Physisorption		BFSE16 BFSE18 PaDTA1 PaDTA9 PaDTA10 PaDTA11	?	*S.* Typhimurium	N/A								N/A	?
Cellulose (paper)	Fundamental research	Physisorption		T4	Myoviridae (Long-tailed)	*E. coli*	N/A								N/A	?
Cellulose (paper)	Fundamental research	Physisorption		T4	Myoviridae (Long-tailed)	*E. coli*	Colorimetric								N/A	?

Glass/silicate	Detection	Electrostatic Physisorption	Poly-L-lysine	PRD1 E79	Tectiviridae, Myoviridae (Icosahedral, long-tailed)	*P. aeruginosa* *S.* Typhimurium	QCM w/ dissipation monitoring	✓		✓	✓		?	1.6 - 2.2 μg/cm²
Glass/silicate	Fundamental research	Amino-silanization + electrostatic physisorption	APTES	fd-tet	Inoviridae (Filamentous)	*E. coli*	N/A		✓	✓	✓		N/A	?
Glass/silicate	Fundamental research	Amino-silanization + electrostatic physisorption	ED3A PEG APTS	VB_EcoM-AG2 VB_LinM-AG8 VB_SenS-AG11 VB_SboM-AG3	Myoviridae, Myoviridae, Siphoviridae, Myoviridae (Long-tailed)	*E. coli* O126:H8 *L. innocua* *S.* Enteritidis *S. boydii*	N/A	✓		✓			N/A	?
Glass/silicate	Structural	Physisorption	PolyDADMAC	M13	Inoviridae (Filamentous)	*N/A*	SERS						N/A	N/A
Glassy carbon electrode	Detection	Electrostatic Physisorption*	Polyethylenimine + PBSE	T2	Myoviridae (Long-tailed)	*E. coli*	EIS	✓		✓			10^3 CFU/mL	?
Gold	Detection	Physisorption		1G40 fd	Inoviridae (Filamentous)	Beta-galactosidase	SPR						10^-12 M	3nm thick adlayer
Gold	Detection	Physisorption		bacteriophage 12600	?	*S. aureus*	SPR	✓	✓				10^4 CFU/mL	3.1 ng/mm²
Gold	Detection	Physisorption		E2	Inoviridae (Filamentous)	*S. aureus*	Acoustic wave						10^2 CFU/mL	300 PFU/μm²
Gold	Detection	Physisorption		E2	Inoviridae (Filamentous)	*S.* Typhimurium	Magnetoelastic						2.03 log CFU/mL	?
Gold	Detection	Physisorption		E2	Inoviridae (Filamentous)	*S.* Typhimurium	Magnetoelastic						5×10^3 CFU/mL	?
Gold	Detection	Physisorption		E2	Inoviridae (Filamentous)	*S.* Typhimurium	Magnetoelastic						10^3 CFU/mL	?
Gold	Detection	Physisorption		E2	Inoviridae (Filamentous)	*S.* Typhimurium	Magnetostrictive						?	?
Gold	Detection	Physisorption		E2	Inoviridae (Filamentous)	*S.* Typhimurium	Magnetoelastic						5×10^2 CFU/mL	?
Gold	Detection	Physisorption		E2	Inoviridae (Filamentous)	*S.* Typhimurium	Magnetoelastic		✓				?	?
Gold	Detection	Physisorption		E2	Inoviridae (Filamentous)	*S.* Typhimurium	Magnetoelastic						1.6×10^2 CFU/cm2	~50%
Gold	Detection	Physisorption		E2	Inoviridae (Filamentous)	*S.* Typhimurium	Magnetoelastic		✓				?	?
Gold	Detection	Physisorption		E2	Inoviridae (Filamentous)	*S.* Typhimurium	Magnetoelastic						?	?
Gold	Detection	Physisorption		E2	Inoviridae (Filamentous)	*S.* Typhimurium	Magnetoelastic		✓				1.94 log CFU/spinach	?
Gold	Detection	Physisorption		E2	Inoviridae (Filamentous)	*S.* Typhimurium	Magnetoelastic						?	?
Gold	Detection	Physisorption		E2	Inoviridae (Filamentous)	*S.* Typhimurium	Magnetoelastic						?	12.5%
Gold	Detection	Physisorption		E2	Inoviridae (Filamentous)	*S.* Typhimurium	Magnetoelastic						5×10^2 CFU/mL	?

Gold	Detection	Physisorption		E2	Inoviridae (Filamentous)	*S.* Typhimurium *B. anthracis* spores	Magnetoelastic							5×10^3 CFU/mL	?
Gold	Detection	Physisorption		fd	Inoviridae (Filamentous)	*B. anthracis* spores	Magnetoelastic							10^3 spores/mL	?
Gold	Detection	Physisorption		fd	Inoviridae (Filamentous)	*B. anthracis* spores	Magnetoelastic							5×10^3 CFU/mL	?
Gold	Detection	Physisorption		fd	Inoviridae (Filamentous)	*Beta-galactosidase*	QCM							10^-9 M	?
Gold	Detection	Physisorption		fd-tet	Inoviridae (Filamentous)	*B. anthracis* spores	Magnetoelastic							?	?
Gold	Detection	Physisorption		JRB7	Inoviridae (Filamentous)	*B. anthracis* spores	Magnetoelastic							10^2 CFU/mL	?
Gold	Detection	Physisorption		JRB7	Inoviridae (Filamentous)	*B. anthracis* spores	Magnetostrictive							10^4 spores/mL	?
Gold	Detection	Physisorption		JRB7	Inoviridae (Filamentous)	*B. anthracis Sterne* spores *Bacillus cereus* spores *Bacillus megaterium* spores	Magnetoelastic							10^3 CFU/mL	?
Gold	Detection	Physisorption		JRB7	Inoviridae (Filamentous)	*B. anthracis* spores	Magnetoelastic							10^3 spores/mL	?
Gold	Detection	Physisorption		Lm P4:A8 M13K07	Inoviridae (Filamentous)	*L. monocytogenes*	SPR							2×10^6 CFU/mL	?
Gold	Detection	Physisorption		M13	Inoviridae (Filamentous)	*S.* Typhimurium	Magnetoelastic	✓			✓			7.85×10^3 CFU/mm^2	?
Gold	Detection	Physisorption		bacteriophage 12600	?	*S. aureus*	Magnetoelastic							1.76 log CFU/25 mm^2	26 PFU/μm^2
Gold	Detection	Physisorption		T4	Myoviridae (Long-tailed)	*E. coli*	EIS	✓		✓				10^4 CFU/mL	?
Gold	Detection	Physisorption*	PolyDADMAC	S13′	Podoviridae (Short-tailed)	*S. aureus*	Dark-field microscopy							8×10^4 CFU/mL	?
Gold	Detection	Physisorption*		bacteriophage 12600	?	*S. aureus*	Magnetoelastic							10^3 CFU/mL	0.455 µm/phage
Gold	Detection	Physisorption*		T4	Myoviridae (Long-tailed)	*E. coli*	Confocal microscopy	✓	✓				✓	10^2 CFU/mL	14.3 PFU/μm^2
Gold	Detection	Physisorption*		T4	Myoviridae (Long-tailed)	*E. coli*	EIS	✓		✓		✓		10^3 CFU/mL	?
Gold	Fundamental research, detection	Physisorption		fd	Inoviridae (Filamentous)	*S.* Typhimurium	Flow cytometry				✓			?	?

Gold	Structural	Genetic engineering	methionine	fd†	Inoviridae (Filamentous)	*E. coli*	N/A			✓	✓	✓	N/A	?
Gold	Structural, detection	Physisorption*		M13	Inoviridae (Filamentous)	Streptavidin	SPR						10^-15 M	?
Magnetic bead	Capture, biocontrol	Streptavidin / biotin	Sulfo-NHS-biotin + Streptavidin / biotin	SJ2	?	*S.* Enteritidis	N/A						?	?
Magnetic bead Alumina nanofibers Cellulose	Capture, detection	Streptavidin / biotin*	Streptavidin / biotin Cellulose-binding module	T4†	Myoviridae (Long-tailed)	*E. coli* *S.* Typhimurium	Magnetic separation + ATP bioluminescence						6×10^3 CFU/mL	?
Metallic glass (Fe80B20 alloy)	Detection	Physisorption		E2	Inoviridae (Filamentous)	*S.* Typhimurium	Magnetoelastic						50 CFU/mL	?
Optical fiber	Detection	Physisorption		T4	Myoviridae (Long-tailed)	*E. coli*	Resonance wavelength shift						?	?
Organic-inorganic nanoflowers	Detection	Physisorption		T4	Myoviridae (Long-tailed)	*E. coli*	EIS	✓			✓		1 CFU/mL	?
Paper	Fundamental research	Physisorption	PolyDADMAC	T4	Myoviridae (Long-tailed)	*E. coli*	N/A						N/A	?
Polyethylene (optical fiber)	Detection	Physisorption		T4	Myoviridae (Long-tailed)	*E. coli*	Optical fiber transmission	✓	✓		✓		10^4 CFU/mL	10%
Silver	Detection	Physisorption		M13	Inoviridae (Filamentous)	Paraquat (herbicide)	SERS						N/A	?

N/A Not applicable
% Surface coverage
† Phage was genetically engineered
*** Oriented immobilization**

Table A.4 Phage immobilization techniques based on genetic engineering

								Purification								
Substrate	**Paper Category**	**Immobilization Category**	**Surface treatment**	**Phage**	**Phage morphology (geometry)**	**Analyte/ Host**	**Detection scheme (for biosensors)**	**Centrifugation**	**Ultracentrifugation**	**Solvent precipitation**	**PEG precipitation**	**Filtration**	**Dialysis**	**Chromatography**	**Limit of detection (for biosensors)**	**Phage surface density**
Cellulose Magnetic bead	Fundamental research, detection	Streptavidin / biotin*	Streptavidin / biotin Cellulose-binding module	T4†	Myoviridae (Long-tailed)	*E. coli*	Magnetic separation + qPCR								800 CFU/mL (with PCR)	84 - 98%
Glass/silicate	Structural	Amino-silanization	APTES	fd†	Inoviridae (Filamentous)	*E. coli*	N/A	✓			✓				N/A	?
Glass/silicate Magnetic bead	Fundamental research	Amino-silanization*	APTES + formylglycine	fd-tet†	Inoviridae (Filamentous)	*E. coli*	N/A	✓			✓				N/A	?
Gold	Detection	Genetic engineering	Peptide linkers	M13†	Inoviridae (Filamentous)	*E. coli*	SPR				✓				N/A	?
Gold	Detection	Thiol SAM + streptavidin / biotin*	Sulfo-NHS-SS-biotin + streptavidin / biotin	T4†	Myoviridae (Long-tailed)	*E. coli*	ECIS	✓				✓			?	4.4 PFU/µm^2
Gold	Structural	Genetic engineering	methionine	fd†	Inoviridae (Filamentous)	*E. coli*	N/A				✓	✓	✓		N/A	?
Magnetic bead	Capture, detection	Streptavidin / biotin	Streptavidin / biotin	T7†	Autographiviridae (Short-tailed)	*E. coli*	Magnetic separation + PCR	✓	✓			✓			10^2 CFU/mL (with PCR)	248 PFU/bead
Magnetic bead Alumina nanofibers Cellulose	Capture, detection	Streptavidin / biotin*	Streptavidin / biotin Cellulose-binding module	T4†	Myoviridae (Long-tailed)	*E. coli* *S.* Typhimurium	Magnetic separation + ATP bioluminescence								6×10^3 CFU/mL	?
Platinum	Fundamental research	Genetic engineering*		fd†	Inoviridae (Filamentous)	*E. coli*	CV, EIS								N/A	?
PMMA	Fundamental research	Genetic engineering*	PMMA-binding peptide	M13†	Inoviridae (Filamentous)	*E. coli*	N/A								N/A	?
Quantum dot	Detection	Streptavidin / biotin*	Streptavidin / biotin	T4†	Myoviridae (Long-tailed)	*E. coli*	Fluorescence								10 CFU/mL	?

N/A Not applicable
% Surface coverage
† Phage was genetically engineered
*** Oriented immobilization**

Table A.5 Summary of immobilized antimicrobial peptides

Peptide	Storage buffer	Sequence	Tether	Ref.
Bactenecin	PBS + 5% glycerol	MPA-βA-βA-βA-RLARIVVIRVAR-NH_2	3-MPA	[489]
Bactenecin derivative	PBS + 5% glycerol	MPA-βA-βA-βA-RRWRIVVIRVRR-NH_2	3-MPA	[490]
Cecropin A-melittin	PBS + 5% glycerol	MPA-βA-βA-βA-KWKLFKKIGAVLKVL-NH_2	3-MPA	[491]
Penetratin	PBS + 5% glycerol	MPA-βA-βA-βA-RQIKIWFQNRRMKWKK-NH_2	3-MPA	[492]
Magainin	DMSO	GIGKFLHSAGKFGKAFVGEIMKS-AEEA-C-NH_2	L-cysteine amide	[493]

Table A.6 Summary table of infectious titer loss for phages 44AHJD, P68, and gh-1; after storage in various labware for 1, 2, 7, and 14 days.

44AHJD

	Glass			PP			PP + BSA			PP 'LoBind'			PS			PS + BSA		
	Log_{10} reduction		n	Log_{10} reduction		n	Log_{10} reduction		n	Log_{10} reduction		n	Log_{10} reduction		n	Log_{10} reduction		n
Day 1	2.17	±0.91	4	0.45	±0.28	7	0.12	±0.05	8	0.29	±0.11	8	0.45	±0.14	4	0.17	±0.1	7
Day 2	2.14	±0.71	12	0.65	±0.23	7	0.06	±0.03	12	0.45	±0.16	8	0.39	±0.11	9	-0.05	±0.03	12
Day 7	3.17	±1.22	16	2.14	±1.22	8	0.40	±0.16	10	0.32	±0.12	12	1.15	±0.41	9	0.43	±0.27	8
Day 14*	3.67	±1.44	12	3.11	±1.31	12	0.70	±0.28	8	0.80	±0.34	12	2.21	±0.9	12	0.78	±0.42	12

P68

	Glass			PP			PP + BSA			PP 'LoBind'			PS			PS + BSA		
	Log_{10} reduction		n	Log_{10} reduction		n	Log_{10} reduction		n	Log_{10} reduction		n	Log_{10} reduction		n	Log_{10} reduction		n
Day 1	2.14	±1.24	4	2.06	±0.89	4	2.04	±1.06	2	0.78	±0.22	8	1.80	±0.8	4	1.92	±0.66	4
Day 2	2.88	±1.73	8	1.40	±0.84	7	1.20	±0.54	7	2.54	±1.12	4	1.14	±0.7	8	1.10	±0.51	8
Day 7	3.48	±2.34	14	2.77	±1.93	11	1.88	±0.95	8	3.48	±1.28	12	1.92	±0.8	8	1.23	±0.74	6
Day 14*	3.40	±1.82	12	3.47	±0.9	12	1.14	±0.51	8	4.65	±1.14	5	1.78	±0.68	8	0.79	±0.28	8

gh-1

Glass	PP	PP + BSA	PP 'LoBind'	PS	PS + BSA

	Log_{10} reduction		n	Log_{10} reduction		n	Log_{10} reduction		n	Log_{10} reduction		n	Log_{10} reduction		n	Log_{10} reduction		n
Day 1	-0.22	±0.1	8	0.05	±0.02	4	-0.29	±0.19	1	0.97	±0.61	5	0.00	±0	8	-0.15	±0.07	8
Day 2	0.06	±0.03	5	0.16	±0.07	8	-0.22	±0.19	4	1.04	±0.67	8	0.08	±0.01	3	-0.03	±0.01	4
Day 7	2.26	±0.65	4	1.00	±0.24	3	-0.27	±0.18	10	1.78	±1.2	12	1.04	±0.06	12	0.00	±0	10
Day 14*	2.40	±1.14	8	1.54	±0.52	5	0.22	±0.15	5	4.22	±2.81	4	2.00	±0.12	10	0.20	±0.08	11

Data shown are the mean of *n* replicates.
*Day 15 for PP 'LoBind'

Table A.7 Summary table of water contact angle measurements performed on each container type, collated with log_{10} of infectious titer loss of each phage following 14 days of storage

Container	Contact angle	Log_{10} infectious titer loss after 14 days		
		44AHJD	**P68**	**gh-1**
Glass	13.6°	3.67±1.44 (n=12)	3.4±1.82 (n=12)	2.4±1.14 (n=8)
PP	84.5°	3.11±1.31 (n=12)	3.47±0.9 (n=12)	1.54±0.52 (n=5)
PP + BSA	59.3°	0.7±0.28 (n=8)	1.14±0.51 (n=8)	0.22±0.15 (n=5)
PP "LoBind"	63.4°	0.8±0.34 (n=12)	4.65±1.14 (n=5)	4.22±2.81 (n=4)
PS	99.5°	2.21±0.9 (n=12)	1.78±0.68 (n=8)	2±0.12 (n=10)
PS + BSA	64.1°	0.78±0.42 (n=12)	0.79±0.28 (n=8)	0.2±0.08 (n=11)

Data shown are the mean of n replicates

Table A.8 Summary of immobilized antimicrobial peptides

Peptide	Storage buffer	Sequence	Tether	Ref.
Bactenecin	PBS + 5% glycerol	MPA-βA-βA-βA-RLARIVVIRVAR-NH_2	3-MPA	[489]
Bactenecin derivative	PBS + 5% glycerol	MPA-βA-βA-βA-RRWRIVVIRVRR-NH_2	3-MPA	[490]
Cecropin A-melittin	PBS + 5% glycerol	MPA-βA-βA-βA-KWKLFKKIGAVLKVL-NH_2	3-MPA	[491]
Penetratin	PBS + 5% glycerol	MPA-βA-βA-βA-RQIKIWFQNRRMKWKK-NH_2	3-MPA	[492]
Magainin	DMSO	GIGKFLHSAGKFGKAFVGEIMKS-AEEA-C-NH_2	L-cysteine amide	[493]

Bibliography

1. Murray, C. J. L. *et al.* Global burden of bacterial antimicrobial resistance in 2019: a systematic analysis. *Lancet* **6736**, (2022) doi: https://doi.org/10.1016/S0140-6736(21)02724-0

2. Jim O'Neill. Antimicrobial Resistance : Tackling a crisis for the health and wealth of nations. *Rev. Antimicrob. Resist.* 1–16 (2014) doi:10.1038/510015a doi: https://doi.org/10.1038/510015a

3. WHO COVID-19 Dashboard. *World Health Organization* https://covid19.who.int/ (2020)

4. *Antimicrobial Resistance Global Report on Surveillance*. (2014)

5. Kirchhelle, C. Pharming animals: a global history of antibiotics in food production (1935–2017). *Palgrave Commun.* **4**, (2018) doi: https://doi.org/10.1057/s41599-018-0152-2

6. Goldewijk, K. K., Beusen, A., Doelman, J. & Stehfest, E. Anthropogenic land use estimates for the Holocene - HYDE 3.2. *Earth Syst. Sci. Data* **9**, 927–953 (2017) doi: https://doi.org/10.5194/essd-9-927-2017

7. United Nations, Department of Economic and Social Affairs, P. D. *World Population Prospects 2019, Online Edition. Rev. 1*. https://population.un.org/wpp/Download/Standard/Population/ (2019)

8. Pirnay, J. P. *et al.* The magistral phage. *Viruses* **10**, 1–7 (2018) doi: https://doi.org/10.3390/v10020064

9. Rice, L. B. Federal funding for the study of antimicrobial resistance in nosocomial pathogens: No ESKAPE. *J. Infect. Dis.* **197**, 1079–1081 (2008) doi: https://doi.org/10.1086/533452

10. Żaczek, M., Weber-Dąbrowska, B., Międzybrodzki, R., Łusiak-Szelachowska, M. & Górski, A. Phage Therapy in Poland – a Centennial Journey to the First Ethically Approved Treatment Facility in Europe. *Front. Microbiol.* **11**, (2020) doi: https://doi.org/10.3389/fmicb.2020.01056

11. Spratt, B. G. Resistance to antibiotics mediated by target alterations. *Science (80-.).* **264**, 388–393 (1994) doi: https://doi.org/10.1126/science.8153626

12. McDowell, T. D. & Reed, K. E. Mechanism of penicillin killing in the absence of bacterial lysis. *Antimicrob. Agents Chemother.* **33**, 1680–1685 (1989) doi: https://doi.org/10.1128/AAC.33.10.1680

13. Llarrull, L. I., Testero, S. A., Fisher, J. F. & Mobashery, S. The future of the β-lactams. *Curr Opin Microbiol.* **13**, 551–557 (2010) doi: https://doi.org/10.1016/j.mib.2010.09.008

14. Bush, K. Beta-lactamase inhibitors from laboratory to clinic. *Clin. Microbiol. Rev.* **1**, 109–123 (1988) doi: https://doi.org/10.1128/CMR.1.1.109

15. Pages, J.-M. *et al.* Efflux pump, the masked side of beta-lactam resistance in Klebsiella pneumoniae clinical isolates. *PLoS One* **4**, e4817 (2009) doi: https://doi.org/10.1371/journal.pone.0004817

16. Ubukata, K., Nonoguchi, R., Matsuhashi, M. & Konno, M. Expression and inducibility in Staphylococcus aureus of the mecA gene, which encodes a methicillin-resistant S. aureus-specific penicillin-binding protein. *J. Bacteriol.* **171**, 2882–2885 (1989) doi: https://doi.org/10.1128/jb.171.5.2882-2885.1989

17. Essack, S. Y. The development of β-lactam antibiotics in response to the evolution of β-lactamases. *Pharm. Res.* **18**, 1391–1399 (2001) doi: https://doi.org/10.1023/A:1012272403776

18. Knox, J. R. Extended-spectrum and inhibitor-resistant TEM-type beta-lactamases: mutations, specificity, and three-dimensional structure. *Antimicrob. Agents Chemother.* **39**, 2593–2601 (1995) doi: https://doi.org/10.1128/AAC.39.12.2593

19. Prescott, J. M. W., Sherwood, L., Woolverton, C. J. & M, L. Microbiology - Chapter 34: Antimicrobial Chemotherapy. in *Microbiology* 852 (McGraw-Hill, 2008). doi:10.1017/CBO9781107415324.004 doi: https://doi.org/10.1017/CBO9781107415324.004

20. Spellberg, B., Srinivasan, A. & Chambers, H. F. New societal approaches to empowering antibiotic stewardship. *JAMA - J. Am. Med. Assoc.* **315**, 1229–1230 (2016) doi: https://doi.org/10.1001/jama.2016.1346

21. Gillings, M. R. & Stokes, H. W. Are humans increasing bacterial evolvability? *Trends Ecol. Evol.* **27**, 346–352 (2012) doi: https://doi.org/10.1016/j.tree.2012.02.006

22. Wright, G. D. Antibiotic resistance in the environment: A link to the clinic? *Curr. Opin. Microbiol.* **13**, 589–594 (2010) doi: https://doi.org/10.1016/j.mib.2010.08.005

23. Finley, R. L. *et al.* The scourge of antibiotic resistance: The important role of the environment. *Clin. Infect. Dis.* **57**, 704–710 (2013) doi: https://doi.org/10.1093/cid/cit355

24. Smillie, C., Garcillán-Barcia, M. P., Francia, M. V., Rocha, E. P. C. & de la Cruz, F. Mobility of plasmids. *Microbiol. Mol. Biol. Rev.* **74**, 434–452 (2010) doi: https://doi.org/10.1128/MMBR.00020-10

25. Levin, A. S. *et al.* Intravenous colistin as therapy for nosocomial infections caused by multidrug-resistant Pseudomonas aeruginosa and Acinetobacter baumannii. *Clin. Infect. Dis. an Off. Publ. Infect. Dis. Soc. Am.* **28**, 1008–1011 (1999) doi: https://doi.org/10.1086/514732

26. Walsh, C. *Antibiotics: Actions, Origins, Resistance*. (ASM Press, 2003).

27. Liu, Y. Y. *et al.* Emergence of plasmid-mediated colistin resistance mechanism MCR-1 in animals and human beings in China: A microbiological and molecular biological study. *Lancet Infect. Dis.* **16**, 161–168 (2016) doi: https://doi.org/10.1016/S1473-3099(15)00424-7

28. Gogry, F. A., Siddiqui, M. T., Sultan, I. & Haq, Q. M. R. Current Update on Intrinsic and Acquired Colistin Resistance Mechanisms in Bacteria. *Front. Med.* **8**, 1–19 (2021) doi: https://doi.org/10.3389/fmed.2021.677720

29. *Antibiotic Resistance Threats in the United States*. *CDC* (2019)

30. Towse, A. *et al.* Time for a change in how new antibiotics are reimbursed: Development of an insurance framework for funding new antibiotics based on a policy of risk mitigation. *Health Policy (New. York).* **121**, 1025–1030 (2017) doi: https://doi.org/10.1016/j.healthpol.2017.07.011

31. Broughton, C. E., Van Den Berg, H. A., Wemyss, A. M., Roper, D. I. & Rodger, A. Beyond the discovery void: New targets for antibacterial compounds. *Sci. Prog.* **99**, 153–182 (2016) doi: https://doi.org/10.3184/003685016X14616130512308

32. Fischbach, M. A. & Walsh, C. T. Antibiotics for emerging pathogens. *Science (80-.).* **325**, 1089–1093 (2009) doi: https://doi.org/10.1126/science.1176667

33. WHO. *2020 Antibacterial Agents in Clinical and Preclinical Development*. *World Health Organization 2021* (2021).

34. Abedon, S. T. The Bacteriophages - Chapter 5: Phage Ecology. in *Oxford University Press* (ed. Calendar, R.) (2006).

35. Wommack, K. E. & Colwell, R. R. Virioplankton: viruses in aquatic ecosystems. *Microbiol. Mol. Biol. Rev.* **64**, 69–114 (2000) doi: https://doi.org/10.1128/mmbr.64.1.69-114.2000

36. Chibani-Chennoufi, S., Bruttin, A., Brüssow, H., Dillmann, M. & Bru, H. Phage-Host Interaction : An Ecological

Perspective. *J. Bacteriol.* **186**, 3677–3686 (2004) doi: https://doi.org/10.1128/JB.186.12.3677

37. Ashelford, K. E., Day, M. J. & Fry, J. C. Elevated abundance of bacteriophage infecting bacteria in soil. *Appl. Environ. Microbiol.* **69**, 285–289 (2003) doi: https://doi.org/10.1128/AEM.69.1.285-289.2003

38. Al-Shayeb, B. *et al.* Clades of huge phages from across Earth's ecosystems. *Nature* **578**, 425–431 (2020) doi: https://doi.org/10.1038/s41586-020-2007-4

39. Danovaro, R., Manini, E. & Dell'Anno, A. Higher abundance of bacteria than of viruses in deep Mediterranean sediments. *Appl. Environ. Microbiol.* **68**, 1468–1472 (2002) doi: https://doi.org/10.1128/aem.68.3.1468-1472.2002

40. Rodriguez-Reyes, M. G. & Rios-Velazquez, C. Soil metagenome datasets underneath the Arecibo Observatory reflector dish. *Data Br.* **27**, 104710 (2019) doi: https://doi.org/10.1016/j.dib.2019.104710

41. Suttle, C. A. The significance of viruses to mortality in aquatic microbial communities. *Microb. Ecol.* **28**, 237–243 (1994) doi: https://doi.org/10.1007/BF00166813

42. Prescott, J. M. W., Sherwood, L., Woolverton, C. J. & M, L. *Microbiology*. (2008). doi:10.1017/CBO9781107415324.004 doi: https://doi.org/10.1017/CBO9781107415324.004

43. Duckworth, D. H. Who Discovered Bacteriophage? *Bacteriol. Rev.* **40**, 793–802 (1976)

44. Myelnikov, D. An Alternative Cure: The Adoption and Survival of Bacteriophage Therapy in the USSR, 1922-1955. *J. Hist. Med. Allied Sci.* **73**, 385–411 (2018) doi: https://doi.org/10.1093/jhmas/jry024

45. Babalova, E. *et al.* [Preventive value of dried dysentery bacteriophage]. *Zh Mikrobiol Epidemiol Immunobiol.* **45**, 143–5 (1968)

46. McCallin, S. *et al.* Safety analysis of a Russian phage cocktail: From MetaGenomic analysis to oral application in healthy human subjects. *Virology* **443**, 187–196 (2013) doi: https://doi.org/10.1016/j.virol.2013.05.022

47. Summers, W. C. Bacteriophage Therapy. *Annu. Rev. Microbiol.* 437–51 (2001)

48. Levy, S. B. & Bonnie, M. Antibacterial resistance worldwide: Causes, challenges and responses. *Nat. Med.* **10**, S122–S129 (2004) doi: https://doi.org/10.1038/nm1145

49. Ferry, T. *et al.* Phage therapy in bone and joint infection: history, scientific basis, feasibility and perspectives in France. *Virologie* **24**, 49–56 (2020) doi: https://doi.org/10.1684/vir.2020.0808

50. Kutateladze, M. & Adamia, R. Phage therapy experience at the Eliava Institute. *Med. Mal. Infect.* **38**, 426–430 (2008) doi: https://doi.org/10.1016/j.medmal.2008.06.023

51. Abedon, S. T. Chapter 1. Phages. in *Bacteriophages in Health and Disease* (eds. Hyman, P. & Abedon, S. T.) (2012).

52. Stone, R. Stalin's Forgotten Cure. *Sci. (New York, N.Y.)cience* **298**, 63–66 (2002)

53. Salmond, G. P. C. & Fineran, P. C. A century of the phage: Past, present and future. *Nat. Rev. Microbiol.* **13**, 777–786 (2015) doi: https://doi.org/10.1038/nrmicro3564

54. Pirnay, J.-P., Ferry, T. & Resch, G. Recent progress toward the implementation of phage therapy in Western medicine. *FEMS Microbiol Rev.* **46**, (2022) doi: https://doi.org/10.1093/femsre/fuab040

55. Summers, W. C. *Félix d'Herelle and the origins of molecular biology*. (Yale University Press, 1999).

56. Summers, W. C. Cholera and plague in india: The bacteriophage inquiry of 1927-1936. *J. Hist. Med. Allied Sci.* **48**, 275–301 (1993) doi: https://doi.org/10.1093/jhmas/48.3.275

57. Almeida, G. M. de F. & Sundberg, L. R. The forgotten tale of Brazilian phage therapy. *Lancet Infect. Dis.* **20**, e90–e101 (2020) doi: https://doi.org/10.1016/S1473-3099(20)30060-8

58. Alisky, J., Iczkowski, K., Rapoport, A. & Troitsky, N. Bacteriophages show promise as antimicrobial agents. *J. Infect.* **36**, 5–15 (1998) doi: https://doi.org/10.1016/s0163-4453(98)92874-2

59. Sulakvelidze, A. & Alavidze, Z. Bacteriophage Therapy- A Mini Review. *Antimicrob. Agents Chemother.* **45**, 649–659 (2001) doi: https://doi.org/10.1128/AAC.45.3.649

60. Eskenazi, A. *et al.* Combination of pre-adapted bacteriophage therapy and antibiotics for treatment of fracture-related infection due to pandrug-resistant Klebsiella pneumoniae. *Nat. Commun.* **13**, (2022) doi: https://doi.org/10.1038/s41467-021-27656-z

61. Mateczun, A. J. *et al.* Development and Use of Personalized Bacteriophage-Based Therapeutic Cocktails To Treat a Patient with a Disseminated Resistant Acinetobacter baumannii Infection. *Antimicrob. Agents Chemother.* **61**, 1–14 (2017) doi: https://doi.org/10.1128/aac.00954-17

62. Dedrick, R. M. *et al.* Engineered bacteriophages for treatment of a patient with a disseminated drug-resistant Mycobacterium abscessus. *Nat. Med.* **25**, 730–733 (2019) doi: https://doi.org/10.1038/s41591-019-0437-z

63. Abedon, S. T. Phage therapy of pulmonary infections. *Bacteriophage* **5**, (2015) doi: https://doi.org/10.1080/21597081.2015.1020260

64. Jault, P. *et al.* Efficacy and tolerability of a cocktail of bacteriophages to treat burn wounds infected by Pseudomonas aeruginosa (PhagoBurn): a randomised, controlled, double-blind phase 1/2 trial. *Lancet Infect. Dis.* **3099**, 1–11 (2018) doi: https://doi.org/10.1016/S1473-3099(18)30482-1

65. Servick, K. Beleaguered phage therapy trial presses on. *Science (80-.).* **352**, 1506 (2016) doi: https://doi.org/10.1126/science.352.6293.1506

66. Huang, G., Wei, Z. & Wang, D. What do we lean from the “PhagoBurn” project. *Burns* **45**, 260 (2019) doi: https://doi.org/10.1016/j.burns.2018.11.008

67. Bakken, J. S. *et al.* Treating Clostridium difficile infection with fecal microbiota transplantation. *Clin. Gastroenterol. Hepatol.* **9**, 1044–1049 (2011) doi: https://doi.org/10.1016/j.cgh.2011.08.014

68. Goudarzi, M., Seyedjavadi, S. S., Goudarzi, H., Aghdam, E. M. & Nazeri, S. Clostridium difficile infection: An update on epidemiology, risk factors, and therapeutic options. *Sci.* (2014) doi:10.1155/2014/916826 doi: https://doi.org/10.1155/2014/916826

69. Ott, S. J. *et al.* Efficacy of Sterile Fecal Filtrate Transfer for Treating Patients With Clostridium difficile Infection. *Gastroenterology* **152**, 799-811.e7 (2017) doi: https://doi.org/10.1053/j.gastro.2016.11.010

70. Jiang, Z. D. *et al.* Randomised clinical trial: faecal microbiota transplantation for recurrent Clostridum difficile infection – fresh, or frozen, or lyophilised microbiota from a small pool of healthy donors delivered by colonoscopy. *Aliment. Pharmacol. Ther.* **45**, 899–908 (2017) doi: https://doi.org/10.1111/apt.13969

71. Chan, B. K. & Abedon, S. T. *Phage therapy pharmacology. Phage cocktails*. *Advances in Applied Microbiology* vol. 78 (Elsevier Inc., 2012). doi: https://doi.org/10.1016/B978-0-12-394805-2.00001-4

72. Abedon, S. T. Bacteriophage Clinical Use as Antibacterial “Drugs”: Utility and Precedent. *Microbiol. Spectr.* **5**, (2017) doi: https://doi.org/10.1128/microbiolspec.bad-0003-2016

73. Speck, P. & Smithyman, A. Safety and efficacy of phage therapy via the intravenous route. *FEMS Microbiol. Lett.* **363**, (2015) doi: https://doi.org/10.1093/femsle/fnv242

74. Orzechowska, B. The War between Bacteria and Bacteriophages. in (ed. Mishra, M. M. E.-M.) Ch. 6 (IntechOpen, 2019). doi:10.5772/intechopen.87247 doi: https://doi.org/10.5772/intechopen.87247

75. Mulani, M. S., Kamble, E. E., Kumkar, S. N., Tawre, M. S. & Pardesi, K. R. Emerging strategies to combat ESKAPE pathogens in the era of antimicrobial resistance: A review. *Front. Microbiol.* **10**, (2019) doi: https://doi.org/10.3389/fmicb.2019.00539

76. Lia, I. N. The radiological accident in Lia, Georgia. *Int. At. Energy Agency* (2014)

77. ‘Hot’ Legacy Raises Alarm in the Caucasus. *Science (80-.).* **295**, 777–9 (2002) doi: https://doi.org/10.1126/science.295.5556.777b

78. Krishnan, P., Frew, Q., Green, A., Martin, R. & Dziewulski, P. Cause of death and correlation with autopsy

findings in burns patients. *Burns* **39**, 583–588 (2013) doi: https://doi.org/10.1016/j.burns.2012.09.017

79. Jikia, D. *et al.* The use of a novel biodegradable preparation capable of the sustained release of bacteriophages and ciprofloxacin, in the complex treatment of multidrug-resistant Staphylococcus aureus-infected local radiation injuries caused by exposure to Sr90. *Clin. Exp. Dermatol.* **30**, 23–26 (2005) doi: https://doi.org/10.1111/j.1365-2230.2004.01600.x

80. Sulakvelidze, A., Markoishvili, K., Tsitlanadze, G., Katsarava, R. & Morris Jr., J. G. A novel sustained-release matrix based on biodegradable poly(ester amide)s and impregnated with bacteriophages and an antibiotic shows promise in management of infected venous stasis ulcers and other poorly healing wounds. *Int. J. Dermatol.* **41**, 453–458 (2002) doi: https://doi.org/10.1046/j.1365-4362.2002.01451.x

81. Brüssow, H. The Bacteriophages - Chapter 3: Prophage Genomics. in *Oxford University Press* (ed. Calendar, R.) (2006).

82. Hans-W. Ackermann. The Bacteriophages - Chapter 2: Classification of Bacteriophages. in *Oxford University Press* (ed. Calendar, R.) (2006).

83. Hyman, P. & Abedon, S. T. *Bacteriophage Host Range and Bacterial Resistance*. *Advances in Applied Microbiology* vol. 70 (Elsevier Inc., 2010). doi: https://doi.org/10.1016/S0065-2164(10)70007-1

84. Loc-Carrillo, C. & Abedon, S. T. Pros and cons of phage therapy. *Bacteriophage* **1**, 111–114 (2011) doi: https://doi.org/10.4161/bact.1.2.14590

85. Ghebremedhin, M. *et al.* Personalized Therapeutic Cocktail of Wild Environmental Phages Rescues Mice from Acinetobacter baumannii Wound Infections. *Antimicrob. Agents Chemother.* **60**, 5806–5816 (2016) doi: https://doi.org/10.1128/aac.02877-15

86. Comeau, A. M., Tétart, F., Trojet, S. N., Prère, M. F. & Krisch, H. M. Phage-antibiotic synergy (PAS): β-lactam and quinolone antibiotics stimulate virulent phage growth. *PLoS One* **2**, 8–11 (2007) doi: https://doi.org/10.1371/journal.pone.0000799

87. Tortora, G. J., Funke, B. R. & Case, C. L. *Microbiology: An Introduction*. (Benjamin Cummings, 2012).

88. Gill, J. & Hyman, P. Phage Choice, Isolation, and Preparation for Phage Therapy. *Curr. Pharm. Biotechnol.* **11**, 2–14 (2010) doi: https://doi.org/10.2174/138920110790725311

89. Kakasis, A. & Panitsa, G. Bacteriophage therapy as an alternative treatment for human infections. A comprehensive review. *Int. J. Antimicrob. Agents* **53**, 16–21 (2019) doi: https://doi.org/10.1016/j.ijantimicag.2018.09.004

90. Wanger, A. *et al.* Antibiotics, Antimicrobial Resistance, Antibiotic Susceptibility Testing, and Therapeutic Drug Monitoring for Selected Drugs. in *Microbiology and Molecular Diagnosis in Pathology* 119–153 (2017). doi:10.1016/b978-0-12-805351-5.00007-7 doi: https://doi.org/10.1016/b978-0-12-805351-5.00007-7

91. *Methods for Dilution Antimicrobial Susceptibility Tests for Bacteria That Grow Aerobically (11th edn.)*. (2018)

92. Joshi, S. Hospital antibiogram: A necessity. *Indian J. Med. Microbiol.* **28**, 277 (2010) doi: https://doi.org/10.4103/0255-0857.71802

93. BAUER, A. W., KIRBY, W. M. . M. ., SHERRIS, J. . C. . & TURCK, M. Antibiotic Susceptibility Testing by a Standardized Single Disk Method. *Am. J. Clin. Pathol.* **45**, 493–496 (1966)

94. Belkum, A. Van & Dunne, W. M. Pathogens : Wanted — Dead or Alive. *Microbe* **10**, 513–520 (2015) doi: https://doi.org/10.1128/microbe.12.513.1

95. Mittman, S. A., Huard, R. C., Della-Latta, P. & Whittier, S. Comparison of BD Phoenix to Vitek 2, MicroScan MICroSTREP, and Etest for antimicrobial susceptibility testing of Streptococcus pneumoniae. *J. Clin. Microbiol.* **47**, 3557–3561 (2009) doi: https://doi.org/10.1128/JCM.01137-09

96. Jorgensen, J. H. & Ferraro, M. J. Antimicrobial Susceptibility Testing: A Review of General Principles and Contemporary Practices. *Clin. Infect. Dis.* **49**, 1749–1755 (2009) doi: https://doi.org/10.1086/647952

97. Hyman, P. Phages for Phage Therapy: Isolation, Characterization, and Host Range Breadth. *Pharmaceuticals* **12**, 35 (2019) doi: https://doi.org/10.3390/ph12010035

98. Carlson, K. Working with Bacteriophages: Common Techniques and Methodological Approaches. in *Bacteriophages: Biology and Applications* (eds. Kutter, E. & Sulakvelidze, A.) (2004).

99. Adams, M. H. *Bacteriophages*. (Interscience Publishers, 1959).

100. Dougherty, P. F., Yotter, D. W. & Matthews, T. R. Microdilution transfer plate technique for determining in vitro synergy of antimicrobial agents. *Antimicrob. Agents Chemother.* **11**, 225–228 (1977) doi: https://doi.org/10.1128/AAC.11.2.225

101. Agún, S. *et al.* Study of the interactions between bacteriophage phiIPLA-RODI and four chemical disinfectants for the elimination of Staphylococcus aureus contamination. *Viruses* **10**, (2018) doi: https://doi.org/10.3390/v10030103

102. Cooper, C. J., Denyer, S. P. & Maillard, J. Y. Rapid and quantitative automated measurement of bacteriophage activity against cystic fibrosis isolates of Pseudomonas aeruginosa. *J. Appl. Microbiol.* **110**, 631–640 (2011) doi: https://doi.org/10.1111/j.1365-2672.2010.04928.x

103. McLaughlin, M. R. Simple colorimetric microplate test of phage lysis in Salmonella enterica. *J. Microbiol. Methods* **69**, 394–398 (2007) doi: https://doi.org/10.1016/j.mimet.2007.01.006

104. Henry, M. *et al.* Development of a high throughput assay for indirectly measuring phage growth using the OmniLog TM system. *Bacteriophage* **2**, 159–167 (2012) doi: https://doi.org/10.4161/bact.21440

105. Estrella, L. A. *et al.* Characterization of novel Staphylococcus aureus lytic phage and defining their combinatorial virulence using the OmniLog® system . *Bacteriophage* **6**, e1219440 (2016) doi: https://doi.org/10.1080/21597081.2016.1219440

106. Adaptive Phage Therapeutics: The Science. https://web.archive.org/web/20210514230354/https://www.aphage.com/science/

107. Schasfoort, R. B. M. *Handbook of Surface Plasmon Resonance*. (Royal Society of Chemistry, 2017). doi:10.1039/9781788010283 doi: https://doi.org/10.1039/9781788010283

108. Homola, J. *Surface Plasmon Resonance Based Sensors (Springer Series on Chemical Sensors and Biosensors, Volume 4)*. doi:10.1007/b100321 doi: https://doi.org/10.1007/b100321

109. Homola, J. Surface plasmon resonance sensors for detection of chemical and biological species. *Chem. Rev.* **108**, 462–493 (2008) doi: https://doi.org/10.1021/cr068107d

110. Hurot, C. *et al.* Highly sensitive olfactory biosensors for the detection of volatile organic compounds by surface plasmon resonance imaging. *Biosens. Bioelectron.* **123**, 230–236 (2019) doi: https://doi.org/10.1016/j.bios.2018.08.072

111. Pardoux, É., Roux, A., Mathey, R., Boturyn, D. & Roupioz, Y. Antimicrobial peptide arrays for wide spectrum sensing of pathogenic bacteria. *Talanta* **203**, 322–327 (2019) doi: https://doi.org/10.1016/j.talanta.2019.05.062

112. NanoCapture™ Antibody Discovery Microarray Slides. *Plexera* https://web.archive.org/web/20080218144219/http://www.plexera.com/Products/NanoCapture.php

113. Khansili, N., Rattu, G. & Krishna, P. M. Label-free optical biosensors for food and biological sensor applications. *Sensors Actuators B Chem.* **265**, 35–49 (2018) doi: https://doi.org/https://doi.org/10.1016/j.snb.2018.03.004

114. Tripp, R. A., Dluhy, R. A. & Zhao, Y. Novel nanostructures for SERS biosensing. *Nano Today* **3**, 31–37 (2008) doi: https://doi.org/https://doi.org/10.1016/S1748-0132(08)70042-2

115. DaPalma, T., Doonan, B. P., Trager, N. M. & Kasman, L. M. A systematic approach to virus-virus interactions. *Virus Res.* **149**, 1–9 (2010) doi: https://doi.org/10.1016/j.virusres.2010.01.002

116. McAllister, W. T. & Barrett, C. L. Superinfection exclusion by bacteriophage T7. *J. Virol.* **24**, 709–711 (1977) doi:

https://doi.org/10.1128/jvi.24.2.709-711.1977

117. Wagner, R. R. Viral Interference. Some Considerations of Basic Mechanisms and Their Potential Relationship To Host Resistance1. *Bacteriol. Rev.* **24**, 151–166 (1960) doi: https://doi.org/10.1128/mmbr.24.1.151-166.1960

118. Doermann, A. H. Lysis inhibition with Escherichia coli bacteriophages. *Genetics* **33**, 102 (1948)

119. Abedon, S. T. Lysis of Lysis-Inhibited Bacteriophage T4-Infected Cells. **174**, 8073–8080 (1992)

120. Delbrück, M. Interference Between Bacterial Viruses III. The Mutual Exclusion Effect and the Depressor Effect. *J. Bacteriol.* **50**, 151–170 (1945) doi: https://doi.org/10.1128/jb.50.2.151-170.1945

121. Závada, J. Viral pseudotypes and phenotypic mixing. *Arch. Virol.* **50**, 1–15 (1976) doi: https://doi.org/10.1007/BF01317996

122. Paul, S. & B., K. G. Effect of Salt Shock on Stability of λimm434 Lysogens. *J. Bacteriol.* **189**, 3115–3123 (2007) doi: https://doi.org/10.1128/JB.01857-06

123. Dhritiman, G. *et al.* Acyl-Homoserine Lactones Can Induce Virus Production in Lysogenic Bacteria: an Alternative Paradigm for Prophage Induction. *Appl. Environ. Microbiol.* **75**, 7142–7152 (2009) doi: https://doi.org/10.1128/AEM.00950-09

124. Molina, F., Menor-Flores, M., Fernández, L., Vega-Rodríguez, M. A. & García, P. Systematic analysis of putative phage-phage interactions on minimum-sized phage cocktails. *Sci. Rep.* **12**, 1–12 (2022) doi: https://doi.org/10.1038/s41598-022-06422-1

125. O'Connell, L., Roupioz, Y. & Marcoux, P. R. Container Material Dictates Stability of Bacteriophage Suspensions: Light Scattering & Infectivity Measurements Reveal Mechanisms of Infectious Titer Decay. *J. Appl. Microbiol.* 1–15 (2022) doi:10.1111/jam.15581 doi: https://doi.org/10.1111/jam.15581

126. Wilhelm, S. W. & Suttle, C. A. Viruses and Nutrient Cycles in in the Sea. *Bioscience* **49**, 781–788 (1999)

127. Boratýnski, J. *et al.* Preparation of Endotoxin-free Bacteriophages. *Cell. Mol. Biol. Lett.* **9**, 253–259 (2004)

128. Naidoo, R. *et al.* Surface-immobilization of chromatographically purified bacteriophages for the optimized capture of bacteria. *Bacteriophage* **2**, 15–24 (2012) doi: https://doi.org/10.4161/bact.19079

129. Fazzino, L., Anisman, J., Chacón, J. M., Heineman, R. H. & Harcombe, W. R. Lytic bacteriophage have diverse indirect effects in a synthetic cross-feeding community. *ISME J.* **14**, 123–134 (2020) doi: https://doi.org/10.1038/s41396-019-0511-z

130. Singh, A., Arutyunov, D., Szymanski, C. M. & Evoy, S. Bacteriophage based probes for pathogen detection. *Analyst* **137**, 3405–3421 (2012) doi: https://doi.org/10.1039/c2an35371g

131. Dubin, S. B., Benedek, G. B., Bancroft, F. C. & Freifelder, D. Molecular weights of coliphages and coliphage DNA II. Measurement of Diffusion Coefficients Using Optical Mixing Spectroscopy, and Measurement of Sedimentation Coefficients. *J. Mol. Biol.* **54**, 547–556 (1970) doi: https://doi.org/10.1016/0022-2836(70)90125-7

132. Pirnay, J.-P., Merabishvili, M., Van Raemdonck, H., De Vos, D. & Verbeken, G. Bacteriophage Production in Compliance with Regulatory Requirements. in *Bacteriophage Therapy: From Lab to Clinical Practice* (eds. Azeredo, J. & Sillankorva, S.) 233–252 (Springer New York, 2018). doi:10.1007/978-1-4939-7395-8_18 doi: https://doi.org/10.1007/978-1-4939-7395-8_18

133. O'Connell, L., Marcoux, P. R. & Roupioz, Y. Strategies for Surface Immobilization of Whole Bacteriophages: A Review. *ACS Biomater. Sci. Eng.* **7**, 1987–2014 (2021) doi: https://doi.org/10.1021/acsbiomaterials.1c00013

134. Farooq, U. *et al.* High-density phage particles immobilization in surface-modified bacterial cellulose for ultra-sensitive and selective electrochemical detection of Staphylococcus aureus. *Biosens. Bioelectron.* **157**, 112163 (2020) doi: https://doi.org/10.1016/j.bios.2020.112163

135. Bone, S. *et al.* Physisorption and chemisorption of T4 bacteriophages on amino functionalized silica particles. *J. Colloid Interface Sci.* **532**, 68–76 (2018) doi: https://doi.org/10.1016/j.jcis.2018.07.107

136. Cademartiri, R. *et al.* Immobilization of bacteriophages on modified silica particles. *Biomaterials* **31**, 1904–1910 (2010) doi: https://doi.org/10.1016/j.biomaterials.2009.11.029

137. Singh, A. *et al.* Immobilization of bacteriophages on gold surfaces for the specific capture of pathogens. *Biosens. Bioelectron.* **24**, 3645–3651 (2009) doi: https://doi.org/10.1016/j.bios.2009.05.028

138. Hosseinidoust, Z., Van De Ven, T. G. M. & Tufenkji, N. Bacterial capture efficiency and antimicrobial activity of phage-functionalized model surfaces. *Langmuir* **27**, 5472–5480 (2011) doi: https://doi.org/10.1021/la200102z

139. Xu, J., Zhao, C., Chau, Y. & Lee, Y. K. The synergy of chemical immobilization and electrical orientation of T4 bacteriophage on a micro electrochemical sensor for low-level viable bacteria detection via Differential Pulse Voltammetry. *Biosens. Bioelectron.* **151**, 111914 (2020) doi: https://doi.org/10.1016/j.bios.2019.111914

140. Choi, I. Y. *et al.* Studies on lytic, tailed Bacillus cereus-specific phage for use in a ferromagnetoelastic biosensor as a novel recognition element. *J. Microbiol. Biotechnol.* **28**, 87–94 (2018) doi: https://doi.org/10.4014/jmb.1710.10033

141. Fernandes, E. *et al.* A bacteriophage detection tool for viability assessment of Salmonella cells. *Biosens. Bioelectron.* **52**, 239–246 (2014) doi: https://doi.org/10.1016/j.bios.2013.08.053

142. Hermanson, G. T. *Bioconjugate Techniques*. (Elsevier, 2013).

143. Park, M.-K. & Chin, B. A. Novel Approach of a Phage-Based Magnetoelastic Biosensor for the Detection of Salmonella enterica serovar Typhimurium in Soil. *J. Microbiol. Biotechnol.* **26**, 2051–2059 (2016) doi: https://doi.org/10.4014/jmb.1609.09062

144. Lakshmanan, R. S. *et al.* Detection of Salmonella typhimurium in fat free milk using a phage immobilized magnetoelastic sensor. *Sensors Actuators, B Chem.* **126**, 544–550 (2007) doi: https://doi.org/10.1016/j.snb.2007.04.003

145. Singh, R. *Membrane Technology and Engineering for Water Purification*. *Membrane Technology and Engineering for Water Purification, Second Edition: Application, Systems Design and Operation* (Butterworth-Heinemann, 2014). doi:10.1016/c2013-0-15275-0 doi: https://doi.org/10.1016/c2013-0-15275-0

146. Grzenia, D. L., Carlson, J. O. & Wickramasinghe, S. R. Tangential flow filtration for virus purification. *J. Memb. Sci.* **321**, 373–380 (2008) doi: https://doi.org/10.1016/j.memsci.2008.05.020

147. Liu, P. *et al.* Hollow-fiber ultrafiltration for simultaneous recovery of viruses, bacteria and parasites from reclaimed water. *J. Microbiol. Methods* **88**, 155–161 (2012) doi: https://doi.org/10.1016/j.mimet.2011.11.007

148. Olszewski, J., Winona, L. & Oshima, K. H. Comparison of 2 ultrafiltration systems for the concentration of seeded viruses from environmental waters. *Can. J. Microbiol.* **51**, 295–303 (2005) doi: https://doi.org/10.1139/w05-011

149. Jiang, S., Noble, R. & Chu, W. Human adenoviruses and coliphages in urban runoff-impacted coastal waters of Southern California. *Appl. Environ. Microbiol.* **67**, 179–184 (2001) doi: https://doi.org/10.1128/AEM.67.1.179-184.2001

150. Rhodes, E. R., Hamilton, D. W., See, M. J. & Wymer, L. Evaluation of hollow-fiber ultrafiltration primary concentration of pathogens and secondary concentration of viruses from water. *J. Virol. Methods* **176**, 38–45 (2011) doi: https://doi.org/10.1016/j.jviromet.2011.05.031

151. De Keuckelaere, A., Baert, L., Duarte, A., Stals, A. & Uyttendaele, M. Evaluation of viral concentration methods from irrigation and processing water. *J. Virol. Methods* **187**, 294–303 (2013) doi: https://doi.org/10.1016/j.jviromet.2012.11.028

152. Rembhotkar, G. W. & Khatri, G. S. Large scale preparation of bacteriophage λ by tangential flow ultrafiltration for isolation of λ DNA. *Anal. Biochem.* **176**, 373–374 (1989) doi: https://doi.org/10.1016/0003-2697(89)90326-6

153. Erickson, H. P. Size and shape of protein molecules at the nanometer level determined by sedimentation, gel filtration, and electron microscopy. *Biol. Proced. Online* **11**, 32–51 (2009) doi: https://doi.org/10.1007/s12575-009-9008-x

154. Sharpe, P. T. Chapter 3: Centrifugation. in *Laboratory Techniques in Biochemistry and Molecular Biology — Methods of Cell Separation* (1988).

155. Kohno, T. *et al.* A new improved method for the concentration of HIV-1 infective particles. *J. Virol. Methods* **106**, 167–173 (2002) doi: https://doi.org/10.1016/S0166-0934(02)00162-3

156. Vajda, B. P. Concentration and purification of viruses and bacteriophages with polyethylene glycol. *Folia Microbiol. (Praha).* **23**, 88–96 (1978) doi: https://doi.org/10.1007/BF02876605

157. Kanarek, A. D. & Tribe, G. W. Concentration of certain myxoviruses with polyethylene glycol. *Nature* **214**, 927–928 (1967) doi: https://doi.org/10.1038/214927a0

158. Warner, C. M., Barker, N., Lee, S. W. & Perkins, E. J. M13 bacteriophage production for large-scale applications. *Bioprocess Biosyst. Eng.* **37**, 2067–2072 (2014) doi: https://doi.org/10.1007/s00449-014-1184-7

159. Clokie, M. R. J. & Kropinski, A. M. *Bacteriophages - Methods and Protocols, Volume 1: Isolation, Characterization, and Interactions*. *Humana Press* (Humana Press, 2009). doi:10.1007/978-1-60327-164-6 doi: https://doi.org/10.1007/978-1-60327-164-6

160. Lane, J. R. Quantitation of cell-free HIV by reverse transcriptase activity. in *HIV Protocols* (eds. Michael, N. L. & Kim, J. H.) 17–22 (Humana Press, 1999).

161. Greene, R. A. *et al.* Determination of HIV-1 susceptibility to reverse transcriptase (RT) inhibitors by a quantitative cell-free RT assay. *Clin. Diagn. Virol.* **7**, 111–119 (1996)

162. Sarmati, L. *et al.* High rate of HIV isolation from plasma of asymptomatic patients through polyethylene glycol (PEG) treatment. *J. Acquir. Immune Defic. Syndr.* **7**, 10–14 (1994)

163. Yamamoto, R. & Alberts, M. Rapid Bacteriophage Glycol Sedimentation Its Application in the to Virus of Polyethylene Purification. *Virology* **40**, 734–744 (1970) doi: https://doi.org/10.1016/0042-6822(70)90218-7

164. Atha, D. H. & Inghamg, K. C. Mechanism of Precipitation of Proteins by Polyethylene Glycols. *J. Biol. Chem.* **256**, 12108–12117 (1981)

165. Fahie-Wilson, M. & Halsall, D. Polyethylene glycol precipitation: proceed with care. *Ann. Clin. Biochem.* **45**, 233–235 (2008) doi: https://doi.org/10.1258/acb.2008.007262

166. Thurber, R. V., Haynes, M., Breitbart, M., Wegley, L. & Rohwer, F. Laboratory procedures to generate viral metagenomes. *Nat. Protoc.* **4**, 470–483 (2009) doi: https://doi.org/10.1038/nprot.2009.10

167. Bachrach, U. & Friedmann, A. Practical procedures for the purification of bacterial viruses. *Appl. Microbiol.* **22**, 706–15 (1971)

168. Archer, M. J. & Liu, J. L. Bacteriophage T4 nanoparticles as materials in sensor applications: Variables that influence their organization and assembly on surfaces. *Sensors* **9**, 6298–6311 (2009) doi: https://doi.org/10.3390/s90806298

169. Holmfeldt, K. *et al.* Twelve previously unknown phage genera are ubiquitous in global oceans. *Proc. Natl. Acad. Sci.* **110**, 12798–12803 (2013) doi: https://doi.org/10.1073/pnas.1305956110

170. Handa, H. *et al.* Recognition of Salmonella typhimurium by immobilized phage P22 monolayers. *Surf. Sci.* **602**, 1392–1400 (2008) doi: https://doi.org/10.1016/j.susc.2008.01.036

171. Richter, Ł. *et al.* Ordering of bacteriophages in the electric field: Application for bacteria detection. *Sensors Actuators B Chem.* **224**, 233–240 (2016) doi: https://doi.org/10.1016/j.snb.2015.09.042

172. Lawrence, J. E. & Steward, G. F. Purification of viruses by centrifugation. *Man. Aquat. Viral Ecol.* **2**, 166–181 (2010) doi: https://doi.org/10.4319/mave.2010.978-0-9845591-0-7.166

173. Akhwale, J. K. *et al.* Isolation, characterization and analysis of bacteriophages from the haloalkaline lake Elmenteita, Kenya. *PLoS One* **14**, 1–19 (2019) doi: https://doi.org/10.1371/journal.pone.0215734

174. Clokie, M. R. J. & Kropinski, A. M. *Bacteriophages - Methods and Protocols, Volume 2: Molecular and Applied Aspects*. *Humana Press* (2009). doi:10.1007/978-1-60327-565-1 doi: https://doi.org/10.1007/978-1-60327-

565-1

175. Richter, Ł. *et al.* Dense Layer of Bacteriophages Ordered in Alternating Electric Field and Immobilized by Surface Chemical Modification as Sensing Element for Bacteria Detection. *ACS Appl. Mater. Interfaces* **9**, 19622–19629 (2017) doi: https://doi.org/10.1021/acsami.7b03497

176. McConkey, E. H. Composition of mammalian ribosomal subunits: a reevaluation. *Proc. Natl. Acad. Sci. U. S. A.* **71**, 1379–1383 (1974) doi: https://doi.org/10.1073/pnas.71.4.1379

177. Lee, L. F. & Boezi, J. A. Sedimentation Analysis of Pseudomonas putida A . 3 . 12 Bacteriophage gh-1 Deoxyribonucleic Acid. *J. Virol.* **1**, 1274–1276 (1967)

178. Ceglarek, I. *et al.* A novel approach for separating bacteriophages from other bacteriophages using affinity chromatography and phage display. *Sci. Rep.* 1–6 (2013) doi:10.1038/srep03220 doi: https://doi.org/10.1038/srep03220

179. Adriaenssens, E. M., Lehman, S. M. & Vandersteegen, K. CIM Monolithic Anion-Exchange Chromatography as a Useful Alternative to CsCl Gradient Purification of Bacteriophage Particles. *Virology* **434**, 265–270 (2015) doi: https://doi.org/10.1016/j.virol.2012.09.018.CIM

180. Sorokulova, I. B. *et al.* Landscape phage probes for Salmonella typhimurium. *J. Microbiol. Methods* **63**, 55–72 (2005) doi: https://doi.org/10.1016/j.mimet.2005.02.019

181. Nanduri, V., Balasubramanian, S., Sista, S., Vodyanoy, V. J. & Simonian, A. L. Highly sensitive phage-based biosensor for the detection of β-galactosidase. *Anal. Chim. Acta* **589**, 166–172 (2007) doi: https://doi.org/10.1016/j.aca.2007.02.071

182. Kwak, E. A. & Jaworski, J. Controlled surface immobilization of viruses via site-specific enzymatic modification. *J. Mater. Chem. B* **1**, 3486–3493 (2013) doi: https://doi.org/10.1039/c3tb20526f

183. Nanduri, V. *et al.* Phage as a molecular recognition element in biosensors immobilized by physical adsorption. *Biosens. Bioelectron.* **22**, 986–992 (2007) doi: https://doi.org/10.1016/j.bios.2006.03.025

184. Lee, J. H. *et al.* Production of tunable nanomaterials using hierarchically assembled bacteriophages. *Nat. Protoc.* **12**, 1999–2013 (2017) doi: https://doi.org/10.1038/nprot.2017.085

185. Guliy, O. I., Velichko, N. S., Fedonenko, Y. P. & Bunin, V. D. Use of an electro-optical sensor and phage antibodies for immunodetection of Herbaspirillum. *Talanta* **202**, 362–368 (2019) doi: https://doi.org/10.1016/j.talanta.2019.04.086

186. Kovalyova, I. V. & Kropinski, A. M. The complete genomic sequence of lytic bacteriophage gh-1 infecting Pseudomonas putida - Evidence for close relationship to the T7 group. *Virology* **311**, 305–315 (2003) doi: https://doi.org/10.1016/S0042-6822(03)00124-7

187. Berne, B. J. & Robert Pecora. *Dynamic Light Scattering: With Applications to Chemistry, Biology, and Physics*. (Wiley, 1976).

188. Lu, X. & Murphy, R. M. Nanoparticle tracking for protein aggregation research. in *Methods in Molecular Biology — Peptide Self-Assembly* vol. 1777 145–158 (2018). doi: https://doi.org/10.1007/978-1-4939-7811-3_7

189. Malvern Instruments Ltd. NANOSIGHT NS300 - User manual. (2017)

190. Du, S., Kendall, K., Morris, S. & Sweet, C. Measuring number-concentrations of nanoparticles and viruses in liquids on-line. *J. Chem. Technol. Biotechnol.* **85**, 1223–1228 (2010) doi: https://doi.org/10.1002/jctb.2421

191. Malvern. Viruses and Viral Vaccines : Characterization by Nanoparticle Tracking Analysis. (2017)

192. Kaletta, J. *et al.* A rigorous assessment and comparison of enumeration methods for environmental viruses. *Sci. Rep.* **10**, 1–12 (2020) doi: https://doi.org/10.1038/s41598-020-75490-y

193. Hsiao, Y. H. *et al.* Continuous microfluidic assortment of interactive ligands (CMAIL). *Sci. Rep.* **6**, 1–11 (2016) doi: https://doi.org/10.1038/srep32454

194. Szakács, Z., Mészáros, T., Jonge, M. I. de & Gyurcsányi, R. E. Selective counting and sizing of single virus particles

using fluorescent aptamer-based nanoparticle tracking analysis. *Nanoscale* **10**, 13942–13948 (2018) doi: https://doi.org/10.1039/c8nr01310a

195. Lee, L. F. & Boezi, J. A. Characterization of bacteriophage gh-1 for Pseudomonas putida. *J. Bacteriol.* **92**, 1821–1827 (1966)

196. Nakazawa, T. Travels of a Pseudomonas, from Japan around the world. *Environ. Microbiol.* **4**, 782–786 (2002) doi: https://doi.org/10.1046/j.1462-2920.2002.00310.x

197. Wu, X. *et al.* Comparative genomics and functional analysis of niche-specific adaptation in Pseudomonas putida. *FEMS Microbiol. Rev.* **35**, 299–323 (2011) doi: https://doi.org/10.1111/j.1574-6976.2010.00249.x

198. Ackermann, H. W. Bacteriophage observations and evolution. *Res. Microbiol.* **154**, 245–251 (2003) doi: https://doi.org/10.1016/S0923-2508(03)00067-6

199. Carroll-Portillo, A. *et al.* Standard bacteriophage purification procedures cause loss in numbers and activity. *Viruses* **13**, 1–16 (2021) doi: https://doi.org/10.3390/v13020328

200. Suhanovsky, M. M. & Teschke, C. M. Bacteriophage P22 capsid size determination: Roles for the coat protein telokin-like domain and the scaffolding protein amino-terminus. *Virology* **417**, 418–429 (2011) doi: https://doi.org/10.1016/j.virol.2011.06.025

201. Teramoto, K. *et al.* Phylogenetic Classification of Pseudomonas putida Strains by MALDI-MS Using Ribosomal Subunit Proteins as Biomarkers. *Anal. Chem.* **79**, 8712–8719 (2007) doi: https://doi.org/10.1021/ac701905r

202. Franken, L. E. *et al.* A general mechanism of ribosome dimerization revealed by single-particle cryo-electron microscopy. *Nat. Commun.* **8**, 722 (2017) doi: https://doi.org/10.1038/s41467-017-00718-x

203. Matzov, D. *et al.* The cryo-EM structure of hibernating 100S ribosome dimer from pathogenic Staphylococcus aureus. *Nat. Commun.* **8**, 723 (2017) doi: https://doi.org/10.1038/s41467-017-00753-8

204. *NanoSight NTA 2.1 Analytical Software Operating Manual*. (NanoSight Ltd., 2010).

205. Richter, Ł. *et al.* Adsorption of bacteriophages on polypropylene labware affects reproducibility of phage research. *Sci. Rep.* **11**, (2021) doi: https://doi.org/10.1038/s41598-021-86571-x

206. Willey, J. M., Sherwood, L., Prescott, L. M. & Woolverton, C. J. Chapter 17 - The Viruses: Viruses of Bacteria and Archaea. in *Microbiology* (ed. McGraw-Hill) 427–446 (2008).

207. Richard Calendar. *The Bacteriophages*. *Oxford University Press* (Oxford University Press, 2006).

208. Elhani, D. L'émergence de la résistance aux antibiotiques annonce-t-elle le retour des âges sombres ? *Ann. Biol. Clin. (Paris).* **69**, 637–646 (2011) doi: https://doi.org/10.1684/abc.2011.0632

209. Projan, S. J. Why is big Pharma getting out of antibacterial drug discovery? *Curr. Opin. Microbiol.* **6**, 427–430 (2003) doi: https://doi.org/10.1016/j.mib.2003.08.003

210. Gouvêa, D. M., Mendonça, R. C. S., Soto, M. L. & Cruz, R. S. Acetate cellulose film with bacteriophages for potential antimicrobial use in food packaging. *LWT - Food Sci. Technol.* 1–7 (2015) doi:10.1016/j.lwt.2015.03.014 doi: https://doi.org/10.1016/j.lwt.2015.03.014

211. Lone, A. *et al.* Development of prototypes of bioactive packaging materials based on immobilized bacteriophages for control of growth of bacterial pathogens in foods. *Int. J. Food Microbiol.* **217**, 49–58 (2016) doi: https://doi.org/10.1016/j.ijfoodmicro.2015.10.011

212. Wan, J., Johnson, M. L., Guntupalli, R., Petrenko, V. A. & Chin, B. A. Detection of Bacillus anthracis spores in liquid using phage-based magnetoelastic micro-resonators. *Sensors Actuators, B Chem.* **127**, 559–566 (2007) doi: https://doi.org/10.1016/j.snb.2007.05.017

213. Chen, I. H., Petrenkc, V. A., Huang, S. & Chin, B. A. Phage-Based Magnetoelastic Wireless Biosensors for Detecting Bacillus Anthracis Spores. *IEEE Sens. J.* **7**, 470–477 (2007) doi: https://doi.org/10.1109/JSEN.2006.890135

214. Wan, J., Johnson, M. L., Horikawa, S., Chin, B. A. & Petrenko, V. A. Characterization of phage-coupled

magnetoelastic micro-particles for the detection of Bacillus anthracis Sterne spores. in *Proceedings of IEEE Sensors* 1085–1088 (2007). doi:10.1109/ICSENS.2007.4388594 doi: https://doi.org/10.1109/ICSENS.2007.4388594

215. Huang, S. *et al.* The Effect of Salt and Phage Concentrations on the Binding Sensitivity of Magnetoelastic Biosensors for Bacillus anthracis Detection. *Biotechnol. Bioeng.* **101**, 1014–1021 (2008) doi: https://doi.org/10.1002/bit.21995

216. Fu, L. *et al.* Detection of Bacillus anthracis spores using phage-immobilized magnetostrictive milli/micro cantilevers. *IEEE Sens. J.* **11**, 1684–1691 (2011) doi: https://doi.org/10.1109/JSEN.2010.2095002

217. Johnson, M. L. *et al.* A wireless biosensor using microfabricated phage-interfaced magnetoelastic particles. *Sensors Actuators, A Phys.* **144**, 38–47 (2008) doi: https://doi.org/10.1016/j.sna.2007.12.028

218. Ionescu, R. E., Cosnier, S., Herrmann, S. & Marks, R. S. Amperometric immunosensor for the detection of anti-West Nile virus IgG. *Anal. Chem.* **79**, 8662–8668 (2007) doi: https://doi.org/10.1021/ac0707129

219. Yang, L. M. C., Diaz, J. E., McIntire, T. M., Weiss, G. A. & Penner, R. M. Covalent virus layer for mass-based biosensing. *Anal. Chem.* **80**, 933–943 (2008) doi: https://doi.org/10.1021/ac071470f

220. Yang, L. M. C., Diaz, J. E., McIntire, T. M., Weiss, G. A. & Penner, R. M. Direct electrical transduction of antibody binding to a covalent virus layer using electrochemical impedance. *Anal. Chem.* **80**, 5695–5705 (2008) doi: https://doi.org/10.1021/ac8008109

221. Yang, L. M. C. *et al.* Virus electrodes for universal biodetection. *Anal. Chem.* **78**, 3265–3270 (2006) doi: https://doi.org/10.1021/ac052287u

222. Donavan, K. C., Arter, J. A., Weiss, G. A. & Penner, R. M. Virus-PEDOT Biocomposite Films. *Langmuir* **28**, 12581–12587 (2012) doi: https://doi.org/doi:10.1021/la302473j

223. Han, L., Xia, H., Yin, L., Petrenko, V. A. & Liu, A. Selected landscape phage probe as selective recognition interface for sensitive total prostate-specific antigen immunosensor. *Biosens. Bioelectron.* **106**, 1–6 (2018) doi: https://doi.org/10.1016/j.bios.2018.01.046

224. Jia, Y. *et al.* Label-free biosensor: A novel phage-modified Light Addressable Potentiometric Sensor system for cancer cell monitoring. *Biosens. Bioelectron.* **22**, 3261–3266 (2007) doi: https://doi.org/10.1016/j.bios.2007.01.018

225. Kang, Y. R., Park, E. J., Kim, J. H., Min, N. K. & Kim, S. W. Development of bio-nanowire networks using phage-enabled assembly for biological sensor application. *Talanta* **81**, 1425–1430 (2010) doi: https://doi.org/10.1016/j.talanta.2010.02.047

226. Anany, H., Chen, W., Pelton, R. & Griffiths, M. W. Biocontrol of Listeria monocytogenes and Escherichia coli O157:H7 in meat by using phages immobilized on modified cellulose membranes. *Appl. Environ. Microbiol.* **77**, 6379–6387 (2011) doi: https://doi.org/10.1128/AEM.05493-11

227. Wang, C., Sauvageau, D. & Elias, A. Immobilization of Active Bacteriophages on Polyhydroxyalkanoate Surfaces. *ACS Appl. Mater. Interfaces* **8**, 1128–1138 (2016) doi: https://doi.org/10.1021/acsami.5b08664

228. Nogueira, F. *et al.* Immobilization of bacteriophage in wound-dressing nanostructure. *Nanomedicine Nanotechnology, Biol. Med.* **13**, 2475–2484 (2017) doi: https://doi.org/10.1016/j.nano.2017.08.008

229. Vonasek, E., Lu, P., Hsieh, Y. Lo & Nitin, N. Bacteriophages immobilized on electrospun cellulose microfibers by non-specific adsorption, protein–ligand binding, and electrostatic interactions. *Cellulose* **24**, 4581–4589 (2017) doi: https://doi.org/10.1007/s10570-017-1442-3

230. Chung, W. J. *et al.* Biomimetic self-templating supramolecular structures. *Nature* **478**, 364–368 (2011) doi: https://doi.org/10.1038/nature10513

231. Merzlyak, A., Indrakanti, S. & Lee, S. W. Genetically engineered nanofiber-like viruses for tissue regenerating materials. *Nano Lett.* **9**, 846–852 (2009) doi: https://doi.org/10.1021/n18036728

232. Lee, B. Y. *et al.* Virus-based piezoelectric energy generation. *Nat. Nanotechnol.* **7**, 351–356 (2012) doi:

https://doi.org/10.1038/nnano.2012.69

233. Oh, J. W. *et al.* Biomimetic virus-based colourimetric sensors. *Nat. Commun.* **5**, 1–8 (2014) doi: https://doi.org/10.1038/ncomms4043

234. Chen, J., Alcaine, S. D., Jiang, Z., Rotello, V. M. & Nugen, S. R. Detection of Escherichia coli in Drinking Water Using T7 Bacteriophage-Conjugated Magnetic Probe. *Anal. Chem.* **87**, 8977–8984 (2015) doi: https://doi.org/10.1021/acs.analchem.5b02175

235. Wang, Z., Wang, D., Chen, J., Sela, D. A. & Nugen, S. R. Development of a novel bacteriophage based biomagnetic separation method as an aid for sensitive detection of viable Escherichia coli. *Analyst* **141**, 1009–1016 (2016) doi: https://doi.org/10.1039/c5an01769f

236. Wang, D., Hinkley, T., Chen, J., Talbert, J. N. & Nugen, S. R. Phage based electrochemical detection of: Escherichia coli in drinking water using affinity reporter probes. *Analyst* **144**, 1345–1352 (2019) doi: https://doi.org/10.1039/c8an01850b

237. Dixon, D. V., Hosseinidoust, Z. & Tufenkji, N. Effects of environmental and clinical interferents on the host capture efficiency of immobilized bacteriophages. *Langmuir* **30**, 3184–3190 (2014) doi: https://doi.org/10.1021/la500059u

238. Olsson, A. L. J., Wargenau, A. & Tufenkji, N. Optimizing Bacteriophage Surface Densities for Bacterial Capture and Sensing in Quartz Crystal Microbalance with Dissipation Monitoring. *ACS Appl. Mater. Interfaces* **8**, 13698–13706 (2016) doi: https://doi.org/10.1021/acsami.6b02227

239. Anany, H. *et al.* Print to detect: a rapid and ultrasensitive phage-based dipstick assay for foodborne pathogens. *Anal. Bioanal. Chem.* **410**, 1217–1230 (2018) doi: https://doi.org/10.1007/s00216-017-0597-y

240. Bhardwaj, N., Bhardwaj, S. K., Mehta, J., Kim, K. H. & Deep, A. MOF-bacteriophage biosensor for highly sensitive and specific detection of staphylococcus aureus. *ACS Appl. Mater. Interfaces* **9**, 33589–33598 (2017) doi: https://doi.org/10.1021/acsami.7b07818

241. Zhou, Y., Marar, A., Kner, P. & Ramasamy, R. P. Charge-Directed Immobilization of Bacteriophage on Nanostructured Electrode for Whole-Cell Electrochemical Biosensors. *Anal. Chem.* **89**, 5734–5741 (2017) doi: https://doi.org/10.1021/acs.analchem.6b03751

242. Yue, H. *et al.* Label-free electrochemiluminescent biosensor for rapid and sensitive detection of pseudomonas aeruginosa using phage as highly specific recognition agent. *Biosens. Bioelectron.* **94**, 429–432 (2017) doi: https://doi.org/10.1016/j.bios.2017.03.033

243. Zhou, Y. & Ramasamy, R. P. Isolation and separation of Listeria monocytogenes using bacteriophage P100-modified magnetic particles. *Colloids Surfaces B Biointerfaces* **175**, 421–427 (2019) doi: https://doi.org/10.1016/j.colsurfb.2018.12.007

244. Tawil, N., Sacher, E., Mandeville, R. & Meunier, M. Surface plasmon resonance detection of E. coli and methicillin-resistant S. aureus using bacteriophages. *Biosens. Bioelectron.* **37**, 24–29 (2012) doi: https://doi.org/10.1016/j.bios.2012.04.048

245. Tlili, C. *et al.* Bacteria Screening, Viability, And Confirmation Assays Using Bacteriophage-Impedimetric/Loop-Mediated Isothermal Amplification Dual-Response Biosensors. *Anal. Chem.* (2013)

246. Bhardwaj, N. *et al.* Phage Immobilized Antibacterial Silica Nanoplatform: Application against Bacterial Infections. *Adv. Anim. Vet. Sci.* **3**, 1–9 (2015) doi: https://doi.org/10.14737/journal.aavs/2015/3.1s.1.9

247. Bhardwaj, N., Bhardwaj, S. K., Mehta, J., Nayak, M. K. & Deep, A. Bacteriophage conjugated IRMOF-3 as a novel opto-sensor for S. arlettae. *New J. Chem.* **40**, 8068–8073 (2016) doi: https://doi.org/10.1039/c6nj00899b

248. Shabani, A., Marquette, C. A., Mandeville, R. & Lawrence, M. F. Carbon microarrays for the direct impedimetric detection of Bacillus anthracis using Gamma phages as probes. *Analyst* **138**, 1434–1440 (2013) doi: https://doi.org/10.1039/c3an36830k

249. He, F., Xiang, M. & Mi, X. A New Bacteriophage-Modified Piezoelectric Sensor for Rapid and Specific detection of Mycobacterium. *Anal. Lett.* **45**, 1242–1253 (2012) doi: https://doi.org/10.1080/00032719.2012.673106

250. Liébana, S. *et al.* Phagomagnetic separation and electrochemical magneto-genosensing of pathogenic bacteria. *Anal. Chem.* **85**, 3079–3086 (2013) doi: https://doi.org/10.1021/ac3024944

251. Laube, T., Cortés, P., Llagostera, M., Alegret, S. & Pividori, M. I. Phagomagnetic immunoassay for the rapid detection of Salmonella. *Appl. Microbiol. Biotechnol.* **98**, 1795–1805 (2014) doi: https://doi.org/10.1007/s00253-013-5434-4

252. Rippa, M. *et al.* Dodecagonal plasmonic quasicrystals for phage-based biosensing. *Nanotechnology* **29**, (2018) doi: https://doi.org/10.1088/1361-6528/aad2f5

253. Imai, M. *et al.* Dark-Field Microscopic Detection of Bacteria using Bacteriophage-Immobilized SiO2@AuNP Core-Shell Nanoparticles. *Anal. Chem.* **91**, 12352–12357 (2019) doi: https://doi.org/10.1021/acs.analchem.9b02715

254. Tawil, N., Sacher, E., Mandeville, R. & Meunier, M. Strategies for the immobilization of bacteriophages on gold surfaces monitored by surface plasmon resonance and surface morphology. *J. Phys. Chem. C* **117**, 6686–6691 (2013) doi: https://doi.org/10.1021/jp400565m

255. Szermer-Olearnik, B. *et al.* Aggregation/dispersion transitions of T4 phage triggered by environmental ion availability. *J. Nanobiotechnology* **15**, 1–15 (2017) doi: https://doi.org/10.1186/s12951-017-0266-5

256. Langlet, J., Gaboriaud, F., Duval, J. F. L. & Gantzer, C. Aggregation and surface properties of F-specific RNA phages: Implication for membrane filtration processes. *Water Res.* **42**, 2769–2777 (2008) doi: https://doi.org/10.1016/j.watres.2008.02.007

257. Langlet, J., Gaboriaud, F. & Gantzer, C. Effects of pH on plaque forming unit counts and aggregation of MS2 bacteriophage. *J. Appl. Microbiol.* **103**, 1632–1638 (2007) doi: https://doi.org/10.1111/j.1365-2672.2007.03396.x

258. Baran, G. J. & Bloomfield, V. A. Tail-fiber attachement in bacteriophage T4D studied by quasielastic light scattering–band electrophoresis. *Biopolymers* **17**, 2015–2028 (1978) doi: https://doi.org/10.1002/bip.1978.360170815

259. Minikh, O., Tolba, M., Brovko, L. Y. & Griffiths, M. W. Bacteriophage-based biosorbents coupled with bioluminescent ATP assay for rapid concentration and detection of Escherichia coli. *J. Microbiol. Methods* **82**, 177–183 (2010) doi: https://doi.org/10.1016/j.mimet.2010.05.013

260. Ahn, S., Jeon, S., Kwak, E. A., Kim, J. M. & Jaworski, J. Virus-based surface patterning of biological molecules, probes, and inorganic materials. *Colloids Surfaces B Biointerfaces* **122**, 851–856 (2014) doi: https://doi.org/10.1016/j.colsurfb.2014.08.019

261. Zurier, H. S., Duong, M. M., Goddard, J. M. & Nugen, S. R. Engineering Biorthogonal Phage-Based Nanobots for Ultrasensitive, in Situ Bacteria Detection. *ACS Appl. Bio Mater.* **3**, 5824–5831 (2020) doi: https://doi.org/10.1021/acsabm.0c00546

262. Edgar, R. *et al.* High-sensitivity bacterial detection using biotin-tagged phage and quantum-dot nanocomplexes. *Proc. Natl. Acad. Sci. U. S. A.* **103**, 4841–4845 (2006) doi: https://doi.org/10.1073/pnas.0601211103

263. Tolba, M. *et al.* Oriented Immobilization of Bacteriophages for Biosensor Applications. *Appl. Environ. Microbiol.* **76**, 528–535 (2010) doi: https://doi.org/10.1128/AEM.02294-09

264. White, S. J. *et al.* Directed surface attachment of nanomaterials via coiled-coil-driven self-assembly. *Nanotechnology* **23**, (2012) doi: https://doi.org/10.1088/0957-4484/23/49/495304

265. Korkmaz, N. Recombinant bacteriophages as gold binding bio-templates. *Colloids Surfaces B Biointerfaces* **112**, 219–228 (2013) doi: https://doi.org/10.1016/j.colsurfb.2013.07.063

266. Sawada, T. & Serizawa, T. Immobilization of highly oriented filamentous viruses onto polymer substrates. *J. Mater. Chem. B* **1**, 149–152 (2013) doi: https://doi.org/10.1039/c2tb00066k

267. Kim, Y. J., Jin, Y. H., Salieb-Beugelaar, G. B., Nam, C. H. & Stieglitz, T. Genetically engineered bacteriophage delivers a tumor necrosis factor alpha antagonist coating on neural electrodes. *Biomed. Mater.* **9**, (2014) doi: https://doi.org/10.1088/1748-6041/9/1/015009

268. Gervais, L. *et al.* Immobilization of biotinylated bacteriophages on biosensor surfaces. *Sensors Actuators, B Chem.* **125**, 615–621 (2007) doi: https://doi.org/10.1016/j.snb.2007.03.007

269. *Phage Display: Methods and Protocols*. (Humana Press, 2018).

270. Hosseinidoust, Z., Olsson, A. L. J. & Tufenkji, N. Going viral: Designing bioactive surfaces with bacteriophage. *Colloids Surfaces B Biointerfaces* **124**, 2–16 (2014) doi: https://doi.org/10.1016/j.colsurfb.2014.05.036

271. Serwer, P. & Hayes, S. J. Agarose gel electrophoresis of bacteriophages and related particles. I. Avoidance of binding to the gel and recognizing of particles with packaged DNA. *Electrophoresis* **3**, 76–80 (1982) doi: https://doi.org/10.1002/elps.1150030203

272. Leppänen, M., Maasilta, I. J. & Sundberg, L. R. Antibacterial Efficiency of Surface-Immobilized Flavobacterium-Infecting Bacteriophage. *ACS Appl. Bio Mater.* **2**, 4720–4727 (2019) doi: https://doi.org/10.1021/acsabm.9b00242

273. Busch, R. T. *et al.* Optimization and Structural Stability of Gold Nanoparticle-Antibody Bioconjugates. *ACS omega* **4**, 15269–15279 (2019) doi: https://doi.org/10.1021/acsomega.9b02276

274. Couto, C., Vitorino, R. & Daniel-da-silva, A. L. Gold nanoparticles and bioconjugation : a pathway for proteomic applications applications. *Crit. Rev. Biotechnol.* **8551**, (2016) doi: https://doi.org/10.3109/07388551.2016.1141392

275. Love, J. C., Estroff, L. A., Kriebel, J. K., Nuzzo, R. G. & Whitesides, G. M. *Self-Assembled Monolayers of Thiolates on Metals as a Form of Nanotechnology*. *Chem. Rev.* vol. 105 (2005). doi: https://doi.org/10.1021/cr0300789

276. Huang, S. *et al.* The effect of annealing and gold deposition on the performance of magnetoelastic biosensors. *Mater. Sci. Eng. C* **28**, 380–386 (2008) doi: https://doi.org/10.1016/j.msec.2007.04.006

277. Janshoff, A., Galla, H. & Steinem, C. Piezoelectric Mass-Sensing Devices as Biosensors: An Alternative to Optical Biosensors? *Angew Chem Int Ed Engl.* **39**, 4004–4032 (2000) doi: https://doi.org/10.1002/1521-3773(20001117)39:22<4004::aid-anie4004>3.0.co;2-2

278. Amendola, V., Pilot, R. & Frasconi, M. Surface plasmon resonance in gold nanoparticles : a review. *J. Phys. Condens. Matter* **29**, (2017) doi: https://doi.org/10.1088/1361-648X/aa60f3

279. Shabani, A., Marquette, C. A., Mandeville, R. & Lawrence, M. F. Magnetically-assisted impedimetric detection of bacteria using phage-modified carbon microarrays. *Talanta* **116**, 1047–1053 (2013) doi: https://doi.org/10.1016/j.talanta.2013.07.078

280. Zhang, Y., Yan, C., Yang, H., Yu, J. & Wei, H. Rapid and selective detection of E. coli O157:H7 combining phagomagnetic separation with enzymatic colorimetry. *Food Chem.* **234**, 332–338 (2017) doi: https://doi.org/10.1016/j.foodchem.2017.05.013

281. Sun, W., Brovko, L. & Griffiths, M. Use of bioluminescent Salmonella for assessing the efficiency of constructed phage-based biosorbent. *J. Ind. Microbiol. Biotechnol.* **27**, 126–128 (2001) doi: https://doi.org/10.1038/sj.jim.7000198

282. Lee, P. T., Goncalves, L. M. & Compton, R. G. Electrochemical determination of free and total glutathione in human saliva samples. *Sensors Actuators B Chem.* **221**, 962–968 (2015) doi: https://doi.org/https://doi.org/10.1016/j.snb.2015.07.050

283. Filik, H. & Aslıhan Avan, A. Conducting polymer modified screen-printed carbon electrode coupled with magnetic solid phase microextraction for determination of caffeine. *Food Chem.* **242**, 301–307 (2018) doi: https://doi.org/https://doi.org/10.1016/j.foodchem.2017.09.068

284. Hayat, A. & Marty, J. Disposable Screen Printed Electrochemical Sensors: Tools for Environmental Monitoring. *Sensors* **14**, 10432–10453 (2014) doi: https://doi.org/10.3390/s140610432

285. González-Sánchez, M. I., Gómez-Monedero, B., Agrisuelas, J., Iniesta, J. & Valero, E. Highly activated screen-printed carbon electrodes by electrochemical treatment with hydrogen peroxide. *Electrochem. commun.* **91**, 36–40 (2018) doi: https://doi.org/10.1016/j.elecom.2018.05.002

286. Shabani, A. *et al.* Bacteriophage-Modified Microarrays for the Direct Impedimetric Detection of Bacteria. *Anal. Chem.* **80**, 9475–9482 (2008)

287. Bhardwaj, N., Bhardwaj, S. K., Mehta, J., Mohanta, G. C. & Deep, A. Bacteriophage immobilized graphene electrodes for impedimetric sensing of bacteria (Staphylococcus arlettae). *Anal. Biochem.* **505**, 18–25 (2016) doi: https://doi.org/10.1016/j.ab.2016.04.008

288. Wang, S. *et al.* Peptides with selective affinity for carbon nanotubes. *Nat. Mater.* **2**, 196–200 (2003) doi: https://doi.org/10.1038/nmat833

289. Li, X. *et al.* Direct measurements of interactions between polypeptides and carbon nanotubes. *J. Phys. Chem. B* **110**, 12621–12625 (2006) doi: https://doi.org/10.1021/jp061518d

290. Kase, D. *et al.* Affinity selection of peptide phage libraries against single-wall carbon nanohorns identifies a peptide aptamer with conformational variability. *Langmuir* **20**, 8939–8941 (2004) doi: https://doi.org/10.1021/la048968m

291. Morita, Y., Ohsugi, T., Iwasa, Y. & Tamiya, E. A screening of phage displayed peptides for the recognition of fullerene (C60). *J. Mol. Catal. B Enzym.* **28**, 185–190 (2004) doi: https://doi.org/10.1016/j.molcatb.2004.01.018

292. Ma, W., Panecka, M., Tufenkji, N. & Rahaman, M. S. Bacteriophage-based strategies for biofouling control in ultrafiltration: In situ biofouling mitigation, biocidal additives and biofilm cleanser. *J. Colloid Interface Sci.* **523**, 254–265 (2018) doi: https://doi.org/10.1016/j.jcis.2018.03.105

293. Lentini, G. *et al.* Rapid detection of Pseudomonas aeruginosa by phage-capture system coupled with micro-Raman spectroscopy. *Vib. Spectrosc.* **86**, 1–7 (2016) doi: https://doi.org/10.1016/j.vibspec.2016.05.003

294. Mazhorova, A. *et al.* Label-free bacteria detection using evanescent mode of a suspended core terahertz fiber. *2012 Conf. Lasers Electro-Optics, CLEO 2012* **20**, 20675–20683 (2012) doi: https://doi.org/10.1364/oe.20.005344

295. Arter, J. A., Taggart, D. K., McIntire, T. M., Penner, R. M. & Weiss, G. A. Virus-PEDOT nanowires for biosensing. *Nano Lett.* **10**, 4858–4862 (2010) doi: https://doi.org/10.1021/nl1025826

296. Donavan, K. C., Arter, J. A., Weiss, G. A. & Penner, R. M. Virus-Poly(3,4-ethylenedioxythiophene) biocomposite films. *Langmuir* **28**, 12581–12587 (2012) doi: https://doi.org/10.1021/la302473j

297. Adey, N. B., Mataragnon, A. H., Rider, J. E., Carter, J. M. & Kay, B. K. Characterization of phage that bind plastic from phage-displayed random peptide libraries. *Gene* **156**, 27–31 (1995) doi: https://doi.org/10.1016/0378-1119(95)00058-E

298. Berglund, J., Lindbladh, C., Nicholls, I. A. & Mosbach, K. Selection of phage display combinatorial library peptides with affinity for a yohimbine imprinted methacrylate polymer. *Anal. Commun.* **35**, 3–7 (1998) doi: https://doi.org/10.1039/A708046H

299. Sanghvi, A. B., Miller, K. P., Belcher, A. M. & Schmidt, C. E. Biomaterials functionalization using a novel peptide that selectively binds to a conducting polymer. *Nat. Mater.* **4**, (2005) doi: https://doi.org/10.1038/nmat1397

300. Serizawa, T., Sawada, T., Matsuno, H., Matsubara, T. & Sato, T. A Peptide Motif Recognizing a Polymer Stereoregularity. *J. Am. Chem. Soc.* **127**, 13780–13781 (2005) doi: https://doi.org/10.1021/ja054402o

301. Serizawa, T., Sawada, T. & Kitayama, T. Peptide Motifs That Recognize Differences in Polymer-Film Surfaces. *Angew. Chemie* **46**, 723–726 (2007) doi: https://doi.org/10.1002/anie.200603212

302. Serizawa, T., Sawada, T. & Matsuno, H. Highly Specific Affinities of Short Peptides against Synthetic Polymers. *Langmuir* **23**, 11127–11133 (2007) doi: https://doi.org/10.1021/la701822n

303. Serizawa, T. & Techawanitchai, P. Isolation of Peptides that Can Recognize Syndiotactic Polystyrene. *ChemBioChem* **8**, 989–993 (2007) doi: https://doi.org/10.1002/cbic.200700133

304. Kamide, K. *Cellulose and Cellulose Derivatives*. (Elsevier, 2005). doi:10.1016/B978-044482254-3/50003-5 doi: https://doi.org/10.1016/B978-044482254-3/50003-5

305. Kamel, S., Ali, N., Jahangir, K. & Shah, S. M. Pharmaceutical significance of cellulose : A review. **2**, 758–778 (2008) doi: https://doi.org/10.3144/expresspolymlett.2008.90

306. Dincer, C. *et al.* Disposable Sensors in Diagnostics , Food , and Environmental Monitoring. **1806739**, (2019) doi: https://doi.org/10.1002/adma.201806739

307. Links, D. A. Portable self-contained cultures for phage and bacteria made of paper and tape. *Lab Chip* (2012) doi:10.1039/c2lc40391a doi: https://doi.org/10.1039/c2lc40391a

308. Jabrane, T., Dubé, M. & Mangin, P. J. Bacteriophage Immobilization on Paper Surface: Effect of Cationic Pre-coat Layer. (2009)

309. Jabrane, T., Jeaidi, J., Dubé, M. & Mangin, P. J. Gravure printing of enzymes and phages. *Adv Print Media Technol* **35**, 279–288 (2008)

310. Jabrane, T., Laloi, M., Dubé, M. & Mangin, P. Printing and coating of T4 phage based bioactive paper. *Adv. Print. Media Technol.* **37**, 351–358 (2010)

311. Yetisen, A. K., Akram, M. S. & Lowe, C. R. Paper-based microfluidic point-of-care diagnostic devices. *Lab Chip* 8–15 (2013) doi:10.1039/c3lc50169h doi: https://doi.org/10.1039/c3lc50169h

312. Higgins, R. L. *et al.* Longitudinal SARS-CoV-2 antibody study using the Easy Check COVID-19 IgM/IgG™ lateral flow assay. *PLoS One* **16**, e0247797 (2021) doi: https://doi.org/10.1371/journal.pone.0247797

313. Tortorich, R. P., Shamkhalichenar, H. & Choi, J. Inkjet-Printed and Paper-Based Electrochemical Sensors. (2018) doi:10.3390/app8020288 doi: https://doi.org/10.3390/app8020288

314. Kong, M., Shin, J. H., Heu, S., Park, J.-K. & Ryu, S. Lateral flow assay-based bacterial detection using engineered cell wall binding domains of a phage endolysin. *Biosens. Bioelectron.* **96**, 173–177 (2017) doi: https://doi.org/10.1016/j.bios.2017.05.010

315. Shoseyov, O., Shani, Z. & Levy, I. Carbohydrate Binding Modules : Biochemical Properties and Novel Applications. **70**, 283–295 (2006) doi: https://doi.org/10.1128/MMBR.00028-05

316. Tripathi, S. M. *et al.* Long period grating based biosensor for the detection of Escherichia coli bacteria. *Biosens. Bioelectron.* **35**, 308–312 (2012) doi: https://doi.org/10.1016/j.bios.2012.03.006

317. Li, Y. *et al.* Immobilized optical fiber microprobe for selective and sensitive Escherichia coli detection. *J. Biophotonics* (2017) doi:10.1002/jbio.201700162 doi: https://doi.org/10.1002/jbio.201700162

318. Smietana, M. *et al.* Detection of bacteria using bacteriophages as recognition elements immobilized on long-period fiber gratings. *Opt. Express* **19**, 7971 (2011) doi: https://doi.org/10.1364/oe.19.007971

319. Handa, H., Gurczynski, S., Jackson, M. P. & Mao, G. Immobilization and molecular interactions between bacteriophage and lipopolysaccharide bilayers. *Langmuir* **26**, 12095–12103 (2010) doi: https://doi.org/10.1021/la1013413

320. Jeon, D. Y. *et al.* Controlled surface adsorption of fd filamentous phage by tuning of the pH and the functionalization of the surface. *J. Appl. Phys.* **109**, (2011) doi: https://doi.org/10.1063/1.3549113

321. Yoo, S. Y., Oh, J. W. & Lee, S. W. Phage-chips for novel optically readable tissue engineering assays. *Langmuir* **28**, 2166–2172 (2012) doi: https://doi.org/10.1021/la203840n

322. Koh, E. H. *et al.* M13 Bacteriophage/Silver Nanowire Surface-Enhanced Raman Scattering Sensor for Sensitive and Selective Pesticide Detection. *ACS Appl. Mater. Interfaces* **10**, 10388–10397 (2018) doi: https://doi.org/10.1021/acsami.8b01470

323. Chen, C. & Wang, J. Optical biosensors: An exhaustive and comprehensive review. *Analyst* **145**, 1605–1628 (2020) doi: https://doi.org/10.1039/c9an01998g

324. Pinet, E., Pham, A. & Rioux, S. Miniature fiber optic pressure sensor for medical applications: an opportunity for intra-aortic balloon pumping (IABP) therapy. *17th Int. Conf. Opt. Fibre Sensors* **5855**, 234 (2005) doi: https://doi.org/10.1117/12.623806

325. Hamel, C. & Pinet, É. Temperature and pressure fiber-optic sensors applied to minimally invasive diagnostics and therapies. *Opt. Fibers Sensors Med. Diagnostics Treat. Appl. VI* **6083**, 608306 (2006) doi: https://doi.org/10.1117/12.659935

326. Fischer, M. J. E. Chapter 3: Amine Coupling Through EDC/NHS: A Practical Approach. in *Surface Plasmon Resonance: Methods and Protocols (Methods in Molecular Biology, 627)* (eds. Mol, N. J. de & Fischer, M. J. E.) 55–58 (Humana Press, 2010).

327. Liu, F., Luo, Z., Ding, X., Zhu, S. & Yu, X. Phage-displayed protein chip based on SPR sensing. *Sensors Actuators, B Chem.* **136**, 133–137 (2009) doi: https://doi.org/10.1016/j.snb.2008.11.031

328. Karoonuthaisiri, N. *et al.* Development of a M13 bacteriophage-based SPR detection using Salmonella as a case study. *Sensors Actuators, B Chem.* **190**, 214–220 (2014) doi: https://doi.org/10.1016/j.snb.2013.08.068

329. Xu, J. Bacteriophage based Micro Electrochemical Sensors and Extended Gate FET Sensors for Bacteria Detection. (2019)

330. Sedki, M., Chen, X., Chen, C., Ge, X. & Mulchandani, A. Non-lytic M13 phage-based highly sensitive impedimetric cytosensor for detection of coliforms. *Biosens. Bioelectron.* **148**, 111794 (2020) doi: https://doi.org/10.1016/j.bios.2019.111794

331. Ma, L., Green, S. I., Trautner, B. W., Ramig, R. F. & Maresso, A. W. Metals Enhance the Killing of Bacteria by Bacteriophage in Human Blood. *Sci. Rep.* **8**, 1–11 (2018) doi: https://doi.org/10.1038/s41598-018-20698-2

332. Grabarek, Z. & Gergely, J. Zero-length crosslinking procedure with the use of active esters. *Anal. Biochem.* **185**, 131–135 (1990) doi: https://doi.org/https://doi.org/10.1016/0003-2697(90)90267-D

333. Singh, A. *et al.* Bacteriophage tailspike proteins as molecular probes for sensitive and selective bacterial detection. *Biosens. Bioelectron.* **26**, 131–138 (2010) doi: https://doi.org/10.1016/j.bios.2010.05.024

334. Peng, H. & Chen, I. A. Rapid Colorimetric Detection of Bacterial Species through the Capture of Gold Nanoparticles by Chimeric Phages. *ACS Nano* **13**, 1244–1252 (2019) doi: https://doi.org/10.1021/acsnano.8b06395

335. Lenz, R. W. & Marchessault, R. H. Bacterial Polyesters: Biosynthesis, Biodegradable Plastics and Biotechnology. *Biomacromolecules* **6**, 1–8 (2005) doi: https://doi.org/10.1021/bm049700c

336. Vericat, C., Vela, M. E., Benitez, G., Carro, P. & Salvarezza, R. C. Self-assembled monolayers of thiols and dithiols on gold: New challenges for a well-known system. *Chem. Soc. Rev.* **39**, 1805–1834 (2010) doi: https://doi.org/10.1039/b907301a

337. Arya, S. K. *et al.* Chemically immobilized T4-bacteriophage for specific Escherichia coli detection using surface plasmon resonance. *Analyst* **136**, 486–492 (2011) doi: https://doi.org/10.1039/c0an00697a

338. Srivastava, S. K. *et al.* Highly sensitive and specific detection of E. coli by a SERS nanobiosensor chip utilizing metallic nanosculptured thin films. *Analyst* **140**, 3201–3209 (2015) doi: https://doi.org/10.1039/c5an00209e

339. Horikawa, S. *et al.* Effects of surface functionalization on the surface phage coverage and the subsequent performance of phage-immobilized magnetoelastic biosensors. *Biosens. Bioelectron.* **26**, 2361–2367 (2011) doi: https://doi.org/10.1016/j.bios.2010.10.012

340. Batten, S. R. *et al.* Terminology of metal–organic frameworks and coordination polymers (IUPAC Recommendations 2013). *Pure Appl. Chem.* **85**, 1715–1724 (2013) doi: https://doi.org/10.1351/PAC-REC-12-11-20

341. Li, P. *et al.* Synthesis of nanocrystals of Zr-based metal-organic frameworks with csq-net: Significant enhancement in the degradation of a nerve agent simulant. *Chem. Commun.* **51**, 10925–10928 (2015) doi: https://doi.org/10.1039/c5cc03398e

342. Niyomdecha, S. *et al.* Phage-based capacitive biosensor for Salmonella detection. *Talanta* **188**, 658–664 (2018) doi: https://doi.org/10.1016/j.talanta.2018.06.033

343. Liana, A. E. *et al.* Adsorption of T4 bacteriophages on planar indium tin oxide surface via controlled surface

tailoring. *J. Colloid Interface Sci.* **468**, 192–199 (2016) doi: https://doi.org/10.1016/j.jcis.2016.01.052

344. Liana, A. E., Marquis, C. P., Gunawan, C., Justin Gooding, J. & Amal, R. Antimicrobial activity of T4 bacteriophage conjugated indium tin oxide surfaces. *J. Colloid Interface Sci.* **514**, 227–233 (2018) doi: https://doi.org/10.1016/j.jcis.2017.12.029

345. Ginley, D., Hosono, H. & Paine, D. C. *Handbook of Transparent Conductors*. *Handbook of transparent conductors* (Springer, 2010).

346. Aydın, E. B. & Sezgintürk, M. K. Indium tin oxide (ITO): A promising material in biosensing technology. *Trends Anal. Chem.* **97**, 309–315 (2017) doi: https://doi.org/https://doi.org/10.1016/j.trac.2017.09.021

347. Rana, T. M. & Meares, C. F. N-terminal modification of immunoglobulin polypeptide chains tagged with isothiocyanato chelates. *Bioconjug. Chem.* **1**, 357–362 (1990) doi: https://doi.org/10.1021/bc00005a010

348. Situmorang, M., Gooding, J. J., Hibbert, D. B. & Barnett, D. Electrodeposited polytyramine as an immobilisation matrix for enzyme biosensors. *Biosens. Bioelectron.* **13**, 953–962 (1998) doi: https://doi.org/10.1016/S0956-5663(98)00033-5

349. Vilian, A. T. E. *et al.* Immobilization of myoglobin on Au nanoparticle-decorated carbon nanotube/polytyramine composite as a mediator-free H2O2 and nitrite biosensor. *Sci. Rep.* **5**, 18390 (2015) doi: https://doi.org/10.1038/srep18390

350. Tran, L. D. *et al.* A polytyramine film for covalent immobilization of oligonucleotides and hybridization. *Synth. Met.* **139**, 251–262 (2003) doi: https://doi.org/https://doi.org/10.1016/S0379-6779(03)00131-0

351. Surface-activated Dynabeads: Product Portfolio. (2010)

352. Huang, S. *et al.* Sequential detection of Salmonella typhimurium and Bacillus anthracis spores using magnetoelastic biosensors. *Biosens. Bioelectron.* **24**, 1730–1736 (2009) doi: https://doi.org/10.1016/j.bios.2008.09.006

353. Shen, W., Lakshmanan, R. S., Mathison, L. C., Petrenko, V. A. & Chin, B. A. Phage coated magnetoelastic micro-biosensors for real-time detection of Bacillus anthracis spores. *Sensors Actuators, B Chem.* **137**, 501–506 (2009) doi: https://doi.org/10.1016/j.snb.2009.01.027

354. Li, S. *et al.* Direct detection of Salmonella typhimurium on fresh produce using phage-based magnetoelastic biosensors. *Biosens. Bioelectron.* **26**, 1313–1319 (2010) doi: https://doi.org/10.1016/j.bios.2010.07.029

355. Park, M. K., Oh, J. H. & Chin, B. A. The effect of incubation temperature on the binding of Salmonella typhimurium to phage-based magnetoelastic biosensors. *Sensors Actuators, B Chem.* **160**, 1427–1433 (2011) doi: https://doi.org/10.1016/j.snb.2011.10.003

356. Chai, Y. *et al.* Rapid and Sensitive Detection of Salmonella Typhimurium on Eggshells by Using Wireless Biosensors. *J. Food Prot.* **75**, 631–636 (201AD)

357. Park, M. K. *et al.* The effect of incubation time for Salmonella Typhimurium binding to phage-based magnetoelastic biosensors. *Food Control* **26**, 539–545 (2012) doi: https://doi.org/10.1016/j.foodcont.2012.01.061

358. Chai, Y. *et al.* Design of a surface-scanning coil detector for direct bacteria detection on food surfaces using a magnetoelastic biosensor. *J. Appl. Phys.* **114**, (2013) doi: https://doi.org/10.1063/1.4821025

359. Park, M. K., Park, J. W., Wikle, H. C. & Chin, B. A. Evaluation of phage-based magnetoelastic biosensors for direct detection of Salmonella Typhimurium on spinach leaves. *Sensors Actuators, B Chem.* **176**, 1134–1140 (2013) doi: https://doi.org/10.1016/j.snb.2012.10.084

360. Park, M. K., Li, S. & Chin, B. A. Detection of Salmonella typhimurium Grown Directly on Tomato Surface Using Phage-Based Magnetoelastic Biosensors. *Food Bioprocess Technol.* **6**, 682–689 (2013) doi: https://doi.org/10.1007/s11947-011-0708-2

361. Chen, I. H. *et al.* Bacterial assessment of phage magnetoelastic sensors for Salmonella enterica Typhimurium detection in chicken meat. *Food Control* **71**, 273–278 (2017) doi:

https://doi.org/10.1016/j.foodcont.2016.07.003

362. Wang, F. *et al.* Detection of Salmonella typhimurium on spinach using phage-based magnetoelastic biosensors. *Sensors* **17**, 1–9 (2017) doi: https://doi.org/10.3390/s17020386

363. Mejri, M. B. *et al.* Impedance biosensing using phages for bacteria detection: Generation of dual signals as the clue for in-chip assay confirmation. *Biosens. Bioelectron.* **26**, 1261–1267 (2010) doi: https://doi.org/10.1016/j.bios.2010.06.054

364. Moghtader, F., Congur, G., Zareie, H. M., Erdem, A. & Piskin, E. Impedimetric detection of pathogenic bacteria with bacteriophages using gold nanorod deposited graphite electrodes. *RSC Adv.* **6**, 97832–97839 (2016) doi: https://doi.org/10.1039/c6ra18884b

365. Li, S. *et al.* Amorphous metallic glass biosensors. *Intermetallics* **30**, 80–85 (2012) doi: https://doi.org/10.1016/j.intermet.2012.03.030

366. Li, Y. *et al.* A new biosensor based on the recognition of phages and the signal amplification of organic-inorganic hybrid nanoflowers for discriminating and quantitating live pathogenic bacteria in urine. *Sensors Actuators, B Chem.* **258**, 803–812 (2018) doi: https://doi.org/10.1016/j.snb.2017.11.155

367. Balasubramanian, S., Sorokulova, I. B., Vodyanoy, V. J. & Simonian, A. L. Lytic phage as a specific and selective probe for detection of Staphylococcus aureus — A surface plasmon resonance spectroscopic study. *Biosens. Bioelectron.* **22**, 948–955 (2007) doi: https://doi.org/10.1016/j.bios.2006.04.003

368. Hiremath, N., Guntupalli, R., Vodyanoy, V., Chin, B. A. & Park, M. K. Detection of methicillin-resistant Staphylococcus aureus using novel lytic phage-based magnetoelastic biosensors. *Sensors Actuators, B Chem.* **210**, 129–136 (2015) doi: https://doi.org/10.1016/j.snb.2014.12.083

369. Byeon, H. M., Vodyanoy, V. J., Oh, J.-H., Kwon, J.-H. & Park, M.-K. Lytic Phage-Based Magnetoelastic Biosensors for On-site Detection of Methicillin-Resistant Staphylococcus aureus on Spinach Leaves. *J. Electrochem. Soc.* **162**, B230–B235 (2015) doi: https://doi.org/10.1149/2.0681508jes

370. Nanduri, V., Bhunia, A. K., Tu, S. I., Paoli, G. C. & Brewster, J. D. SPR biosensor for the detection of L. monocytogenes using phage-displayed antibody. *Biosens. Bioelectron.* **23**, 248–252 (2007) doi: https://doi.org/10.1016/j.bios.2007.04.007

371. Lakshmanan, R. S. *et al.* Phage immobilized magnetoelastic sensor for the detection of Salmonella typhimurium. *J. Microbiol. Methods* **71**, 55–60 (2007) doi: https://doi.org/10.1016/j.mimet.2007.07.012

372. Fu, L. *et al.* Magnetostrictive microcantilever as an advanced transducer for biosensors. *Sensors* **7**, 2929–2941 (2007) doi: https://doi.org/10.3390/s7112929

373. Olsen, E. V. *et al.* Affinity-selected filamentous bacteriophage as a probe for acoustic wave biodetectors of Salmonella typhimurium. *Biosens. Bioelectron.* **21**, 1434–1442 (2006) doi: https://doi.org/10.1016/j.bios.2005.06.004

374. Kim, Y.-K. *et al.* Control of adsorption and alignment of V2O5nanowires via chemically functionalized patterns. *Nanotechnology* **18**, 15304 (2006) doi: https://doi.org/10.1088/0957-4484/18/1/015304

375. Gu, G. *et al.* V2O5 nanofibre sheet actuators. *Nat. Mater.* **2**, 316–319 (2003) doi: https://doi.org/10.1038/nmat880

376. Devaraj, V., Han, J., Kim, C., Kang, Y. C. & Oh, J. W. Self-assembled nanoporous biofilms from functionalized nanofibrous M13 bacteriophage. *Viruses* **10**, 1–11 (2018) doi: https://doi.org/10.3390/v10060322

377. Chen, R. J., Zhang, Y., Wang, D. & Dai, H. Noncovalent sidewall functionalization of single-walled carbon nanotubes for protein immobilization. *J. Am. Chem. Soc.* **123**, 3838–3839 (2001) doi: https://doi.org/10.1021/ja010172b

378. Kim, W. *et al.* Biomimetic self-templating optical structures fabricated by genetically engineered M13 bacteriophage. *Biosens. Bioelectron.* **85**, 853–859 (2016) doi: https://doi.org/10.1016/j.bios.2016.05.099

379. Sherman E. Ross, Steven D. Carson, L. M. F. Effects of detergents on avidin–biotin interaction. *Biotechniques* **4**,

350–353 (1986)

380. Petrenko, V. A. & Sorokulova, I. B. Detection of biological threats. A challenge for directed molecular evolution. *J. Microbiol. Methods* **58**, 147–168 (2004) doi: https://doi.org/10.1016/j.mimet.2004.04.004

381. Mao, C., Liu, A. & Cao, B. Virus-Based Chemical and Biological Sensing. *Angew Chem Int Ed Engl* **48**, 6790–6810 (2009) doi: https://doi.org/10.1002/anie.200900231

382. Kim, I., Moon, J.-S. & Oh, J.-W. Recent advances in M13 bacteriophage-based optical sensing applications. *Nano Converg.* **3**, (2016) doi: https://doi.org/10.1186/s40580-016-0087-5

383. Wu, L. *et al.* Specific detection of live Escherichia coli O157: H7 using tetracysteine-tagged PP01 bacteriophage. *Biosens. Bioelectron.* **86**, 102–108 (2016) doi: https://doi.org/10.1016/j.bios.2016.06.041

384. Li, Q., Shivachandra, S. B., Zhang, Z., Rao, V. B. & Ave, M. Assembly of the Small Outer Capsid Protein , Soc , on Bacteriophage T4 : A Novel System for High Density Display of Multiple Large Anthrax Toxins and Foreign Proteins on Phage Capsid. 1006–1019 (2007) doi:10.1016/j.jmb.2007.05.008 doi: https://doi.org/10.1016/j.jmb.2007.05.008

385. Ren, Z. & Black, L. W. Phage T4 SOC and HOC display of biologically active , full-length proteins on the viral capsid. *Gene* **215**, 439–444 (1998) doi: https://doi.org/10.1016/s0378-1119(98)00298-4

386. Naik, R. R., Stringer, S. J., Agarwal, G., Jones, S. E. & Stone, M. O. Biomimetic synthesis and patterning of silver nanoparticles. *Nat. Mater.* **1**, 169–172 (2002) doi: https://doi.org/10.1038/nmat758

387. Sano, K. I. & Shiba, K. A Hexapeptide Motif that Electrostatically Binds to the Surface of Titanium. *J. Am. Chem. Soc.* **125**, 14234–14235 (2003) doi: https://doi.org/10.1021/ja038414q

388. Seker, U. O. S. *et al.* Adsorption Behavior of Linear and Cyclic Genetically Engineered Platinum Binding Peptides. *Langmuir* **23**, 7895–7900 (2007) doi: https://doi.org/10.1021/la700446g

389. Brown, S. Engineered iron oxide-adhesion mutants of the Escherichia coli phage λ receptor. *Proc. Natl. Acad. Sci. U. S. A.* **89**, 8651–8655 (1992) doi: https://doi.org/10.1073/pnas.89.18.8651

390. Barbas, C. F., Rosenblum, J. S. & Lerner, R. A. Direct selection of antibodies that coordinate metals from semisynthetic combinatorial libraries. *Proc. Natl. Acad. Sci. U. S. A.* **90**, 6385–6389 (1993) doi: https://doi.org/10.1073/pnas.90.14.6385

391. Naik, R. R., Brott, L. L., Clarson, S. J. & Stone, M. O. Silica-Precipitating Peptides Isolated from a Combinatorial Phage Display Peptide Library. *J. Nanosci. Nanotechnol.* **2**, 95–100 (2002) doi: https://doi.org/10.1166/jnn.2002.074

392. Whaley, S. R. & Belcher, A. M. Borrowing ideas from nature: peptide specific binding to gallium arsenide. in *Materials Research Society Symposium - Proceedings* vol. 599 189–199 (2000). doi: https://doi.org/10.1557/proc-599-189

393. Whaley, S. R., English, D. S., Hu, E. L., Barbara, P. F. & Belcher, A. M. Selection of peptides with semiconductor binding specificity for directed nanocrystal assembly. *Nature* **405**, 665–668 (2000) doi: https://doi.org/10.1038/35015043

394. Thirumurugan, P., Matosiuk, D. & Jozwiak, K. Click Chemistry for Drug Development and Diverse Chemical-Biology Applications. *Chem. Rev* **113**, 4905–4979 (2013) doi: https://doi.org/10.1021/cr200409f

395. Kolb, H. C. & Sharpless, K. B. The growing impact of click chemistry on drug discovery. *Drug Discovery Today* vol. 8 1128–1137 (2003) doi: https://doi.org/10.1016/S1359-6446(03)02933-7

396. Grass, R. N., Athanassiou, E. K. & Stark, W. J. Covalently functionalized cobalt nanoparticles as a platform for magnetic separations in organic synthesis. *Angew. Chemie - Int. Ed.* **46**, 4909–4912 (2007) doi: https://doi.org/10.1002/anie.200700613

397. Schätz, A., Grass, R. N., Stark, W. J. & Reiser, O. TEMPO supported on magnetic C/Co-nanoparticles: A highly active and recyclable organocatalyst. *Chemistry (Easton).* **14**, 8262–8266 (2008) doi: https://doi.org/10.1002/chem.200801001

398. Duong, M. M., Carmody, C. M., Ma, Q., Peters, J. E. & Nugen, S. R. Optimization of T4 phage engineering via CRISPR/Cas9. *Sci. Rep.* **10**, 18229 (2020) doi: https://doi.org/10.1038/s41598-020-75426-6

399. Broeker, N. K. *et al.* In Vitro Studies of Lipopolysaccharide-Mediated DNA Release of Podovirus HK620. *Viruses* **10**, (2018) doi: https://doi.org/10.3390/v10060289

400. Andres, D. *et al.* Tail morphology controls DNA release in two Salmonella phages with one lipopolysaccharide receptor recognition system. *Mol. Microbiol.* **83**, 1244–1253 (2012) doi: https://doi.org/10.1111/j.1365-2958.2012.08006.x

401. Andres, D. *et al.* Tailspike interactions with lipopolysaccharide effect DNA ejection from phage P22 particles in vitro. *J. Biol. Chem.* **285**, 36768–36775 (2010) doi: https://doi.org/10.1074/jbc.M110.169003

402. Mack, J. D. *et al.* Phage-Based Biosensor and Optimization of Surface Blocking Agents to Detect Salmonella Typhimurium on Romaine Lettuce. *J. Food Saf.* **37**, (2017) doi: https://doi.org/10.1111/jfs.12299

403. Bennett, A. R., Davids, F. G. C., Vlahodimou, S., Banks, J. G. & Betts, R. P. The use of bacteriophage-based systems for the separation and concentration of Salmonella. *J. Appl. Microbiol.* **83**, 259–265 (1997) doi: https://doi.org/10.1046/j.1365-2672.1997.00257.x

404. O'Connell, L., Roupioz, Y. & Marcoux, P. Optical bacteriophage susceptibility testing by SPR (surface plasmon resonance). *Proc.SPIE* **11661**, (2021) doi: https://doi.org/10.1117/12.2578753

405. Rosenblum, E. D. & Tyrone, S. Serology, Density, and Morphology of Staphylococcal Phages. *J. Bacteriol.* **88**, 1737–1742 (1964) doi: https://doi.org/10.1128/jb.88.6.1737-1742.1964

406. Vandersteegen, K. *et al.* Romulus and Remus, Two Phage Isolates Representing a Distinct Clade within the Twortlikevirus Genus, Display Suitable Properties for Phage Therapy Applications. *J. Virol.* **87**, 3237–3247 (2013) doi: https://doi.org/10.1128/jvi.02763-12

407. Vybiral, D. *et al.* Complete nucleotide sequence and molecular characterization of two lytic Staphylococcus aureus phages: 44AHJD and P68. *FEMS Microbiol. Lett.* **219**, 275–283 (2003) doi: https://doi.org/10.1016/S0378-1097(03)00028-4

408. Chen, W. *et al.* Structural changes in bacteriophage T7 upon receptor-induced genome ejection. *Proc. Natl. Acad. Sci.* **118**, (2021) doi: https://doi.org/10.1073/PNAS.2102003118

409. Ionel, A. *et al.* Molecular rearrangements involved in the capsid shell maturation of bacteriophage T7. *J. Biol. Chem.* **286**, 234–242 (2011) doi: https://doi.org/10.1074/jbc.M110.187211

410. Veesler, D. *et al.* Structure of the phage TP901-1 1.8 MDa baseplate suggests an alternative host adhesion mechanism. *Proc. Natl. Acad. Sci. U. S. A.* **109**, 8954–8958 (2012) doi: https://doi.org/10.1073/pnas.1200966109

411. Bebeacua, C. *et al.* Visualizing a complete Siphoviridae member by single-particle electron microscopy: the structure of lactococcal phage TP901-1. *J. Virol.* **87**, 1061–1068 (2013) doi: https://doi.org/10.1128/jvi.02836-12

412. Aksyuk, A. A. *et al.* The tail sheath structure of bacteriophage T4: a molecular machine for infecting bacteria. *EMBO J.* **28**, 821–829 (2009) doi: https://doi.org/10.1038/emboj.2009.36

413. Conway, J. H. & Sloane, N. J. A. *Sphere packings, lattices, and groups*. (Springer, 1998).

414. Staquicini, D. I. *et al.* Design and proof of concept for targeted phage-based COVID-19 vaccination strategies with a streamlined cold-free supply chain. *PNAS* **118**, (2021) doi: https://doi.org/10.1073/pnas.2105739118

415. Hu, J. Y. *et al.* Removal of MS2 bacteriophage using membrane technologies. *Water Sci. Technol. a J. Int. Assoc. Water Pollut. Res.* **47**, 163–168 (2003)

416. Fedorenko, A., Grinberg, M., Orevi, T. & Kashtan, N. Survival of the enveloped bacteriophage Phi6 (a surrogate for SARS-CoV-2) in evaporated saliva microdroplets deposited on glass surfaces. *Sci. Rep.* **10**, 22419 (2020) doi: https://doi.org/10.1038/s41598-020-79625-z

417. Ferry, T. *et al.* Salvage debridement, antibiotics and implant retention (“DAIR”) with local injection of a selected cocktail of bacteriophages: Is it an option for an elderly patient with relapsing staphylococcus aureus prosthetic-joint infection? *Open Forum Infect. Dis.* **5**, 1–4 (2018) doi: https://doi.org/10.1093/ofid/ofy269

418. Wright, A., Hawkins, C. H., Änggård, E. E. & Harper, D. R. A controlled clinical trial of a therapeutic bacteriophage preparation in chronic otitis due to antibiotic-resistant Pseudomonas aeruginosa ; a preliminary report of efficacy. *Clin. Otolaryngol.* **34**, 349–357 (2009) doi: https://doi.org/10.1111/j.1749-4486.2009.01973.x

419. Biswas, B. *et al.* Phage Therapy for a Multidrug-Resistant Acinetobacter baumannii Craniectomy Site Infection. *Open Forum Infect. Dis.* **5**, 1–3 (2018) doi: https://doi.org/10.1093/ofid/ofy064

420. Perlemoine, P. *et al.* Phage susceptibility testing and infectious titer determination through wide-field lensless monitoring of phage plaque growth. *PLoS One* **16**, 1–14 (2021) doi: https://doi.org/10.1371/journal.pone.0248917

421. Wdowiak, M., Ochirbat, E. & Paczesny, J. Gold—polyoxoborates nanocomposite prohibits adsorption of bacteriophages on inner surfaces of polypropylene labware and protects samples from bacterial and yeast infections. *Viruses* **13**, (2021) doi: https://doi.org/10.3390/v13071206

422. Duyvejonck, H. *et al.* Evaluation of the stability of bacteriophages in different solutions suitable for the production of magistral preparations in Belgium. *Viruses* **13**, 1–11 (2021) doi: https://doi.org/10.3390/v13050865

423. Chhibber, S., Kaur, P. & Gondil, V. S. Simple drop cast method for enumeration of bacteriophages. *J. Virol. Methods* **262**, 1–5 (2018) doi: https://doi.org/10.1016/j.jviromet.2018.09.001

424. Trouwborst, T., Kuyper, S., De Jong, J. C. & Plantinga, A. D. Inactivation of some bacterial and animal viruses by exposure to liquid air interfaces. *J. Gen. Virol.* **24**, 155–165 (1974) doi: https://doi.org/10.1099/0022-1317-24-1-155

425. Rossi, P. & Aragno, M. Analysis of bacteriophage inactivation and its attenuation by adsorption onto colloidal particles by batch agitation techniques. *Can. J. Microbiol.* **45**, 9–17 (1999) doi: https://doi.org/10.1139/cjm-45-1-9

426. Howes, D. W. Overlap and the Errors of Plaque Counting I. The Overlap Biases of Observed Counts and their Correction. *J. Hyg. (Lond).* **67**, 317–334 (1969) doi: https://doi.org/10.1017/S0022172400041723

427. Howes, D. W. & Fazekas de St Groth, S. Overlap and the Errors of Plaque Counting II. The Bias of the Variance and the Concealment of Errors. *J. Hyg. (Lond).* **67**, 335–342 (1969) doi: https://doi.org/10.1017/S0022172400041735

428. Bechtold, B. Violin Plots for Matlab, Github Project. (2016) doi:10.5281/zenodo.4559847 doi: https://doi.org/10.5281/zenodo.4559847

429. Hintze, J. L. & Nelson, R. D. Violin Plots: A Box Plot-Density Trace Synergism. *Am. Stat.* **52**, 181–184 (1998) doi: https://doi.org/10.1080/00031305.1998.10480559

430. Schindelin, J. *et al.* Fiji: an open-source platform for biological-image analysis. *Nat. Methods* **9**, 676–682 (2012) doi: https://doi.org/10.1038/nmeth.2019

431. Kramberger, P., Ciringer, M., Trancar, A. & Peterka, M. Evaluation of nanoparticle tracking analysis for total virus particle determination. *Virol. J.* **9**, 1–10 (2012) doi: https://doi.org/10.1186/1743-422X-9-265

432. Lytle, C. D. *et al.* Important factors for testing barrier materials with surrogate viruses. *Appl. Environ. Microbiol.* **57**, 2549–2554 (1991) doi: https://doi.org/10.1128/aem.57.9.2549-2554.1991

433. Thompson, S. S. & Yates, M. V. Bacteriophage inactivation at the air-water-solid interface in dynamic batch systems. *Appl. Environ. Microbiol.* **65**, 1186–1190 (1999) doi: https://doi.org/10.1128/aem.65.3.1186-1190.1999

434. Thompson, S. S., Flury, M., Yates, M. V. & Jury, W. A. Role of the Air-Water-Solid Interface in Bacteriophage Sorption Experiments. *Appl. Environ. Microbiol.* **64**, 304–309 (1998) doi: https://doi.org/10.1128/aem.64.1.304-309.1998

435. Shezad, K. *et al.* Surface Roughness Modulates Diffusion and Fibrillation of Amyloid-β Peptide. *Langmuir* **32**, 8238–8244 (2016) doi: https://doi.org/10.1021/acs.langmuir.6b01756

436. Hanke, M., Yang, Y., Ji, Y., Grundmeier, G. & Keller, A. Nanoscale surface topography modulates hiapp aggregation pathways at solid–liquid interfaces. *Int. J. Mol. Sci.* **22**, (2021) doi: https://doi.org/10.3390/ijms22105142

437. Co, N. T. & Li, M. S. Effect of surface roughness on aggregation of polypeptide chains: A monte carlo study. *Biomolecules* **11**, 1–16 (2021) doi: https://doi.org/10.3390/biom11040596

438. Kam, K. R. *et al.* The effect of nanotopography on modulating protein adsorption and the fibrotic response. *Tissue Eng. - Part A* **20**, 130–138 (2014) doi: https://doi.org/10.1089/ten.tea.2012.0772

439. Nie, H. Y., Walzak, M. J., Berno, B. & McIntyre, N. S. Atomic force microscopy study of polypropylene surfaces treated by UV and ozone exposure: Modification of morphology and adhesion force. *Appl. Surf. Sci.* **144–145**, 627–632 (1999) doi: https://doi.org/10.1016/S0169-4332(98)00879-4

440. Dika, C., Ly-Chatain, M. H., Francius, G., Duval, J. F. L. & Gantzer, C. Non-DLVO adhesion of F-specific RNA bacteriophages to abiotic surfaces: Importance of surface roughness, hydrophobic and electrostatic interactions. *Colloids Surfaces A Physicochem. Eng. Asp.* **435**, 178–187 (2013) doi: https://doi.org/10.1016/j.colsurfa.2013.02.045

441. Rabe, M., Verdes, D. & Seeger, S. Understanding protein adsorption phenomena at solid surfaces. *Adv. Colloid Interface Sci.* **162**, 87–106 (2011) doi: https://doi.org/10.1016/j.cis.2010.12.007

442. Lytle, C. D. & Routson, L. B. Minimized virus binding for tests of barrier materials. *Appl. Environ. Microbiol.* **61**, 643–649 (1995) doi: https://doi.org/10.1128/aem.61.2.643-649.1995

443. Ferry, T., Kolenda, C. & Resch, G. Personalized bacteriophage therapy to treat pandrug-resistant spinal P . aeruginosa infection. 1–7

444. Rajnovic, D., Muñoz-Berbel, X. & Mas, J. Fast phage detection and quantification: An optical density-based approach. *PLoS One* **14**, 1–14 (2019) doi: https://doi.org/10.1371/journal.pone.0216292

445. Genuer, V. *et al.* Optical elastic scattering for early label-free identification of clinical pathogens. *Adv. Biomed. Clin. Diagnostic Surg. Guid. Syst. XIV* **9698**, 96980A (2016) doi: https://doi.org/10.1117/12.2211021

446. Tardif, M. *et al.* On-Chip Optical Nano-Tweezers for Culture-Less Fast Bacterial Viability Assessment. *Small* **18**, 2103765 (2022) doi: https://doi.org/10.1002/smll.202103765

447. le Galudec, J., Dupoy, M., Rebuffel, V. & Marcoux, P. R. Mid-infrared multispectral lensless imaging for wide-field and label-free microbial identification. *Proc.SPIE* **11359**, (2020) doi: https://doi.org/10.1117/12.2557502

448. Marcoux, P. R. *et al.* Optical forward-scattering for identification of bacteria within microcolonies. *Appl. Microbiol. Biotechnol.* **98**, 2243–2254 (2014) doi: https://doi.org/10.1007/s00253-013-5495-4

449. Tardif, M. *et al.* Single-cell bacterium identification with a SOI optical microcavity. *Appl. Phys. Lett.* **109**, 1–6 (2016) doi: https://doi.org/10.1063/1.4963070

450. Tang, Z. *et al.* Whey protein improves survival and release characteristics of bacteriophage Felix O1 encapsulated in alginate microspheres. *Food Res. Int.* **52**, 460–466 (2013) doi: https://doi.org/10.1016/j.foodres.2012.12.037

451. Mandula, O. *et al.* Phase and fluorescence imaging with a surprisingly simple microscope based on chromatic aberration. *Opt. Express* **28**, 2079 (2020) doi: https://doi.org/10.1364/oe.28.002079

452. Tinevez, J. Y. *et al.* TrackMate: An open and extensible platform for single-particle tracking. *Methods* **115**, 80–90 (2017) doi: https://doi.org/10.1016/j.ymeth.2016.09.016

453. Harwood, C. S., Fosnaugh, K. & Dispensa, M. Flagellation of Pseudomonas putida and analysis of its motile behavior. *J. Bacteriol.* **171**, 4063–4066 (1989) doi: https://doi.org/10.1128/jb.171.7.4063-4066.1989

454. Pollitt, E. J. G. & Diggle, S. P. Defining motility in the Staphylococci. *Cell. Mol. Life Sci.* **74**, 2943–2958 (2017) doi:

https://doi.org/10.1007/s00018-017-2507-z

455. Li, X. *et al.* An accessory wall teichoic acid glycosyltransferase protects Staphylococcus aureus from the lytic activity of Podoviridae. *Sci. Rep.* **5**, 1–10 (2015) doi: https://doi.org/10.1038/srep17219

456. Rajaure, M., Berry, J., Kongari, R., Cahill, J. & Young, R. Membrane fusion during phage lysis. *Proc. Natl. Acad. Sci. U. S. A.* **112**, 5497–5502 (2015) doi: https://doi.org/10.1073/pnas.1420588112

457. Bradley, D. E. Spheroplast formation in cells of Escherichia coli infected with a phi-X 174 type bacteriophage. *J. Gen. Virol.* **3**, 141–142 (1968) doi: https://doi.org/10.1099/0022-1317-3-1-141

458. Ramanathan, S., Gopinath, S. C. B., Ismail, Z. H., Md Arshad, M. K. & Poopalan, P. Aptasensing nucleocapsid protein on nanodiamond assembled gold interdigitated electrodes for impedimetric SARS-CoV-2 infectious disease assessment. *Biosens. Bioelectron.* **197**, 113735 (2022) doi: https://doi.org/https://doi.org/10.1016/j.bios.2021.113735

459. Wang, L. *et al.* A sensitive DNA capacitive biosensor using interdigitated electrodes. *Biosens. Bioelectron.* **87**, 646–653 (2017) doi: https://doi.org/10.1016/j.bios.2016.09.006

460. Fiedler, S., Shirley, S. G., Schnelle, T. & Fuhr, G. Dielectrophoretic Sorting of Particles and Cells in a Microsystem. *Anal. Chem.* **70**, 1909–1915 (1998)

461. Alexander, F., Price, D. T. & Bhansali, S. Optimization of interdigitated electrode (IDE) arrays for impedance based evaluation of Hs 578T cancer cells. in *Journal of Physics: Conference Series* vol. 224 (2010). doi: https://doi.org/10.1088/1742-6596/224/1/012134

462. Dos Santos-Neto, I. S. *et al.* Interdigitated electrode for electrical characterization of commercial pseudo-binary biodiesel–diesel blends. *Sensors* **21**, (2021) doi: https://doi.org/10.3390/s21217288

463. Mazlan, N. S. *et al.* Interdigitated electrodes as impedance and capacitance biosensors: A review. *AIP Conf. Proc.* **1885**, (2017) doi: https://doi.org/10.1063/1.5002470

464. Tsouti, V., Boutopoulos, C., Zergioti, I. & Chatzandroulis, S. Capacitive microsystems for biological sensing. *Biosens. Bioelectron.* **27**, 1–11 (2011) doi: https://doi.org/10.1016/j.bios.2011.05.047

465. Khan, R. R. & Kang, S. W. Highly sensitive multi-channel IDC sensor array for low concentration taste detection. *Sensors (Switzerland)* **15**, 13201–13221 (2015) doi: https://doi.org/10.3390/s150613201

466. Avenas, Q. *et al.* Performance improvement of plasmonic sensors using a combination of AC electrokinetic effects for (bio)target capture. *Electrophoresis* **40**, 1426–1435 (2019) doi: https://doi.org/10.1002/elps.201800436

467. Costella, M. *et al.* Dielectrophoretic cell trapping for improved surface plasmon resonance imaging sensing. *Electrophoresis* **40**, 1417–1425 (2019) doi: https://doi.org/10.1002/elps.201800439

468. Batra, N., Ansari, M. A., Singh, S. & Urooj, S. Fabrication of Interdigitated Electrodes based biosensor and Prediction of Covid-19 cases using Linear Regression. *Int. J. Disaster Recover. Bus. Contin.* **11**, 2514–2527 (2020)

469. Madou, M. J. Volume 2 Part I: Lithography. in *Fundamentals of Microfabrication and Nanotechnology* (CRC Press, 2011).

470. Hart, C. *et al.* Rapid nanofabrication of nanostructured interdigitated electrodes (NIDES) for long-term in vitro analysis of human induced pluripotent stem cell differentiated cardiomyocytes. *Biosensors* **8**, 1–10 (2018) doi: https://doi.org/10.3390/bios8040088

471. Terao, K. & Kondo, S. AC-Electroosmosis-Assisted Surface Plasmon Resonance Sensing for Enhancing Protein Signals with a Simple Kretschmann Configuration. *Sensors* **22**, (2022) doi: https://doi.org/10.3390/s22030854

472. Colniță, A., Marconi, D. & Turcu, I. Fabrication of Interdigitated Electrodes using Molecular Beam Epitaxy and Optical Lithography. *Anal. Lett.* **49**, 378–386 (2016) doi: https://doi.org/10.1080/00032719.2015.1033719

473. Tran, V. T., Wei, Y., Liau, W. J., Yang, H. & Du, H. Preparing of interdigitated microelectrode arrays for AC electrokinetic devices using inkjet printing of silver nanoparticles ink. *Micromachines* **8**, (2017) doi:

https://doi.org/10.3390/mi8040106

474. Gaál, G. *et al.* 3D printed e-tongue. *Front. Chem.* **6**, 1–8 (2018) doi: https://doi.org/10.3389/fchem.2018.00151

475. Contreras-Saenz, M., Hassard, C., Vargas-Chacon, R., Gordillo, J. L. & Camacho-Leon, S. Maskless fabrication of a microfluidic device with interdigitated electrodes on PCB using laser ablation. in *Proc. SPIE 9705, Microfluidics, BioMEMS, and Medical Microsystems XIV, 97050N* vol. 9705 18–24 (2016). doi: https://doi.org/10.1117/12.2222961

476. Tender, L. M., Worley, R. L., Fan, H. & Lopez, G. P. Electrochemical Patterning of Self-Assembled Monolayers onto Microscopic Arrays of Gold Electrodes Fabricated by Laser Ablation. *Langmuir* **12**, 5515–5518 (1996) doi: https://doi.org/10.1021/la960627o

477. Manzoli, A. *et al.* Femtosecond laser ablation of gold interdigitated electrodes for electronic tongues. *Opt. Laser Technol.* **69**, 148–153 (2015) doi: https://doi.org/10.1016/j.optlastec.2014.12.026

478. Barik, A. *et al.* Dielectrophoresis-enhanced plasmonic sensing with gold nanohole arrays. *Nano Lett.* **14**, 2006–2012 (2014) doi: https://doi.org/10.1021/nl500149h

479. Song, Y. *et al.* AC Electroosmosis-Enhanced Nanoplasmofluidic Detection of Ultralow-Concentration Cytokine. *Nano Lett.* **17**, 2374–2380 (2017) doi: https://doi.org/10.1021/acs.nanolett.6b05313

480. Tai, Y. H., Chang, D. M., Pan, M. Y., Huang, D. W. & Wei, P. K. Sensitive detection of small particles in fluids using optical fiber tip with dielectrophoresis. *Sensors* **16**, 1–9 (2016) doi: https://doi.org/10.3390/s16030303

481. Cottet, J. *et al.* MyDEP: A New Computational Tool for Dielectric Modeling of Particles and Cells. *Biophys. J.* **116**, 12–18 (2019) doi: https://doi.org/10.1016/j.bpj.2018.11.021

482. Gagnon, Z. R. Cellular dielectrophoresis: Applications to the characterization, manipulation, separation and patterning of cells. *Electrophoresis* **32**, 2466–2487 (2011) doi: https://doi.org/10.1002/elps.201100060

483. Green, N. G., Ramos, A., González, A., Morgan, H. & Castellanos, A. Fluid flow induced by nonuniform ac electric fields in electrolytes on microelectrodes. I. Experimental measurements. *Phys. Rev. E - Stat. Physics, Plasmas, Fluids, Relat. Interdiscip. Top.* **61**, 4011–4018 (2000) doi: https://doi.org/10.1103/PhysRevE.61.4011

484. Ramos, A., Morgan, H., Green, N. G. & Castellanos, A. AC electric-field-induced fluid flow in microelectrodes. *J. Colloid Interface Sci.* **217**, 420–422 (1999) doi: https://doi.org/10.1006/jcis.1999.6346

485. Kim, J. & Na, S. Metal thin film ablation with femtosecond pulsed laser. *Opt. Laser Technol.* **39**, 1443–1448 (2007) doi: https://doi.org/10.1016/j.optlastec.2006.10.001

486. Radke, S. M. & Alocilja, E. C. Design and fabrication of a microimpedance biosensor for bacterial detection. *IEEE Sens. J.* **4**, 434–440 (2004) doi: https://doi.org/10.1109/JSEN.2004.830300

487. Laczka, O., Baldrich, V., Muñoz, F. X. & Campo, J. del. Detection of Escherichia coli and Salmonella typhimurium Using Interdigitated Microelectrode Capacitive Immunosensors: The Importance of Transducer Geometry. *Anal. Chem.* **80**, 7239–7247 (2008)

488. Schaffer, C. B., Brodeur, A., García, J. F. & Mazur, E. Micromachining bulk glass by use of femtosecond laser pulses with nanojoule energy. *Opt. Lett.* **26**, 93–95 (2001)

489. Romeo, D., Skerlavaj, B., Bolognesi, M. & Gennaro, R. Structure and bactericidal activity of an antibiotic dodecapeptide purified from bovine neutrophils. *J. Biol. Chem.* **263**, 9573–9575 (1988) doi: https://doi.org/10.1016/s0021-9258(19)81553-3

490. Hilpert, K., Volkmer-Engert, R., Walter, T. & Hancock, R. E. W. High-throughput generation of small antibacterial peptides with improved activity. *Nat. Biotechnol.* **23**, 1008–1012 (2005) doi: https://doi.org/10.1038/nbt1113

491. Andreu, D. *et al.* Shortened cecropin A-melittin hybrids Significant size reduction retains potent antibiotic activity. *FEBS Lett.* **296**, 190–194 (1992) doi: https://doi.org/10.1016/0014-5793(92)80377-S

492. Derossi, D., Joliot, A. H., Chassaing, G. & Prochiantz, A. The third helix of the Antennapedia homeodomain translocates through biological membranes. *J. Biol. Chem.* **269**, 10444–10450 (1994) doi:

https://doi.org/10.1016/s0021-9258(17)34080-2

493. Zasloff, M. Magainins, a class of antimicrobial peptides from Xenopus skin: Isolation, characterization of two active forms, and partial cDNA sequence of a precursor. *Proc. Natl. Acad. Sci. U. S. A.* **84**, 5449–5453 (1987) doi: https://doi.org/10.1073/pnas.84.15.5449

494. Galvan, D. D., Parekh, V., Liu, E., Liu, E. L. & Yu, Q. Sensitive Bacterial Detection via Dielectrophoretic-Enhanced Mass Transport Using Surface-Plasmon-Resonance Biosensors. *Anal. Chem.* **90**, 14635–14642 (2018) doi: https://doi.org/10.1021/acs.analchem.8b05137

495. Bisceglia, E. *et al.* Micro-organism extraction from biological samples using DEP forces enhanced by osmotic shock. *Lab Chip* 1037–1043 (2014)

496. Bisceglia, E. *et al.* A generic and label free method based on dielectrophoresis for the continuous separation of microorganism from whole blood samples. *Sensors Actuators, B Chem.* **212**, 335–343 (2015) doi: https://doi.org/10.1016/j.snb.2015.02.024

497. Zhang, Y. & Chen, X. Dielectrophoretic microfluidic device for separation of red blood cells and platelets: a model-based study. *J. Brazilian Soc. Mech. Sci. Eng.* **42**, (2020) doi: https://doi.org/10.1007/s40430-020-2169-x

498. Sang, S. *et al.* Portable microsystem integrates multifunctional dielectrophoresis manipulations and a surface stress biosensor to detect red blood cells for hemolytic anemia. *Sci. Rep.* **6**, 1–8 (2016) doi: https://doi.org/10.1038/srep33626

499. Yang, J., Huang, Y., Wang, X. B., Becker, F. F. & Gascoyne, P. R. C. Differential analysis of human leukocytes by dielectrophoretic field- flow-fractionation. *Biophys. J.* **78**, 2680–2689 (2000) doi: https://doi.org/10.1016/S0006-3495(00)76812-3

500. Hashimoto, M., Kaji, H. & Nishizawa, M. Selective capture of a specific cell type from mixed leucocytes in an electrode-integrated microfluidic device. *Biosens. Bioelectron.* **24**, 2892–2897 (2009) doi: https://doi.org/10.1016/j.bios.2009.02.025

501. Henslee, E. A., Sano, M. B., Rojas, A. D., Schmelz, E. M. & Davalos, R. V. Selective concentration of human cancer cells using contactless dielectrophoresis. *Electrophoresis* **32**, 2523–2529 (2011) doi: https://doi.org/10.1002/elps.201100081

502. Nobile, M. S., Cazzaniga, P., Tangherloni, A. & Besozzi, D. Graphics processing units in bioinformatics, computational biology and systems biology. *Brief. Bioinform.* **18**, 870–885 (2017) doi: https://doi.org/10.1093/bib/bbw058

503. Jumper, J. *et al.* Highly accurate protein structure prediction with AlphaFold. *Nature* **596**, 583–589 (2021) doi: https://doi.org/10.1038/s41586-021-03819-2

504. Tunyasuvunakool, K. *et al.* Highly accurate protein structure prediction for the human proteome. *Nature* **596**, 590–596 (2021) doi: https://doi.org/10.1038/s41586-021-03828-1

505. Grover, N. AI firm DeepMind puts database of the building blocks of life online. *The Guardian* (2021)

506. Zhou, F. *et al.* PHISDetector: A tool to detect diverse in silico phage–host interaction signals for virome studies. *Genomics. Proteomics Bioinformatics* (2022) doi:doi.org/10.1016/j.gpb.2022.02.003 doi: https://doi.org/doi.org/10.1016/j.gpb.2022.02.003

507. Goulet, A. & Cambillau, C. Structure and topology prediction of phage adhesion devices using alphafold2: The case of two oenococcus oeni phages. *Microorganisms* **9**, 1–13 (2021) doi: https://doi.org/10.3390/microorganisms9102151

508. Leite, D. M. C. *et al.* Computational prediction of inter-species relationships through omics data analysis and machine learning. *BMC Bioinformatics* **19**, (2018) doi: https://doi.org/10.1186/s12859-018-2388-7

509. Molina, F. *et al.* A New Pipeline for Designing Phage Cocktails Based on Phage-Bacteria Infection Networks. *Front. Microbiol.* **12**, 1–14 (2021) doi: https://doi.org/10.3389/fmicb.2021.564532

510. Niu, Y. D. *et al.* Efficacy of Individual Bacteriophages Does Not Predict Efficacy of Bacteriophage Cocktails for Control of Escherichia coli O157. *Front. Microbiol.* **12**, (2021) doi: https://doi.org/10.3389/fmicb.2021.616712

511. Truchado, P., Elsser-Gravesen, A., Gil, M. I. & Allende, A. Post-process treatments are effective strategies to reduce Listeria monocytogenes on the surface of leafy greens: A pilot study. *Int. J. Food Microbiol.* (2019)

512. Cordero-Bueso, G., Moraga, J., Rios-Carrasco, M., Ruiz-Muñoz, M. & Cantoral, J. M. Isolation of bacteriophages from must and wine for the elimination of contaminating bacteria as an alternative to the use of sulfurous. *BIO Web Conf.* **15**, (2019)

513. Nojoumi, S. *et al.* Phage capsid nanoparticles with defined ligand arrangement block influenza virus entry - An antiviral strategy. *Nat. Nanotechnol.* (2019) doi:10.1038/s41565-020-0660-2 doi: https://doi.org/10.1038/s41565-020-0660-2

514. Hershey, A. D., Kalmanson, G. M. & Bronfenbrenner, J. Quantitative Methods in the Study of the Phage-Antiphage Reaction. *J. Immunol.* **46**, 267 LP – 279 (1943)

515. Lanni, F. & Lanni, Y. T. Antigenic structure of bacteriophage. in *Cold Spring Harb Symp Quant Biol* 159–168 (1953). doi:10.1101/sqb.1953.018.01.026 doi: https://doi.org/10.1101/sqb.1953.018.01.026

516. Hiatt, C. W. Kinetics of the Inactivation of Viruses. *Bacteriol. Rev.* **28**, 150–163 (1964) doi: https://doi.org/10.1128/mmbr.28.2.150-163.1964

517. Evaluation of measurement data — Guide to the expression of uncertainty in measurement. *JCGM 100:2008 (GUM 1995 with minor corrections)* 19 (2008)

518. *Setting tolerances for pipettes in the laboratory*. http://www.labautopedia.com/mw/index.php/Setting_tolerances_for_pipettes_in_the_laboratory (2021)

519. Kyaw, H. H., Al-Harthi, S. H., Sellai, A. & Dutta, J. Self-organization of gold nanoparticles on silanated surfaces. *Beilstein J. Nanotechnol.* **6**, 2345–2353 (2015) doi: https://doi.org/10.3762/bjnano.6.242

520. Naik, V. V., Crobu, M., Venkataraman, N. V. & Spencer, N. D. Multiple transmission-reflection ir spectroscopy shows that surface hydroxyls play only a minor role in alkylsilane monolayer formation on silica. *J. Phys. Chem. Lett.* **4**, 2745–2751 (2013) doi: https://doi.org/10.1021/jz401440d